VIBRO-ACOUSTIC MONITORING OF NESTED PLANETARY GEAR TRAINS

by

Jianxiong Feng

A Dissertation

Submitted to the Faculty of Purdue University

In Partial Fulfillment of the Requirements for the degree of

Doctor of Philosophy

School of Mechanical Engineering

West Lafayette, Indiana

December 2021

THE PURDUE UNIVERSITY GRADUATE SCHOOL
STATEMENT OF COMMITTEE APPROVAL

Dr. Kai Ming Li, Co-Chair

School of Mechanical Engineering

Dr. Yangfan Liu, Co-Chair

School of Mechanical Engineering

Dr. J. Stuart Bolton

School of Mechanical Engineering

Dr. Fabio Semperlotti

School of Mechanical Engineering

Dr. Robert Nowack

Department of Earth, Atmosphere, and Planetary Science

Approved by:

Dr. Nicole Key

ACKNOWLEDGMENTS

First and foremost, I have to express my gratitude to my advisors, Dr. Kai Ming Li and Dr. Yangfan Liu. Advisors are always the most important people to a student during our Ph.D. study. And indeed, I've never felt my life could be affected by certain people so much before starting my Ph.D. career. I have to be honest that I feel like my life is out of the control of my hands sometimes, and I hate this feeling. But thankfully, my advisors are reasonable persons, and they are willing to help me. I learned a lot of things from each one of them, and I'm sure those I've learned will be the most valuable things for the rest of my professional career.

Then, I need to thank the professors in my advisory committee, Dr. Stuart Bolton, Dr. Fabio Semperlotti, Dr. Robert Nowack. Dr. Bolton is one of the most energetic and happiest people I've ever met. It is hard to believe he has such a positive mentality in his 70s. And I was so honored that I did not just have him on my committee board but also took his two courses in acoustics. To be honest, I have not seen Dr. Semperlotti many times. But he really gave me tremendous help in preparing my final defense presentation. I would say my defense could have been a disaster without his very insightful advice. Unfortunately, I did not have many chances to talk with Dr. Nowack, either. Still, whenever he showed up in my prelim or final exam, he brought a lot of insight that we mechanical engineers would have neglected.

I have to say Midwest is a cold place. Besides the weather, it is also extremely hard to mingle with local people, especially as a Chinese and an Asian male. In this kind of environment full of cultural differences and racial stereotypes, the only cure for my life is friendship. Although my friends and I feel isolated in this society, I made the best friends of my life through the past few years. (Alphabetic Order) Jiayu An, Yidan Cui, Wei Ding, Bin Du, Kairui Hao, Rifeng Huang, Chufan Jiang, Joohyun Lee, Yuchuan Lei, Tao Li, Lu Ling, Ziping Liu, Jiaxin Luo, Zhuang Mo, Weijing Qiu, Guochenhao Song, Wenjing Wang, Yiming Wang, Zhanyu Wang, Feng Wu, Yujian Xu, Yongjie Zhuang, Zijie Zhou, and some other names that may slip my mind for this moment. You guys are the cutest people I've ever known for the past of my life, and I hope our friendship can continue forever.

There is another name that I need to give most special thanks to, Yuan Chen. She took care of me incredibly when I had my knee surgery and saved me from quitting my Ph.D. when I was most vulnerable. I guess most people may regret putting the name of their significant other on their

thesis because love is not robust as friendship. But I'll try my best to keep myself from regretting this decision for the rest of my life.

Last but not least, I would thank myself. I know very few people did this in their acknowledgment part of a thesis. But I feel I have to do this even if this sounds very narcissistic. So many people helped me, and many people tried to save me. But it is me who gets myself together every time; it is me who is determined to persist every time. Do I have a high IQ? No. Do I have a passion for research? Maybe. But I always believe in my mental resistance and perseverance. And that is what I'm proud of myself. Although, to be honest, I do regret the decision to come to a cold place to pursue a Ph.D. degree in a field that I do not love. I could have made wiser choices by not doing this and pursuing my other passions. But once I realize what has been done cannot be undone, I'll endeavor to see the end of the path no matter how hard it is.

Hopefully, I'll be in a new chapter of my life when this document is published. And I hope this new journey can give me a more balanced portion between sweetness and bitterness.

TABLE OF CONTENTS

LIST OF TABLES

LIST OF FIGURES

ABBREVIATIONS

BoB: Best of the Best Gear

WoW: Worst of the Worst Gear

D: Damaged Gear

TSA: Time Synchronous Averaging

NAH: Near-field Acoustical Holography

WBH: Wideband Holography

CVX: Convex Optimization

VRA: virtual rotating array

CESM: equivalent source based compressive sensing holography

ABSTRACT

Gear systems are major components in the modern power transmission system, especially in the automobile industry. In recent years, with the auto transmission function development, more compound gears have been utilized for better transmission speed ratio control and space-saving. The nested planetary gear train is widely applied among the newly designed compound gear trains due to its compactness. However, the nested gear train noise and vibration issue have not been studied extensively. In the current study, the vibrational and acoustical monitoring prototype will be developed to monitor the nested planetary manufacturing accuracy in the production line. Firstly, a novel testing fixture with the vertical and open setup is proposed to be used to monitor the gear, which is different from most gear condition monitoring studies. The open setup allows the accelerometer to be mounted directly on different clutches to monitor both carriers in the nested two-stage gear system closely. The test setup also enables the acoustical array to be implemented. Gear carriers with different pinion faults or damages are tested with both vibrational and acoustical sensors to identify the pinion gear error type and location. The vibrational data are processed with several classical rotating machinery signal processing techniques, including: (1) time synchronous averaging; (2) modulation sideband analysis; (3) modulation sideband modeling; (4) narrowband demodulation. Those techniques are also partially modified to adapt for the nested planetary structure monitoring. The results show that the unground or damaged pinions can be successfully identified and localized. Besides vibrational signal monitoring, an acoustical array is also proposed for noise source visualization and localization of the outer gearset (stage-2). The virtual rotating array (VRA) methods are proposed to de-Ddopperize the rotating source sound signals measured at stationary receivers. The VRA signals are subsequently used as input of the equivalent source based compressive sensing holography for high-resolution localization of the compact rotating sources. Both time-domain VRA and frequency domain VRA methods are studied and further developed for improved computational efficiency in terms of the VRA process. The new developments of the acoustical imaging system for rotating source localization are validated numerically and experimentally. Last but not least, the acoustical imaging system has also been successfully applied to the unground gear condition monitoring in the outer gearset of the nested gear train.

1. INTRODUCTION

1.1 Background and Motivation: Gear Condition Monitoring

Gears have been applied in mechanical mechanisms and machines for hundreds of years, and gear systems are still the major components in the power transmission system, especially in the automobile industry. One main advantage of the gear transmission is that the gear teeth meshing can provide a stable and precise velocity ratio. Aside from its advantages in power transmissions and speed control, the noise and vibration generated by gear meshing are becoming increasingly concerned, especially in the automobile industry, where vehicle NVH is an essential criterion for customer satisfaction. The importance of the powertrain gear NVH characteristics is receiving more attention than before since the trend of developing electrified vehicles obliterates the internal combustion engine, which is considered the most dominant noise source in traditional vehicles. This boosts the demands for producing quieter gear systems to achieve a lower transmission noise level, which is possible only if more accurate gear manufacture can be guaranteed. Thus, it is desired to have an efficient and reliable quality monitoring system for the gear manufacturing process in the automobile manufacturing industry.

To conduct the accurate analysis of gear NVH characteristics and ensure the high quality of the gears, transmission error (TE) is the critical parameter. Transmission error is identified as the most significant source of gear noise excitation. It is defined as the difference between the theoretical position of rigid, fault-free gears and their position in actual operations. Theoretically, there will be no transmission error if the meshing gear teeth have a perfect involute profile and engage with a zero-loading torque. However, if teeth deflection exists, the torsional mesh stiffness will be changed when transferring torque between engaging gears. The changing torsional mesh stiffness can cause variations in gear body rotation, thus causing transmission errors. Although the transmission error is comparatively tiny compared to the gear dimension, those small shifts can be the primary source of noise and vibration near the resonance frequency of gear dynamics. The main factors that can increase the transmission errors are

1. errors in tooth geometry caused by the inaccuracy in manufacturing of gears,
2. elastic deformation of meshing teeth and gear bodies due to the side load,
3. geometric error in alignment due to incorrect mounting of gears.

While the elastic deformation and the gear mounting are usually the factors to consider outside the manufacturing process, the accuracy issues caused by manufacturing itself should be controlled during the manufacturing stage.

Besides the improvement of manufacture equipment's precision and processing procedures, the monitoring of the gear condition in the manufacturing line is also important in ensuring the gear manufacturing accuracy. There are different monitoring techniques that can be applied in the gear product line, such as visual inspection or optical testing. But those examining techniques usually either require high cost and or are not reliable enough when gears are not showing visually inspectable faults. Compared with the visual or optical inspection, vibrational and acoustical testing of the gears is an excellent alternative, due to its high accuracy capability and its non-destructive nature. The existing NVH testing of gears usually employs vibrational or acoustical sensors to monitor the gear train noise emission or the structural vibration. In particular, the vibrational monitoring of the gear condition has been applied extensively to the structural health monitoring for the last few decades. However, for those previous monitoring techniques, most of them focused on monitoring the assembled gear system in operation, in order to predict the gear fatigue or failure. Not many solutions have been developed for a component-level gear manufacturing accuracy monitoring in the product line.

Besides improving manufacturing equipment's precision and processing procedures, monitoring the gear condition in the manufacturing line is also essential in ensuring gear manufacturing accuracy. Different monitoring techniques can be applied in the gear product line, such as visual inspection or optical testing. However, those examining techniques usually require high cost or are not reliable enough when gears are not showing visually inspectable faults. Compared with the visual or optical inspection, vibrational and acoustical testing of the gears is an excellent alternative due to its high accuracy capability and its non-destructive nature. The existing NVH testing of gears usually employs vibrational or acoustical sensors to monitor the gear train noise emission or the structural vibration. In particular, the vibrational monitoring of the gear condition has been applied extensively to structural health monitoring for the last few decades. However, for those previous monitoring techniques, most of them focused on monitoring the assembled gear system in operation to predict gear fatigue or failure. As a result, not many solutions have been developed for component-level gear manufacturing accuracy monitoring in the product line.

Since the current study focuses on testing the individual gear carriers instead of the compete transmission assembly, the background of a single layer gear meshing structure is introduced first. There are two main types of gears from the teeth geometry point of view: spur gear and helical gear (Figure 1.1). Spur gear, also named straight-cut gear, is the most straightforward gear geometry. As its name suggested, the spur gear teeth are straight and parallel to the rotation axis. In comparison, the helical gear teeth are oblique to the axis of rotation. In the current study, all the targeted gears in the gear train are helical.

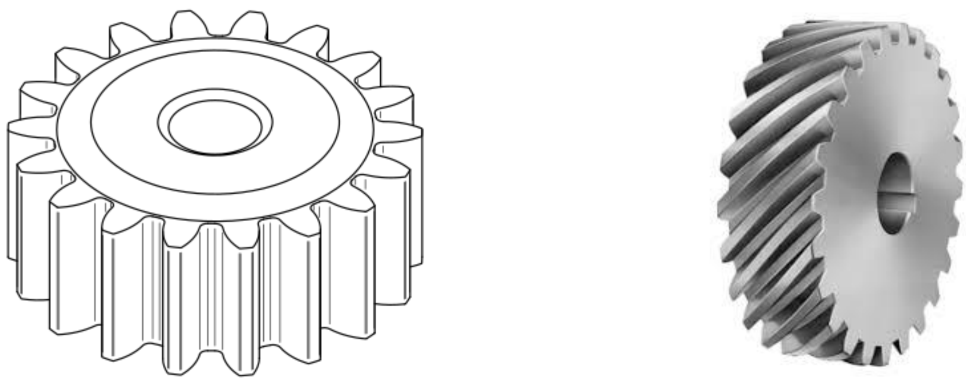

Figure 1.1. Spur gear (left) and helical (right) gear. (WikiPedia; Motion Control Clip)

In terms of the gear train types, two central gear train systems are used in most automobile transmission applications: (1) parallel-axis gear train; (2) planetary gear train. The countershaft parallel-axis gear train provides a constant speed ratio. However, the planetary gear train has the advantages of higher torque to weight ratio, improved compactness, smaller radial bearing loads, reduced noise, and many other benefits. Due to those reasons, the planetary gear train is one of the most widely applied designs in a modern transmission system. The planetary gear system consists of a sun gear, one or more rotating planet gears, and an annulus gear. Besides a single-stage planetary gear, compound planetary gear systems have also been widely used. For example, nested planetary gear has been developed to compact the gear transmission (Dopfert, 2013). As shown in Figure 1.2 (b), a nested transmission gear train integrates a sun gear at outer transmission with the annulus gear at the inner transmission. Due to the further improved structural compactness, the nested planetary gear has become a standard component in the transmission system. However, since the two planetary gear systems are integrated, the vibration excitation and transmission become more complicated within the carrier, making the monitoring more challenging to implement. Due to those reasons, in the current study, the NVH monitoring of the nested planetary gearset is investigated in detail.

In this study, the gear manufacturing inaccuracy that can cause the transmission error includes the following types: (1) tooth damage; (2) insufficient grinding of gears in the system. Some teeth may be damaged during the manufacturing process due to machining errors. In addition, if the grinding process is not completed correctly, the unground gear can exist in the gear system. The unground gear is a particular type of gear for which the surfaces of all teeth are not ground. As all teeth are unground gear, they have a uniform but thicker than standard teeth profile. Therefore, the unground gear meshing will generate more significant impact force and elastic deformation.

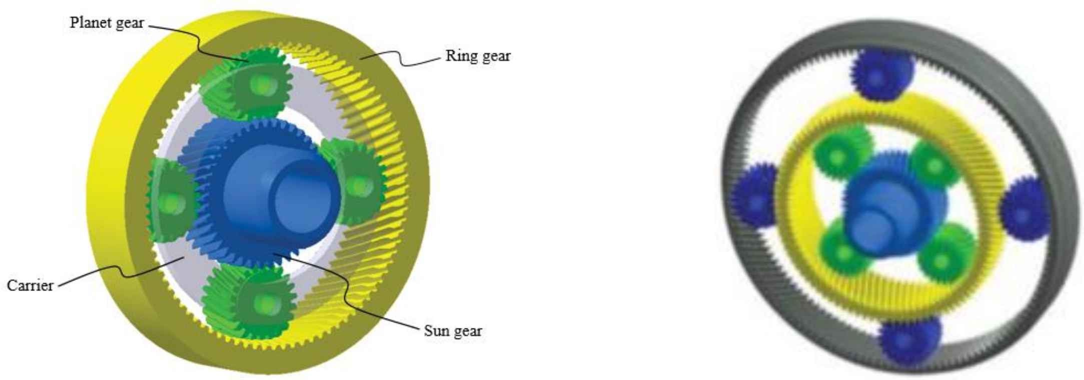

Figure 1.2. Planetary gear train (left) and nested planetary gear train (right) (Liao, 2018)

In the existing literature, there are a variety of vibrational monitoring techniques developed for the gearbox condition monitoring to diagnose the early-stage gear crack or failure. Most of the previous studies utilized the vibrational sensor for gearbox monitoring. However, most of those analyses are done after the gears are assembled and are implemented in actual operation. In addition, all those techniques were developed based on the structure of single-stage counter-shaft gears or planetary gears. There is very little literature on the condition monitoring of nested planetary gear trains. The nested planetary gears contain two planetary gear sets, which can be monitored independently. However, the interaction between the two planetary structures cannot be ignored since the inner annulus gear and the outer sun gear are integrated.

Moreover, the teeth profile defects in one carrier can generate the vibration that then propagates to the other carrier. So more than one vibrational monitoring technique is required to analyze the nested structure. Instead of applying existing techniques directly, modifications and improvements must be made to be implemented in nested structure monitoring.

In addition to vibrational monitoring of the gear conditions, methods based on acoustical sensor arrays are also proposed in the current study. The acoustic monitoring has the advantage of being completely non-contact. However, microphone monitoring of the acoustic emission usually does not contain more information than the vibrational sensor. Therefore, the acoustical array technique can be applied for the noise source localization and sound field visualization, which can, in principle, be applied to locate the problematic gears in the nested gear assembly. The background and the objective of the acoustical array techniques will be explained in more detail in the next section.

1.2 Background and Motivation: Rotating Sound Source Acoustical Imaging

The gear noise generation is primarily due to the impact or contact force between the meshing teeth. For the planetary gear system, the planet gears rotate with the carrier while self-spinning. Therefore, the noise source is not stationary but moving and rotating. For a carrier with unground pinions, it is assumed that the unground pinion generates higher acoustic emission than the other normal pinions at all rotation periods. The reasons mentioned above motivate applying the acoustic array to identify the noise source and the problematic pinion among all the rotating pinions in the planetary gear system. The two most commonly used techniques are noise source localization using acoustical array imaging, beamforming, and near-field holography algorithms. Both methods have been widely applied to the non-destructive testing of the noise source in mechanical systems. Beamforming mainly works well in identifying far-field sources, while the near field holography works better in near field noise source tracking. In the current study, the gear structure is highly compact, so beamforming is not practical in the current application. Therefore, the near-field holography is more suitable for compact rotating sound source identification. However, most of the previous holography work is based on stationary or linearly moving sources. This inspires the current study to develop the holograph approach that can be used to track the near-field compact rotating sources.

Although the beamforming techniques cannot be applied directly to the current study, the background of beamforming is still introduced here because some beamforming techniques are developed for the rotating source tracking, some ideas of which can be applied to the current holography development. The beamforming techniques are widely used in far-field noise trackings, such as airplane noise source visualization and axial fan turbine noise tracking. For mechanical products like engine turbines, a large portion of the total noise is contributed by rotating blades. Those engineering problems necessitate the development of beamforming for the rotating noise source tracking. The beamforming tracking of rotating noise sources can be categorized into two classes: (1) frequency domain methods; (2) time-domain methods. The modal decomposition approach has been proposed for the sound field interpolation in the frequency domain. On the other hand, one of the most used methods for the time domain algorithm is linear interpolation, which interpolates the static array signals to signals measured by a rotating array (a virtual rotating array). Since those methods do not modify the beamforming algorithm directly (it only manipulates the signals before the beamforming), they are explored in the current study to investigate its potential to be used as a preprocessing technique for acoustical holography. In the current study, the measurement of the stationary array is projected onto a virtually rotating array in both frequency and time domain and subsequently used as input for near-field holography for the reconstruction of near-field rotating sources. In addition to combining the virtual rotating array sound field with the holography methods, both the time and frequency domain virtual rotating array algorithms have been improved, and the interpolation efficiency has been improved significantly.

Near-field holography technology has been advanced significantly for the last few decades. The early holography methods based on the Fourier acoustics require the array to be in a specific arrangement (Maynard et al., 1985). With the recent development of the equivalent source-based techniques, not only the requirement for the array shape has been removed, but also the computational efficiency and accuracy have been improved significantly. There are several equivalent sources based compressive sensing techniques developed over the past few years, including the wideband holography (WBH) utilizing the steepest descent method (Hald, 2014), the L1 norm minimization (Fernande-Granade, 2015) using the convex optimization, the hybrid method between those two (Shi, 2019). Those methods have drawn extensive attention for the past few years due to their low requirement for the number of sensors and the high computational efficiency and accuracy. An example of the loudspeaker sound fields reconstruction is shown in Figure 1.3 and Figure 1.4. As shown in Figure 1.4, an acoustical array with 18 microphones is placed 0.5m away from the sound source. It can be seen from Figure 1.3 that the major sources can be identified by different holography methods. The statistically optimized near-field holography (SONAH) shows the most detailed reconstruction. However, the computational cost of SONAH is much higher than the other two equivalent-source-based ones. Despite the advancement in accuracy and efficiency, the acoustical holography methods to identify moving sources have not been highly focused on, especially for the rotating source localization. For the past study of the rotating source sound fields, most of the rotating source sound fields are generated aerodynamically, while the current study focuses on the sources generated by the mechanical impact of rotating components. Hence, the sources in the current study are more compact than aerodynamic sources and can be acoustically modeled as monopoles. In addition, the gear meshing noise is generated by mechanical impact, which suggests that the noise generation mechanism matches the fundamental assumption of those equivalent source-based near-field holography techniques: the sources are compact and sparsely distributed. However, the lack of existing solutions to reproduce the near-field rotating sound source field motivates the current development of the algorithm.

In the current study, the frequency and time domain virtual rotating array techniques are proposed to generate the array signals that the acoustical holography can use for high-resolution reconstruction of the compact rotating sound sources. In addition to the combination between the acoustical holography and the virtual rotating array, two more efficient virtual rotating array signal generation methods have also been developed. The first technique is to generate the virtual rotating array signal in the frequency domain by simple direct sideband summation. The second technique further simplifies the time domain linear interpolation and extends the interpolation to work with the randomized array.

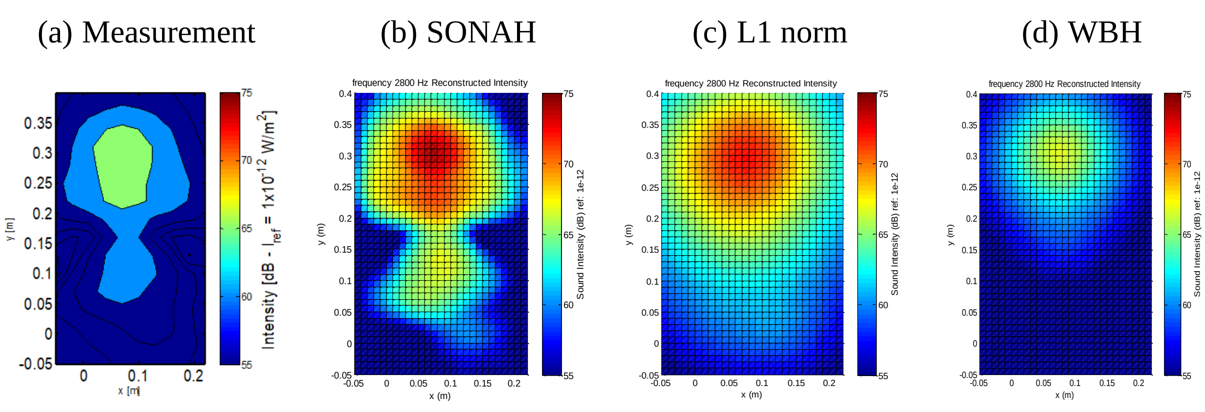

Figure 1.3. Holography Reconstruction results (Shi, 2018)

Figure 1.4. Array measurement for speaker

1.3 Thesis Structure

The first chapter describes the background and motivation for the current study. The development of the current work is based on a practical engineering problem, which is the monitoring of the nested planetary gear accuracy in the manufacturing product line. Therefore, both vibrational and acoustical sensors are proposed to be applied in the current study for a systematic study of the relationship between manufacturing errors and vibration and noise emission. Moreover, acoustical array solutions for rotating source monitoring have also been developed, inspired by the current engineering problem.

The second chapter reviews the literature related to the current study. Overall, four subjects are reviewed. The firstly reviewed topic is the gear vibrational monitoring for gears. The second section reviews the gear dynamics modeling to understand how the gear vibration is generated and transmitted. The third section deals with the rotating source sound field prediction. This part lays the foundation for understanding the reconstruction of the rotating source sound field. The fourth and last section reviews the beamforming and holography methods. Furthermore, this part introduces the current strategy for rotating source or compact source sound field visualization and provides the theoretical basis for developing the rotating source imaging system in the current work.

The third chapter details the experimental setup and procedures for testing the nested planetary gear. Firstly, the structure of the nested planetary gear is introduced. Then, the meshing frequency/order is calculated based on the structure of the gears. Finally, an innovative test fixture design is presented, which enables the collection of both the acoustical and vibrational signals. The test procedures and examples of signals are shown in the last section of the chapter.

The fourth chapter presents the signal processing of the vibrational signal data measured from the accelerometer mounted directly to the gear train clutches. For the nested planetary gear, the data are collected from two locations to enable monitoring both inner and outer planetary trains. Three signal processing techniques are applied: (1) time synchronous averaging; (2) frequency spectra analysis; (3) narrowband demodulation analysis. Those techniques are also extended and modified based on the unique structure of the targeted nested compound gear. The application of the three approaches successfully identified both the gear fault types and the location of the faulty gear for both inner and outer carriers.

In the fifth chapter, the holography algorithm developments for the rotating source localization are presented. The first section of the chapter starts with the derivation of the sound field due to a rotating source, which is the foundation for frequency domain virtual rotating array methods. Then, the traditional frequency-domain modal decomposition methods are introduced, and a simplified formula is introduced to extend the algorithm to be implemented with a non-circular array. The second section presents the time domain virtual rotating array signal generation algorithm in detail. Finally, in the third section, three equivalent-source-based compressive sensing holography are introduced: (1) wideband holography; (2) convex optimization of L1 norm formulation; (3) hybrid method between wideband holography and convex optimization.

The sixth chapter presents the validation of the developed holography algorithm using numerical cases. The first section introduces the numerical generation of the artificial rotating source signal. In the second section, the time domain VRA interpolation algorithms are investigated with numerical simulations. Moreover, the algorithm is tested with both randomized array and circular array. The third section tests if the frequency domain virtual rotating array signal works well with the holography algorithms. Both tonal source signals and broadband source signals are simulated and used to validate the holography development. Finally, the holography reconstruction results are presented with randomized and circular arrays.

The seventh chapter gives details about experimental results processed with the virtual rotating array-based holography methods. The first section presents the experimental setup for using the rotating speakers. The section part of the chapter discusses the rotating speaker experimental data processing with the time domain VRA methods. The third section validates the frequency domain VRA-based holography with the speaker test data. The last section presents the application of both time and frequency domain virtual rotating array methods to dedopplerize the rotating gear noise data measured by the microphone array.

The eighth chapter summarizes the current study and proposes the next step based on the current progress.

2. LITERATURE REVIEW

2.1 Gearbox Vibrational Diagnosis Approaches

The early detection of the mechanical system failure and examination of manufacturing error are of great practical importance as they reduce both risks of mechanical failure and the cost of repairing significantly. The rotating machinery has the unique feature of vibrational signals containing the periodic component with the revolution speed. Therefore, gear is typical rotating machinery, and gearbox condition monitoring has been one popular topic for the past few decades. The gear train has two main types: (1) counter-shaft gear train, for which relative position of the rotating axes do not change; (2) planetary gear train, which contains sun gear, planet gear, and annulus gear. The nested compound planetary gear train condition monitoring is investigated for the current study. Although nested planetary gear has a unique structure, the basic design for the sub-level gear train is still the same as a single-stage planetary gear. Therefore, several well-established methods for gear vibrational signal processing are applied and further extended in the current study: (1) time synchronous averaging; (2) modulation sideband analysis; (3) narrowband demodulation. Therefore, those techniques will be reviewed in this section.

2.1.1 Time synchronous averaging (TSA)

The early TSA processing utilized the convolution between the signal and a finite impulse train. The time between the impulses is the time of one revolution (Trimble, 1968). McFadden (1987) improved the robustness of TSA processing by adding rectangular windows and sampling to the Fourier transform to the existing comb filter model. When the rotational signal reference is not available, the signal needs to be interpolated to generate the phase-locked signals. In a subsequent study, McFadden (1989) examined the effects of using different windows. It was found that higher-order interpolation techniques have flatter passbands and smaller sidelobes, which results in averaged signals with better quality. Despite that the synchronous averaging can separate most signals related to rotating a particular gear-pair, testing consistency can still be an issue for a large gearbox. To tackle the variability in the vibration pattern across multiple experiments, the consecutive matched synchronous average is developed and applied to geartrain seeded faults detection (McFadden, 2000). The experiment is repeated with different tooth defects, and the matched difference for the averaged signals is calculated. The averaged signals and the matched difference can be decomposed using S transform to indicate the structural faults.

To improve the understanding of the relation between the residual signal and gear faults, McFadden et al. (1985) developed the theoretical model of the residual signals. First, signals with a single frequency and harmonics are used to model the gear vibrational signal. Then, amplitude and frequency modulation is added to model the signal derivation caused by gear faults. An experiment with a helicopter gearbox was conducted with a helicopter gearbox to validate the theory, and the tooth crack in gear was successfully identified. Then, McFadden (1987) further improved the theoretical model by conducting a more detailed analysis with broadband signals. The model considered the effects of the modulation sidebands and was also validated using experimental data measured from fixed axis gear pair in a helicopter gearbox. Furthermore, the crack in the input-level bevel pinion gear was located.

The time synchronous averaging usually requires a speed sensor or shaft position encoder to provide the angular position of the gear rotation. However, incorporating the speed sensor or encoder can be inconvenient and even impossible in some situations. In this background, the angular position estimation using the gear vibrational signal under acceleration is developed to obtain the shaft position without the speed sensor (Bonnardot et al., 2005). Furthermore, the peaks in the spectrum can estimate the gear speed because the tooth meshing generates impact input forces, which are usually manifested significantly in the spectrum. In a later study, the angular position estimation is further developed, and the time synchronous averaging of gearbox signal is performed without the speed sensor (Combet et al., 2007).

However, the abovementioned time synchronous averaging technique only works well with fixed axis gear. Therefore, a problem arises when applying the TSA to the epicyclic gear train. The time synchronous average algorithm is further improved to extract the rotational signal from a single planet signal in an annulus-planet-sun gear system (McFadden, 1991). The signals are windowed only for a single planet gear, performed within the time range that the pinion passes by the sensor. Then, the windowed signals are averaged across multiple revolutions, which can cancel out signals unrelated to the planet gear revolution. The effect of the window function was further investigated (McFadden, 1994). Furthermore, it was found that the tapper windows, such as triangular or Hanning windows, have improved performance than the rectangular window while they require higher computational costs.

2.1.2 Frequency spectra analysis and modelling

Frequency spectra analysis is a powerful tool for analyzing the vibrational time-history data collected from gearbox vibration. In the frequency spectra of the rotating machinery vibrational signal, modulation sideband structure around the meshing frequency is one of the most important indicators of the machine condition. For the planetary gear system, the phase and amplitude of the signal collected from a stationary sensor are modulated by the planet gear pass-by (Randall, 1982). It was observed that, for the planetary gear spectra, the sidebands are not symmetric around the meshing frequency for most of the cases. Sometimes, the signals at the meshing frequency are completely suppressed. Therefore, the mathematical model was proposed to explain the asymmetry in the frequency spectrum of the signal measured on a static sensor on annulus gear (McFadden, 1985). It was found that the asymmetry in the sidebands is not from the nonlinearity of vibration but dominated by the phase difference between the adjacent planetary gears. The model was further analyzed by continuous-time Fourier series. It was confirmed that the asymmetry in the sidebands is generated by the natural meshing of gears and may not indicate alarm of gear condition (McNames et al., 2002). In a further study, Moser et al. (2003) also proposed the theoretical model to understand the sideband structure of the flight gear system.

A more detailed study examining the relationship between the number of the planetary gear and the modulation sideband behavior was proposed following the previous work (Inalpolat et al., 2009). It was found if the number of the annulus gear teeth is the multiple of the number of the planetary gear number, the spectrum is symmetric. Otherwise, the modulation sidebands are not symmetric. Several cases were examined in this paper, including

1. equally spaced planet gear & in-phase meshing,
2. equally spaced planet gear & sequentially phased meshing,
3. unequally-spaced planet gear & in-phase meshing,
4. unequally-spaced planet gear & sequentially phased meshing,
5. unequally-spaced planet gear & arbitrarily phased meshing.

A later study extended the sequential phase meshing as a unique condition under out-of-phase meshing (Vicuna, 2012). In addition, this study also includes the effect of the sun/planet meshing.

Except for the direct processing of the measured vibrational signal for sideband analysis, some pre-processing can be applied to improve the accuracy of the analysis. For example, in one of the early studies, McFadden (1985) lowpass filtered the signal collected from gears and analyzed the frequency spectrum. The processed signals show that gear with advanced crack will have significantly different frequency responses than the gear with no crack or tiny crack.

2.1.3 Narrowband demodulation

The direct spectral analysis of the sensor signal acquired from gear vibration is critical in gear faults diagnostics. However, sometimes the modulation sideband structure of early-stage defect might be very similar to healthy gears. In addition, the crack's location cannot be obtained by spectral analysis or time synchronous averaging. After an early study (Randall, 1982) explained that the gear defects could cause the amplitude modulation in the vibration of the gear meshing, the narrow band demodulation of the vibrational data is proposed (McFadden, 1986). The gear vibration signal can be represented as the superposition of periodic vibration signals with phase and amplitude modulation,

$$x(t) = \sum_{m=0}^{M} X_m(1 + a_m(\mathrm{t}))\cos(2\pi mTf_s t + \phi_m + b_m(t)), \tag{2. 1}$$

where $a_m(\mathrm{t})$ represents amplitude modulation, and $b_m(\mathrm{t})$ represents frequency modulation. First, the signal can be band-pass filtered around the meshing frequency. Then, instantaneous amplitude and phase can be calculated using the filtered signal. The unusual change in the demodulated amplitude and phase modulation can be used for indicating the gear defect condition. A later study extended the analysis to determine the gear fatigue crack using the demodulated amplitude and phase (McFadden, 1988).

Based on the demodulated amplitude and phase, several indicators have been developed. Those indicators can be used to relate the demodulated signal to specific gear faults intuitively. In one of the studies, the modulation-based parameters and kurtosis-based parameters are developed to indicate the level of the gear crack (Krishnappa, 1997). Then, in another study, the demodulation technique was applied to the directly measured vibrational signal or synchronously averaged signal and applied to the residual signal (Wang, 2001). This study applied the demodulation to simulated, gear test rig, and in-flight data. In addition, attention was paid to the structural resonance caused by the gear crack, which is shown in the demodulated phase or amplitude. Unfortunately, all demodulation techniques mentioned above require band-passing filtering to extract the signal from a narrow band. This feature renders the methods infeasible to process the wideband signals. Therefore, a model-based demodulation technique has been developed to perform the phase and amplitude demodulation for a wideband signal (Ma et al., 1996).

The gear faults investigation is usually under constant load and speed conditions. However, in the actual operation environment, the load and speed of the gear vary constantly. Therefore, an improved algorithm is proposed to handle the gear signal under varying speed conditions (Guo et al., 2016). First, the time history data are collected under varying conditions. Then, the collected data are resampled using computed order tracking analysis in the angular domain. Finally, the resampled signals are demodulated to obtain the phase and amplitude modulation, using the improved demodulation algorithm utilized for the frequency shift.

2.2 Planetary Gear Train Dynamics Modelling

In this study, the planetary gear trains are investigated from a signal processing point of view. However, to process the signal acquired by vibrational and acoustical sensors more efficiently, understanding the planetary gear's dynamics is essential. The study of planetary gear dynamics starts in the 1970s. The lumped parameter model and the deformable gear model are two primary models that have been developed to analyze the gear train dynamics. However, the literature mainly focused on static analysis, natural frequencies and vibration modes, dynamic force, response, and meshing forces' cancellation. Although numerous lumped parameter models are developed to model the gear vibration frequency and modes, they are not widely used in the industry. On the other hand, the numerical tools developed for gear dynamics analysis are widely applied in academia and industry. Due to those reasons, both major tools for analyzing the planetary gear train dynamics and vibration are reviewed in the current section.

2.2.1 Analytical Model for Planetary Gear Vibration

A gear vibration model is usually needed to predict the relation the acoustic and vibrational signals emitted from a gear structure under investigation. Most of the previous theoretical gear dynamics studies treated gears as rigid bodies and their connection were represented as linear spring, as shown in Figure 1.1 (Lin & Parker, 1999). In this model, the deflection of the sun gear and the planet gear can be modelled as,

$$\vec{r}_h = x_h \vec{e}_1 + y_h \vec{e}_2 \,, \tag{2. 2}$$

$$\vec{r}_i = (r_c + \zeta_i)\vec{e}_1^{\,i} + \eta_i \vec{e}_2^{\,i} \,. \tag{2. 3}$$

where $\vec{r}_h$ reflects the deflection of the sun gear, $\vec{r}_i$ represents the deflection of the planet gears, r_c is the carrier's translation, ζ_i and η_i are radial and tangential translations of planet gear. The second order time derivatives of the deflections that define the acceleration can be expressed as,

$$\ddot{\vec{r}}_h = (\ddot{x}_h - 2\Omega_c \dot{y}_h - \Omega_c^2 x_h)\vec{e}_1 + (\ddot{y}_h + 2\Omega_c \dot{x}_h - \Omega_c^2 y_h)\vec{e}_2 \, , \qquad 2.4$$

$$\ddot{\vec{r}}_i = \left[\ddot{\zeta}_i - 2\Omega_c \dot{\eta}_i - \Omega_c^2 (r_c + \zeta_i)\right]\vec{e}_1^{\,i} + \left(\ddot{\eta}_i + 2\Omega_c \dot{\zeta}_i - \Omega_c^2 \eta_i\right)\vec{e}_2^{\,i} \, . \qquad 2.5$$

Establish the equilibrium condition of the system, the Newtonian mechanics gives the governing equation,

$$m_s(\ddot{x}_s - 2\Omega_c \dot{y}_s - \Omega_c^2 x_s) - \sum_{n-1}^{N} k_{si}\delta_{si} sin\psi_{si} + k_{sx}x_s = 0 \, , \qquad 2.6$$

$$m_s(\ddot{y}_s + 2\Omega_c \dot{x}_s - \Omega_c^2 y_s) - \sum_{n-1}^{N} k_{si}\delta_{si} cos\psi_{si} + k_{sy}y_s = 0 \, , \qquad 2.7$$

$$\left(\frac{I_s}{r_s^2}\right)\ddot{x}_s + \sum_{n-1}^{N} k_{si}\delta_{si} + k_{su}u_s = \frac{T_s}{r_s} \, , \qquad 2.8$$

where $\delta_{si} = -x_s sin\psi_{si} + y_s cos\psi_{si} - \zeta_i sin\alpha_s - \eta_i cos\alpha_s + u_s + u_i + e_{si}(t)$, which is the compressive mesh deflection of sun- planet i pair, and $\psi_{si} = \psi_i - \alpha_s$; $2\Omega_c \dot{y}_s$ and $2\Omega_c \dot{x}_s$ are Coriolis acceleration. Combining the governing equations for all the gear meshes, the governing equation system in the matrix form is,

$$\boldsymbol{M}\ddot{\boldsymbol{q}} + \Omega_c \boldsymbol{G}\dot{\boldsymbol{q}} + [\boldsymbol{K}_b + \boldsymbol{K}_m(t) - \Omega_c^2 \boldsymbol{K}_\Omega]\boldsymbol{q} = \boldsymbol{c} + \boldsymbol{T}(t) + \boldsymbol{F}(t) \, , \qquad 2.9$$

where $\boldsymbol{M}, \boldsymbol{G}, \boldsymbol{K}_\Omega$ are mass, gyroscopic, centripetal matrices. And the $\boldsymbol{K}_b$ and $\boldsymbol{K}_m(t)$ are elastic support matrix and tooth mesh stiff matrix, separately. The forces due to transmission torque are expressed in $\boldsymbol{T}(t)$, and the vector $\boldsymbol{F}(t)$ represents the force due to transmission error or tooth modification.

The lumped parameter model introduced above has been widely applied to characterize the gear vibrational modes and frequency under various conditions. For example, an earlier study was carried out to investigate gear train's torsional vibration and dynamic loads using a nine degree-of-freedom model (August et at., 1986); a three-dimensional model was developed for a dynamic analysis of six rigid bodies including sun gear and carriers. It was shown by Kanraman that the above generic formulation enables the analysis with an arbitrary number of planet gears (Kanraman, 1994 (a)). In the same year, the natural modes of the planetary gear were investigated in a separate paper by the same author (Kanraman, 1994 (b)). In addition, the sensitivity of natural frequencies and vibration modes to certain parameters was investigated using the lumped parameter model (Lin and Parker, 2001). Effects investigated in that work includes support and mesh stiffness, component masses, and moment of inertia. The changing contact condition can also cause the mesh stiffness variation, thus causing the parametric instability of planetary gear systems (Lin & Parker, 2002). For most of the above-mentioned models, only the spur shaped gears are investigated. A linear and time-invariant model was proposed to model double helical gears (Sondkar & Kahraman, 2013).

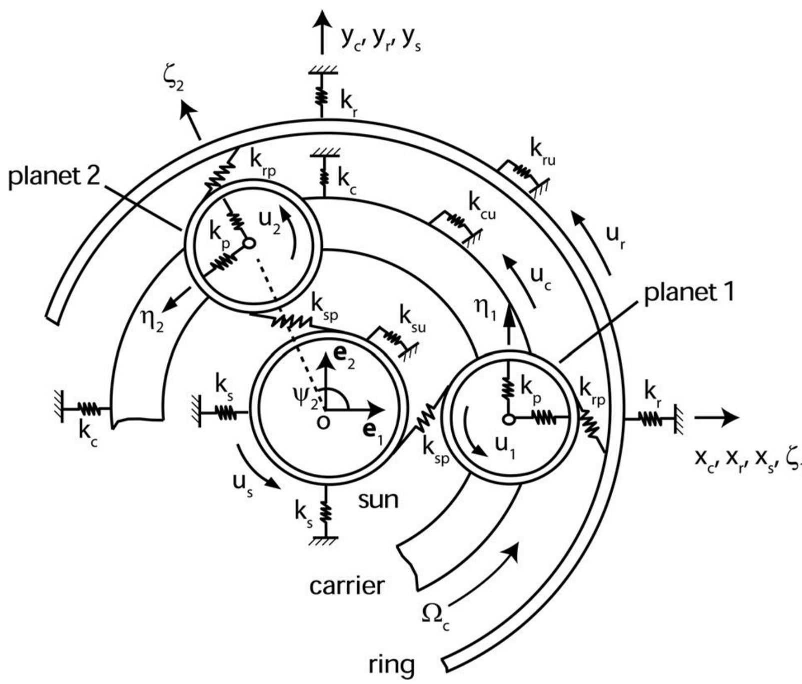

Figure 1.1. Lumped Parameter Planetary Gear Model (Lin & Parker, 1999)

Besides lumped parameter models that represent the gear mesh as linear spring, non-linear effect in the planetary gear has drawn more attention in the past two decades as it was found that the linear representation fails to explain certain vibration phenomena. To improve the prediction accuracy of the vibrational modelling, non-linear effects were also considered in lumped parameter models. A lateral-torsional couple model that incorporate the non-linear effect caused by multiple backlashes, time-varying stiffness, error excitation was established to model the gear with multiple clearances (Ambarisha & Parker, 2007). Based on that model, a 2D lumped parameter model was developed to represent the gear meshes as non-linear springs with tooth contact loss, and the supports as linear springs. The prediction of this theoretical model was verified using a finite element analysis. At the same time, another non-linear torsional vibration model is proposed (Al-Shyaab & Karahman, 2007). In this model, the non-linear equations of motion are solved using harmonic balance method. More recently, a dynamic model was proposed to simulate the meshing signal sidebands from planetary gears with manufacturing errors (Inalpolat & Kahraman, 2010). In that study, the vibrational signal spectrum is predicted with non-linear vibration model, and the spectrum structure can be used as an indicator for the detection of various gear defects.

Although the abovementioned models lay the foundation of of the gear vibrational and dynamic analysis, however, they are not comprehensive enough for the gear systems that contains multiple meshes, for example, compound planetary gear trains. Therefore, more advanced mathematical models were developed for the compound gears with multiple stage transmission (Kahraman, 2001; Kiracofe et al., 2007; Inalpolat et al., 2008; Guo et al. 2010). Kahraman (2001) where the vibration modes of a compound planetary gear train was investigated by assuming only rotational degree of freedoms. This study was able to identify three vibrational modes for the compound gear, which are rigid body mode, asymmetric planet mode, and axisymmetric planet mode. In a later study, Kiracofe and Parker (2007) derived a set of generalized governing equations for compound planetary gears by incorporating both translational and rotational degree of freedoms for each rigid body. The formulation includes all configurations, such as multistage, meshed-planets, and stepped-planets. The model reveals that distinct vibration mode structures identified in the single stage gear (Lin & Parker, 1999) also occurs for compound planetary gears. In a further analysis by Guo and Parker (2010), a general rotational degree of freedom model was developed for compound planetary gear, which clarified the rotational models in the previous publication. The study showed that there are two vibration mode types: overall modes and planet modes. However, this conclusion is in contrast with the conclusion of three mode types found in Kahraman’s work (2001), and it was found that rigid body mode is actually an overall mode. Besides the abovementioned models, nonlinear effects in a compound planetary gear dynamics has also been considered by Al-Shyaab et al, (2009), where discrete, non-linear, time-varying, torsional dynamic model of a multi-stage planetary train that includes an arbitrary number of simple planetary stages was proposed. This model includes the time-varying mesh stiffness and the blacklash non-linearities that allows tooth separation. The governing equations were solved semi-analytically by a hybrid harmonic balance method, and the accuracy of the semi-analytical was validated again numerical simulation results.

After introducing the models that have been developed to predict single or multi-stage planetary gear train dynamics, one prominent characteristic, the loading sharing among the pinions, will be discussed in this paragraph, because of its strong connections to the diagnostics of the planet gear defects. One practical advantage of planetary gear is that all the planet gears share equal load in an ideal condition. However, if manufacturing error is present, the loads for pinions will be different. Analytical models including both lumped parameter dynamic model and simplified physical model were used to investigate the planet load sharing. In one early study of the load sharing characteristics,a nonlinear dynamic model was developed to calculated load sharing factors (Kahmaran, 1994). This model allows the analysis of a gear train with any number of pinions that are spaced arbitrarily around the sun gear. To further improve on the prediction accuracy of the loading sharing, a generalized mathematical model was developed for a single stage planetary gear train to predict the planet load under quasi-static condition (Kahraman, 1999). However, the above studies focused on the load sharing of an ideal planetary gearset. To investigate the load sharing with carrier planet position errors, simplified discrete model (Singh, 2009) was developed to predict the variation in load sharing under this condition. Then, a generalized close-form non-dimensional equation set that can predict planet load sharing behaviors with position errors was also developed (Singh, 2010). In a recent study, this load distribution model was further developed for simulating the planetary gear sets having design variations in component or system level (He et al., 2018).

2.2.2 Computational Model

Besides analytical models, numerical models have also been employed extensively to characterize vibration modes and natural frequency of planetary gears. Compared with lumped parameter models, which assumed each individual gear is a rigid body, numerical tools can model the gear deformation effects in dynamics, which leads to better match with experimental data. Parker et al. (2000) proposed a semi-analytical finite element model that admits precise representation of the tooth geometry and contact forces in gear dynamics. This study showed comprehensive dynamic response results under a range of operation speed and torques. In addition, the finite element model also has the capability of modelling the non-linear tooth contact and stiffness variation. This comprehensive study provides benchmarking for later analytical model using lumped parameters. In a subsequent study, the finite element model was also used as the tool to validate the lumped parameter model calculation (Ambarisha et al., 2007).

Other than using finite element method to establish a comprehensive understanding of planetary gears, certain behavior of planetary gear vibration was also investigated by numerical modelling. Kahraman et al. (2001) employed a finite element/semi-analytical nonlinear contact mechanics formulation to model an automatic transmission planetary unit. The model considered each gear as deformable bodies and predict loads, stresses as well as deformations of the gears based on gear deformation. And the flexibility effect of an internal gear on the quasi-static behavior of a planetary gearset was investigated. Then, the finite element model was used to investigate the dynamic effects on gear stress and its dependence on gear rim thickness parameters and the number of planets in the system (Kahraman et al, 2003). It was shown that a deformable body analysis is necessary when the gear rims are flexible, in order to include the rim bending modes properly and to predict the overall planetary gear modes more accurately.

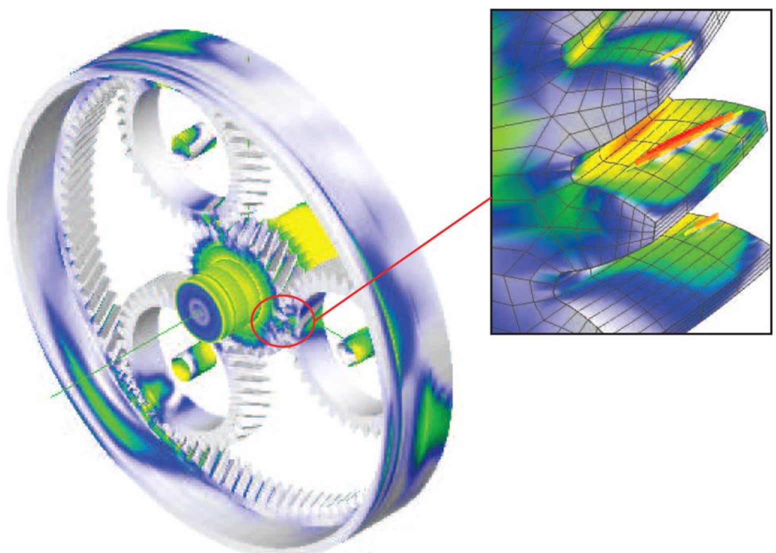

Figure 2.2. Finite Element Gear Model using Calyx (Vijayakar, 2005)

In addition to investigating the eigen behavior of a normal planetary gear train, the effect of gear parameters or faults have also been investigated computationally. A dynamic analysis using a hybrid finite element method was performed to characterize the effects of various manufacturing errors on bearing forces and critical tooth stress for a planetary gear system (Cheon and Parker, 2004). It was found that the carrier indexing error for the planet assembly and planet runout error are the most critical factors in reducing the planet bearing force and maximizing load sharing, as well as in reducing the critical stress. Then, a computational model is utilized to study the influence of surface wearing on the dynamic behavior of a typical planetary gear set (Yuksel and Kahraman, 2004). The computational scheme combines a wear model that defines geometric description of contacting gear tooth surfaces with wear and a deformable-body dynamic model. The results of a planetary gear set having a fixed planet carrier indicated that the dynamic behavior is nonlinear due to tooth separations in its resonance regions. The results for worn gear surfaces indicated that surface wear has a significant influence in off-resonance speed ranges while its influence diminishes near resonance peaks primarily due to tooth separations. The contact mechanic finite element model has also been utilized to analyze the effect of manufacturing and assembly error on the planet load sharing in a planetary gear train (Bodas and Kahraman, 2004). In this study, three types of errors were analyzed and design guidelines were proposed for improving planet load sharing robustness.

A finite element package called GSAM (Gear System Analysis Module) has been developed specializing in the planetary gear dynamics analysis by GM company. The load sharing behavior has been investigated using GSAM for 4, 5, and 6-pinion variants of a planetary transmission (Singh, 2005). It is shown that as the number of pinions increase in a planetary transmission, the pin-hole position error tolerance has to be tightened to maintain the equal load sharing between the pinions. In a later study, Singh (2007) examined the influence of bearing tilting on the gear load distribution and contact pattern. The study found that the tilting stiffnesses of the needle bearings have a major influence on gear contact pattern, consequently on contact and bending stresses. In addition, the double pinion planetary arrangement tends to result in off-centered loading.

More recently, a numerical scheme was proposed to solve a lumped parameter gear system model (Xiang et al, 2018). The analytical formulation is established considering time-varying meshing stiffness, comprehensive gear error and piece-wise backlash nonlinearities, a torsional nonlinear dynamic model of multistage gear of planetary gear system is established. By using Runge-Kutta numerical integration method, the dynamic responses can be solved, analyzed, and illustrated with the bifurcation parameters variation including excitation frequency, gear backlash and damping.

In our study, the planetary gear defects need to be detected using vibrational and acoustic signals. Therefore, understanding gear dynamics plays a critical role in processing the measured data. In particular, understanding the physics of gear vibration can build a bridge between the information hidden in data and gear structure. Given the reasons mentioned above, the literature review in this section will provide invaluable insight into the analysis of Vibro-acoustical data measured for nested planetary gear diagnosis.

2.3 Rotating sound source field calculation

One main component of the current study is to apply sound field reconstruction techniques for rotating sources to detect manufacture faults of rotating pinions in a planetary gear train. Most rotating source localization techniques rely on the sound field expression of a rotating fundamental source which was studied in many previous studies. Therefore, the rotating source sound field analysis is reviewed in this section. The gear meshing noise sources are usually compact in size and has dominant tonal components near the meshing frequency and its harmonics. On the other hand, for the aerodynamic noise source generated by gear rotation induced air disturbances, the resulted signals usually have broadband spectra without dominating peaks. Despite the difference in the spectral characteristics between the mechanically and aerodynamically generated noise, the sound field calculation can still be carried out by the same procedures. In this section, both analytical and numerical methods for calculating different types of rotating source sound fields are reviewed.

In the early analytical study of the aerodynamic noise, Ffowcs and Hawkings (1969) developed the famous Ffowcs Williams-Hawkings equation, which is the governing equation for the sound source in arbitrary motion and is the basis of most studies on sound field from rotating sources,

$$\Box^2 p' = \frac{\partial}{\partial t}[\rho_0 v_n \delta(f)] - \frac{\partial}{\partial x_i}[\rho_0 n_i \delta(f)] + \frac{\partial^2}{\partial x_i \partial x_j}[H(f) T_{ij}], \tag{2.10}$$

where $\Box$ is the D'Lembertian operator, $H(f)$ is the Heaviside unit function, T_{ij} is the Lighthill stress tensor, ρ_0 is the air density, $\delta(f)$ is impulse function, v_n is the flow velocity and f is frequency. The equations concerning thickness and loading noise can be expressed separately from the above equation,

$$\Box^2 p'_T = \frac{\partial}{\partial t}[\rho_0 v_n \delta(f)], \tag{2.11}$$

$$\Box^2 p'_L = \frac{\partial}{\partial x_i}[\rho_0 n_i \delta(f)]. \tag{2.12}$$

This formulation of this general sound generation problem for moving sources laid the foundation for the following work of sound field prediction of sources with various characteristics. Most of work on rotating source sound field calculation is based on solving these governing equations. Farassat has performed many studies that focus on solving the equation for the rotating sources. The famous 1 and 1A formula were developed to solve the Ffowcs William-Hawkings equation for rotating sources (Farassat, 1976, 2006; Bretner, 1980). The formular 1 for the thickness and loading noise can be found in the following expression,

$$4\pi p_T'(x,t) = \frac{\partial}{\partial t}\int_{f=0}\left[\frac{\rho_0 v_n}{r[1-M_r]}\right]_{ret} ds\ , \qquad 2.\ 13$$

$$4\pi p_L'(x,t) = \frac{1}{c}\frac{\partial}{\partial t}\int_{f=0}\left[\frac{pcos\theta}{cr[1-M_r]}\right]_{ret} + \left[\frac{pcos\theta}{r^2[1-M_r]}\right]_{ret} ds\ . \qquad 2.\ 14$$

Based on formula 1, the formula 1A was further developed:

$$4\pi p_T'(x,t) = \int_{f=0}\left[\frac{\rho_0 \dot{v}_n}{r(1-M_r)^2} + \frac{\rho_0 v_n \hat{r}_i \dot{M}_i}{r(1-M_r)^3}\right]_{ret} ds + \int_{f=0}\left[\frac{\rho_0 c v_n (M_r - M^2)}{r^2(1-M_r)^3}\right]_{ret} ds\ , \qquad 2.\ 15$$

$$4\pi p_L'(x,t) = \int_{f=0}\left[\frac{\dot{p}cos\theta}{cr(1-M_r)^2} + \frac{\hat{r}_i \dot{M}_i pcos\theta}{r(1-M_r)^3}\right]_{ret} ds + \int_{f=0}\left[\frac{p(cos\theta - M_i n_i)}{r^2(1-M_r)^2}\frac{(M_r - M^2)pcos\theta}{r^2(1-M_r)^3}\right]_{ret} ds\ . \qquad 2.\ 16$$

The integral solution proposed by Farassat makes the analytical computation of the rotating sources with complex shape possible. Based on Farassat work, Chapman (1993) further developed a rotating source prediction formula, which transformed the time domain integration into the frequency domain. In this new formulation, the Ffowcs William-Hawkings equation for thickness and loading noise of rotating sources was solved by using Rayleigh integral. The thickness noise is described as,

$$p(\vec{x},\omega) = -\frac{\epsilon M^2 n^2}{2\pi}\int_0^{2\pi}\int_0^1 \frac{f_n(r_1)}{R} e^{in(\theta-\theta_1+MR)}\, r_1 dr_1 d\theta_1\ , \qquad 2.\ 17$$

$$\text{where} \quad R = (r^2 + r_1^2 - 2rr_1 cos\theta_1 + z^2)^{\frac{1}{2}}\ , \qquad 2.\ 18$$

and $M = \frac{a\Omega}{c}$ is the tip Mach number; r_1, θ_1 are integration variables denoting the position on the blade. While the loading noise has the following expression

$$L = -\frac{1}{4\pi}\frac{\partial}{\partial z}\int_0^{2\pi}\int_0^1 \frac{g_n(r_1)}{R} e^{in(\theta-\theta_1+MR)}\, r_1 dr_1 d\theta_1\ . \qquad 2.\ 19$$

Those integrals are solved in his study to visualize the sound field for rotating blades. In recent years, based on the frequency domain integration of the sound field, it was found that the exponential terms in the integral can be evaluated using Legendre series, thus improving the efficiency of the integral evaluation. The first series expansion application was first proposed to construct the sound field of vibrating piston (Mast et al., 2005). Although this development is not for rotating sources, it provided an insight for how to apply the series expansion formulation in the rotating sound field integral. The first application of Legendre series in the generalized rotating source was proposed Carley in 2006. In this study, the rotating propeller noise is investigated. The frequency domain integration formulation follows the thickness noise formulation of Chapman (1993) with minor modification, which was expressed as

$$p(\vec{x},\omega) = \frac{-\epsilon M^2 n^2}{4\pi}\int_0^{2\pi}\int_0^1 \frac{s_n(r_1)}{R} e^{in\theta+in\theta_1+ikR} r_1 dr_1 d\theta_1 , \qquad 2.20$$

The integral can be evaluated using Legendre polynomial series expansion expression,

$$I_n = j\pi^{\frac{3}{2}} 2^{n-2} \sum_{M=0}^{\infty} \frac{(4m+2n+1)\Gamma(2m+1)}{\Gamma(2m+1)\Gamma(2m+1)\Gamma(2m+1)} \times \int_0^a \frac{1}{(\rho S)^{\frac{1}{2}}} J_{n+2m+\frac{1}{2}}(k\rho) H^{(1)}_{n+2m+\frac{1}{2}}(kS) \times P^n_{n+2m}(cos\beta) r_1 dr_1 . \qquad 2.21$$

The Legendre polynomial series is substitute into the integration, so it can be evaluated analytically. And Carley shows in his study that the series expansion solution can give a higher accuracy. In a later study, the series expansion solution is extended to be applied to a ring acoustical source (Carley, 2010). The integration needs to be rearranged to adapt to the shape of the ring source, and the rest of the procedures are still the same as the sound field evaluation for rotating propeller.

In a more recent study, a series expansion formula under spherical coordinates for monochromatic monopole sources was derived (Pelloti, 2010), which has the following form,

$$p(\vec{r},t) = -i\sum_{m=-\infty}^{m=\infty} k_m e^{i\omega t} \sum_{n=|m|}^{\infty} N^2(n,m) j_n(k_m r_<)\, h_n^{\delta}\ (k_m r_>) Y_m^n(\theta,\varphi) Y_m^n(\theta_s,\varphi_s) , \qquad 2.22$$

where k_m is m^{th} rotating shifted wave number, j_n is Bessel function of first kind, h_n^2 is Hankel function of second kind, Y_m^n is the spherical harmonic function of order *m* and degree *n*. In a later study, the series expansion calculation accuracy was compared with two numerical methods: advanced time approach and retarded time approach (Pelotti, 2011). And it was verified that the three calculation approaches yield results with close values.

In following work of the sparse source series expansion calculation, Mao et al. (2012, 2014) extended the prediction from monopoles to dipoles and quadrupoles. They started with the retarded time integration of sound field,

$$p(\vec{x},t) = \int_{-\infty}^{\infty} \frac{q(\vec{y}(\tau),\tau)}{4\pi r_0(\tau)} \delta(t-\tau-\frac{r_0(\tau)}{c})\, d\tau \,, \qquad 2.23$$

where t is the observer time, $r_0(\tau)$ is the distance between $\vec{r}_s$ and $\vec{r}$. For the rotating sources with constant speed, the time domain expression can be transformed into frequency domain using the Fourier transform,

$$p(\vec{x},\omega) = \int_{-\infty}^{\infty} q(\vec{y}(\tau),\tau) \frac{e^{ikr_0(\tau)}}{4\pi r_0(\tau)}, \qquad 2.24$$

Then, the dipole or quadrupole source expression formulae were substituted into the integration for evaluation. All of the abovementioned series expansion calculation of rotating sound fields were performed with the absence of axial flow, an analytical sound field expression for monopole sources with axial flow of the air media is further calculated (Mao, 2015).

2.4 Rotating Source Sound Field Reconstruction using Beamforming

The last section reviews the sound field calculation of rotating sources. The analytical expression of the rotating source sound field will provide the basis for the reconstruction of the sound source from sound field measurement data. This section will address the sound source visualization and localization of the rotating source using beamforming. Beamforming technique is one of the most widely applied acoustical source localization and visualization techniques, especially for rotating sources. Rotating sound sources are of interest in numerous engineering problems, such as the sound source localization in wind turbines and axial fans. However, sound source localization of these rotating sound sources is challenging due to the need for de-dopplerization and motion compensation. In order to tackle the issue of sound field distortion caused by source rotation, different beamforming techniques have been developed over the past two decades. Most beamforming techniques for rotating sources can be categorized into three techniques: (1) direct time-domain inverse method; (2) virtual rotating array method in frequency domain; (3) virtual rotating array method in the time domain. The early development of the rotating beamforming algorithm compensates for the rotating motion using the direct time-domain inverse method that modifies the delay and sum (D&S) beamforming algorithm. However, the resolution and accuracy of the direct inverse time-domain algorithm are not high enough for sources with small rotation diameter, such as small fans. To improve the reconstruction's resolution, the virtual rotating array algorithms in frequency domain and time domain have been developed to de-dopplers the signals and subsequently used as input for the beamforming algorithm with static sources.

2.4.1 Rotating Source Identifier (ROSI) Algorithm

Since its first appearance in literature, the ROSI algorithm has been one of the most applied methods for rotating source reconstruction. By reformulating the delay and sum beamforming (D&S) equations in the time domain, the beamforming can be utilized to track rotating sound sources at free space conditions for the first time (Sijtsma, 2001). The advanced time approach (Casilino, 2003) is used for calculating the time delay between the rotating source and a stationary receiver. Then, the receiver signals are interpolated using the time delay correction. Finally, the sources signal is reconstructed using the interpolated data and monopole sources' time-domain transfer function. The algorithm was verified by reconstructing the sound field of a rotating whistle, helicopter blades, and wind turbine, respectively. In a later study, the accuracy of the time domain inverse has been further improved (Bi et al., 2017) by using the retarded time approach for calculating the time delay instead of the advanced time approach. With this approach, the receiver to source inverse problem is not solved by using interpolated receiver signals, instead, the actual source signal is calculated by interpolating the inversed data using the new source time vector calculated by the retarded time approach.

The algorithm improves the accuracy of the original ROSI algorithm and enables the calculation of sound pressure in real time. The ROSI method was further improved by separating the rotating into small segments (Zhang et al., 2020), which is referred to as segmented ROSI. The segmentation treatment of the signal from rotating sources enhances the resolution of the source sound field reconstruction at a certain angle. Even though ROSI can suppress the time distortion caused by source rotation, Ma (2020) examined if the ROSI algorithm fully compensates for the doppler effect. It was found that the ROSI cannot eliminate the Doppler effect. Therefore, a rotational symmetric array was proposed for ROSI to eliminate the signals at the rotational-related sideband frequencies. It can be concluded from the studies mentioned above that serval improved versions of the ROSI algorithm have been developed since its invention for both accuracy enhancement and computational cost reduction.

Except for the application mentioned in the previous papers, some other works also contribute to the ROSI algorithm application. The main application of beamforming in the rotating source is fan noise visualization and localization. Since Sjitsma first proposed the algorithm in 2001, it has been utilized for fan noise imaging in multiple pieces of research. In a 2007 study, Sjitsma explored the application of ROSI for the imaging of fan and stator in a turbofan engine. The conventional beamforming was used to localize the stator noise while the ROSI was applied to the rotating fan soundtracking. Later in a 2010 study, Sjitsma (2010) extends the investigation in applying the beamforming algorithms. The conventional DAS algorithm, deconvolutional CLEAN algorithm, and ROSI for the turbofan noise imaging are applied to a Rolls-Royce fan rig noise data measured by two circular phased arrays.

Furthermore, it was shown that ROSI has better reconstruction performance of rotor noise source than the beamforming without the motion compensation. Minck et al. (2012) applied ROSI to identify in-duct rotating fan noise. The study confirmed that the ROSI algorithm can separate the rotating and static sources. In addition, it can also be used for high-speed rotating fan noise tracking. In a study published in 2013, Benedek et al. (2013) conducted a series of studies investigating the application of ROSI on industrial axial fans noise. They applied ROSI for the noise source imaging of an axial ducted fan in a noisy environment for the first time. The paper presented the processing and analyses of the phased array microphone system. The wind noise-dominated cross-spectral matrix is analyzed, and source positions are obtained with beamforming procedures for both stationary and rotating sources. The ROSI results show that the rotor noise strength has a higher level at a larger radius in the higher frequency range, meeting the theoretical expectation. Then, Benedek et al. (2014, 2015) extended the work by investigating the effect of axial fan parameters on noise generation using ROSI. Both upstream and downstream source map was shown for the noise source localization. The momentum thickness parameter was introduced in those works, which offers the basis for a fan design to reduce the noise. In a follow-up study published in 2016, Benedek et al. developed a more generalized diagnosing prototype for the unducted or short-ducted rotor-only fans. The noise sources, such as tip leakage flow, were identified. The correlation between aerodynamic noise and the aerodynamic loss of the blade span was pointed out in this study.

2.4.2 Frequency Domain Virtual Rotating Array

In spite of having the capability of calculating the source field in real-time, one disadvantage of the time-domain rotating source beamforming algorithm is the long computational time due to the need for oversampling. In addition, it has low spatial resolution at low frequencies because it does not use a cross-spectral matrix (CSM) which is necessary for high-resolution deconvolution algorithms. To overcome these drawbacks, researchers proposed rotating source beamforming algorithms in the frequency domain. Lowis and Joseph (2006) proposed a frequency-domain cylindrical-ducted rotating beamforming to localize rotating fan noise sources with a circular microphone array with equal microphone angular intervals in ducted conditions. A virtual rotating array (VRA) method was proposed, the virtual array is rotating at the same angular speed as the rotating sources. The sound pressure at each microphone on the virtual array is calculated (interpolated) from the pressures measured at real stationary microphones based on in-duct Green's function and the spinning mode decomposition method. The interpolated data are subsequently used to generate the CSM for the sound source reconstruction. In order to consider the effects of the inner duct, Dougherty and Walker (2009) developed a frequency-domain annular-ducted rotating beamforming for visualizing broadband rotating fan sources. The sound pressures at the virtual rotating microphones, which are subsequently used in CSM, are interpolated from the pressures measured at the actual stationary microphones.

The early frequency domain VRA is developed in ducted conditions. However, in many applications, rotating sources are operated without boundaries. For these applications, Pannert and Maier (2014) proposed a frequency-domain virtual rotating array interpolation method under free-space conditions based on the free-space Green's function for rotating monopole sources (Pelotti et al., 2011). The sound pressures at the virtual rotating microphones were also calculated using the measured pressures at actual static microphones based on the mode decomposition, following Lowis and Joseph (2006). In this free-space rotating source beamforming, the rotational motion of the medium in the rotating reference frame is compensated by computing Green's function with a shifted frequency, which describes the radiation from a rotating sound source in the rotating reference frame. And the frequency of each mode is shifted due to this rotation. The interpolated frequency domain data are used in different beamforming algorithms to reconstruct rotating sources. In a later study, Ocker and Pannert (2017) extended this free-space rotation beamforming algorithm to localize sound sources on fan blades in a uniform axial flow. Compared to the spherical Green's function used in Pannart and Maier's work, a series expansion formula for the rotating monopole in uniform axial flow is used (Mao, 2014). This new algorithm development was validated by case studies on localization of rotating fan noise sources with external axial flow.

Similar to ROSI, the frequency mode decomposition method has also been mainly applied in identifying aerodynamic noise sources of the rotating axial fan. Lowis et al. (2006) and Dougherty et al. (2009) applied their frequency-domain algorithms to localize broadband noise sources in annular-ducted fan in ducted conditions. In 2017, Caldas et al. applied the free-field VRA frequency domain interpolation algorithm for a in-duct noise experiment for the first time. A 16-bladed rotor fan was tested using 77 wall-flush-mounted circular-shaped array. The beamforming maps across a broad frequency range (1kHz-7kHz) were presented, and the noise maps showed that the significant noise sources can be identified on the rotor blades. However, the frequency domain algorithm cannot be applied to the rotating sources with varying speed, neither can the algorithm work with the data measured by the randomized shaped array. In this thesis, the frequency domain VRA interpolation will be modified to handle the data collected by a non-circular array for tonal noise.

2.4.3 Time Domain Virtual Rotating Array

Besides compensating the doppler effect in the frequency domain, the virtual rotating array method can also be implemented directly in the time domain. Herold and Sarradj (2015) proposed calculating sound pressures at the VRA microphones, which are subsequently used in CSM, from the pressures at neighboring stationary microphones using linear interpolation. This treatment defines the spatial sound field resampling proposed by Dougherty and Walker (2009) as a linear interpolation of the time domain signal. This rotating source beamforming can be applied to both constant and varying rotational source motions, while the frequency domain interpolation can only work with sources rotating at a constant speed. In addition, this linear interpolation technique has also been claimed to have higher computational efficiency because it uses the relatively simple linear interpolation involving only adjacent microphones. The algorithm was validated by a reconstruction application of the sound field from a fan with rotating blades. Herold et al. (2018) established a benchmark case for comparing the frequency and time domain virtual rotating array interpolation methods, where both algorithms were reported to show comparable results for the rotating source localizations. Recently, Jekosch and Sarradj (2020) extended the virtual rotating array interpolation from a ring-shaped array to a random array. They use piecewise interpolation instead of interpolating the pressure between the neighboring microphones on a circular ring. This study explored two algorithms, Barycentric interpolation, and radial basis function interpolation. It was shown that both methods are capable of interpolating the data of the randomly arranged array. However, both interpolations are more time-consuming than linear interpolation using a circular array due to the increasing complexity in the interpolating algorithms. Besides the investigations on the virtual rotating array interpolation, the interpolation has also been combined with the latest beamforming development to enhance source localization accuracy (Bu et al., 2018). The compressive sensing beamforming algorithm is used for reconstructing sound sources from the VRA interpolated data. The combination between the VRA and compressive sensing algorithm further improves the efficiency of sound source reconstruction.

The time-domain virtual rotating array is a popular method for rotating noise localization due to its robustness and efficiency. After proposing the method, Herold and Sarradj (2015) applied this development to rotating fan noise localization. The experimental study showed that the trailing edge noise can be successfully located. Later in 2016, the same group applied the virtual rotating array for the fan noise localization in a ducted engine fan. Noise maps for a wide frequency range were given in this study. Different beamforming techniques were used to process the VRA data for comparison. Moreover, it was found that DAMAS has better performance than CLEAN-SC for the rotor noise reconstruction. In the 2017 study, this group extended the study to investigate the effect of blade skew on trailing edge and leading edge fan noise.

2.4.4 Other Algorithms

Without utilizing the idea of a virtual rotating array, Ma et al. (2020) proposed a new frequency-domain algorithm for the rotating source sound reconstruction, which is called mode composition beamforming (MCB). This algorithm has the same capability as ROSI but higher reconstruction accuracy. In addition, this new method does not have the restriction of a circular-shaped array arrays with arbitrary shapes can be used.

2.5 Sound Source Field Reconstruction-Recent Development of Acoustical Holography

Nearfield holography has been extensively used to reconstruct and visualize sound sources, usually based on nearfield microphone array measurements. The near field holography is widely applied to the near field source reconstruction, while the beamforming focuses on the far-field sound field prediction. Compared to beamforming, nearfield holography works better when the measurement is conducted close to the source. In addition, holography usually has a higher reconstruction resolution than beamforming methods. In the current study, the gear system is compact, and the microphone array is placed within 0.5m distance to the rotating source plane. Therefore, the nearfield holography is better for source localization than beamforming methods in this particular condition.

The traditional Fourier acoustics-based approaches require a specific microphone arrangement (Maynard 1985; Veroseni, 1987). Nevertheless, recent development in the nearfield holography removed the requirement that the measurement array needs to have a specific shape, and the computational efficiency has been improved significantly. More specifically, the compressive sensing method is one of the most widely studied approaches over the last decades due to its high efficiency and accuracy for the localization of sparsely distributed sources. However, there are few developments regarding the rotating sources for nearfield holography study. Therefore, the compressive sensing holography targeting the reconstruction of stationary sources will be reviewed in this section.

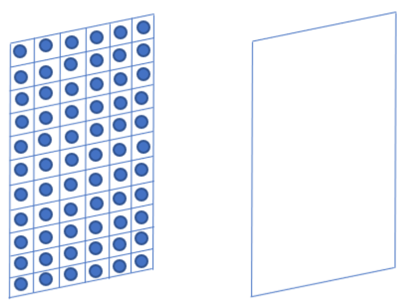

Figure 2.3. Illustration of equivalent source holography reconstruction plane and measurement plane

2.5.1 Fourier acoustics based compressive sensing holography

The compressive sensing technique is introduced to the acoustical imaging area by proposing an L1 norm formulation to solve the ill-posed inverse problem for source calculation. The first application is in the acoustical imaging area is applying the L1 norm formulation to the beamforming algorithm (Takoa, 2011). Then, in the acoustical holography, the compressive sensing with L1 norm penalty formulation was proposed by Chardon et al. in 2012 for the first time. This study proposed to perform the regularization in the Fourier-based holography process, by reformulating the inverse problem and adding L1 norm terms. Furthermore, it was demonstrated by this paper that, in the case of a star-shaped homogeneous plate, sparse regularization principles and compressive sampling techniques lead to significant improvements over standard Fourier-based NAH techniques. The L1 norm formulation reformulates the inverse problem by replacing the Tiknohov regularization with the following formula,

$$\text{minimize } \lambda\|\vec{q}\|_1 + \|\vec{p} - A\vec{q}\|_2^2 \,. \qquad 2.25$$

where the vector $\vec{q}$ is the source strength vector, $\vec{p}$ is the measurement vector, and **A** is the transfer function between source and receiver. The L1 norm of $\vec{q}$ and L2 norm of $\vec{p} - A\vec{q}$ are optimized simultaneously for both source accuracy and source sparsity. The parameter controls the proportion between the accuracy and sparsity. The current formulation has a convex function so that the convex optimization tools can obtain the solution. Applying the compressive sensing algorithm in the NAH process significantly reduces the number of microphones needed for high-frequency sound prediction. In the following study (Kirchner et al., 2014), the compressive sensing holography algorithm was extended to sound field reconstruction of cylindrical geometry. The parameter λ controls the proportion between the accuracy and sparsity. Since the current formulation has the form of a convex function, so that the convex optimization tools can be used to obtain the solution. The application of compressive sensing algorithm in the NAH process reduce the number microphone needed for high frequency sound prediction significantly. In a following study (Kirchner et al., 2014), the compressive sensing holography algorithm was extended to sound field reconstruction of cylindrical geometry.

2.5.2 Equivalent source method based compressive sensing (CESM) holography, iterative solution

In the last section, applying the compressive sensing principle to the inverse calculation of Fourier-based holography is reviewed. A more efficient algorithm has been proposed to apply the CS algorithm to equivalent source-based holography. One iterative algorithm that minimizes the algorithm using the L1 norm formulation using the steepest descent method has been proposed, referred to as wideband holography (WBH) (J. Hald, 2014; J. Hald, 2016). Wideband holography has recently been implemented in many source visualization applications because of its improved efficiency and wide frequency processing range. In the WBH process, the ill-posed inverse problem of calculating sound field based on the measurement is reformulated as an optimization problem,

$$\text{minimize } \|\vec{q}\|_1 \quad \text{subject to} \quad \|\vec{p} - \boldsymbol{A}\vec{q}\|_2^2 < \delta \,, \tag{2. 26}$$

The formulation is a standard formulation of the compressive sensing problem, which makes the source distribution sparse. The calculation procedures utilize the steepest descent method in each iterative step. The algorithm was validated against several simulated monopole cases and experimentally measured data of baffled plate. It was shown that the method works well not only for the sparsely distributed sources but also for distributed sources such as plates, where WBH can provide similar reconstruction accuracy compared with the Fourier-acoustics based compressive sensing holography. In addition, the WBH has a higher computational efficiency than CVX-based holography. However, the WBH using the steepest descent algorithm does not work accurately at lower frequencies, especially when the sources are within a wavelength of the sound wave. Therefore, a hybrid algorithm was proposed to overcome this disadvantage by using another iterative algorithm at lower frequencies (Ping et al., 2016). A frequency threshold is established first. Then, the iterative weighted algorithm based on the L2 norm penalty formulation is used below the threshold frequency. The steepest descent algorithm based on the L1 norm formulation is used above this frequency. It was validated that the approach can achieve accurate reconstruction in sparsely distributed sources at frequency range using simulated signals and experimental measurement. A later study further develops the iterative solution of the compressive sensing problem (Hald, 2018). In this study, different types of iterative algorithms were developed to reconstruct the sources based on L2 norm penalty formulations, which has the following form,

$$\text{minimize } \|\vec{q}\|_2 \quad \text{subject to} \quad \|\vec{p} - \boldsymbol{A}\vec{q}\|_2^2 < \delta \,, \tag{2. 27}$$

The performances of those iterative methods are compared using simulated monopole cases. The abovementioned wideband holography mainly works for the source distribution within a plane. In order to achieve the source reconstruction in a 3D space, the spherical array is proposed to be used for wideband holography reconstruction (Ping et at., 2018). The inverse calculation procedures follow the standard wideband holography method, except that the calculation is performed using spherical coordinates.

Except for investigating the iterative solution of the compressive sensing formulation, the developed algorithm has also been applied to practical application in several cases. Shi et al. (2016) applied the wideband holography algorithm to identify the loudspeaker sources. The results show a successful reconstruction of simple loudspeaker sources. In the following study, Shi et al. (2017) applied the wideband holography to a more complicated engineering problem, for which the automotive engine noise sources are visualized and identified. A similar study was done by Lepak et al. (2019), and they applied wideband holography to the localization of the outdoor HVAC unit noise.

2.5.3 CESM holography, convex optimization (CVX)

Except for the iterative methods to solve the compressive sensing formulation, such as wideband holography, there is another approach developed to solve L1 norm minimization in equivalent source based acoustical holography. It was found that the objective function using the L1 norm minimization forms a convex problem (Fernandez-Granade et at., 2015; Fernandez-Granade et at., 2017). Therefore, the standard convex optimization package can be applied to solve the proposed using the L1 norm formulation to tackle the ill-posed problem in the equivalent source method inverse procedures. The algorithm is examined with numerical simulation using sparsely distributed monopoles and experimentally measured acoustical guitar. It was shown that the method is also applicable to the source reconstruction at a wideband frequency range and achieves the balance between accuracy and sparsity. However, in the actual application of holography reconstruction, most of the sources are not sparsely distributed.

In order to enhance the source reconstruction accuracy for distributed sources, it was proposed that the equivalent sources can be decomposed into a sparse basis. In this process, L1 norm reconstruction can be performed to the orthogonal basis series of the sound field rather than the monopole sound field directly (Bi et al., 2017). In this study, the methodology development is validated using the reconstruction of vibration plates sound field, for which the sources are not sparely distributed. However, although the reconstruction accuracy has been improved compared to the compressive sensing ESM method, the accuracy still cannot be fully guaranteed for reconstructing non-sparse sources. Therefore, in a later study, Hu et al. (2018) further extended Bi's work and improved the reconstruction resolution by using the complex value pressure since the complex value pressure gives more phase information. The method is validated using the benchmark plate vibration case, and it was shown that it had improved accuracy compared to Bi's method and the conventional ESM.

The abovementioned CVX compressive sensing techniques have been summarized and compared in a recent study (Hald, 2020). The study compares the performance of those algorithms using simulated array measurements of plate vibration with different configurations. In addition, two arrays, one randomized array, and one circular array were used for the measurement. It was shown that the modal methods work better for reconstructing the sound field of freely vibrating plates. However, the modal methods do not show superiority over the standard ESM-based compressive sensing method for reconstructing the sound field of a baffled plate. Furthermore, the equivalent source-based CS methods show significantly higher computational efficiency than the modal methods in calculating time consumption.

2.5.4 CESM holography, others

The iteratively solved wideband holography and convex optimization have their strengths and weakness in different aspects. Compared to CVX, wideband holography usually works better to estimate the source strength and reconstruct a more complicated distributed source. On the other hand, CVX can achieve source prediction with higher resolution at low frequencies. Therefore, a hybrid algorithm is proposed to bridge these two solutions and enhance the reconstruction quality of the source sound field using compressive sensing principles (Shi et al., 2019). According to this study, the output of CVX-based holography is further processed by wideband holography. As a result, the CVX can provide a more accurate initial condition for wideband holography at lower frequencies, thus enhancing the reconstruction resolution. Following this work, Shi et al. (2020) further investigated the effect of the array density and measurement distance on the reconstruction quality of the compressive sensing method experimentally.

In addition to solving the compressive sensing formulation by iterative methods and convex optimization, there are some other types of algorithms that have been proposed in recent years. As described in the last section, the CVX-based compressive sensing has a high computational cost and does not work well for distributed sources. Moreover, for the iterative approach, such as wideband holography, the improvement in the reconstruction quality of continuous sources is still limited. To overcome those disadvantages, Fernandez-Granade et al. (2018) and Bai et al. (2018) proposed using block sparse regularization algorithms to improve the compressive sensing reconstruction capacity for extended sources. First, Bai's work reformulated the inverse problem as an unconstrained convex problem with a cost function. Then, Newton's method is used to minimize the objective function iteratively. The algorithm is validated with the experimental setup with a fan and a hand cutter. Furthermore, the results show that the proposed approach can reconstruct the block sources with high accuracy. On the other hand, Fernandez-Granade et al.

approached this problem from a different angle of view. This work still follows the L1 norm penalty formulation of the objective function; however, the second-order derivative is used for the source matrix,

$$\text{minimize} \quad \left\| \begin{bmatrix} L \\ I \end{bmatrix} \vec{q} \right\|_1 \quad \text{subject to} \quad \|\vec{p} - \boldsymbol{A}\vec{q}\|_2^2 < \delta \ , \qquad 2.\,28$$

where L is the second order derivative operator and I is identity matrix. This formulation ensures the sparsity for block sources. The methodology development is validated against the experiment using two speakers placed very close to each other, forming a dipole source. The results show that the proposed algorithm can reconstruct spatially extended sources successfully. Moreover, the accuracy is higher than the previously published compressive sensing algorithms.

3. EXPERIMENTAL SETUP FOR NESTED PLANETARY GEAR TESING

The main goal of the current study is to monitor the condition of the nested planetary gear train, to diagnose the gear manufacturing faults and inaccuracies. An upgraded testing fixture is designed to measure vibration and acoustical signals when the gear train is in unloaded operation. The testing equipment and setup are introduced in detail to facilitate understanding of the data analysis in later chapters. The first section shows the structure of the compound two-carrier nested gear train, which provides the basis for the development of the experimental setup and strategy. In addition, the relation between the input speed and meshing frequency of the gear train is also studied. The second section shows the structure of the testing fixture and NVH data acquisition equipment. Compared to the traditional horizontal encased gear train testing setup used in most other gear studies, the current experiment utilizes an open vertical setup to enable data collection from acoustical and vibrational sensors. The last section in the chapter outlines the testing procedures and explains the data structure.

3.1 Nested Planetary Gear Structure

The nested planetary gear train is a compound gear train that consists of two co-axial planetary gear sets. A simplified 2D model of the gear train is demonstrated in Figure 3.1, and a 3D model is shown in Figure 3.2. The sun gear for the outer gear set is integrated with the annulus gear of the inner gear set. Furthermore, the pinion gears on both the outer gear train and inner gear train are placed on the same carrier, rotating synchronously. The outer gearset carrier is named carrier-2, while the carrier for the inner gearset is named carrier-1. Figure 3.1, for the inner planetary gear train, the letter “P1” represents the pinion gear, “S1” represents the sun gear of the inner gear set, “A1” is the annulus gear for the inner gear set. For the outer planetary gear train, the letter “P2” represents the pinion gear, “S2” represents the sun gear of the outer gear set, “A2” is the annulus gear for the outer gear set. For this gear train, the input shaft is connected to A1/S2 so that the annulus gear 1 and sun gear 2 has the same speed as the input shaft. The nested gear train can transmit power through two paths when a different clutch is engaged. For the first power transmission path, when A2 is engaged, the accelerometer can be installed on the outer rim of A2 to monitor the external gearset condition. For the second transmission path, when S1 is engaged, the signals can be measured from the structure connected with S1 for the inner carrier monitoring.

For the gear train used in the current study, the number of teeth for each gear component are: $N_{S1} = 42; N_{P1} = 22; N_{A1} = 86; N_{s2} = 94; N_{P2} = 21; N_{A2} = 138$. The outer and inner gear train are two epicyclic gear system. For each individual epicyclic gear system, the gear ratio can be computed using the following equation,

$$-\frac{N_A}{N_s} = \frac{f_S - f_C}{f_A - f_C}, \tag{3. 1}$$

where f_S is the sun gear rotating frequency, f_C is the carrier rotating frequency, f_A is the annulus gear rotating frequency. The detailed computation of the meshing frequencies can be found in Appendix-1. And the results are summarized in Table 3.1.

Table 3.1. Gear Meshing Frequencies/Orders

	Carrier-1	Carrier-2
S1 Engaged	• 28.22 order • 470.34Hz @ 1000rpm	• 30.84 order • 514.05Hz @ 1000rpm
A2 Engaged	• 51.16 order • 852.6Hz @ 1000rpm	• 55.91 order • 931.9Hz @ 1000rpm

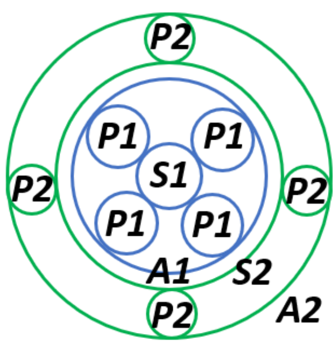

Figure 3.1. Illustration of nested planetary gear structure

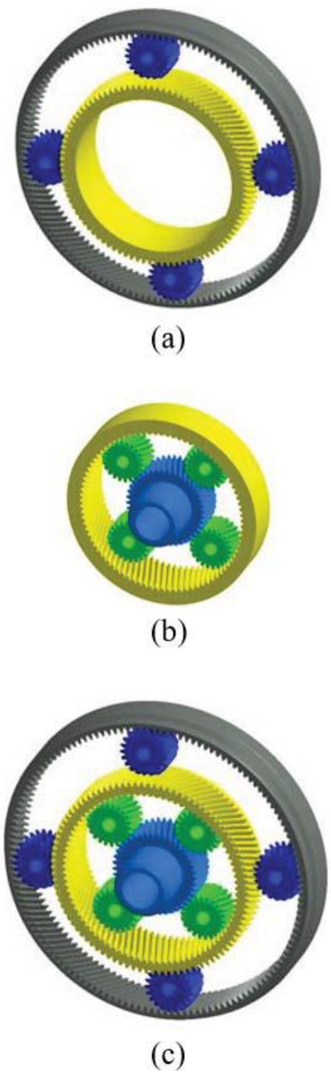

Figure 3.2. Nested Planetary Gear Train 3D Illustration. (a) Outer geartrain; (b) inner gear train; (c) complete gear train (Liao, 2018)

In the current study, the focus is to detect the gear defect of pinions. In addition, sun gear and annulus gear defect detection are not within the current scope. Five carriers with different types of defects are investigated in this experiment. As shown in Figure 3.4, ‘BoB’ is short for ‘best of the best’, representing the carrier manufactured with high precision and passed the inspection test. While ‘WoW’ means ‘worst of the worst’, which means the carrier contains at least one unground pinion. In this study, the unground gear teeth represent the teeth that do not go through the grinding process, illustrated in Figure 3.3 (a). For WoW-1, there is one unground pinion at carrier-2, while for WoW-2, there is one unground pinion within carrier-1. The WoW3 has two adjacent unground gears in carrier-2. The carrier D1 is a carrier that has a partially damaged pinion. The carrier D1 contains a pinion for which two adjacent teeth are dented using the impact of hammer and chisel (Figure 3.3 (b)).

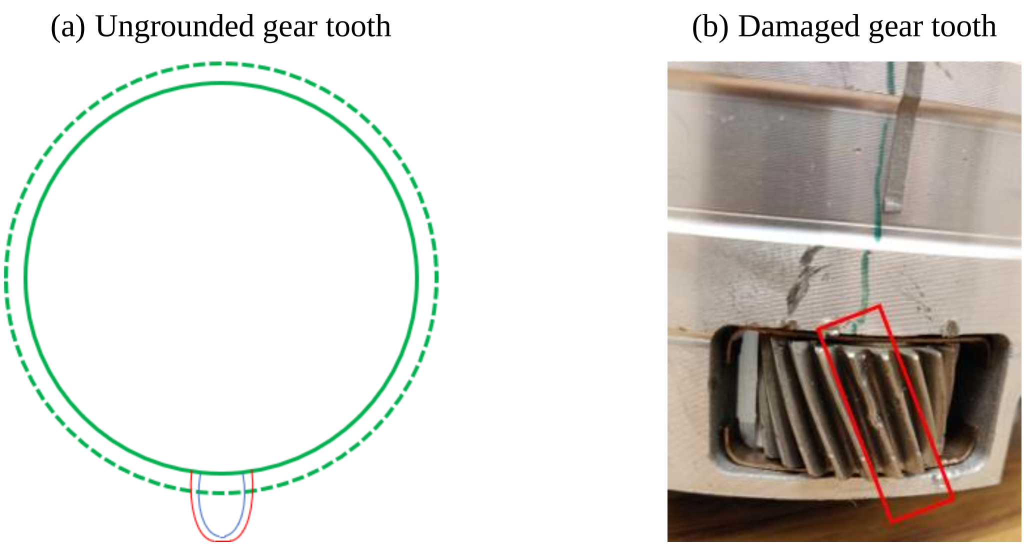

Figure 3.3. Gear Damage Illustration.

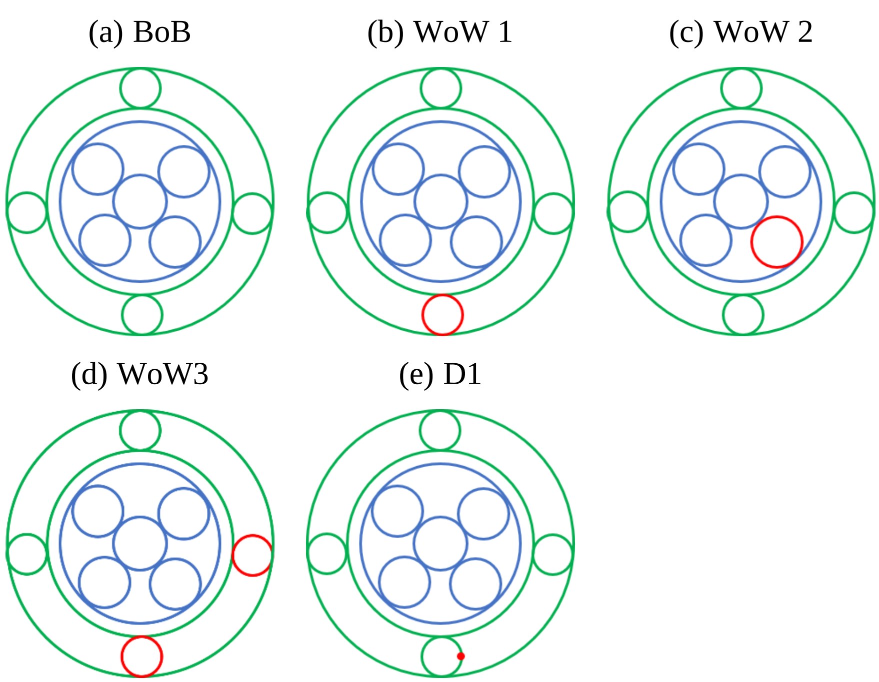

Figure 3.4. Carries for experiment.

3.2 Testing Equipment and Instrumentation

This section presents the test setup and configuration for measuring the vibrational and acoustical signals from the nested planetary gear. The test setup in the previous gear studies is built horizontally and enclosed in a case. However, the test fixture for the current study is built vertically, and the gear train is open to the air, which is shown in Figure 3.5. The gear train is open in the air and operates without lubrication. This setup is designed to be implemented in the actual manufacturing product line because it is convenient to assemble and disassemble the gear train without encasement. Furthermore, the open setup also allows more flexible vibrational sensor mounting location selection. In addition, an acoustical array is implemented, so an open setup is required for the acoustic emission to be detected.

In Figure 3.5, for the stability of the fixture, four struts are used to connect two plates and support the main structure of the test fixture. The top and bottom of a modified transmission case are bolted to the testing fixture. The transmission case is modified by cutting the excess materials, which is shown in Figure 3.6. Eighty-four holes are cut for microphone array mounting on the top plate; see Figure 3.7. The gear train is held in a modified transmission case and driven by the input shaft. Both the top plate and the modified cases are coated with damping materials to reduce the sound reflection and enhance the sound quality collected by microphones. In addition to the surface coating, the damping polymer layer is also added bottom plate surface for noise reduction.

After introducing the main structure of the test fixture, it is reasonable to illustrate how the torque is generated and transmitted to the gear train. The input shaft is connected with the motor using a rigid jaw coupling to drive the gear to rotate. The gear train is held in the transmission case, and no external load is applied to the gear train. So during the gear operation, the primary resistance for the drive train comes from the gear train itself and friction. Since there is no lubrication for the gear train, the current no-loading testing strategy reduces the possibility of gear damage during testing. The carrier is mounted on clutch-D and clutch-C, for which clutch-D is the ring for A2, and clutch-C is connected to S1. Therefore, when the clutch-D is fixed, the accelerometer can be mounted on clutch-D to monitor the carrier-2 condition. And while the accelerometer can be mounted on clutch-C as clutch-C/S1 is engaged.

Except for serving as the mounting base for the DC motor, the top plate can also be used as the insertion base for the microphone array. The details testing array is shown in Figure 3.7. Totally 84 holes are drilled on the plate. In this experiment, 64 out of 84 holes can be chosen for microphone installation. The thickness of the plate is ½ inch, and the microphone length is about 1 inch. Therefore, the microphone can be mounted on the plate using a rubber grommet by fixing both ends.

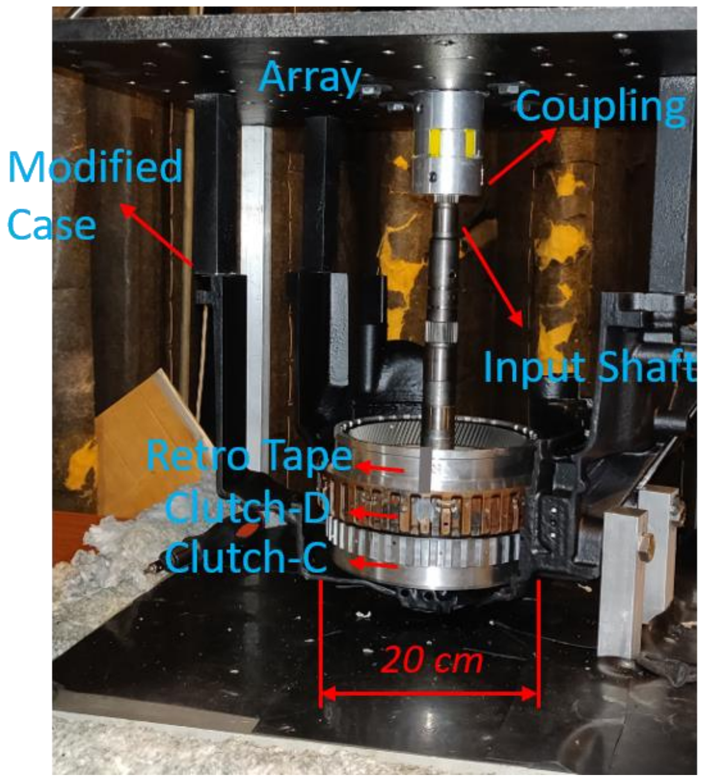

Figure 3.5. Testing Fixture

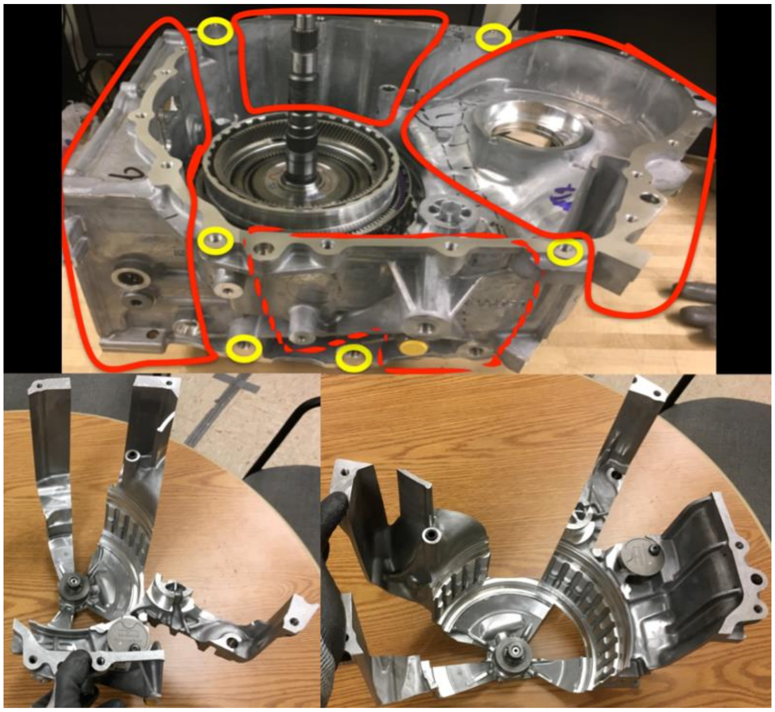

Figure 3.6. Transmission Case Modification for Testing

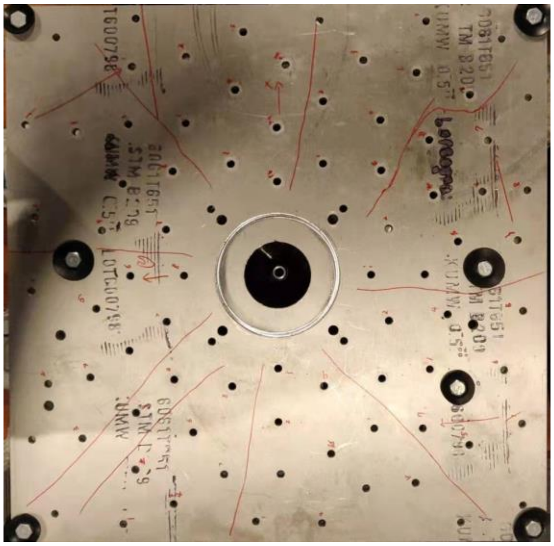

Figure 3.7. Testing Microphone Array

(a) Uncoated modified case (b) Coated modified case

(c) Uncoated plate (d) Coated plate

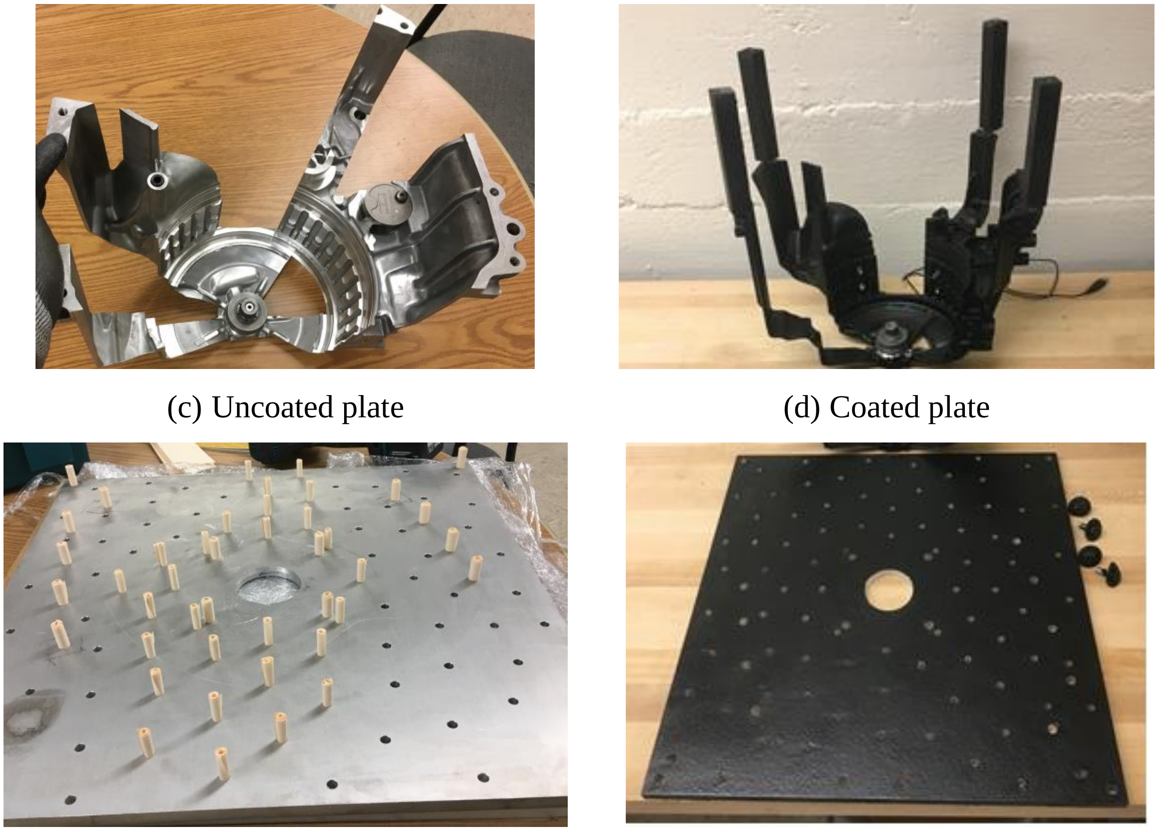

Figure 3.8. Plate Array and Modified Case, before and after Surface Coating

The previous chapters in this section have presented the structure of the test fixture. With the current design of the test configuration, three testing instruments can be utilized, which include: (1) accelerometers; (2) microphones; (3) laser tachometer. The accelerometer used here is the B&K type 4560 triple-axis accelerometer. The accelerometer can record the vibration signal in x, y, z directions with the sensitivity of 100mV/g. The microphones used in the experiment are B&K type 4958, which has a sensitivity of 11.2mV/Pa. The microphones have the dimension of 1 inch in length and ¼ inch in diameter. Except for the vibrational and acoustical transducers, laser tachometer Type 2981 is also used, shown in Figure 3.9 (a). The laser tachometer can record the revolution of the gears. All three types of test equipment are connected to the B&K LAN-XI data acquisition system. As shown in Figure 3.10, the LAN-XI system is composed of three parts: (1) frame, (2) DAQ module, (3) front end panel. The B&K LAN-XI system can digitize the collected analog signals and feed them to a computer. In the computer, the data acquisition software is B&K CONNECT V2019.5. The software can display multi-channel data simultaneously and record the data time history. The recorded data can be saved in '.csv' or '.h5' format, and those data can be processed to obtain the information of gear condition.

(a) Laser Tacho-probe (b) Accelerometer (c) Microphone

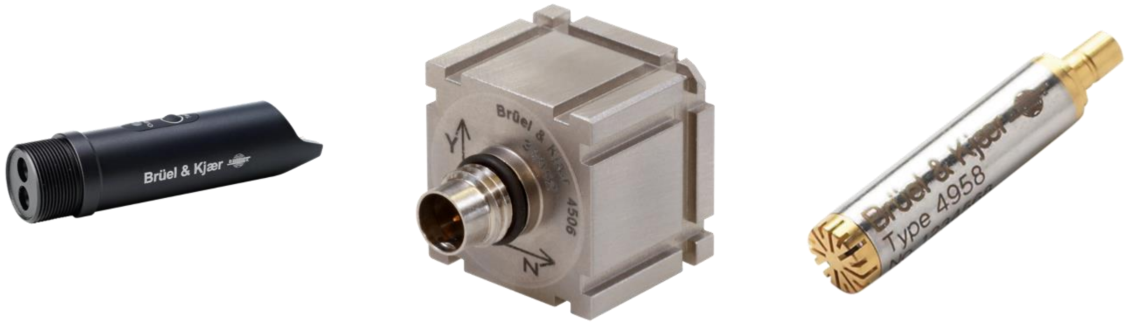

Figure 3.9. Instrumentation Sensors

(a) LAN-XI frame (b) LAN-XI DAQ (c) LAN-XI panel

Figure 3.10. Testing Microphone Array and Modified Case before and after Surface Coating

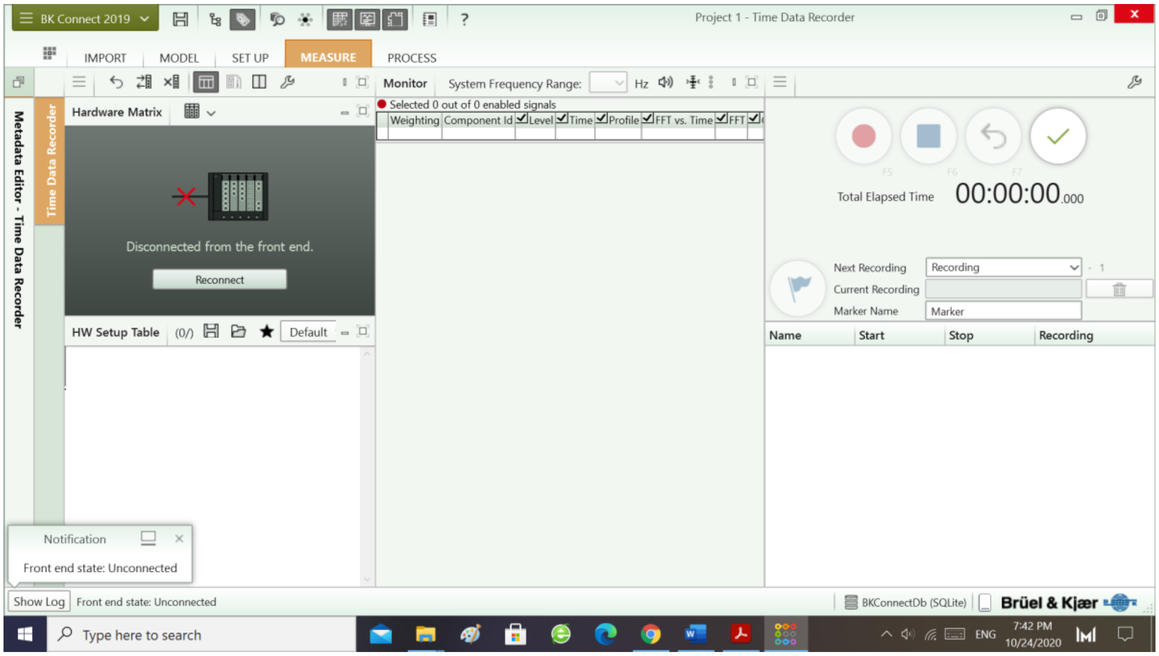

Figure 3.11. B&K connect interface demonstration

3.3 Testing Procedures

Before starting the experiment, preparation work needs to be performed. Firstly, the retro-reflective tape needs to be attached to the carrier. The retro-reflective tape works with a laser tachometer for revolution monitoring. Every time the laser beam hits the retro-reflective tape, the beam will be reflected in the opposite direction and received by the tachometer. Subsequently, the tachometer will generate an electric impulse and transmit it to the DAQ system. After properly handling the retro-tape, the microphones will be mounted on the plate and connected to the DAQ system using B&K SMB to SMB cable.

After completing the preparation mentioned above, the gear train can be assembled. The carrier, A1/S2, and the input shaft are assembled in this step. Then, the coupling will be used to connect the input shaft and the DC motor. After completing the assembly and mounting the laser tachometer, the accelerometer needs to be attached to the gear train. In addition, the accelerometer position needs to be changed for carrier 1 and 2 monitoring during the test, respectively. For example, when monitoring carrier-2, the accelerometer needs to be attached to clutch-D while the accelerometer is attached to clutch-C for carrier-1 monitoring. The test matrix for one carrier is shown in Table 3.2. The testing procedures follow the test matrix and are detailed below:

(1) Check the connection of the testing fixture. Attach accelerometer to clutch-D.

(2) Turn on the B&K LAN-XI system and connect the DAQ system to computer.

(3) Start the B&K CONNECT software and then the 'Time Data Recorder Module'.

(4) Turn on the motor, then set the speed to 500rpm. Record the data for 30-50 seconds.

(5) Set the speed to 1000rpm. Record the data again. Turn off the motor.

(6) If necessary, set the speed to 1500rpm. Record the data again. Turn off the motor.

(7) Change the accelerometer location to clutch-C. Repeat step (4) & (5) or (6).

(8) Turn off the motor. Detach the accelerometer. Change to another carrier and repeat step (1)-(7) until all the carriers are tested.

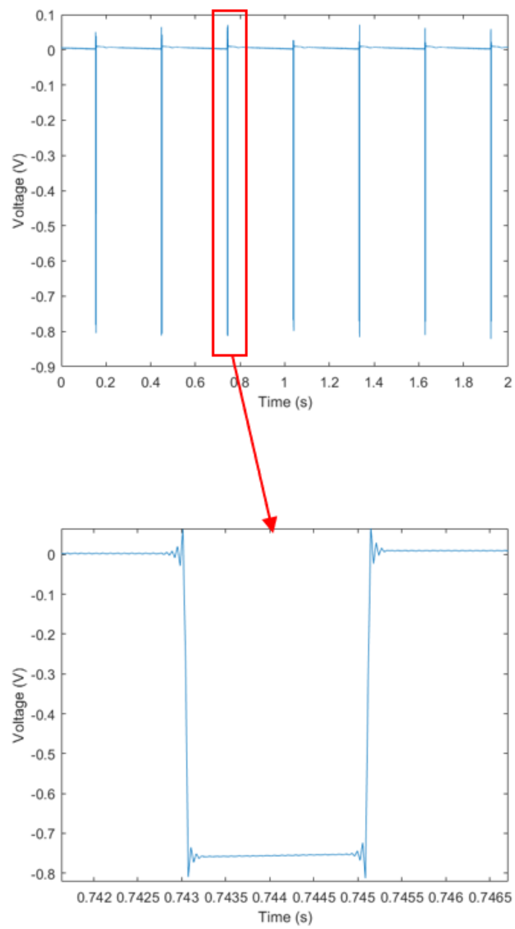

Figure 3.12. Tachometer sensor signal illustration

Table 3.2. Test Matrix for One Carrier

Clutch-C/ Array	500rpm
	1000rpm
Clutch-D/ Array	500rpm
	1000rpm

The tachometer sensor time history is illustrated in Figure 3.12. An impulse will be generated as the laser signal is reflected by the retro-reflective tape. And the signal will remain at high value for a very short duration. In the current data processing, the starting time of the impulse is chosen as the time of completing one revolution.

4. VIBRATIONAL MONITORING OF NESTED PLANETARY GEAR

Monitoring the gear condition, especially the planetary gearbox, has been studied for many years and is still a widely-concerned topic that draws the attention of numerous ongoing research due to the high-volume engineering application of the gear system. There have been plenty of previous studies focusing on the gear tooth failure prediction at an early stage since disassembling the gear system demands high human resources. One of the most effective early-stage gear monitoring methods is analyzing the signals measured by the vibration sensor. In order to process the signal from the accelerometer, many signal processing methods have been developed. However, most methods are developed for the counter-shaft gear or single-stage planetary gear. There is little information available in the literature regarding monitoring the nested planetary gear train. The current study aims to establish a vibroacoustic monitoring system of pinion gear quality for nested planetary gearset. More specifically, the focus of this chapter is to establish the gear monitoring system using the vibration signals for different types of gear faults diagnosis. The nested planetary gear train integrates two individual planetary gear trains in one carrier. Therefore, monitoring the nested planetary gear train requires multiple sensors monitoring locations and the combination of multiple signal processing techniques. In the current study, three monitoring systems are established to monitor different types of gear trains with different fault types. There are three types of faults studied:

1. One unground pinion within the inner or outer carrier
2. One or two unground gears within the outer carrier
3. The pinion gear with partial tooth defects

For fault type-1, system one is established by utilizing three techniques: (1) spectral analysis; (2) time synchronous averaging; (3) modulation sideband analysis; for faults2, the system-2 utilizes two methods: (1) frequency spectral analysis; (2) narrowband demodulation; for system-3, one technique is used, which is time synchronous averaging by windowing the signal of one pinion. The nested gear train with an unground pinion can be identified by combining the abovementioned testing strategies. The unground pinion can be localized among the four rotating pinions within the same carrier. In addition, the pinion with partial tooth defect can also be identified, and it will be shown that the tooth failure location can be found.

4.1 Gear Diagnosis System-1, Identification of the Number of Unground Pinion in Carrier-2

Narrowband demodulation has been widely applied to localization of gear crack in the fixed axis gear. For the fixed axis gear, the tooth damage will cause signal change at the same angular location for each revolution. The signal variation per revolution will modulate the original meshing signal, and the modulation will generate sidebands around the meshing frequency in the frequency spectrum. For the planetary gear system, the accelerometer signals are modulated the windowing effect caused by the pass-by of pinions. So that the local defect of the pinion cannot be defected by demodulation analysis. However, the current study subjects are gear carrier with unground planet gear. As analyzed in the last section, the unground pinions have uniformly enlarged amplitudes as passing by the sensor. This change in the signal can modify the sideband behavior around the meshing frequency. If the signal is demodulated around the meshing frequency, the demodulated phase and amplitude is inferred to show frequency components at rotating frequency, and this will be confirmed in the analysis in the current section.

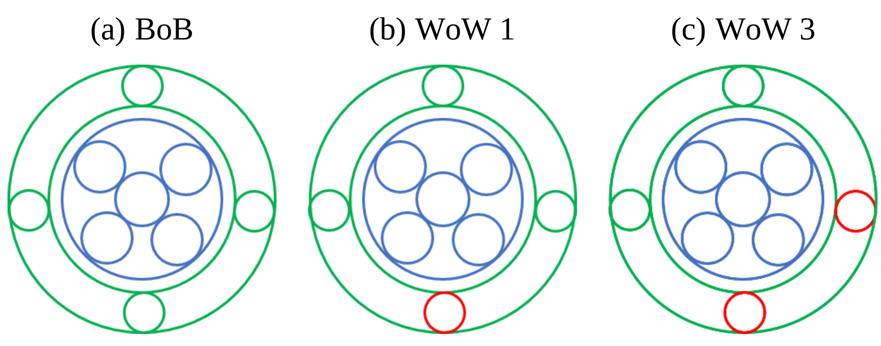

Figure 4.1. Carriers for Diagnosis with Monitoring System-2

4.1.1 Narrowband Demodulation Algorithm and Simulation Validation

This section introduces the signal processing methodology used for the phase and amplitude demodulation. Before performing the narrowband demodulation, the automatic peak finding algorithm was implemented to preprocess input signals for the demodulation process. The flow chart of the procedures is shown Figure 4.2. The automatic peak finding algorithm starts with low pass filtering of the measured time history vibration and acoustic data,

$$x_l(t) = h(t) * x(t), \quad 4.1$$

where $x(t)$ is the directly measured signal and $h(t)$ is the impulse response function of a digital low-pass filter. A Butterworth filter is used for the down-sampling process, and the cut-off frequency is chosen to be 4500Hz, which is higher than the signal frequency related to gear meshing. The low pass filtering can remove the unwanted high-frequency components in the signal to avoid potential aliasing. The lowpass filtered signals are subsequently processed with downsampling. The down-sampling can facilitate the peak finding process by reducing the size of the data. In addition, the reduction in sampling frequency can also simplify the Hilbert transform filter design by reducing the order of the filter. The time discretized signal after the down sampling process can be expressed as:

$$x_{l,d}(n) = x_l(nD), \quad 4.2$$

which suggests a selection of one signal sample in the low-passed signal $x_l(n)$ for every D samples. Then, the power spectrum density (PSD) of the down sampled signal, $S_{x,ld}(f)$, is computed based on the time domain signal.

The peak finding algorithm compares the PSD at each frequency, $S_{x,ld}(f)$, with the PSD value obtained by a moving average on the PSD in a narrow band around that frequency. The moving average PSD can be expressed as:

$$\bar{S}_{x,ld}(f) = \frac{1}{2N+1}\sum_{k=-N}^{N} S_{x,ld}(f + k\Delta_f), \quad 4.3$$

where Δ_f is the frequency interval in the power spectrum and the moving average is perform in a frequency band centered at f with a band width of $(2N+1)\Delta_f$. In the current work, the bandwidth is set to be 100Hz, and Δ_f is 1Hz. The level difference between the original PSD and the averaged PSD is then calculated as:

$$\Delta S_{x,ld}(f) = \left| S_{x,ld}(f) - \bar{S}_{x,ld}(f) \right|. \quad 4.4$$

If $\Delta S_{x,ld}(f) > 6$ dB, the frequency is identified as a peak frequency f_m. The peak frequency parameters are needed in the following Hilbert transform based demodulation analysis.

The downsampled signal is bandpass filtered around the selected m^{th} peak frequencies f_m for the narrowband demodulation analysis, i.e., to compute its instantaneous amplitude and phase for each identified peak frequency. The bandpass filter can eliminate the signal not related to the demodulated meshing harmonics. Furthermore, the bandpass filtered signals also meet the requirement that the modulation frequency is much lower than the carrier frequency, which allows the signal to be processed by the Hilbert transformer. The band-passed signal can then be represented mathematically in the form of amplitude and frequency modulated signal with a carrier frequency of f_m as:

$$y_m(t) = X_m(\mathrm{t})(1 + a_m(t))\cos\,(2\pi f_m t + \varphi_m + b_m(t))\,. \tag{4. 5}$$

where X_m is the time averaged amplitude, φ_m is the initial phase, $a_m(t)$ is the amplitude modulation signal, and $b_m(t)$ is the phase modulation signal. A digital Hilbert transformer is then applied to this down sampled and band-passed signal. The signal can be transformed into

$$h_m(t) = X_m\big(1 + a_m(t)\big)sin\,(2\pi f_m t + \varphi_m + b_m(t))\,. \tag{4. 6}$$

With the knowledge of the signal carried by both sine and cosine signals, a complex analytic signal can be obtained as:

$$c_m(t) = y_m(t) + ih_m(t) \; = X_m(1 + a_m(t))(t)e^{i(2\pi f_m t + \varphi_m + b_m(t))}. \tag{4. 7}$$

With the help of the analytic signal constructed from Hilbert transform, the envelope of signal can be computed by,

$$X_m(a_m(t) + 1) = |c(t)|. \tag{4. 8}$$

Furthermore, the instantaneous phase can be calculated as,

$$b_m(t) - 2\pi f_m t + \varphi_m = \arg\big(c_m(t)\big). \tag{4. 9}$$

By following the above procedures, the instantaneous phase and amplitude envelope around m^{th} peak can be determined. The instantaneous frequency $f_{i,m}(t)$ can be calculated from the instantaneous phase,

$$f_{i,m}(t) = \frac{\arg\big(c_m(t)\big) - 2\pi f_m t + \varphi_m}{2\pi t}. \tag{4. 10}$$

Numerical experiments have been conducted to validate the Hilbert demodulation approach and the automatic peak finding algorithm for different types of modulated signals. In the current numerical simulations, three types of periodic signals at different frequencies are synthesized, see Table 4.1 for the parameters used. The first signal component is a 1000 Hz sinusoidal wave with only periodic amplitude modulation. The second signal component is a 2000 Hz sinusoidal wave with periodic frequency modulation (FM) and periodic amplitude modulation (AM). The third signal component is a 4000 Hz sin wave with low-passed random FM. The peak finding results and power spectral density functions of bandpass filtered signals are shown in Figure 4.3. In Figure 4.3 (a), the blue line represents the original power spectrum of the downsampled signal, and the red line represents the moving averaged power spectral density function. It is shown that the major peaks can be identified, and the signal is bandpass filtered around the peaks. The demodulation results are shown in Figure 4.4. For a source frequency at 1000 Hz, the signal is demodulated accurately with 2 Hz amplitude modulation. Both frequency and amplitude modulation of the second signal component is identified with the accurate parameter. For the third signal component at 4000 Hz, the demodulated frequency shows broadband frequency components, matching the numerical simulation signal parameter. The demodulated phase and amplitude analysis confirm that the signal with different modulation types at different peak carrier frequencies can be successfully demodulated, using the combination of peak finding and demodulation algorithms.

Table 4.1. Simulated Signal Parameters

Component-1	• 500Hz • P/M: $a_1(t) = 0$ • A/M: $b_1(t) = 1 + 0.1\cos(2\pi 10t)$
Component-2	• 1000Hz • P/M: $a_2(t) = 2\cos(2\pi 10t)$ • A/M: $b_2(t) = 1.5 + 0.15\cos(2\pi 10t)$
Component-3	• 2000Hz • P/M: random, 2Hz standard deviation, low passed filtered 100Hz • A/M: $b_3(t) = 0$

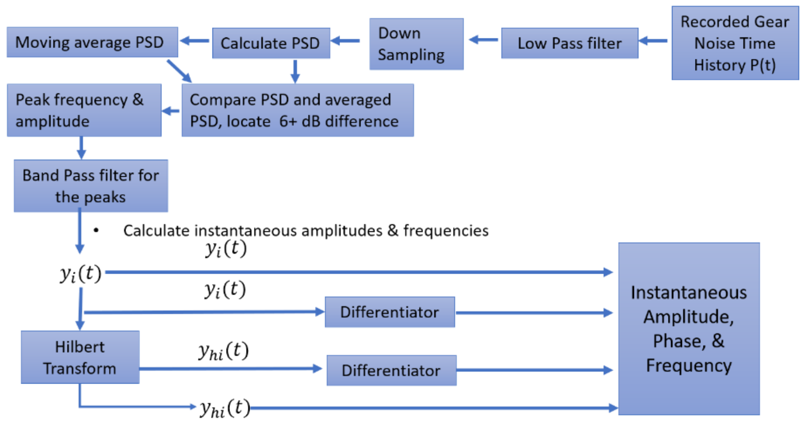

Figure 4.2. Procedures for Automatic Peak Finding and Demodulation

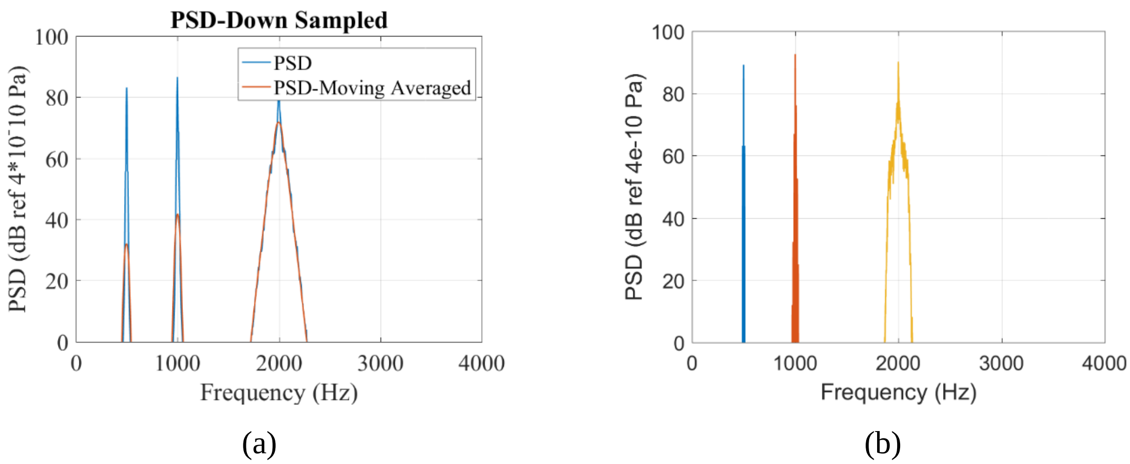

Figure 4.3. (a) PSD and (b) Bandpass filtered PSD, simulated signal

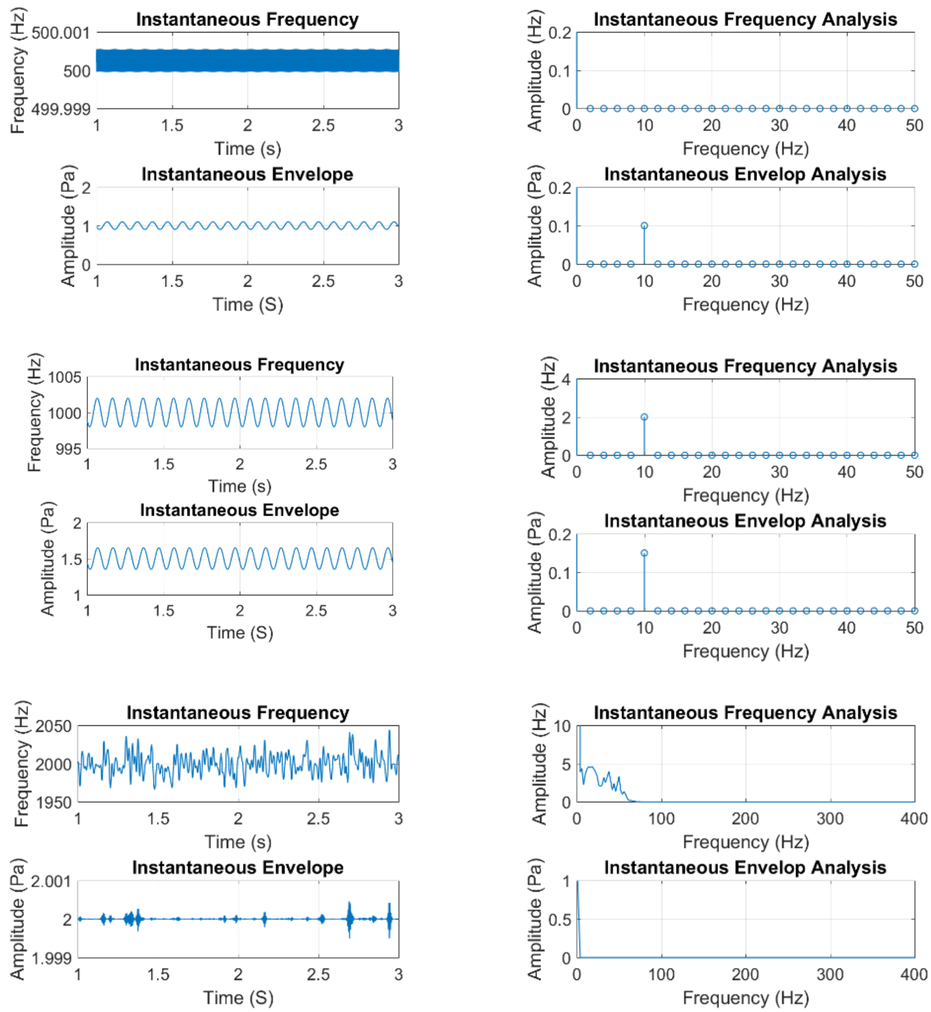

Figure 4.4. Demodulated phase/amplitude time history (left) and frequency component (right)

4.1.2 Application of Narrowband Demodulation to Nested Planetary Gear Monitoring

In this section, experimental results for both vibrational signals demodulation and their application in detecting gear grinding defects are discussed. For most experimental data used in this study, the input shaft speed is 1000 RPM. The carrier rotating frequency, i.e., the pinions' frequency about the center axis, is 6.75 Hz. Firstly, the broadband frequency spectrum of three planetary gear trains is analyzed and compared. The frequency spectrum results show a significant difference between BoB and WoWs, while the difference between WoW1 and WoW3 is not very clear. A demodulation analysis needs to be performed to investigate the number of unground pinions further. The repeatability of the experiment was validated initially using WoW 1 data, where the experiment was repeated three times with the same setup, and the power spectral density of the measurement signals and the AM/FM results of all three experiments were compared. The speed effect is also investigated using the 500rpm and 1000rpm demodulation results. Then, the demodulation results of BoB, WoW 1, and WoW 3 were compared to show how the signal signatures can be used for the geartrain diagnosis. It will be seen in the latter part of this section that the frequency spectra of the demodulated frequency and amplitudes exhibit prominent spectral peaks at the rotation frequency of pinion carriers and their harmonics, which suggests that the main contributor to the signal modulation is the carrier rotation. The appropriate features of the demodulated signals will be chosen to diagnose the gear grinding defect. Furthermore, an autonomous diagnosis system can be established using the results of the current study for pinion grinding defect detection. It also needed to be pointed out that the time history plots of the demodulated results are not presented in this work since the signals are contaminated by measurement noise. In addition, the time domain demodulated signals do not show apparent signal features that are connected to physical phenomena.

The power spectral density functions of the vibrational data for BoB/WoW1/WoW3 are shown in Figure 4.5, respectively. For the vibrational data, it can be observed that there are apparent peaks at the meshing frequency and its harmonics for WoWs, while the spectrum of BoB does not show obvious peaks. In addition, the WoWs also show higher PSD levels than BoB over most of the frequency range. However, the difference between the two WoWs is not distinguishable with a visual inspection. Therefore, based on the vibrational signal power spectrum, the meshing frequency (932Hz) is chosen as the center frequency for the narrowband demodulation analysis. The bandwidth of the bandpass filter is 100Hz.

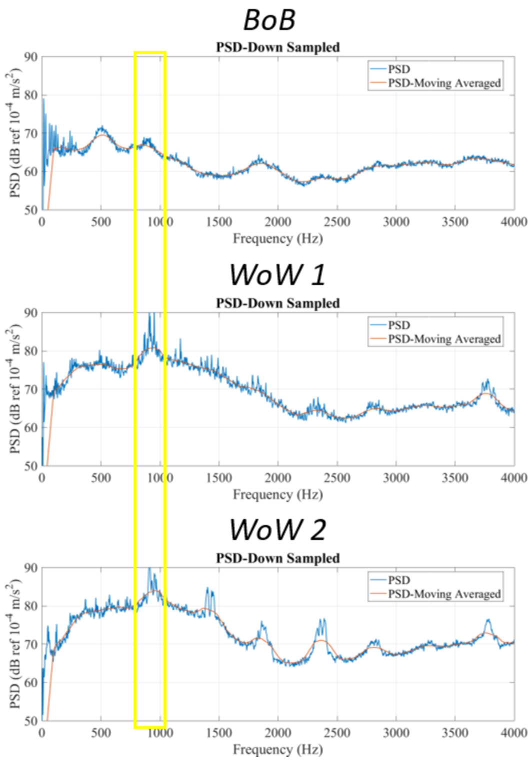

Figure 4.5. Power Spectral Density and its Moving Average, Vibrational Data

In order to establish an autonomous system for gear diagnosis, the data has to be repeatable for gear trains with comparable manufacturing errors. In addition, the optimal testing speed needs to be chosen based on the actual manufacturing considerations. Therefore, before using the demodulated frequency and amplitude for the gear diagnosis, the consistency of the demodulation results is analyzed for both repeated experiments under the same condition and at different speeds. In Figure 4.6, the frequency spectra of the demodulated frequency and amplitude for WoW 1 of repeated experiments. Obviously, at the meshing frequency of 932 Hz, both demodulated phase and amplitude spectra show the peaks at frequencies associated with the carrier rotating frequency (Hz) and its harmonics. This characteristic confirms that the signal modulation is mainly caused by the carrier rotation that makes the unground pinion periodically move close to the sensor and then move away. Similar modulation patterns can be observed from the data of repeated experiments with the same setup, which confirms the repeatability of the experiment. The speed effect is investigated by comparing the results at 500rpm and 1000rpm (see Figure 4.7). The frequency spectrum of AM and FM for both speeds shows a similar pattern: peaks can be observed at the gear carrier rotation frequency and its harmonics. It is noted that the carrier rotation frequencies under different input shaft speeds are different, for which rotates at 3.34Hz for 500 rpm input shaft speed. The results confirm that the testing speed does not significantly affect the measured data. Hence, the diagnosis tool developed based on the demodulated signal analysis is, in principle, not restricted to a specific input shaft speed in actual implementations.

After the validation of the repeatability of the measurement, the demodulation results for three different gear trains (BoB, WoW 1, and WoW 3) are compared (see Figure 4.8). It can be observed that BoB does not show significant carrier rotation modulations for the demodulated frequency and amplitude. For vibrational data of WoW 1, both significant frequency and amplitude modulation components can be observed at first-order harmonics of the carrier rotating frequency. An examination of demodulated vibrational data of WoW 3 reveals that 1-3 order peaks can be observed for demodulated amplitude, and first-order can be the observed peak for demodulated frequency. The demodulation results for BoB suggest that the signal amplitudes vary as the pinion gear pass by the sensor. However, suppose there is no unground gear to enhance the pass-by signals for certain pinions. In that case, consequently, the interference between different pinions will be too strong for the modulation at carrier rotation frequency to be detected. Comparing the results between WoW 1 and WoW 3, it is clear that the two adjacent unground pinions can result in a more complex modulation behavior than a single unground pinion for the vibrational observation. A stationary sensor receives the vibrational signal. The signal is dominated by the pinion closest to the accelerometer, while the microphone receives signals from four pinions simultaneously. Therefore, the experimental results suggest that vibrational monitoring is more suitable for unground gear detection.

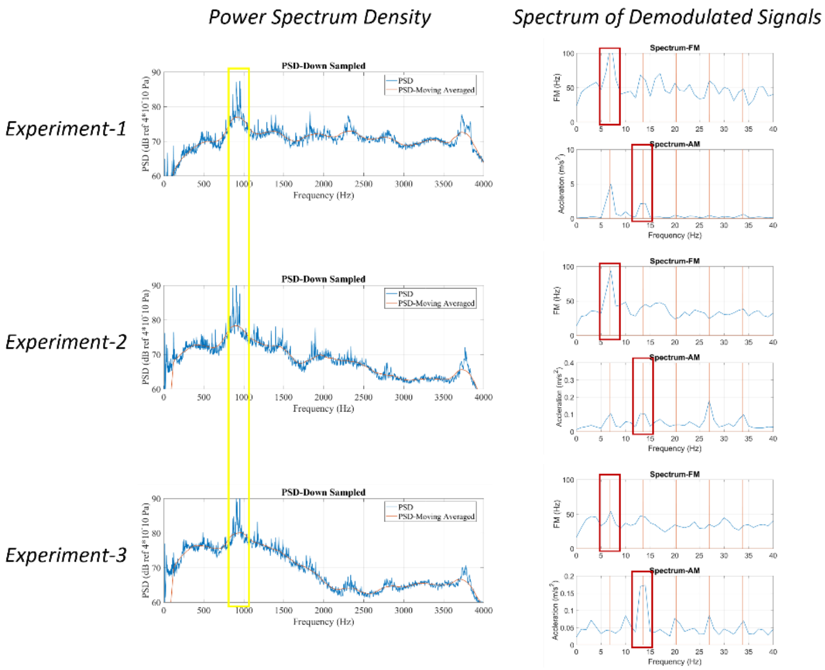

Figure 4.6. Repeatability for Repeated Testing. (a) Power Spectral Density of Measured Vibration (left column); (b) Power Spectral Density of Demodulated Phase and Amplitude.

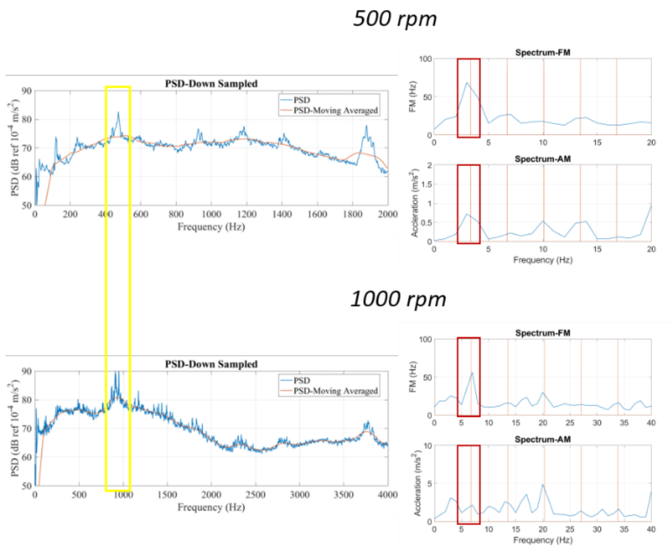

Figure 4.7. Repeatability for Testing Under Different Speeds. (a) Power Spectral Density of Measured Vibration (left column); (b) Power Spectral Density of Demodulated Phase and Amplitude.

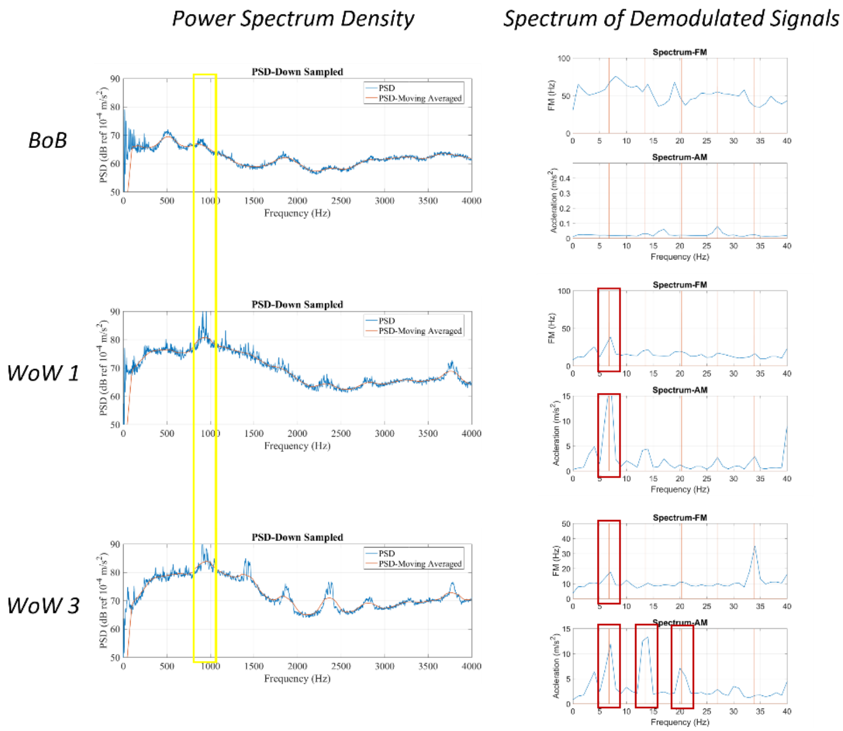

Figure 4.8. Results Comparison for Different Carriers. (a) Power Spectral Density of Measured Vibration (left column); (b) Power Spectral Density of Demodulated Phase and Amplitude.

The demodulated frequency and the amplitude results for three different types of the gear train show a different correlation between the demodulated frequency/amplitude and the pinion rotation with the carrier. The grinding defect of the pinion will amplify the modulation effect of the carrier rotation, thus leading to the changes in demodulated frequency and amplitude, especially for the vibrational measurement. The correlation between the demodulated frequency (or amplitude) and the carrier rotating frequency can be used to develop a procedure for the pinion gear grinding defect monitoring for the nested planetary gear (see Figure 4.9). Firstly, the broadband power spectrum plots are analyzed. If the power spectrum plot does not show significant peaks at the meshing frequency and its harmonics, it can be concluded that there is no unground pinion gear within the system. If the PSD analysis shows significant peaks at the meshing harmonics, further analysis will be conducted using the demodulated vibrational signals around the meshing frequency. For the demodulated frequency and amplitude, if only first-order peaks are found in the AM and FM frequency plots, then only one unground gear is within the system. Otherwise, there will be two adjacent gears existing in the gear train. It also needs to be noted that if the two unground gears are not adjacent to each other but in opposite locations, or if there are more than two unground pinions, these NVH monitoring procedures do not need to be performed because the gear train system cannot be mechanically assembled due to the manufacturing error.

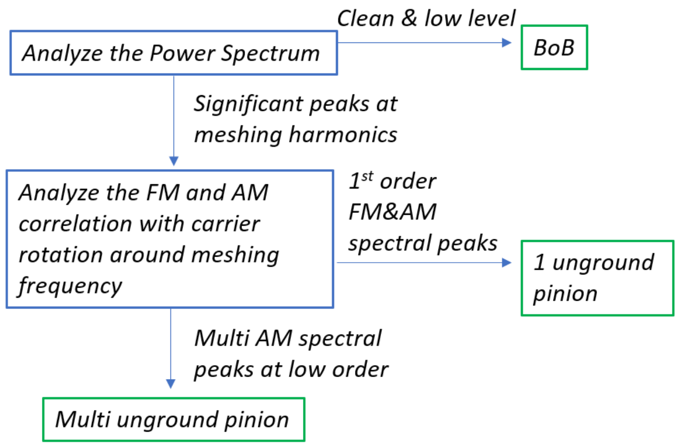

Figure 4.9. Flow Chart for Data Analysis Procedures of Pinion Grinding Faults Diagnosis

In the current study, the classical Hilbert demodulation of phase and amplitude is performed to acoustical and vibrational signals of a nested planetary gearset to detect gear grinding defects. Three different nested planetary gear trains are investigated: an error-free system, a gear train with one unground pinion, and a gear train with two adjacent unground pinions. A vertically configurated and cut-to-open test platform is built to enable the simultaneous collection of vibrational data. In order to perform data analysis, peak frequencies in the power spectral density of the signals are identified initially by an automatic peak finding algorithm. If peak frequencies associated with the pinion-angular gear meshing frequency are found in the power spectrum density analysis, it suggests a possible existence of unground pinions. Therefore, the identified peak frequencies corresponding to gear meshing frequency were chosen for the demodulation analysis. The demodulated signals vibrational data show consistent results across different experiments, which confirms the reproducibility of the test results. Suppose pinions with grinding defects exist in the system. In that case, the spectral analyses of demodulated frequency and amplitude show strong frequency components associated with carrier rotating frequency and its harmonics, which confirms that the carrier rotation is the main contributor to signal modulation characteristics. In addition, the demodulated signals for the gearset with an unground gear are significantly different from gearset with no unground gear. The results suggest that the unground pinion amplifies the local vibrational signals, subsequently changing the transducers' behavior.

The reproducibility of the test results shows that the demodulated frequency and amplitudes can be used as a criterion for identifying an unground gear in the gear set. Moreover, a simple diagnosing protocol can be established based on the visual inspection of the demodulation results. More specifically, the significant frequency component related to carrier rotation in the demodulated signal shows the existence of the unground pinion. Furthermore, the difference between the demodulated signal's frequency spectrum structure indicates the number of unground pinions.

The current study confirms that the Hilbert demodulation can be used for the nested planetary geartrain diagnosis with unground pinions. Therefore, the Hilbert transform can be leveraged to develop an autonomous system for the nested planetary gear grinding error detection. Although consistent results can be obtained for the current experimental setup, it will still be beneficial if theoretical models can be established to assist the understanding of the current demodulated frequency/amplitude structure. In addition, the current gear diagnosis system only focuses on identifying the griding defect. Other types of faults in gears, e.g., gear chipping and crack, are not investigated in this system. In the next section, the monitoring pinion local faults will be discussed.

4.2 Gear Diagnosis System-2, identification of the location of a single unground pinion

The nested planetary gear train with one unground pinion is studied in this section. The unground pinion can be any one of the eight pinions in the system. Therefore, there are two goals for the gear monitoring system to fulfill: (1) identify which carrier has unground pinion; (2) identify which pinion is unground within one carrier. The autonomous system is established to identify the unground pinion and find its location with the following procedures:

1. Using the frequency/order spectrum analysis for preliminary investigation.
2. Using the modulation sideband analysis to identify which carrier has unground pinion.
3. Using the synchronously averaged time history to find which pinion is unground.

This section will start with introducing the method-TSA and the modulation sideband analysis. It will then be followed by discussing the results for the gear monitoring.

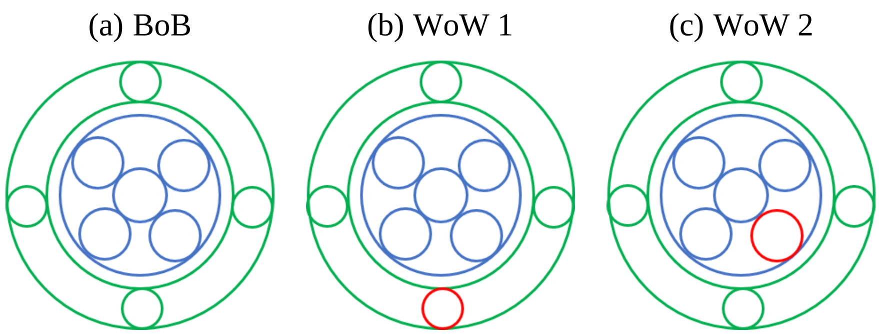

Figure 4.10 Gear Faults Demonstration

4.2.1 Methodology

Three methods are used for the diagnosis of the unground pinion location: (1) frequency spectrum analysis, (2) time synchronous averaging, (3) modulation sideband analysis. The frequency spectrum analysis is a typical procedure for signal analysis, so it will not be discussed here. Instead, the TSA and modulation sideband analysis will be introduced in this section. The modulated signal modeling will also be presented for the modulation sideband analysis.

4.2.1.1 Time Synchronous Averaging

Time synchronous averaging processing of the signals is critical to de-noise the gear vibrational signal because it can reduce the signals not related to the gear meshing. The main idea of time synchronous averaging is to divide the signal time history into individual revolutions and average the signals across multiple rotations. The signals unrelated to the revolution will be filtered out during the averaging processing. Time synchronous averaging has been mainly applied to the countershaft fixed axis gear rather than planetary gear due to the interference of the signals from different pinions in the planetary gear set. However, in the current study, the time synchronous averaging technique is proposed to be applied to the pinion pass-by signals acquired from a sensor mounted on the fixed clutches planetary gear train. For the planetary gear train, although the planet gears have both self-rotation and rotation with the carrier, the impact frequency is still integer multiples of the carrier rotation frequency. Therefore, time synchronous averaging can preserve the impact frequency component and the modulated signals caused by both the carrier rotation. After enhancing the signal quality with synchronous averaging, the gear signals can be analyzed more efficiently with other techniques. On the other hand, the synchronously averaged time history can be used for the gear diagnosis directly because it will be shown that the presence of the unground pinion will cause significant amplitude modulation in the averaged signal. In addition to applying the regular synchronous averaging to identify the unground pinion in the carrier, the synchronous averaging can also be extended to single planet gear monitoring with proper windowing. This type of synchronous averaging can be applied to identify the local defect of the pinions in the compound carrier system.

In order to understand the application of time synchronous averaging, the processing procedures are illustrated using an example, see Figure 4.12. A flow chart summarizing the TSA procedures is shown in Figure 4.11 to facilitate understanding the method. Firstly, the measured signals need to be divided into a period of carrier revolutions based on the tachometer sensor measurement. Then, the signals are resampled to have equal samples per revolution. Due to measurement errors or gear speed variation, the number of samples might not be the same in each revolution. The resampled signals across multiple revolutions are then added and averaged. The last step is to resample the signal back to its original sampling rate to form the synchronously averaged signals.

The residual signals are calculated in standard synchronous average processing for countershaft gears by removing signals at the meshing frequency and lower order sideband in the averaged signals. Furthermore, the residual signals will be used for the gear fault diagnostics. However, the focus is unground gears in a planetary system in the current study. All the teeth will generate a uniform impact that is larger than the normal pinions. Therefore, the synchronous averaged signals are used directly for analysis without calculating the residual signals.

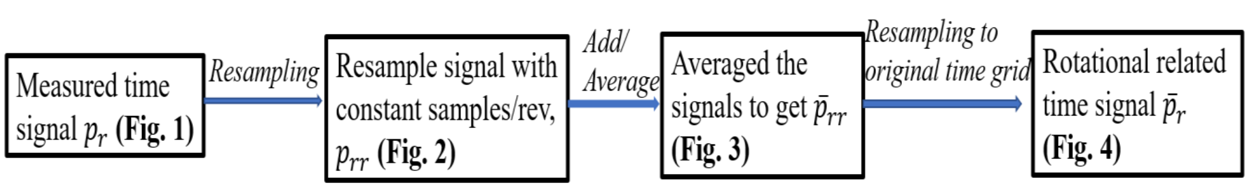

Figure 4.11. Time Synchronous Averaging Algorithm-Flow Chart

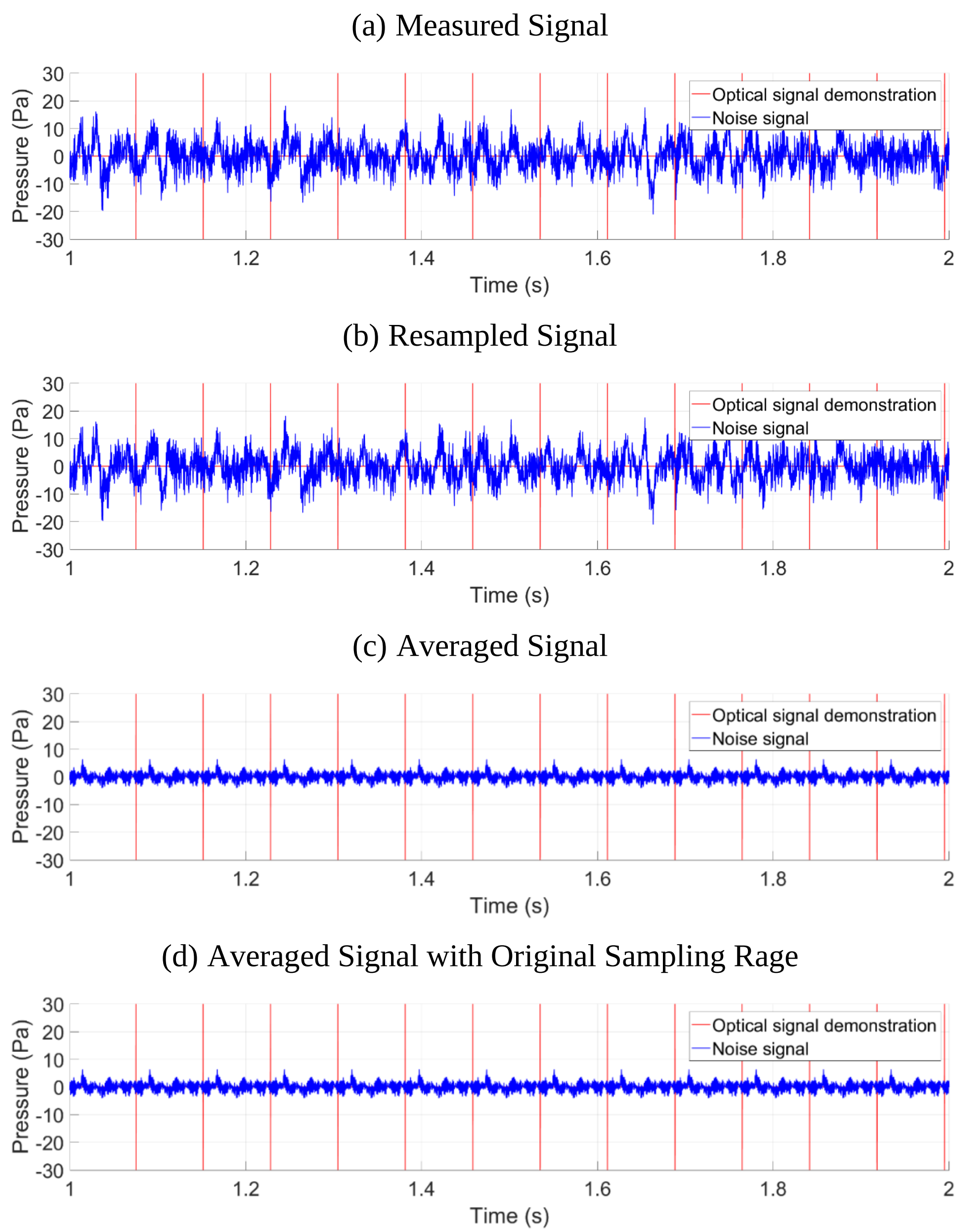

Figure 4.12. Time Synchronous Averaging Algorithm-Example Demonstration

After introducing the fundamentals and procedures of the standard time synchronous averaging procedure, the application of the TSA to the pinion gear diagnosis needs to be investigated. It is straightforward that the time signal measured by the sensor, which is mounted on the planetary gear clutch, will be dominated by the passing-by pinion. There are four opinions on each of the carriers for the nested planetary gear train in this study. Therefore, one revolution of the carrier is divided into four quarters, as shown in Figure 4.26. On the other hand, the time history measured by the sensor is divided into four quarters as well. And it is assumed that the time history within each quarter is dominated by the meshing impact from the closest pinion gear. Finally, the gear angular location and time history are matched according to the laser tachometer measurement, marked as the red vertical line in the time history.

4.2.1.2 Modulation Sideband Analysis and Modelling

If the broadband spectrum is zoomed in around the meshing frequencies or its harmonics, the modulation sideband analysis can be performed by analyzing the sideband structure. In the sideband plots, the dashed vertical lines represent the integer multiples of the modulation frequencies. One example is shown in Figure 4.13. In this example, the signal with amplitude modulation has the sideband at the modulated frequency in the frequency domain.

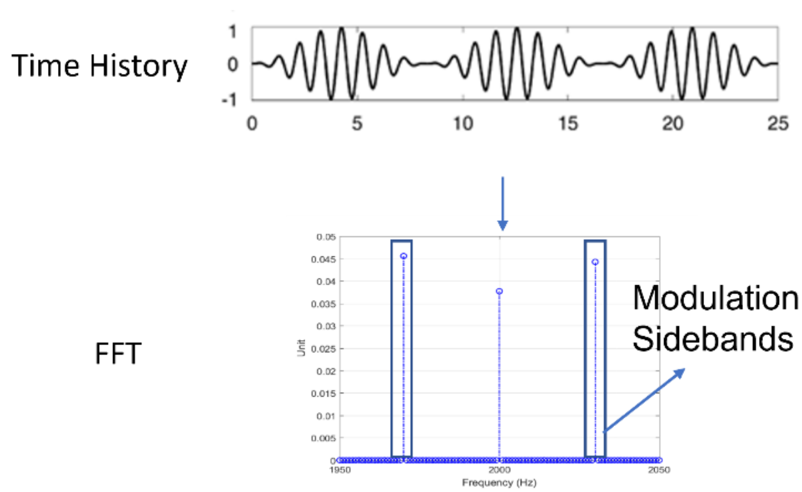

Figure 4.13. Demonstration of phase angle of planet gears (4 planet gears)

The modulation phenomenon in the signals can be modeled using the synthesized signal. And this section will introduce how to model the signal based on the planetary gear train meshing characteristics. The planet gear pass-by signal model was firstly proposed by MaFadden (1986) to explain the asymmetry in the sidebands when multiple planet gears are present. Then, the model was further developed by Inalpolat (2009) to model the sideband behavior of planetary gear trains with different teeth and planet gear numbers. In the current study, the signal model starts with the previously developed derivation. However, the model is modified based on the characteristics of the gear train with unground planet gears. The planet gear relative phase change caused by the unground carrier fitting is proposed to explain the unique sidebands in the current experimental data.

In the current modeling, it is assumed that the accelerometer is mounted on the engaged gear (sun or annulus gear). The derivation is the same for engaged sun or annulus gear measurement, and the annulus gear signal is chosen for analysis. The accelerometer signals collected on the stationary clutch using an acceleration sensor can be modeled as the gear pass-by signals. The fundamental gear tooth meshing frequency is,

$$\omega_m = Z_a \omega_c \,, \tag{4. 11}$$

where Z_a is the teeth number of the annulus gear, ω_c is the carrier rotating frequency. The least mesh angle is,

$$\lambda = \frac{2\pi}{Z_s + Z_a} \,, \tag{4. 12}$$

where Z_s is the sun gear teeth number. Dynamic meshing force generated by local teeth impact can be modelled as periodic signals and expressed in Fourier series form,

$$F_i(t) = \sum_{j=1}^{J} F_{ij} \cos\left(jZ_r\omega_c t + \phi_j + jZ_r\psi_i\right) , \tag{4. 13}$$

where ψ_i is the angle of i^{th} planet, ϕ_j is the phase of the carrier. Planet gear passing-by effect is represented using Hanning window,

$$w(t) = \frac{1}{2} - \frac{1}{2}\cos\left(\frac{2\pi N t}{T_c}\right) \tag{4. 14}$$

For a planet gear at angle ψ_i, the signals transmitted to the sensor are,

$$w_i(t) = W_i w\left(t - \frac{\psi_i}{2\pi} T_c\right) U_i(t), \tag{4. 15}$$

and,

$$U_i(t) = \sum_{n=1}^{\infty} \left\{ u\left[t - \left(\frac{(n-1)N + i - 1}{N}\right) T_c\right] - u\left[t - \left(\frac{(n-1)N + i}{N}\right) T_c\right] \right\} \tag{4. 16}$$

where $u(t-a)$ is unit step function, T_c is the carrier rotation period, N is the total number of planet gear. The total acceleration signals received by accelerometer can be calculated by adding the signals induced by all the planet gears together,

$$a(t) = \sum_{i=1}^{N} a_i(t) = Cw_i(t)F_i(t)\,. \qquad 4.\ 17$$

The signal modeling procedures are demonstrated in Figure 4.14. As shown in the plots, local vibrational signals for three planet gears are $F_1(t)$, $F_2(t)$, and $F_3(t)$. The planetary pass-by transfer functions, $w_1(t)$, $w_2(t)$, and $w_3(t)$, correlate the respective vibrations of the local pinions with the corresponding measured signals. The local vibrational signals take the form of monotonic sine waves, and the transfer functions are chosen to have a form of the Hanning window. The vibrational signals of a planetary gear are then windowed with the corresponding transfer function when it passes by the accelerometer each time. The summation of the windowed signals for all three planet gears, as Eq. 4. 7, yields the total signals recorded by the sensor.

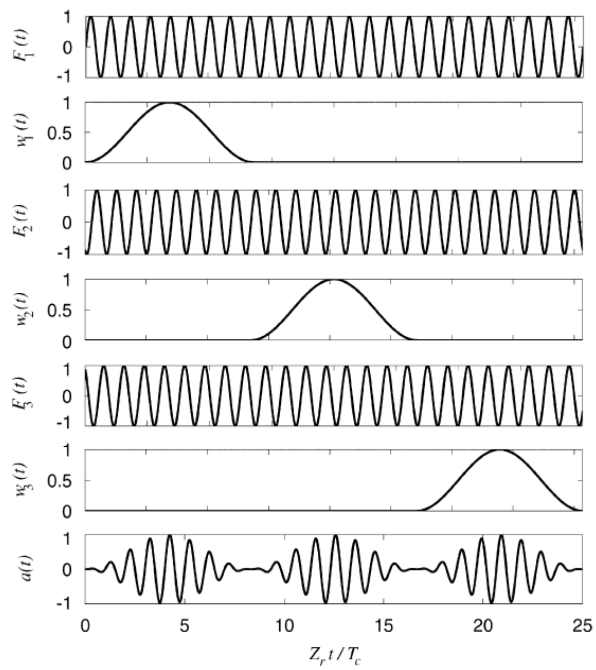

Figure 4.14. Modulation Sidebands Signal Synthesis

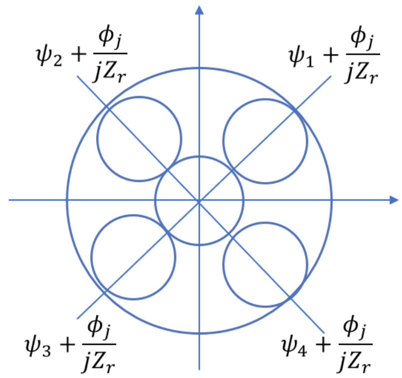

Figure 4.15. Demonstration of phase angle of planet gears (4 planet gears)

4.2.2 Results Analysis for Identification of Unground Pinion in the Carrier

4.2.2.1 Frequency Spectrum Analysis

The analysis of the gear faults starts with frequency spectrum analysis because the frequency spectrum analysis is the basis for further analysis. For signals measured from rotating gears, the frequency spectrum's peaks and harmonics are mostly related to the gear tooth meshing. Therefore, except for the frequency spectrum analysis, order spectrum analysis can also be implemented because the meshing frequency components for gear always remain in the same order regardless of the input speed. The order spectrum is calculated by normalizing the frequency with input shaft speed, representing the number of contacts per input shaft revolution. In this section, firstly, the order and frequency spectrum of the gear are analyzed to identify the meshing component invariant with the input speed. Then, the linear scale spectrum at 1000rpm input speed is analyzed for different carriers. It is shown that the existence of the unground gear can significantly change the energy distribution at different meshing frequency harmonics. In addition, frequency spectral of time synchronously averaged signals are also calculated because the time synchronous averaging can reduce the structural vibration signals substantially and preserve the meshing signal and its harmonics.

The frequency spectra at different speeds are shown, respectively, in Figure 4.16 and Figure 4.17 for the outer and inner planet gears. Since the measurements were conducted at a constant input shaft speed, the order spectrum is calculated by normalizing the frequency with the input shaft speed. The order of the vibrational signals represents the signal frequency normalized with the input shaft revolution frequency.

For the outer planet gear, it can be seen in Figure 4.16 that increasing the gear rotational speed enhances the overall signal level at a broad frequency band but does not cause the peak frequency shift for most of the frequency components. For BoB and WoW2, the frequency and order spectra are similar, which indicates that the inner carrier unground pinion will not cause a significant effect on the energy frequency distribution on the outer carrier. Both BoB and WoW2 show peaks at the meshing frequency at about the 55th order but do not show peaks in any higher-order harmonics. However, when an unground gear is present at carrier-2 (WoW1), it induces vibrations with higher peaks at the meshing frequency and generates higher-order harmonics.

For the inner planetary monitoring data shown in Figure 4.17, the peaks occur differently from the outer planetary gear monitoring, which is about the 28th order instead of the 55th order. The frequency spectra for different speeds show that, except for a few peaks related to the input speed, most of the frequency components only have magnitudes increase as the shaft speed increases. The order spectrum for BoB/WoW1/WoW2 all typical peaks at meshing order and harmonics for different speeds. While for WoW2, which has an unground pinion at carrier 1, the second-order peak magnitude is reduced, and the third and fourth peaks are significantly enhanced.

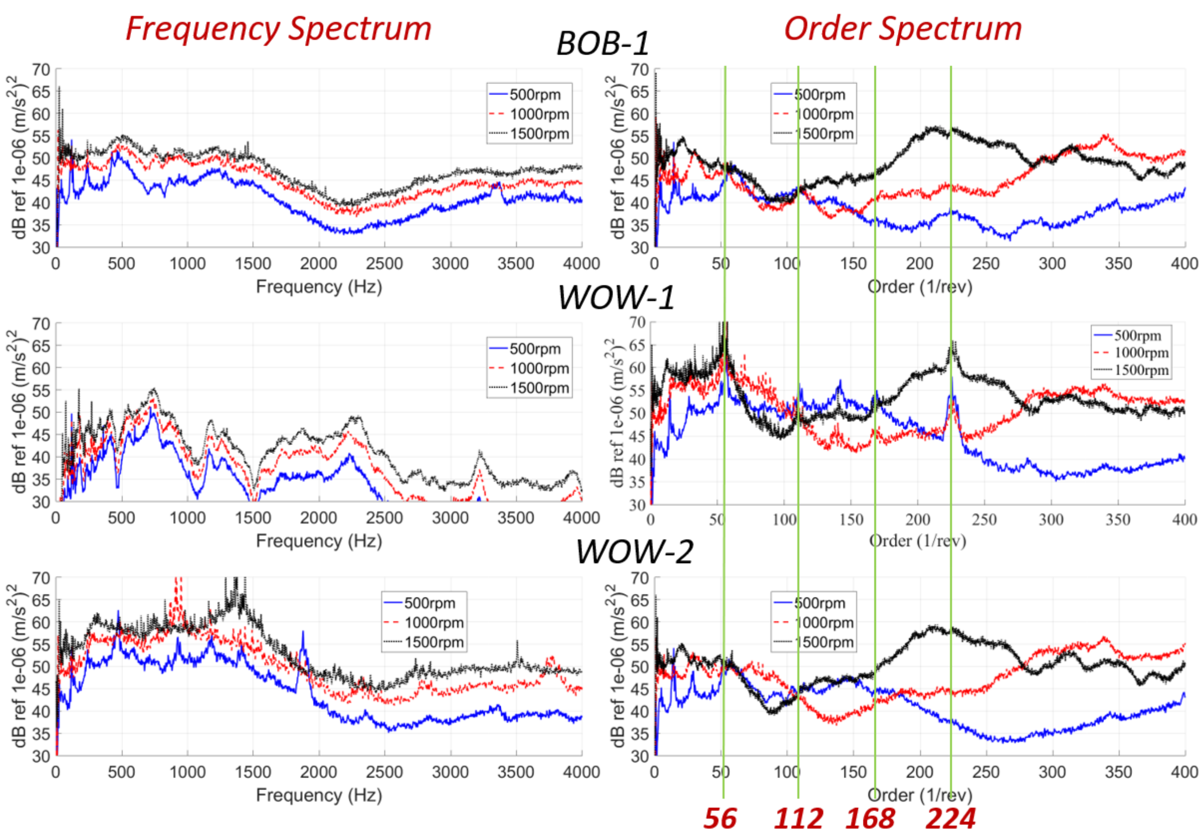

Figure 4.16. Frequency/Order Spectra, dB scale-Clutch D monitoring

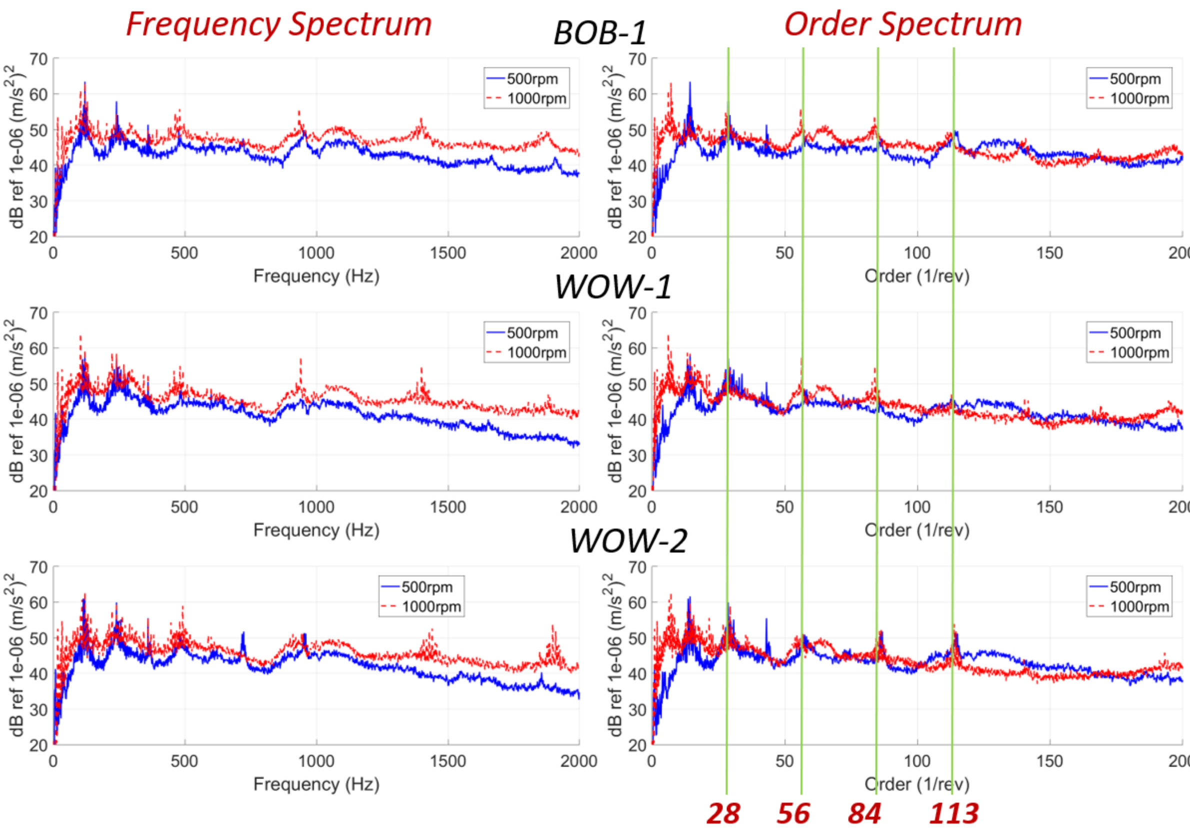

Figure 4.17. Frequency/Order Spectra, dB scale-Clutch C monitoring

After analyzing the frequency/order spectrum of raw data at different speeds, the frequency spectrum at 1000 rpm is chosen for spectral analysis of the synchronously averaged signals. Then, time synchronous averaging is applied to the signals, and the frequency spectra of the averaged signals are compared with the raw data. The frequency spectrum shown in Figure 4.18 and Figure 4.19 is linear rather than dB scale because synchronous averaging can suppress most signals not related to meshing frequency and its harmonics.

For the clutch-D data at 1000rpm (see Figure 4.18), it can be observed that the significant peaks occur at about 930Hz, which corresponds to 56 order of the input shaft speeds. The results confirm that time synchronous averaging can reduce most of the broadband signals caused by the structural vibration and leave the peaks around the meshing frequency and its harmonics. For BoB, the most significant peaks are around meshing frequency, while most of the frequency components below the meshing frequency are eliminated. For WoW1, the meshing frequency peaks have a much higher amplitude than BoB. While for WoW2, the inner carrier unground pinion changes the peak frequency distribution on the outer carrier significantly without a noticeable increase in the peak values.

The frequency spectrum for signals collected from clutch-C at 1000rpm is shown in Figure 4.19. For the spectrum of the measured signal, it can be read from that plot that the low-frequency structural vibration signals have high amplitude. However, most signals can be filtered out by time synchronous averaging. For the spectrum of the averaged signals of both BoB and WoW1, the second harmonic of the meshing frequency has a higher peak than the meshing frequency itself. At the same time, the unground pinion will increase the meshing frequency order and reduce the higher-order harmonics.

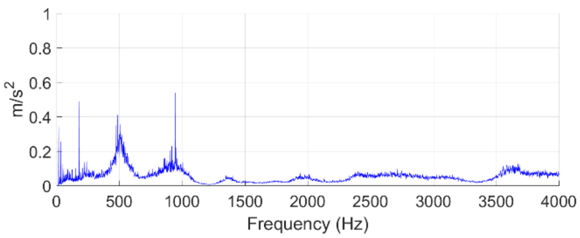

(a) BoB, raw data

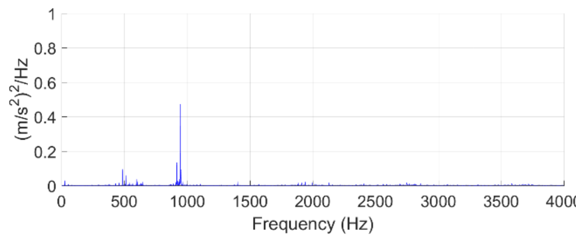

(b) BoB, TSA

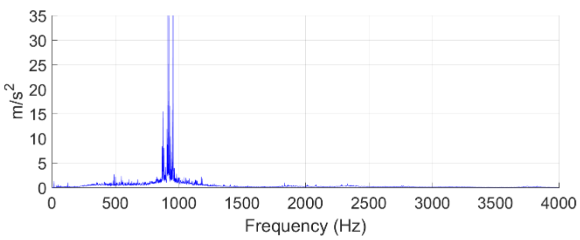

(c) WoW 1, raw data

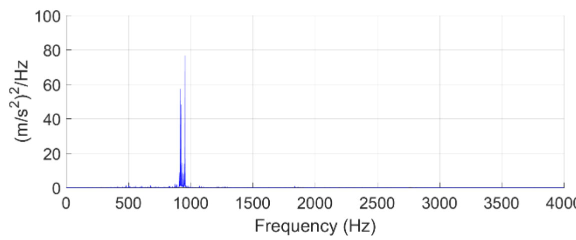

(d) WoW 1, TSA

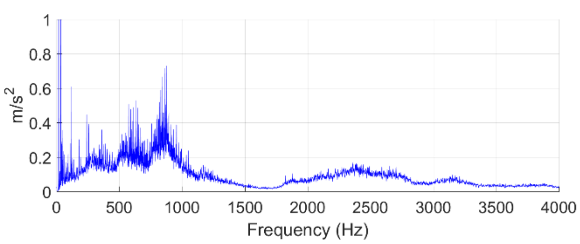

(e) WoW 2, raw data

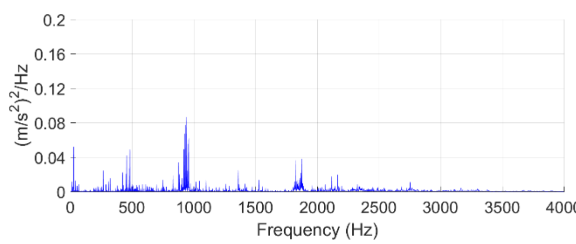

(f) WoW 2, TSA

Figure 4.18. Frequency Spectra-linear scale, Clutch D monitoring, 1000rpm

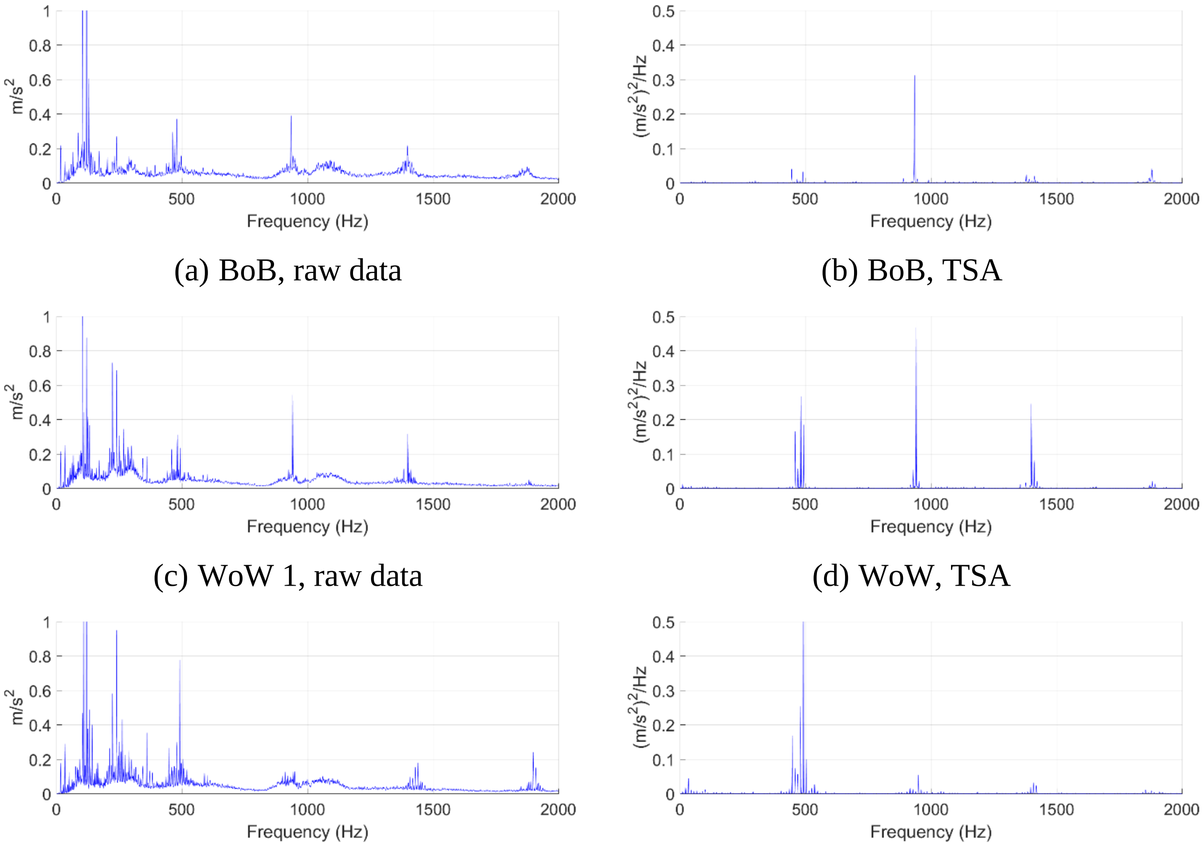

(a) BoB, raw data (b) BoB, TSA

(c) WoW 1, raw data (d) WoW, TSA

(e) WoW 2, raw data (f) WoW, TSA

Figure 4.19. Frequency Spectra-linear scale, clutch-C monitoring, 1000rpm

This section analyzes the frequency and order spectra for three different carriers at different speeds. Although the compound system's inner and outer planetary gearsets are connected, the results demonstrate that the directly measured planetary gear mesh mainly dominates the sensor signals. The unground pinions can cause a significant change in the energy distribution at different harmonics, where this property can be used as an indicator for detecting gear defects. However, the overall frequency spectrum is not accurate enough for concluding the gear conditions during the monitoring process. Therefore, the modulation sideband analysis will be performed on the TSA signals in the following subsection for a more precise analysis of the gear conditions.

4.2.2.2 Modulation Sideband Analysis and Modelling

The unique characteristic of the rotating machinery spectrum is that the low-order sidebands are shown around meshing frequency due to frequency and amplitude modulation, which are called modulation sidebands. In the planetary gear system, unground gear in the carrier can significantly change the modulation sideband. Therefore, this characteristic can be utilized to identify the existence of unground gear in the carrier. In addition to analyzing the sideband structure of the experimental data, theoretical signal modeling is also applied to investigate the mechanism of the sideband change caused by the unground pinion. The majority of the prediction and experimental data match well, which that the relative angle change caused by carrier deformation is the main reason for the sideband behavior variation. For the sideband plot in this section, the red vertical line marks the location of the meshing frequency. Furthermore, the green box locates the primary sidebands in the frequency spectrum.

The 1000rpm input shaft speed signals are analyzed in this study. For clutch-D monitoring, the modulation frequency, which is also the carrier rotating speed, is close to 6.75Hz. It can be seen from the raw data that the meshing signal for BoB and WoW2 are not strong enough to be distinguished. Therefore, the time synchronous averaged data are used for the sideband analysis. For BoB, the major peak occurs at 2 and -2 order. For WoW2, the major peak occurs at -1, +1, +2 order. While for WoW 1, the peaks have significantly larger amplitude, and higher-order sidebands are excited. In addition, for WoW1, the meshing signals are too strong to be masked by the structural vibration signal components.

For the clutch-C signals of BoB, the meshing components are entirely masked by the signal from other sources if the signal is not averaged. After synchronous averaging, the sidebands for BoB are similar to clutch-D signals, which shows symmetric +2 and -2 sidebands. WoW1 exhibits similar sidebands to WoW2 in clutch-D monitoring, which has -1, +1, +2 sidebands. However, WoW2 has -2, +1, +2 sidebands, which is significantly different from WoW1 in clutch-D monitoring. The ungrounded gear does not generate a third-order sideband as WoW1.

From the analysis of modulation sidebands caused by carrier rotation, it can be concluded that the ungrounded pinion changes the broadband spectrum behavior and the behavior of the modulation sidebands significantly. The modulation of several rotating gears simultaneously will reduce the peaks at the meshing frequency and generate strong sidebands. In the following contents, the mechanisms for the modulation sideband alternation will be explained using the physically modeling of the signals.

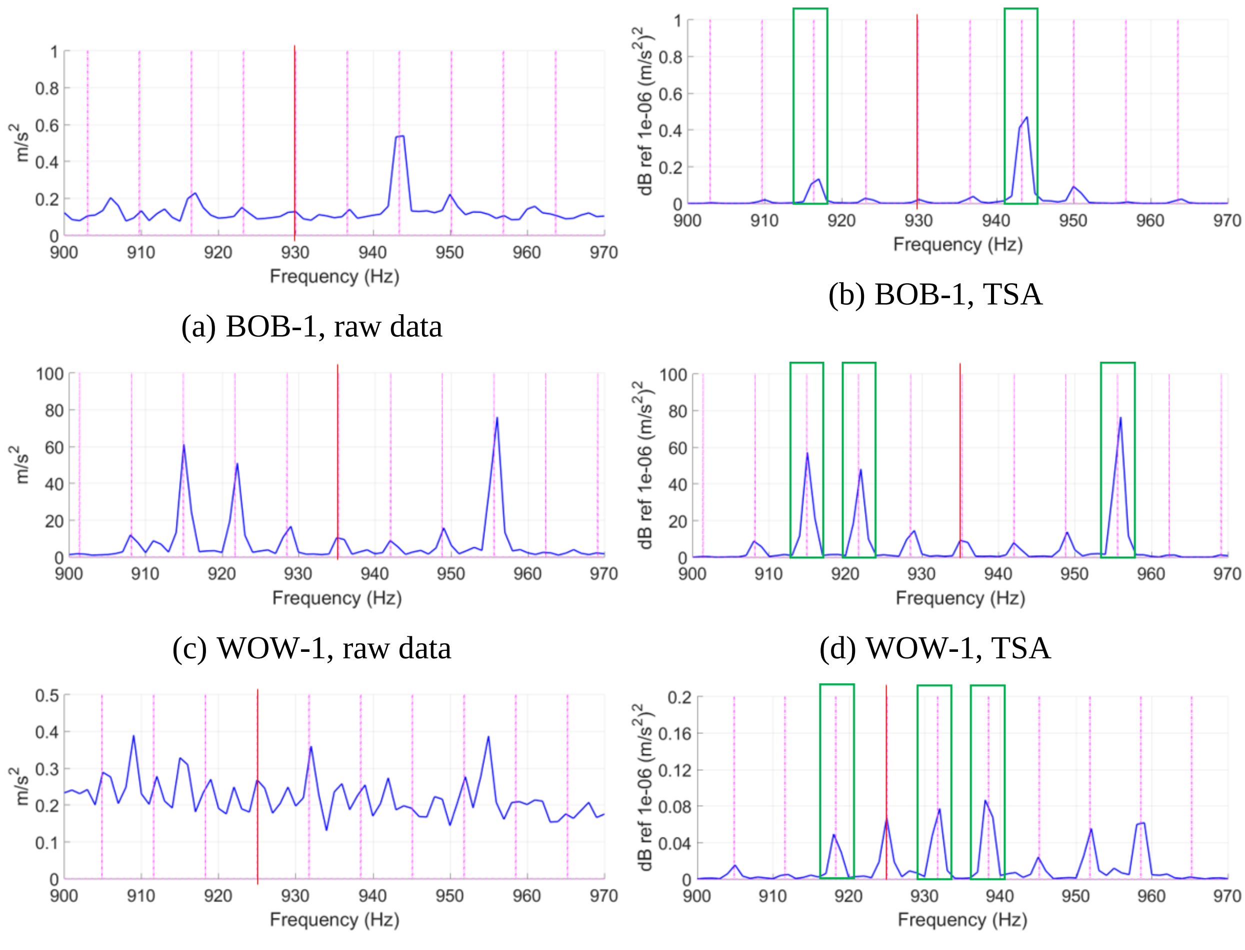

(a) BOB-1, raw data

(b) BOB-1, TSA

(c) WOW-1, raw data

(d) WOW-1, TSA

(e) WOW2, raw data

(f) WOW2, TSA

Figure 4.20. Modulation Sidebands, clutch D monitoring, 1000rpm

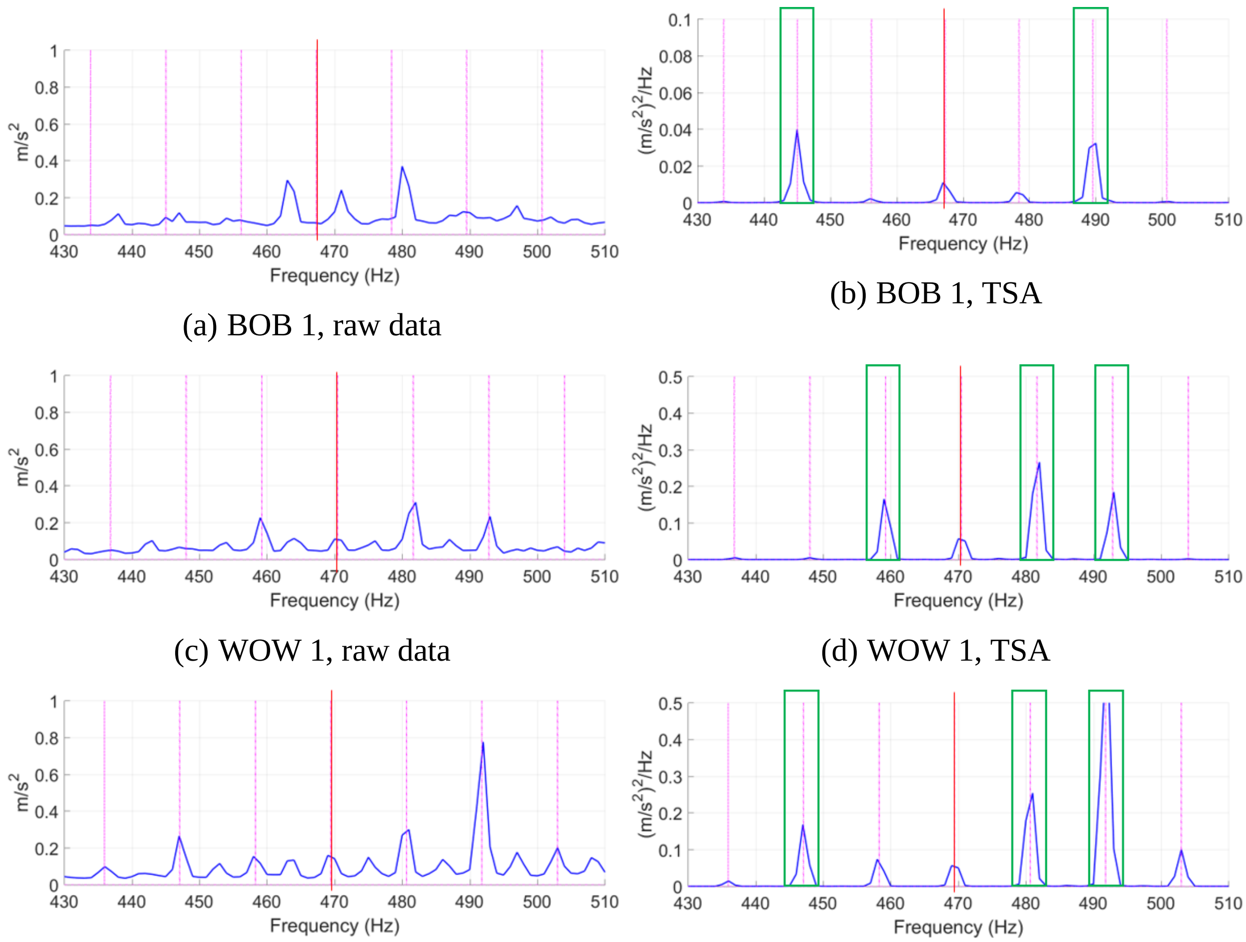

(a) BOB 1, raw data

(b) BOB 1, TSA

(c) WOW 1, raw data

(d) WOW 1, TSA

(e) WOW 2, raw data

(f) WOW 2, TSA

Figure 4.21. Modulation Sidebands, meshing frequency-Clutch C monitoring, 1000rpm

The signal modeling follows the procedures introduced in the last section. However, due to the complicated structure of the nested planetary gear and the effect of the unground pinion, the modeling parameters are modified based on the physical mechanism. The two parameters subject to modification are the pinion local vibration amplitude and phase.

Figure 4.22 shows the shift in pinion angle caused by the unground pinion for the outer planetary gear mesh. All four pinions are 90 degrees apart for BoB because it does not have an unground pinion. There is one unground and three ground pinions within the carrier in WoW 1. Since the size of an unground pinion is larger than that of a standard pinion, it will push the carrier towards the opposite direction. This can cause an angular shift of the two adjacent ground pinions on the side, see Figure 4.22 (b). For WoW 2, the unground pinion in the inner carrier can still cause an angular shift of the outer carrier. The inner carrier pushes the sun gear moving in the directions of the arrow illustrated in Figure 4.22 (c). The change in position of the sun gear leads to a shift in the angle of all four pinions. In addition to the shift in angle, the amplitude of the local vibration will also be affected by the assembling tolerance of the compound gearsets or by the defects in the tooth profile of the pinion.

The change in the relative pinion angle is small compared to the angular position. For modeling WoW 1, 1/5 of teeth angle shift is chosen, and only 1/8 teeth angle shift is used for modeling WoW 2. In summary, the chosen amplitudes and phases for BoB, WoW 1, and WoW 2 are listed in Table 4.4. The prediction results match well for BoB, which has +2 and -2 sidebands. For WoW 2, most of the predicted sidebands match with the measured data except for the -2 sideband. However, the model indicates -2, -1, +1 sidebands for WoW 1, but the experimental data show -3, -2, +2 sidebands instead. The excitation of the third-order sideband indicates a more complicated shift in the angle than those predicted by the current model. This mechanism for the mismatch will be further investigated in later studies.

Table 4.2. Modelling Signal Parameter, outer carrier

	P1	P2	P3	P4
BoB	• Amplitude: 1 • Phase: 0	• Amplitude: 1 • Phase: 0	• Amplitude: 1 • Phase: 0	• Amplitude: 1 • Phase: 0
WoW1	• Amplitude: 1 • Phase: : $\frac{1}{5}\frac{2\pi}{Z_a}$	• Amplitude: 1 • Phase: 0	• Amplitude: 1.5 • Phase: - $\frac{1}{5}\frac{2\pi}{Z_a}$	• Amplitude: 2 • Phase: 0
WoW2	• Amplitude: 2.4 • Phase: $\frac{1}{8}\frac{2\pi}{Z_a}$	• Amplitude: 2.2 • Phase: $\frac{-1}{8}\frac{2\pi}{Z_a}$	• Amplitude: 2 • Phase: $\frac{-1}{8}\frac{2\pi}{Z_a}$	• Amplitude: 1.7 • Phase: $\frac{1}{8}\frac{2\pi}{Z_a}$

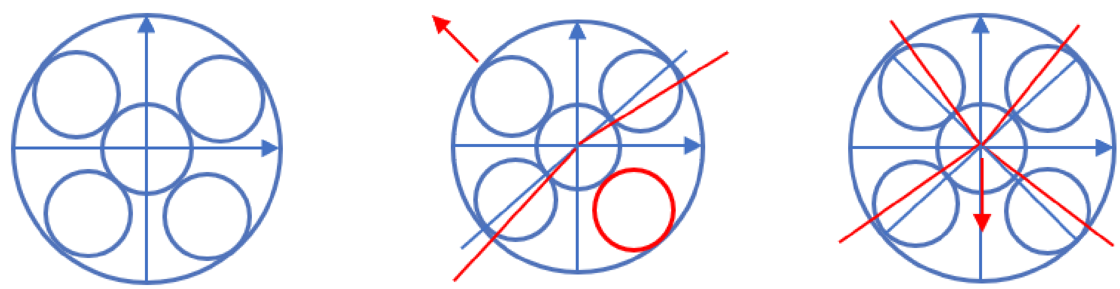

(a) BoB 1 (b) WoW 1 (c) WoW 2

Figure 4.22. Carrier deformation, outer carrier

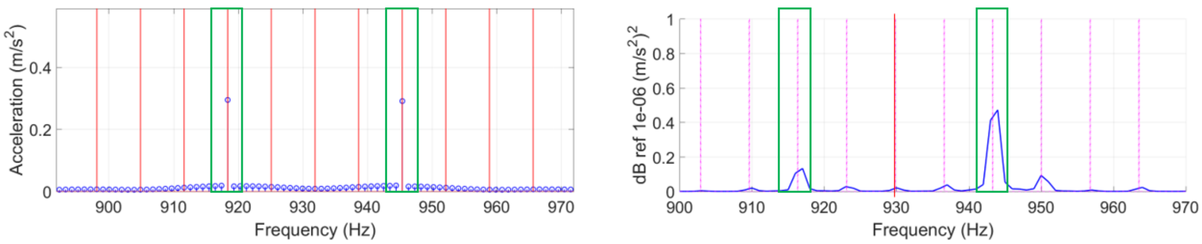

(a) BoB, prediction (b) BoB, TSA

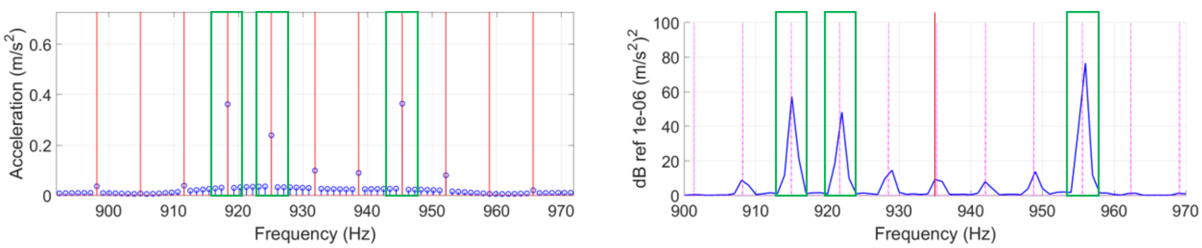

(c) WoW 1, prediction (d) WoW 1, TSA

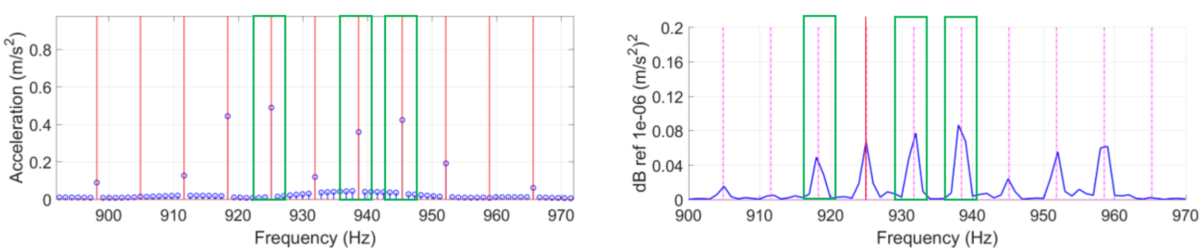

(e) WoW 2, prediction (f) WoW 2, TSA

Figure 4.23. Modulation Sidebands-Clutch D monitoring, 1000rpm

For the inner planetary gear, the theoretical pinion angular shift is illustrated in Figure 4.24. For BoB, the four pinions are 90 degrees apart without any shift in the angle. For WoW 1, the unground gear at the outer carrier pushes the sun gear to move in the arrow direction shown in the schematic diagram, see Figure 4.24 (b). The pinion angular shift for the inner carrier of WoW 2 is similar to the outer carrier of WoW 1. The parameters of the angle shift and amplitude are shown in Table 4.2. Furthermore, the comparison between the prediction and measurement in the signal spectra is shown in Figure 4.25. For the BoB, the results are similar to the outer carrier, which shows -2, +2 sidebands. For the inner carrier of WoW1, the predicted spectrum quite matches quite well with the experimental results, which shows -1, +1, +2 sidebands. The results are similar to the outer carrier of WoW2 because their change in the carrier location has a similar pattern. For the inner carrier of WoW2, although the angular shift pattern is assumed to be the same as the outer carrier of WoW1, the experimental data matches much better with the predicted spectrum, and it shows -2, +1, +2 sidebands.

Table 4.3. Modelling Signal Parameter, inner carrier

	P1	P2	P3	P4
BoB	• Amplitude: 1 • Phase: 0	• Amplitude: 1 • Phase: 0	• Amplitude: 1 • Phase: 0	• Amplitude: 1 • Phase: 0
WoW 1	• Amplitude: 1 • Phase: $\frac{1}{10}\frac{2\pi}{Z_s}$	• Amplitude: 1 • Phase: $-\frac{1}{10}\frac{2\pi}{Z_s}$	• Amplitude: 1 • Phase: $\frac{1}{10}\frac{2\pi}{Z_s}$	• Amplitude: 1 • Phase: $-\frac{1}{10}\frac{2\pi}{Z_s}$
WoW 2	• Amplitude: 2 • Phase: 0	• Amplitude: 1 • Phase: $\frac{-1}{5}\frac{2\pi}{Z_s}$	• Amplitude: 1 • Phase: 0	• Amplitude: 1 • Phase: $\frac{1}{5}\frac{2\pi}{Z_s}$

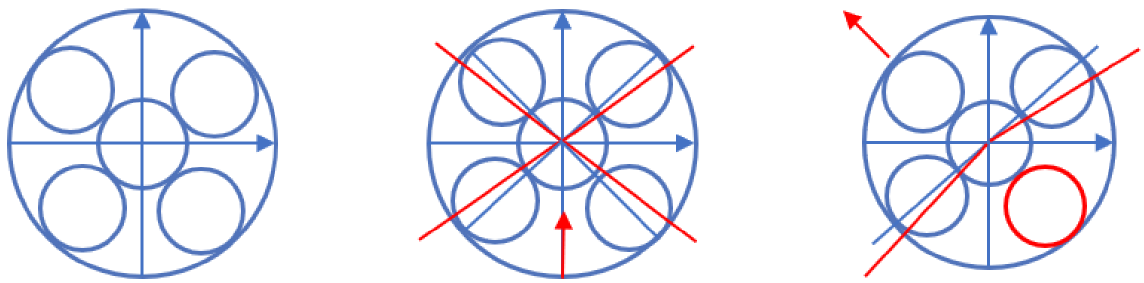

(a) BOB 1 (b) WOW 1 (c) WOW 2

Figure 4.24. Carrier deformation, inner carrier

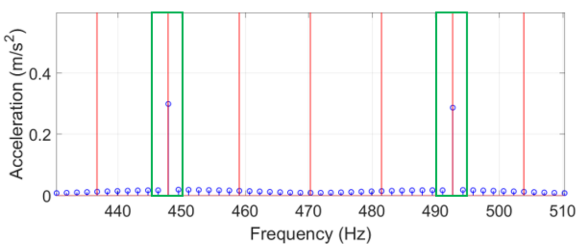

(a) BoB, prediction

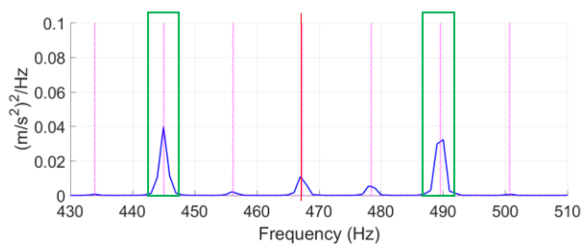

(b) BoB, TSA

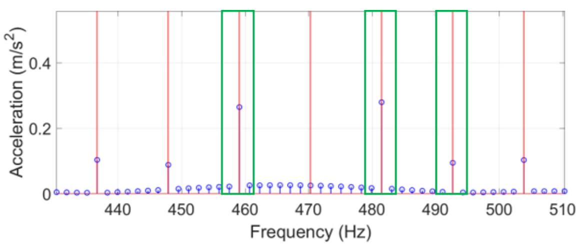

(c) WoW 1, prediction

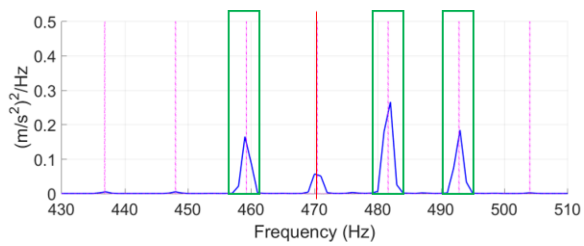

(d) WoW 1, TSA

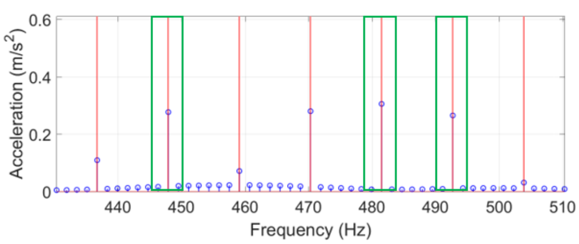

(e) WoW 2, prediction

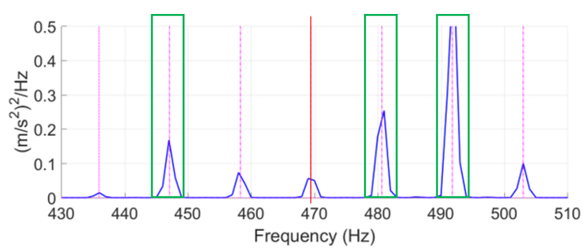

(f) WoW 2, TSA

Figure 4.25. Modulation Sidebands-Clutch C monitoring, 1000rpm

From the analysis of modulation sidebands due to the carrier rotation, it can be concluded that the unground pinion changes not only the behavior of the broadband spectrum but also modifies the behavior of the modulation sidebands significantly. The signal modulation of multiple rotating pinion gears reduces the peaks at the meshing frequency and generates strong sidebands. A physical signal model can explain this change. The model reveals that the modulation sideband behavior is mainly caused by the phase change in the pinion pass-by signals, which results from the change in the relative angle of the pinion. The larger physical size of an unground pinion also changes the fitting between the pinion and the annulus gear, leading to the local vibrational amplitude change. The present physical signal model is extended further by including meshing phase and amplitude changes. This improvement enables the model to explain the main features of the modulation sidebands. Consequently, the modulation sidebands can be used to identify the unground pinions either in the inner or outer meshes. However, it is still not possible to resolve the location of the unground pinion because there are multiple rotating pinions on the same carrier. In the following subsection, the localization of the unground pinion using averaged time history will be elucidated.

4.2.2.3 Unground Gear Localization using Time Synchronous Averaging

The pass-by pinion typically dominates the time signals measured by the accelerometer. There are four pinions on each carrier, so that one revolution of the carrier is divided into four quarters, see Figure 4.26. The time history measured by the accelerometer is divided into four quarters. The time history of the carrier's angular position in real-time is matched according to the laser tachometer data. This is marked as the red vertical line in the time history in Figure 4.27, where the time history plots of accelerometer data for the outer planet gear are also shown. The left column shows the time history for the raw data, and the averaged time history is displayed in the right column. It can be seen from the plots that the time histories of the sensor signals are highly 'noisy' that do not yield much useful information. However, the time history for WoW1 shows significantly higher signals at the 4th quarter after the synchronous averaging. The results match well with the location of the unground pinion. For BoB, the signals for the four quarters do not have distinguishable differences. For WoW2, since the unground pinion is in the inner carrier, the signal measured by the accelerometer mounted on the outer rim is similar to BoB with marginal differences. As explained in subsection 4.2, one of the main reasons for the difference between BoB and WoW2 is the change in the carrier location caused by a tighter fitting of the unground gear. The averaged signal strength within a quarter revolution is quantified and shown in 0. Notably, the 4th quarter region has much stronger signals than the rest of the three quarters. This feature provides the required information for the localization of the unground pinion. For BoB and

WoW2, the four sets of data in four quarters also show a certain amount of variations. These variations are partly due to the misalignment of the input shaft caused by the connection issues between the input shaft and the motor coupling.

For monitoring the inner mesh, the division in the carrier revolution is different from that of the outer planetary gear, see Figure 4.28. Figure 4.29 shows the signals collected from the accelerometer mounted on clutch-C. The averaged time histories of BoB and WoW 1 show a comparable averaged signal strength for each quarter because of the lack of unground pinion within the monitored carrier. For WoW 2, there are two quarters with significantly higher amplitudes. The measured results are displayed in Table 4.5, which shows that both the first and second quarters have high signals for WoW 2 while the 2nd quarter is the dominating one. The unground pinion is located physically in the 1st quarter. The unground gear location predictions based on the measured results are close to the actual location, but they are less accurate compared to the monitoring results of clutch-D. This error is likely to be related to the compact structure of the inner mesh.

The TSA results suggest that the time history of the synchronously averaged signals has a significant modulation when the unground pinion passes by the sensor. Therefore, the time history behavior can be used as an indicator for localizing the unground gear. Using the results of different processing techniques, the presence of the unground pinion can be determined, and the location of the unground pinion can also be identified.

Table 4.4. Time History Averaged Strength within Quarter of Rotation, Clutch D

Carrier Name	BoB	WoW1	WoW2
Averaged Strength	• Q1: 2.51 • Q2: 1.92 • Q3: 2.16 • Q4: 2.18	• Q1: 18.28 • Q2: 12.95 • Q3: 11.94 • Q4: 28.42	• Q1: 2.42 • Q2: 2.22 • Q3: 1.98 • Q4: 1.67

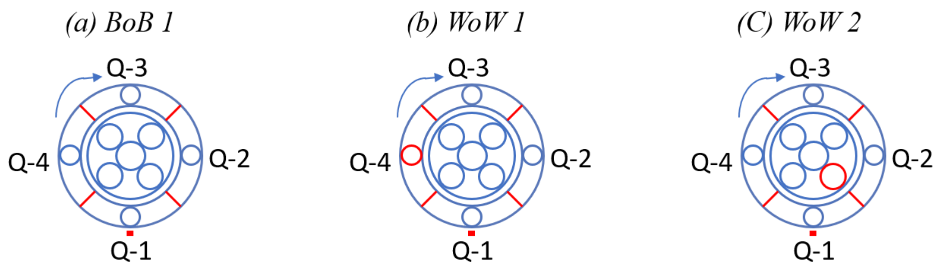

Figure 4.26. Pinions Area Division for Carriers-Outer Gearset

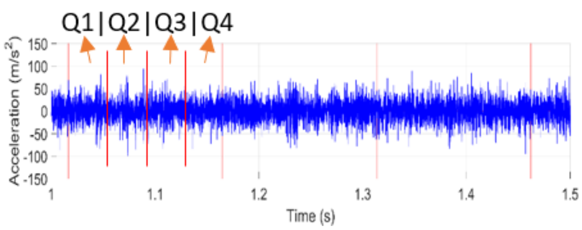

(a) BOB-1, raw

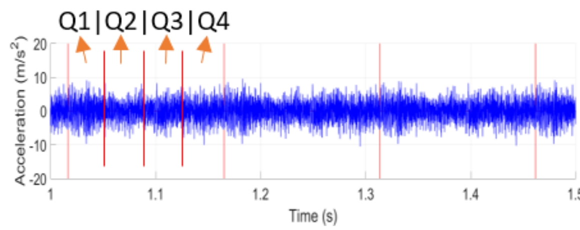

(b) BOB-1, TSA

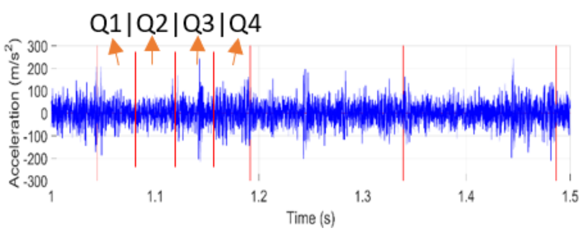

(c) WOW-1, raw

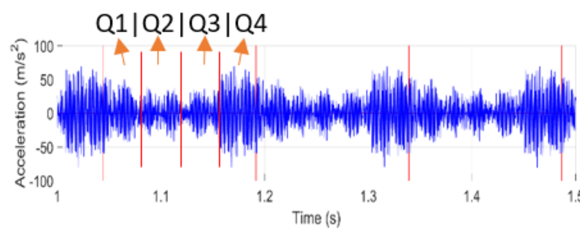

(d) WOW-1, TSA

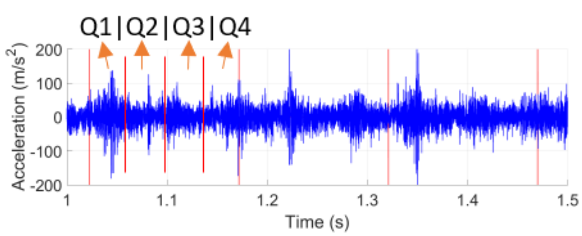

(e) WOW-2, raw

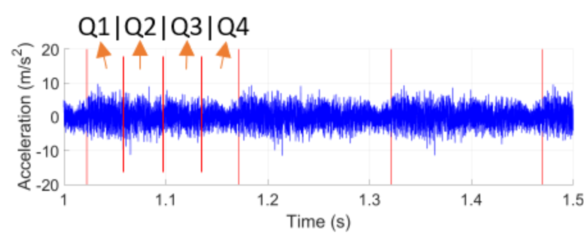

(f) WOW-2, TSA

Figure 4.27. TSA Results, time history-Clutch D monitoring

Table 4.5. Time History Averaged Strength within Quarter Rotation, Clutch C

Carrier Name	BOB-1	WOW-1	WOW-2
Averaged Strength	• Q1: 1.79 • Q2: 1.76 • Q3: 1.64 • Q4: 1.65	• Q1: 1.61 • Q2: 2.19 • Q3: 2.06 • Q4: 2.18	• Q1: 2 • Q2: 2.52 • Q3: 1.58 • Q4: 1.29

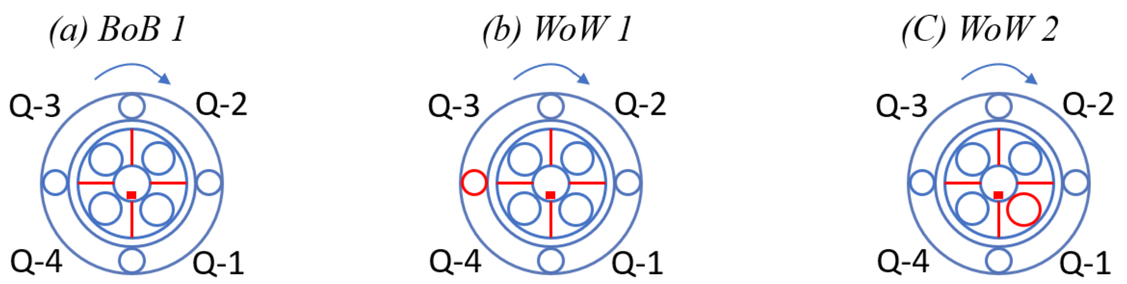

Figure 4.28. Pinions Area Division for Carriers-Inner Gearset

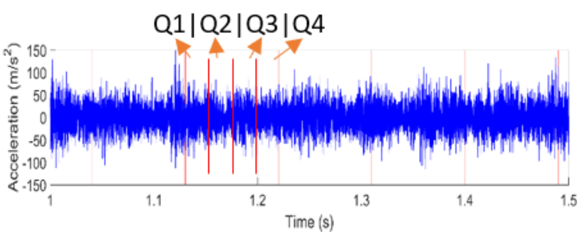

(a) BOB 1, raw

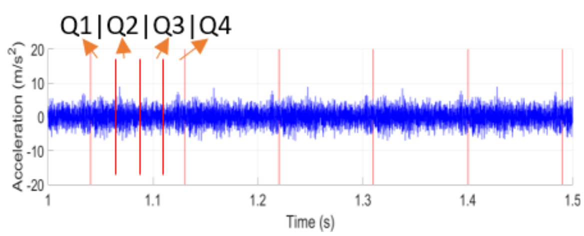

(b) BOB1, TSA

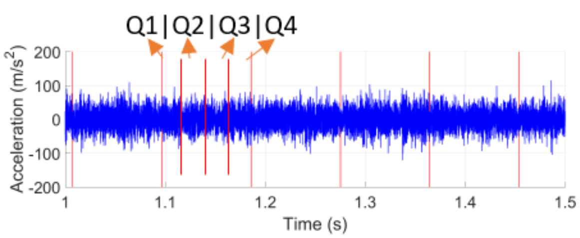

(c) WOW1, raw

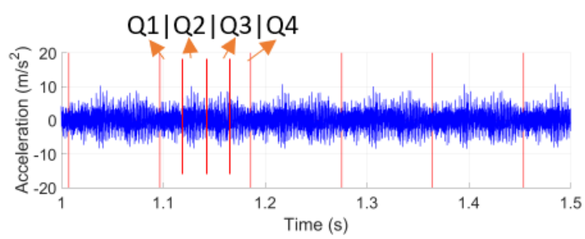

(d) WOW1, TSA

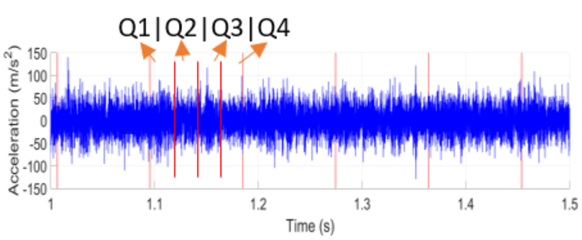

(e) WOW2, raw

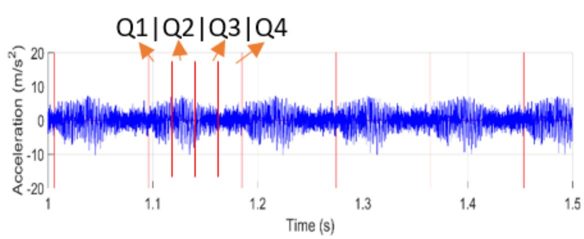

(f) WOW2, TSA

Figure 4.29. TSA Results, time history-Clutch C monitoring

4.3 Gear Diagnosis System-3, Pinion Local Faults Diagnosis

The last two sections established the system for analyzing the pinion grinding faults in a nested planetary gear train. Another type of pinion fault is investigated in this section, which is the pinion denting fault. Compared to the grinding faults, the faults investigated in this section only occur on single teeth and are not evenly distributed on the pinion. Therefore, another signal processing technique is used here for the analysis: the time synchronous averaging by windowing only one pinion pass-by signal. The section will start with introducing the extended TSA method. Then, the experimental data will be processed to diagnose the pinion gear denting faults.

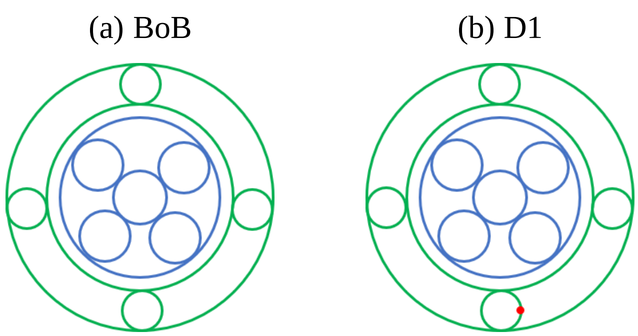

Figure 4.30. Carries for experiment.

4.3.1 Methodology-Time Synchronous Averaging for Single Planet Gear

The last section presents the application of time synchronous averaging for the meshing signals measured on the planetary gear train. Except for the traditional TSA algorithm, the time synchronous averaging for diagnosis of pinions in planetary gear train was proposed by McFadden (1991, 1994). This algorithm is designed to window the signals for single planet gear only, thus the meshing vibrational signal of a single planetary. The key for the windowing is to align the rotating planet window with the carrier rotation. The mathematical procedures for windowing and averaging can be found in McFadden's paper. In the current study, the procedures will be explained in a physically straightforward way without going into the details of the mathematical models, as shown in Figure 4.31. Because the pinion has both self-rotation and rotates with the carrier, the annulus gear teeth are not integer multiples of the pinion teeth number. So that each time the pinion pass by the accelerometer, the window starting and finishing time needs to be adjusted to the window the same pinion teeth contact. This can be achieved by calculating the remainder of the division between the carrier rotating period T_c and the pinion rotating period T_r,

$$T_{re,n} = \text{remainder}\left(\frac{nT_c}{T_r}\right), \qquad 4.\ 18$$

where n represent n^{th} revolution, $T_{re,n}$ is the remainder time for n^{th} revolution. The time for the pulse generated by tachometer can be adjusted using $T_{re,n}$, and the windows will be synchronized for the single pinion. The new adjusted time for the center of the window for nth revolution $T_{w,n}$ is

$$T_{w,n} = nT_c - T_{re,n}\,. \qquad 4.\ 19$$

After obtaining the multiple windowed signals for same pinion gear, the signals from different windows can be added and averaged. The averaging can reduce the signals not related to the planet gear meshing.

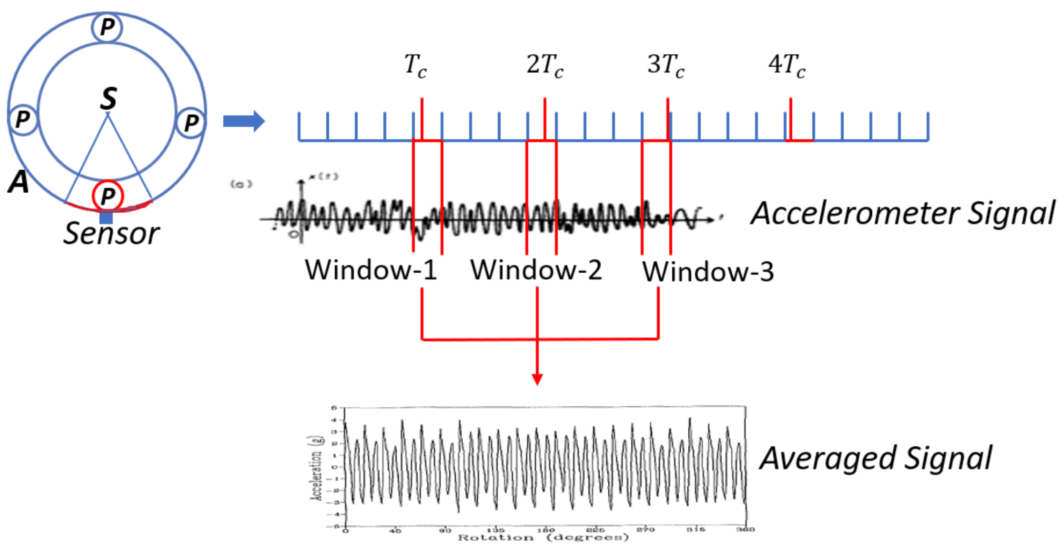

Figure 4.31. TSA for Single Planet Gear Procedure Demonstration

4.3.2 Results and Discussion-Pinion Distributed Defects Analysis

The results for BoB and D1 are shown in Figure 4.32 and Figure 4.34. In those plots, the purple vertical lines mark the time of tachometer impulse, which means one revolution completed for the carrier at nT_c. The red vertical lines are the adjusted time for single pinion windowing $T_{w,n}$.. For BoB, the signal time history does not show a significant peak. However, for D1, the time history shows significant peaks due to impact, for which the time between the peaks is the time to complete half revolution for the pinion. The dented teeth will impact both the ring and sun gear in one revolution and generate two peaks. Therefore, with the signal-averaged, it can be observed that the

D1 time history within one revolution shows two peak regions within one revolution, and the area of the peaks can be matched with the gear rotation location to find the location of the dented teeth. In the current experiment, the teeth dent is larger than average gear teeth damage, so this type of fault generates enormous impact. It can be identified by visual inspection of time history. Sometimes the gear faults might not be evident and other signal processing techniques, such as kurtosis analysis, need to be implemented to find the location of the teeth defect.

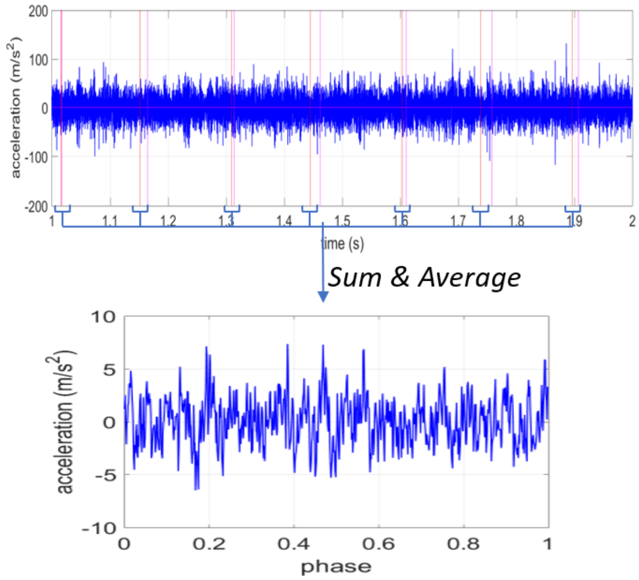

Figure 4.32. Time Synchronous Averaging Results, BoB

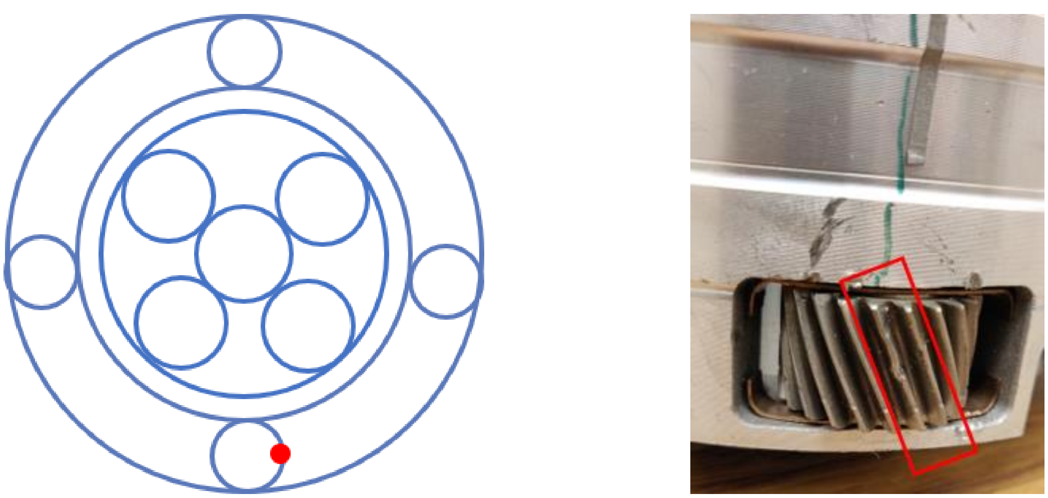

Figure 4.33. D1 damage

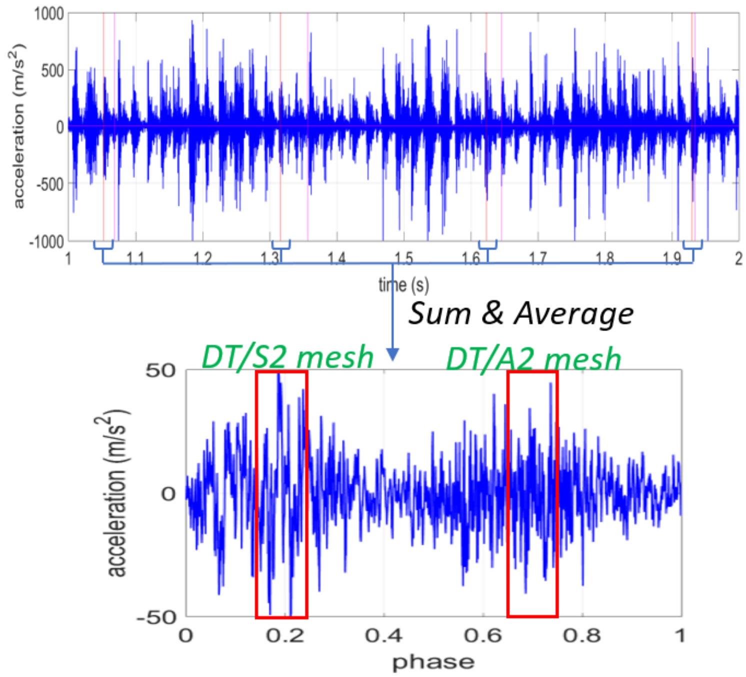

Figure 4.34. Time Synchronous Averaging Results, D1

5. ALGORITHM DEVELOPMENT FOR HIGH-RESOLUTION ROTATING SOURCES IMAGING

The last chapter presents the monitoring of the nested planetary gear with pinion defects using vibrational signals. However, for monitoring the product line, non-contact measurement is required under some conditions. And acoustical array imaging is the technique that best fits the requirement. However, as mentioned in the literature review chapter, there is little information in the literature about near-field localization and visualization of the sound field from rotating sources using acoustical holography. On the other hand, several holography approaches have been well-developed for near-field sound field visualization of stationary sources. However, the existing holography approaches mainly work with static sources or sources in linear motion. Therefore, in this study, the standard compressive sensing equivalent source method holography procedures are proposed to be combined with the virtual rotating array (VRA) methods to reconstruct the rotating source sound field.

Previous studies have proposed a virtual rotating array method to deal with the rotating source sound field to eliminate the Doppler effect caused by the relative motion between the source and microphone. Both time domain and frequency domain virtual rotating array algorithms are studied and further developed in this study. The zeroth-order interpolation is proposed for the time domain interpolation, which works with enhanced efficiency than other time-domain interpolations in the literature. In addition, three other published time-domain interpolation methods are also introduced in this chapter. For the frequency domain algorithm, the well-known modal decomposition method is presented. However, the modal decomposition is restricted to a circular array with equally spaced microphones. In order to overcome those disadvantages of the frequency domain modal VRA method, the formula is simplified, and it can be shown that the simplified formula works well under certain conditions.

Theoretically, there is no relative movement between the rotating source and a corotating measurement frame. However, Green's function for a rotating source and receiver are not the same as stationary source and receiver. Therefore, the motion between source and air medium has to be compensated in Green's function to use the VRA signals as input for holography reconstruction. A standard holographic reconstruction procedure can be performed after obtaining the VRA signals and correcting Green's function. The holography procedures used in this study are chosen to be the equivalent source method based compressive sensing holography due to its high efficiency and capability to work with the irregular array. The following compressive sensing equivalent source based holography (CESM) methods will be introduced in this chapter: (1) wideband holography (WBH); (2) convex optimization of L1 norm penalty formulation (CVX); (3) hybrid method between wideband holography and convex optimization.

5.1 Sound Field Expression for Rotating Source

In this section, the spherical harmonic sound field expression of the rotating sound source in the frequency domain at the stationary receiver is derived first. In the second part of this section, the derivation of the sound field of a rotating receiver exposed to a rotating source is presented. Two derivations will be presented for the sound field of a rotating receiver. This section's derivations of the rotating source sound field lay the foundation for the frequency domain virtual rotating array signal synthesis using the measurement at stationary arrays.

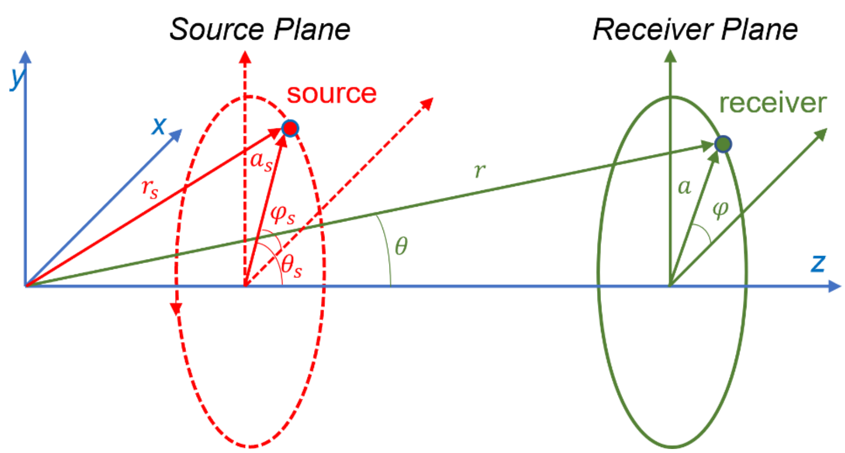

Figure 5.1. Schematic Illustration of Rotating Source and Receiver

5.1.1 Spherical Harmonic Expansion for Rotating Sound Fields

The inhomogeneous wave equation for acoustic pressure, p, due to a moving source $q(\vec{x},t)$ in a medium at rest is given by,

$$\frac{1}{c^2}\frac{\partial^2 p}{\partial t^2} - \Delta p = q(\vec{x},t)\ , \qquad 5.\ 1$$

where c is sound speed in the medium and the source term can be written in a form of the Delta-distribution as follows:

$$q(\vec{x},t) = Q(t)\delta(\vec{x} - \vec{x}_s(t)) \ , \qquad 5.\ 2$$

where $\vec{x}_s(t)$ is the source position at time t, the subscript s denotes the corresponding parameter for the source and time constant factor, $e^{i\omega t}$, is used throughout the analysis. The time varying source term, $Q(t)$, in the time domain is related to $\tilde{Q}(\omega)$ in the frequency domain as,

$$\tilde{Q}(\omega) = \int_{-\infty}^{\infty} Q(t)e^{-i\omega t}\, dt \ . \qquad 5.\ 3$$

The time domain acoustic pressure, $p(\vec{x},\vec{x}_s,t)$, for a receiver due to the moving source can be calculated using the integral form as follows,

$$p(\vec{x},\vec{x}_s,t) = \int_{-\infty}^{\infty} \frac{Q(\tau)}{4\pi R(\tau)} \delta(t - \tau - \frac{R(t,\tau)}{c}) d\tau \ , \qquad 5.\ 4$$

where $R(t,\tau)$ is the source/receiver distance calculated at the retarded time:

$$R(t,\tau) = |\vec{x}(t) - \vec{x}_s(\tau)| = c(t - \tau) \ , \qquad 5.\ 5$$

Here, t and τ are also referred as the emission and reception time, respectively. The frequency domain acoustic pressure, $\hat{p}(\vec{x},\vec{x}_s,\omega)$, is given by,

$$\hat{p}(\vec{x},\vec{x}_s,\omega) = \int_{-\infty}^{\infty}\int_{-\infty}^{\infty} \frac{Q(\tau)}{4\pi R(\tau)} \delta(t - \tau - \frac{R(t,\tau)}{c}) d\tau e^{-i\omega t} dt \ , \qquad 5.\ 6$$

In the current study, a rotating sound field is considered, see Figure 5.1 for the geometric configuration of the problem where a spherical polar coordinate is used in the analysis. Suppose a monopole source rotates about the z-axis with a constant angular speed of Ω_s. Choosing the positive z direction as polar axis of the spherical polar coordinate system, the location of the rotating source can be specified as $(r_s, \theta_s, \varphi_s(\tau))$ in the emission time frame, and the location of receiver can be specified as $(r, \theta, \varphi(t))$ in the reception time frame. For the source rotating in the counterclockwise direction, the source's azimuthal angle is determined by $\varphi_s(\tau) \ = \varphi_{s_0} + \Omega_s\tau$, where $\varphi_{s_0} = \varphi_s(0)$, is the source's initial azimuthal angle at the emission time frame.

A receiver is placed at the $z = z_r$ plane where its azimuthal angle is given by $\varphi(t) \ = \varphi_0 + \Omega t$, where Ω is the angular speed of the rotating receiver and $\varphi_0 = \varphi(0)$ which is its initial azimuthal position at the emission time. Note here that the azimuthal angles for the source and receiver are defined in terms of τ and t, respectively. These two time variables are related according to Eq. 5. 5 where $R(t,\tau)$ is determined from the geometrical consideration of the relative positions of the source and receiver:

$$R(t,\tau) = |\vec{x}(t) - \vec{x}_s(\tau)| = \sqrt{r_s^2 + r^2 - 2r_s r\cos\beta} \ , \qquad 5.\ 7$$

and β is the angle between the position vectors of $\vec{x}(t)$ and $\vec{x}_s(\tau)$ such that

$$cos\beta = \cos(\theta)\cos(\theta_s) + \sin(\theta)\sin(\theta_s)\cos(\Omega_s\tau - \Omega t + \Delta\varphi), \qquad 5.\,8$$

where $\Delta\varphi = \varphi_{s_0} - \varphi_0$ is the relative azimuthal angles. Two steps are needed if the receiver and source have finite rotational speeds, i.e. nether Ω or Ω_s vanish.

The first step involves use of the following identity:

$$\int_{-\infty}^{\infty} \frac{\delta(t-\tau-\frac{R(t,\tau)}{c})}{4\pi R(\tau)} e^{i\omega(\tau-t)} dt = \frac{e^{-ikR(t)}}{4\pi R(t)} \,. \qquad 5.\,9$$

It is then followed by using the spherical wave expansion for the $\frac{e^{-ikR}}{4\pi R}$ and integrating each summand of the series with respect to τ to arrive at an expression for the frequency domain acoustics pressure:

$$\hat{p}\big(\varphi(t), \varphi_{s_0}, \omega\big) = \sum_{m=-\infty}^{\infty}\sum_{n=|m|}^{\infty} \tilde{G}(k,m,n)\tilde{Q}(\omega - m\Omega_s)e^{im(\Delta\varphi-\Omega t)} \,. \qquad 5.\,10$$

where $k = \omega/c$ is the wavenumber. The reduced Green's function $\tilde{G}$ can be written in a general functional form as,

$$\tilde{G}(k,m,n) = -ikj_n(|k|r_<)h_n(|k|r_>)B^2(m,n)P_n^m(cos\theta)P_m^m(cos\theta_s) \,. \qquad 5.\,11$$

where m and n are integers, and $B(m,n)$ is a normalization factor:

$$B(m,n) = \sqrt{\frac{(2n+1)(n-m)!}{4\pi(n+m)!}}\,, \qquad 5.\,12$$

j_n and h_n are the n^{th} order spherical Bessel functions of the first and second kinds, respectively, with $h_n = h_n^2$ if $k > 0$, and, $h_n = h_n^1$ if $k < 0$. The symbols $r_>$ and $r_<$ represent, respectively, the greater or smaller of the radii r and r_s. The m^{th} order and n^{th} degree Legendre polynomial of the first kind is denoted by P_n^m.

In the second step, the time domain pressure is obtained by evaluating the inverse Fourier integral of Eq. 5. 10 to yield,

$$\hat{p}\big(\varphi(t), \varphi_{s_0}, t\big) = \sum_{m=-\infty}^{\infty}\sum_{n=|m|}^{\infty} e^{im\Delta\varphi} \int_{-\infty}^{\infty} \tilde{G}(\frac{\omega'}{c}, m, n)\tilde{Q}(\omega' - m\Omega_s)e^{i(\omega'-m\Omega t)}d\omega' \,. \qquad 5.\,13$$

The frequency domain acoustic pressure for a rotating receiver can be obtained by taking the forward Fourier transform for Eq. 5. 13 to give,

$$\hat{p}\big(\varphi_0, \varphi_{s_0}, \omega\big) = \sum_{m=-\infty}^{\infty}\sum_{n=|m|}^{\infty} e^{im\Delta\varphi} \tilde{G}(k_m, m, n)\tilde{Q}(\omega' - m\Delta\Omega) \,. \qquad 5.\,14$$

where $k_m = k + \frac{m\Omega}{c}$ is the modal wavenumber, $\omega_m = \omega - m\Delta\Omega$ is the frequency of the radiated sound due to the source rotation relative the receiver, and, $\Delta\Omega = \Omega_s - \Omega$ is the relative angular velocities between source and receiver.

In the special case of the stationary receiver, i.e. $\Omega = 0$, Eq. 5. 14 can be reduced to,

$$\hat{p}\left(\varphi_0, \varphi_{s_0}, \omega\right)|_{\Omega=0} = \sum_{m=-\infty}^{\infty} \sum_{n=|m|}^{\infty} e^{im\Delta\varphi}\, \tilde{G}(k, m, n)\tilde{Q}(\omega - m\Omega_s)\ . \qquad 5.\ 15$$

which is a comparable form as those giving in reference (Pannert et al., 2014). Equation 5. 15 , where frequency domain acoustic pressure for a stationary receiver, suggests that $\hat{p}(\vec{x}, \omega)|_{\Omega=0}$ is composed of a sum of modal contribution for each m radiating sound at a frequency of $\omega_m = \omega - m\Omega_s$. It is difficult, if not impossible to de-dopplerize the acoustic pressures in the resulting solutions for a stationary receiver. To remove the Doppler effect on the frequency of the perceived sound field, a rotating frame can be used where Ω is set as the same speed of the source. The frequency domain acoustic pressure, $\hat{p}(\vec{x}, \omega)|_{\Omega=\Omega_s}$, for a co-rotating receiver can be derived by substituting $\Omega = \Omega_s$ in Eq. 5. 14 to offer a closed form expression as,

$$\hat{p}\left(\varphi_0, \varphi_{s_0}, \omega\right)|_{\Omega=\Omega_s} = \sum_{m=-\infty}^{\infty} \sum_{n=|m|}^{\infty} e^{im\Delta\varphi}\, \tilde{G}(k_m, m, n)\tilde{Q}(\omega)\ . \qquad 5.\ 16$$

The above equation is analogous to those in Pannert's and Ma's paper (Pannert et al., 2014; Ma et al., 2020) for the sound field due to a rotating source. Indeed, Eq. 5. 14 generalizes earlier studies to allow a convenient formular for calculating the frequency domain acoustic fields where the rotational speeds of the sources, Ω_s and the receiver, Ω are not identical. The stationary and corotating sound fields, $F_0(\vec{x}, \vec{x}_s, \omega)$ and $F_\Omega(\vec{x}, \vec{x}_s, \omega)$, are respectively given as:

$$F_0(\vec{x}, \vec{x}_s, \omega) \equiv \hat{p}\left(\varphi_0, \varphi_{s_0}, \omega\right)|_{\Omega=\Omega_s} \approx \sum_{m=m^-}^{m^+} \sum_{n=|m|}^{n_u} e^{im\Delta\varphi}\, \tilde{G}(k, m, n)\tilde{Q}(\omega - m\Omega_s)\ , \qquad 5.\ 17$$

$$F_\Omega(\vec{x}, \vec{x}_s, \omega) \equiv \hat{p}\left(\varphi_0, \varphi_{s_0}, \omega\right)|_{\Omega=\Omega_s} \approx \sum_{m=m^-}^{m^+} \sum_{n=|m|}^{n_u} e^{im\Delta\varphi}\, \tilde{G}(k_m, m, n)\tilde{Q}(\omega)\ . \qquad 5.\ 18$$

For numerical implementations, the series for m is truncated with the sum from m^- to m^+ and the upper limit for n is truncated to n_u. These limits are dependent on the rotating radius of the source, a_s and they are determined by (Pellotti, 2011),

$$m^- = \frac{-a_s k}{1 + a_s\Omega_s/c}\ . \qquad 5.\ 19$$

$$m^+ = \frac{a_s k}{1 - a_s\Omega_s/c}\ . \qquad 5.\ 20$$

$$n_u = \max\left(\left\lceil a_s \left|k + \frac{m\Omega_s}{c}\right|\right\rceil, \}, |m|\right), \tag{5. 21}$$

where $a_s = r_s sin\theta_s$ and $\lceil\cdot\rceil$ is the ceiling function.

Equations 5. 17 and 5. 18 reveal that the signal contents in a VRA receiver depends only on the source's frequency content. In other words, the signal is de-dopplerized so that there are no contributions from the rotation sidebands of the source at $\omega \pm m\Omega_s$. On the other hand, the spectral contents in an array of stationary receivers are 'contaminated' by the Doppler effect caused the source motion. This serves to explain the reason for using VRA receiver signals in the source reconstruction for most of the beamforming algorithms (Pannert et al. 2014; Ma et al, 2020). These algorithms have a common limitation that the circular array of equally-spaced microphones is needed.

5.1.2 Numerical Integration Expression for Rotating Source and Rotating Receiver

In the last section, the generalized series expansion formulation of the rotating source sound field is derived for a receiver with arbitrary rotating speed. And the spherical harmonic expression of Green's function for rotating source and corotating receiver can be expressed as,

$$\tilde{G}_{\Omega_1} = -i \sum_{m=-\infty}^{\infty} \sum_{n=|m|}^{\infty} e^{im\Delta\varphi}\, k j_n(|k| r_<) h_n(|k| r_>) B^2(m,n) P_n^m(cos\theta) P_m^m(cos\theta_s)\ . \tag{5. 22}$$

Except for the analytical spherical harmonic expression of the rotating receiver exposed to rotating sources, the solution can also be calculated by evaluating the retarded time integral directly without using series expansion when receiver and source rotate at the same speed.

The numerically solved expression of the Green's function for rotating source and rotating receiver have been presented in Ma's 2020 paper. However, it fails to give the detailed derivation of this expression. This section will derive the sound field of a rotating source at a corotating receiver at the same speed in detail. In addition, the numerically simulated results will be compared to the results in the literature (Ma et al., 2020), and it will be shown that Eq. 5. 22 and the development in this section are equivalent. The derivation in this section also starts with the Fourier transform to the time domain sound field expression, and the distance between source and receiver is related to both emission time and receiver time t due to the rotation of the receivers, and the azimuth angle is a function of time $\varphi(t) = \varphi_0 + \Omega t$ for this case, and $\Omega = \Omega_s$.

$$p(\vec{x},\vec{x}_s,\omega) = \int_{-\infty}^{\infty}\int_{-\infty}^{\infty}\frac{Q(\tau)}{4\pi R(t,\tau)}\delta(t-\tau-\frac{R(t,\tau)}{c})d\tau e^{i\omega t}dt\ , \tag{5. 23}$$

where $R(t,\tau)$ has the same expression in Eq. 5. 7. In this case, the equation $R(t,\tau) = c(t-\tau)$ needs to be solved numerically and the results will be a constant, $t-\tau = a$. Integrating Eq. 5. 23 with respect to τ, utilizing the property of Delta function, the integration can be expressed in the following form,

$$p(\vec{x},\vec{x}_s,\omega) = \int_{-\infty}^{\infty}\frac{e^{ikR(\tau')}}{4\pi R(\tau')}\frac{Q(t-\tau')}{1-\frac{a_s a\Omega\sin(\varphi_0-\varphi_{s_0}+\Omega\tau')}{R(\tau')}}e^{i\omega(t-\tau')}dt\ . \tag{5. 24}$$

where τ' is a constant and it can be solved by calculating $R(t,\tau) = c(t-\tau)$ numerically, where $t-\tau$ is an constant. For the next step, evaluate Eq. 5. 24 with respect to t, it leads to,

$$p(\vec{x},\vec{x}_s,\omega) = \frac{e^{ikR(\tau')}}{4\pi R(\tau')}\frac{Q(\omega)}{1-\frac{a_s a\Omega\sin(\varphi_0-\varphi_{s_0}+\Omega\tau')}{R(\tau')}}\ , \tag{5. 25}$$

And the Green’s function for rotating source and a co-rotating receiver can be expressed as,

$$\tilde{G}_{\Omega_2} = \frac{e^{ikR(\tau')}}{4\pi R(\tau')}\frac{1}{1-\frac{a_s a\Omega\sin(\varphi_0-\varphi_{s_0}+\Omega\tau')}{R(\tau')}}\ . \tag{5. 26}$$

In the literature (Ma, 2020), there is another expression for the frequency domain Green’s function of rotating source and co-rotating receiver, which is in the following form,

$$\tilde{G}_{\Omega_3}(\omega) = \frac{e^{ikR(\tau')}}{4\pi R(\tau')}\frac{1}{1-\frac{a\Omega\cos(\vec{U},\vec{R})}{R(\tau')}}\ , \tag{5. 27}$$

and,

$$\vec{U} = (-\Omega a\sin(\varphi+\Omega\tau'), \Omega a\cos(\varphi+\Omega\tau'), 0)\ , \tag{5. 28}$$

$$\vec{R} = (a\cos(\varphi+\Omega\tau') - a_s\cos(\varphi_s), \sin(\varphi+\Omega\tau') - a_s\cos(\varphi_s), -z)\ . \tag{5. 29}$$

where the vector $\vec{U}$ is the speed vector of the source rotation, and the vector $\vec{R}$ is the vector of the between source and receiver location, which indicates the sound propagation direction. The term $1-\frac{a\Omega\cos(\vec{U},\vec{R})}{R(\tau')}$ represents the relative speed between sound and receiver. Substitute Eq. 5. 28 and Eq. 5. 29 and into Eq. 5. 27, the results are the same as 5. 26, which shows $\tilde{G}_{\Omega_2}$ and $\tilde{G}_{\Omega_3}$ are equivalent to each other. To calculate $\tilde{G}_{\Omega_2}$, the time delay $\tau' = t-\tau$ needs to be calculated numerically by solving the implicit function, $c(t-\tau) = \sqrt{a_s^2 + a^2 + z^2 + 2a_s a\Omega\cos(\varphi_0 - \varphi_{s_0} + \Omega(t-\tau))}$.

5.1.3 Numerical comparison between two expressions for rotating source and rotating receiver

This section compares spherical harmonic expression and numerically expression of the rotating source and receiver Green's functions $\tilde{G}_{\Omega_1}$ and $\tilde{G}_{\Omega_3}$. Ma et al. (2020) show the results of the comparison in their paper, where they investigate four of Green's functions expression (referred to as "steering vector" in Ma et al., 2020, which are shown in Eq. 5. 27). However, no quantitative results were provided in their study. Therefore, in this section, Ma's results are presented first, and then, the author provides a more detailed comparison.

In Ma's paper, they utilize 64 microphone receivers in a ring array shape, which is placed at the plane of $z = 0$ with a radius of 0.4m. The predicted source point coordinate is $(0, -0.13m, 0.5m)$, and source frequency is 1500 Hz. As shown in Figure 5.2, it can be visually observed that shown the plot of SV-C2 ($\tilde{G}_{\Omega_2}$) overlaps with SV-MD ($\tilde{G}_{\Omega_3}$) plot in terms of both amplitude and phase. The results preliminarily confirm that both expressions work for the rotating receiver sound field prediction due to the rotating source. However, a detailed comparison with quantitative results needs to be analyzed for more conclusive verification.

In this study, the author provides a more detailed analysis to take a step further and analyze the percentage of the errors between these two expressions, although they match well in the plot. The parameters used in the current study are different from what was used in Ma's paper. The array used in this study has four concentric circles at 0.1m, 0.2m, 0.3m, 0.4m radius with 10, 14, 18, 22 microphones on each ring. However, only the fourth ring (22 mics, 0.4 m radius) is used for prediction. The source point coordinate is (0.4m, 0.4m, 0). The source is also rotating at 1500rpm and emits the signal at 1250Hz. The amplitude and phases $\tilde{G}_{\Omega_1}$ and $\tilde{G}_{\Omega_3}$ are shown in Figure 5.2. The numerical results of both Green's functions show good agreement in those plots. To further analyze the difference between the two expressions, the error is calculated by the following expression,

$$\varepsilon_{G_\Omega} = \left|\frac{\tilde{G}_{\Omega_3} - \tilde{G}_{\Omega_1}}{\tilde{G}_{\Omega_1}}\right| \times 100\% \,. \qquad 5.\ 30$$

And it can be seen from the plot that the error between two expressions is less than 1%. Theoretically, the error is mainly caused by the truncation error of $\tilde{G}_{\Omega_1}$. Because in the numerical coding of the Green's function, the series has to be truncated with limited terms.

Table 5.1. Steering Vector (Green's Function) Expression in Ma's 2020 Paper

Steering Vector Naming	Steering Vector Expression
SV-st	$\frac{e^{ikR_0}}{4\pi R_0}$
SV-C1	$\frac{e^{ikR(\tau')}}{4\pi R(\tau')}$
SV-C2 / $\tilde{G}_{\Omega_3}$	$\frac{e^{ikR(\tau')}}{4\pi R(\tau')} \frac{1}{1-\frac{a\Omega\cos(\vec{U},\vec{R})}{R(\tau')}}$
SV-MD / $\tilde{G}_{\Omega_1}$	$\sum_{m=-\infty}^{m=\infty} e^{im(\varphi_0-\varphi_{s_0})}$ $k_m \sum_{n=\lvert m\rvert}^{\infty} N^2(n,m) j_n(kr <) \, h_n^2(kr) P_m^n(cos\theta) P_m^n(cos\theta_s)$

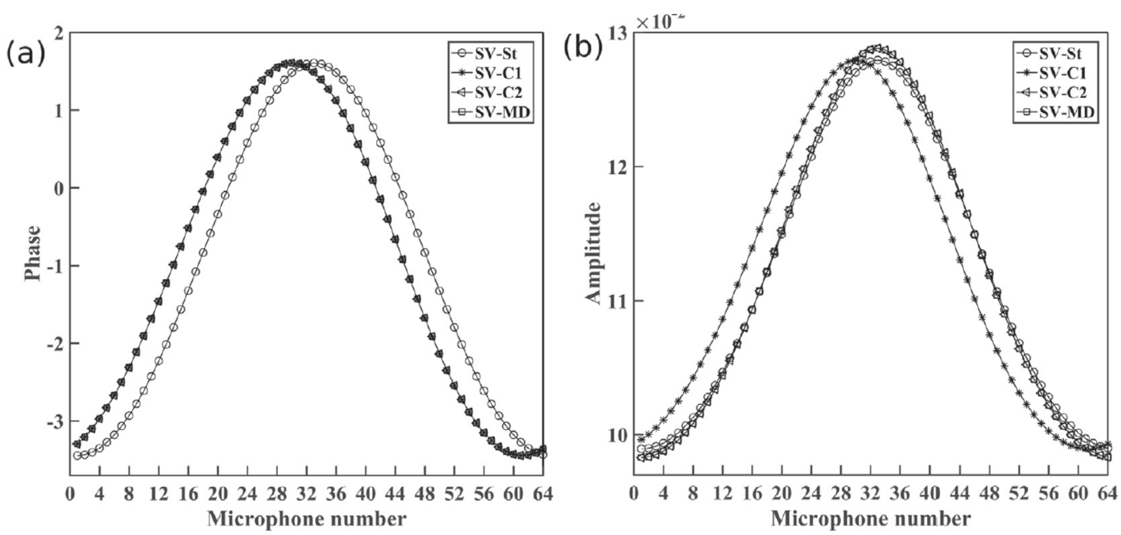

Figure 5.2. Comparison Between the Steering Vector (Green's function) (Ma, 2020)

In summary, the current study confirms that the series expansion expression of Green's function agree well with the theoretical Green's function for rotating source and corotating receiver at the same speed. In the next section of this study, it will be shown that Green's function of both stationary and corotating receivers can be leveraged for the VRA array signal generation.

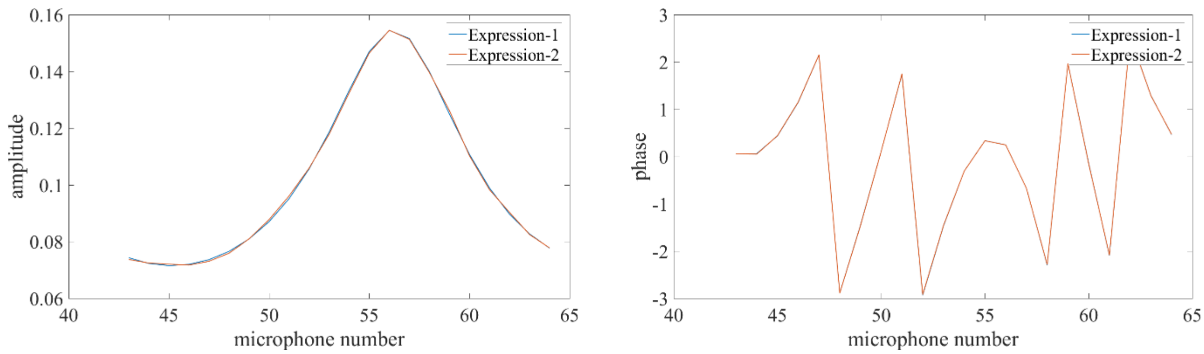

(a) amplitude (b) phase

Figure 5.3. Comparison between G_{Ω_1} and G_{Ω_3}

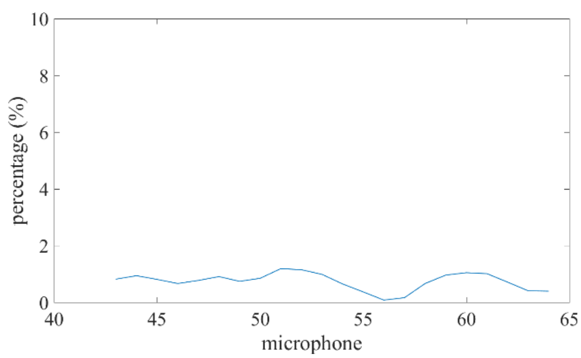

Figure 5.4. Error between G_{Ω_1} and G_{Ω_3}

5.2 Frequency Domain VRA algorithm

The frequency-domain virtual rotating array signal generation algorithm is introduced in this section. First, the section introduces the well-known modal decomposition frequency domain VRA method by Pannert and Maier (2014). Then, the algorithm is further simplified and extended to be used by an irregular array, which optimizes array geometry.

The purpose of virtual rotating array signal generation is to process the acoustic signals measured on the stationary array to obtain signals at a receiver array that would be measured if the array is rotating about the same axis and at the same speed as the source rotation. Suppose a total of L equally-spaced microphones are placed in a circular array at a radius of a_r from the rotation axis in the receiver plane. Their polar coordinates can be specified by $\vec{x}_l = (r_\beta, \theta_\beta, \varphi_l)$ where $a_r = r_\beta sin\theta_\beta$ and $\varphi_l = \varphi_1, \varphi_2 \dots \dots \varphi_L$. According to the beamforming algorithm in Pannert's 2014 paper, the measured acoustic fields $D_0(\vec{x}_l, \vec{x}_s, \omega)$, for each of the L stationary microphones at the array can be used to generate the corresponding VRA signals due to a rotating monochromatic source. Use of the theory for the discrete Fourier expansion, the pressure spectrum, $P_\Omega(\vec{x}_l, \vec{x}_s, \omega)$, at the l^{th} microphones in the VRA are given by

$$P_\Omega(\vec{x}_l, \vec{x}_s, \omega) = \sum_{m=m1}^{m2} [\tfrac{1}{L} \sum_l^L D_0(\varphi_l, \omega + m\Omega) e^{-im\varphi_l}] e^{im\varphi_{r_l}} , \qquad 5.31$$

where $-(L-1)/2$ and $L/2$ are used for the respective limits ($m1$ and $m2$) of the outer summary series.

As shown in Eq. 5. 31, the number of arithmetic operations for representing P_Ω in the circular array is of the order of L^3 where L is the total number of receivers. In order to develop an optimal array of stationary receivers and to improve the computational efficiency for the source reconstruction, a more efficient algorithm is proposed for VRA signal generations at the receiver plane as follows. A set of L microphones are now placed in the optimum locations at the receiver plane instead of aligning them in circular arrays. These receiver positions in an optimized virtual rotating array (Op-VRA) are represented in the spherical polar coordinates by $(r_l, \theta_l, \varphi_l)$ where $z_r = r_l cos\theta_l$, z_r is the distance between the receiver plane and the $z = 0$ plane, and the subscript l $(l = 1,2, \dots, L)$ denotes the corresponding parameters for the l^{th} microphone.

For a monochromatic source or narrow band source with no significant spectral contents at the rotation sidebands of the targeted frequency ($\tilde{Q}(\omega \pm m\Omega) = 0$, if $m \neq 0$), the spinning mode coefficient, $C_m^{(0)}$, for a stationary receiver is defined as:

$$C_m^{(0)}(\vec{x}_l, \vec{x}_s, \omega) = e^{-im\Delta\varphi} \tilde{Q}(\omega - m\Delta\Omega) \sum_{n=|m|}^{\infty} \tilde{G}(k, m, n) . \qquad 5.32$$

according to the modal decomposition. The corresponding mode, $C_m^{(\Omega)}$, in the rotating frame is determined by

$$C_m^{(\Omega)}(\vec{x}_l, \vec{x}_s, \omega) = e^{-im\Delta\varphi} \tilde{Q}(\omega) \sum_{n=|m|}^{\infty} \tilde{G}(k_m, m, n) . \qquad 5.33$$

Consequently, the measured data in the stationary frame, $D_0(\vec{x}_l, \vec{x}_s, \omega)$, can be converted to that of the rotating frame, $\Psi_\Omega(\vec{x}_l, \vec{x}_s, \omega)$, by summing the modal contributions from each of the frequency components $\omega \pm m\Omega$,

$$\Psi_\Omega(\vec{x}_l, \vec{x}_s, \omega) = \sum_{m=m_a}^{m_b} D_0(\vec{x}_l, \vec{x}_s, \omega + m\Omega_s) . \qquad 5.34$$

where the choice of m_a and m_b is dependent of the quality of dataset. If the contribution beyond these two limits are 10dB or below the total sound fields, the summation series terminates at m_a at the lower limit and m_b at the upper limit. However, an accurate estimation of source strength cannot be guaranteed when the source spectrum overlaps with rotating sidebands, i.e. $\tilde{Q}(\omega \pm m\Omega) \neq 0$, if $m \neq 0$. The equation shows that, for sources with more complex spectral contents, the sideband summation includes the contribution of source contents at multiple frequencies. In order to further investigate the application of sideband summation, the rotating Green's function property needs to be used,

$$G_{\Omega_3}(\omega) = \frac{e^{ikR(\tau')}}{4\pi R(\tau')} \frac{1}{1-\frac{a\Omega\cos(\vec{U},\vec{R})}{R(\tau')}} = be^{ikR(\tau')} \,, \qquad 5.35$$

where b is a constant, which represents $\frac{1}{4\pi R(\tau')} \frac{1}{1-\frac{a\Omega\cos(\vec{U},\vec{R})}{R(\tau')}}$. In addition, $R(\tau')$ is also a constant, and the sound traveling time a can be calculated numerically, as explained in Section 5.1. Substitute Eq. 5. 35 into Eq. 5. 34, the following expression can be derived,

$$\Psi_\Omega(\vec{x}_l, \vec{x}_s, \omega) = be^{ikR(\tau')}(\tilde{Q}(\omega) + \sum_{m_0=1}^{m+}(e^{im_0k_\Omega R(\tau')}\tilde{Q}(\omega + m_0\Omega) + e^{-im_0k_\Omega R(\tau')}\tilde{Q}(\omega - m_0\Omega))) \,. \qquad 5.36$$

where $k_\Omega = \frac{2\pi\Omega}{c}$. One special condition is the spectrum of the signal is symmetric about the frequency, i.e., $\tilde{Q}(\omega + m_0\Omega) = \tilde{Q}(\omega - m_0\Omega)$. If this condition is satisfied, Eq. 5. 36 can be reduced to the following form,

$$\Psi_\Omega(\vec{x}_l, \vec{x}_s, \omega) = G_\Omega(\omega + m_0\Omega) (\tilde{Q}(\omega) + \sum_{m_0=1}^{m+} \cos(m_0 k_\Omega R(\tau'))\, \tilde{Q}(\omega + m_0\Omega)) \,. \qquad 5.37$$

If the effect of rotational speed cannot be neglected and the source has symmetric around frequency ω, the sideband summation can still de-Dopperize the signal with overestimated or underestimated strength. More specifically, the strength will be overestimated if $\sum_{m_0=1}^{m+} \cos(m_0 k_\Omega R(\tau'))\, \tilde{Q}(\omega + m_0\Omega) > 0$, and the strength will be underestimated if $\sum_{m_0=1}^{m+} \cos(m_0 k_\Omega R(\tau'))\, \tilde{Q}(\omega + m_0\Omega) < 0$. However, although the source strength estimation is not accurate using sideband summation, if the spectra of different sources are similar to each other, the relative strength between different sources can still be identified correctly, which will be shown in the holography results sections.

5.3 Time Domain Virtual Rotating Array (VRA) Algorithm

This section introduces the algorithms for the time domain virtual rotating array. The virtual rotating array modifies the array signal properties to eliminate the amplitude and phase modulation caused by the doppler effect of the rotating sound sources. For microphone array measurement, if there is no relative motion between the source and the microphones, the sources can be regarded as stationary for the measurement. In this condition, the holography methods for stationary sources can be used with modified Green's function by compensating the receiver's motion against the medium, which will be discussed in Section 5.3.1. However, the measurement using a high-speed rotating array is difficult to be achieved. In order to overcome this disadvantage, the time domain interpolation method has been proposed to generate the virtually rotating microphone signal based on the stationary array measurement. The virtual rotating array method was initially proposed to work with the beamforming methods for rotating source localization. The current study extends the existing time-domain virtual rotating array methods and applies them to near-field holography to reconstruct rotating sound sources. In addition, a more efficient 0 order interpolation is also proposed, which significantly improves the efficiency of traditional time-domain VRA methods.

5.3.1 Algorithms in Literature

There have been three time-domain VRA methods presented in previous publications to the author's best knowledge. Herold et al. proposed a linear interpolation using the adjacent microphones on a ring-shaped array in 2015 (Herold et al., 2015). Despite its high efficiency, the application of this VRA interpolation is restricted to using a circular array. In 2020, Jekosh et al. proposed two more interpolation methods: Barycentric interpolation and radial basis function (RBF) interpolation. Those two interpolation methods extend virtual rotating array methods using arrays in arbitrary shapes. However, the computational efficiency of the decreases compared to linear interpolation. In this section, all three published VRA methods will be introduced.

5.3.1.1 Linear Interpolation

In this subsection, the linear interpolation algorithm is presented, which is illustrated in Figure 5.5. For linear interpolation, the signal is interpolated using two adjacent stationary microphones.

$$p_{v_m}(t) = \frac{\alpha_1 \cdot p_{r_i}(t) + \alpha_2 \cdot p_{r_{i+1}}(t)}{\alpha}, \tag{5. 38}$$

where $\alpha = \frac{2\pi}{M}$, M is the number microphones per circle. Assume that m^{th} virtual rotating microphone is between i and i+1 stationary microphone at time t. The angle α_1 is the angle between m^{th} virtual rotating microphone and i^{th} stationary microphone, the angle α_2 is the angle between m^{th} rotating microphone $(i+1)^{th}$ stationary microphones. It is obvious that the linear interpolation strategy only works with the circular shaped array, because the interpolation requires the virtual rotating microphone to be on the same arc with the stationary microphones.

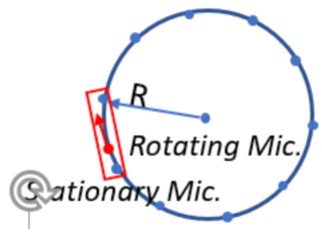

Figure 5.5. Illustration for Linear Interpolation

5.3.1.2 Barycentric Interpolation using Delauney Triangulation

To be able to perform Barycentric interpolation, the 2D mesh needs to be constructed using all of the neighboring microphones. A common way to construct the mesh is to use the Delauney triangulation (Delauney, 1934). The triangulation is constructed in a way that all of the circumferences of the triangles have empty interior. The MATLAB triangulation function is used to construct the mesh. Figure 5.6 shows the Delauney triangulation of a 2D microphone array, which has 84 microphones with the aperture of 1m.

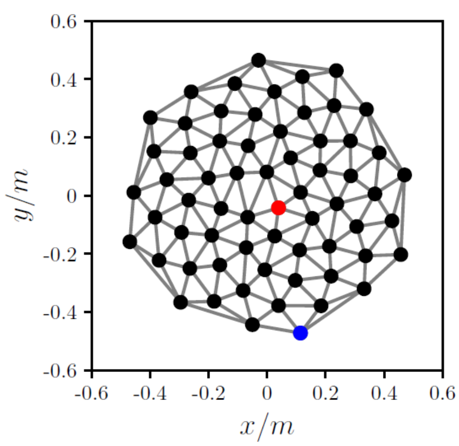

Figure 5.6. Triangle Mesh for Barycentric Interpolation (Jekosh et al., 2020)

The interpolation is performed by the Barycentric interpolation between the neighboring points in a triangle. Assuming i^{th} virtual rotating microphone has the coordinate of $(x_i(t), y_i(t))$ at the moment t. And it is in the n^{th} triangle with the vertices coordinates $(x_n^1, y_n^1), (x_n^2, y_n^2), (x_n^3, y_n^3),$, the Barycentric coordinates (w_1, w_2, w_3) can be calculated using the following equations,

$$\begin{gathered} x_i(t) = w_1 x_n^1 + w_2 x_n^2 + w_3 x_n^3 \\ y_i(t) = w_1 y_n^1 + w_2 y_n^2 + w_3 y_n^3 \\ w_1 + w_2 + w_3 = 1\ . \end{gathered} \qquad 5.\ 39$$

After obtaining the Barycentric coordinates, the pressure at the virtual rotating microphone can be calculated using the following expression,

$$p_i(t) = w_1 p_n^1(t) + w_2 p_n^2(t) + w_3 p_n^3(t)\ , \qquad 5.\ 40$$

where $p_i(t)$ is the pressure at i^{th} virtual rotating microphone, $p_n^m(t)$ is the pressure at m^{th} vertice of n^{th} triangle. To calculate the pressure at all microphones on the virtual rotating array, the procedures need to be repeated for all of the microphones. The limitation of this algorithm is that it can only be performed within convex hull of the original array. Hence, the aperture of the virtual rotating array has to be smaller than the stationary array.

5.3.1.3 Radial Basis Function Interpolation

Radial basis function is a meshless method that does not require the mesh to be constructed using the array. Similar to the Barycentric interpolation, RBF does not require the array to be in a specific shape. A Radial Basis Function is a n-dimensional radially symmetric function, which is evaluated using the Euclidean distance between the center of RBF x^k and the point of evaluation x. The Euclidean distance is defined as $r = \|x - x_k\|_2$. In this study, the cubic radial basis function is used, which is $\Phi = r^3$. The pressure at the i^{th} virtually rotating microphone is,

$$p_{v_i}(t) = \sum_{i=1}^{M} w_i \Phi(\|x - x_i\|_2)\ , \qquad 5.\ 41$$

where w_i is the weighting coefficients between the virtual rotating microphone and i^{th} microphone in the measurement array. The weighting coefficients can be calculated by solving the linear system,

$$\begin{bmatrix} \Phi(\|x_1 - x_1\|_2) & \cdots & \Phi(\|x_M - x_1\|_2 \\ \vdots & \ddots & \vdots \\ \Phi(\|x_1 - x_M\|_2 & \cdots & \Phi(\|x_M - x_M\|_2 \end{bmatrix} \begin{bmatrix} w_1 \\ \vdots \\ w_M \end{bmatrix} = \begin{bmatrix} p_1 \\ \vdots \\ p_M \end{bmatrix} \qquad 5.\ 42$$

where $p_1 \ldots p_M$ are the pressure at the stationary microphone. This linear system can be solved at each time sample. Then, they can be used to calculate the pressure at the virtual rotating array. Compared to Barycentric interpolation, the method works for the microphone outside of the measurement array aperture. However, to make sure that the interpolation works well, the virtually rotating microphone needs to be close to the array. For the points further away from the array, the extrapolation is not valid.

5.3.2 Zeroth order Interpolation

The microphone array is not necessarily arranged in a ring geometry centered around the axis of rotation but in an arbitrary configuration. For a virtual rotating array in time domain, an interpolation scheme is required to obtain the pressure time signals derived from the nearby microphones in a stationary array for compensating the effects of source motion. Different interpolation schemes were introduced in the previous studies (Herold et al., 2015; Jekosch et al., 2020; Yang et al., 2021). For instance, (i) a linear interpolation between two adjacent microphones for a circular array, (ii) a Delaunay triangulation using barycentric interpolation for an arbitrary array, (iii) a meshless system using a radial basis function for interpolations, (iv) an interpolation scheme based on inverse distance weighting, and, (v) a statistical method using a ordinary kriging process with prior covariances. Most of these interpolation schemes involves subtle numerical algorithms for their implementations. However, a simpler, but sufficiently accurate, interpolation scheme is presented in the current study. The main idea of the method is to replace the pressure time signals on the VRA with those obtained at the closest microphone. It is worth noting that there are N stationary microphones locating at Y_n and their respective virtually rotating counterparts can be determined accordingly. To perform the zeroth order interpolation scheme, the distance between the virtually rotating microphones and all the stationary microphones need to be calculated at each time step. The pressure time signals on each virtually rotating microphone is then replaced by the corresponding time signals measured at the closest stationary microphones as follows.

Suppose that $P_{v_n}(t)$ is the acoustic pressure of the n^{th} virtually rotating microphone at time t and $P_{r_i}(t)$ is the acoustic pressure at i^{th} stationary microphone such that the distance between v_n and r_i is the shortest among all other stationary microphones at time \$t\$. Hence,

$$P_{v_n}(t) := P_{r_i}(t) \,, \tag{5. 43}$$

where i and $n = 1, 2, 3, \ldots, N$. For a better understanding of the methodology, this process is illustrated in Figure 5.7 showing the receiver regions of circular shapes. Figure 5.8 (a) shows a stationary microphone array with 4 concentric rings housing a total of 64 microphones (i.e. $N = 64$). Excluding the central region (colored in white), there are 64 matching polygons for each of the microphones locating at their respective centers, r_i. The acoustic pressures are constant within each of the i^{th} polygon. If the virtual rotating microphone v_n is located at any points within the i^{th} polygon, its acoustic pressure is set at P_{r_i}. For the purpose of comparison, Figure 5.8 (b) shows the corresponding polygons for a arbitrary array of 84 microphones. The respective outer radii are 0.4 m and 0.476 m for the circular and arbitrary arrays. The proposed algorithm is sometimes referred as a zeroth order interpolation scheme. On the other hand, the linear interpolation is a first order scheme and the Delaunay triangulation method (with either barycentric or piecewise cubic interpolations) is a second or an even higher order one.

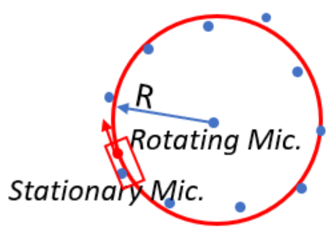

Figure 5.7. Schematic Illustration of 0 Order Interpolation

(a) Circular Array (b) Irregular Array

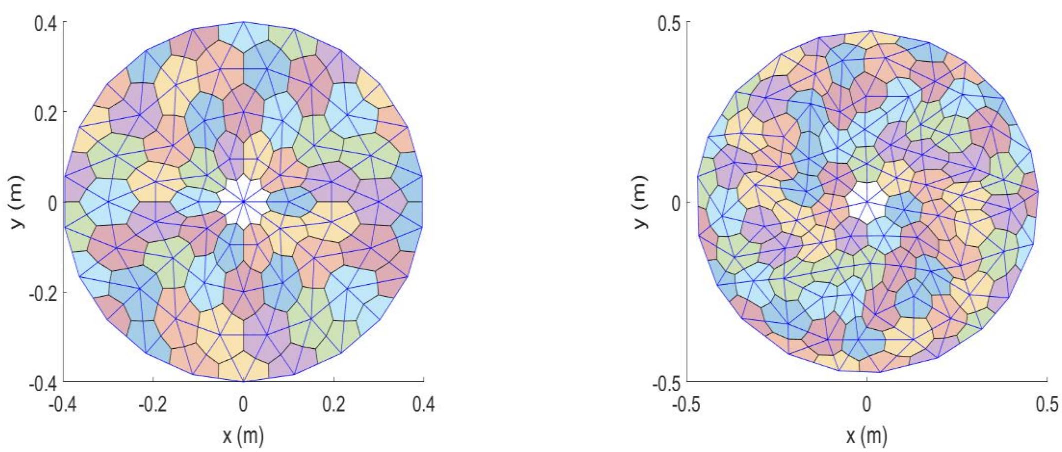

Figure 5.8. Receiver Plane Array Mesh

5.4 Equivalent Source Based Compressive Sensing Acoustical Holography Algorithms

This section introduces the fundamentals of several equivalent source based compressive sensing holography (CESM) approaches, which include: (1) wideband holography (WBH); (2) convex optimization of L1 norm penalty formulation (CVX); (3) hybrid method of WBH and L1 norm method. All three algorithms will be used with virtually rotating array data for near-field rotating source field reconstruction.

5.4.1 Wideband Holography (WBH)

This section introduces the wideband holography algorithm developed by Hald (2016). For a measurement with M microphones on the measurement plane, the microphone measurement can be represented as $\boldsymbol{p} = (p_1, p_2, p_3, \dots\dots, p_M)$. On the source plane, assume there are N grids equivalent monopole, the source strength on the source plane can be represented as $\boldsymbol{q} = (q_1, q_2, \dots\dots, q_N)$. The illustration of the source and receiver plane is shown in Figure 5.9.

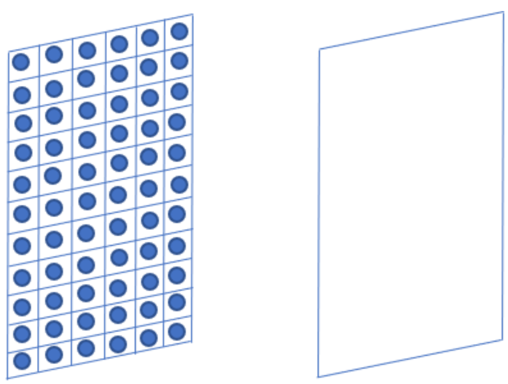

Figure 5.9. Illustration of holography reconstruction plane (left) and measurement plane (right)

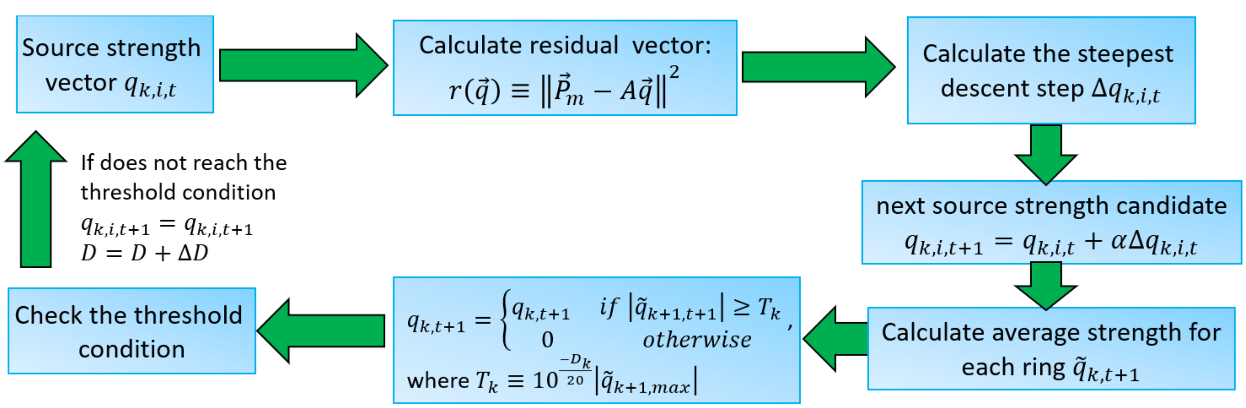

Figure 5.10. Procedures of Wideband Holography Process

Using the source plane and measurement information, the microphone measurement can be calculated from the source strength,

$$\boldsymbol{p} = \boldsymbol{A}\boldsymbol{q} \text{ or } p_{mn} = A_{mn} q_n \, , \tag{5. 44}$$

where the matrix $\boldsymbol{A}$ is the $M \times N$ transfer matrix between source and receiver with $A_{mn} = G_{\Omega,mn}$ as the transfer function between n^{th} rotating source and m^{th} rotating receiver. And k is the wavelength, and R_{mn} is the distance between n^{th} source and m^{th} receiver. In the holographic reconstruction process, the inverse of the linear system:

$$\boldsymbol{q} = \boldsymbol{A}^{-1}\boldsymbol{p} \, , \tag{5. 45}$$

is needed. However, since the linear system is under-determined. The problem needs to be reformulated by considering the Tiknohov regularization. The inverse problem can typically be reformulated by minimizing the objective function with L1 norm of source strength to promote sparsity in the solution,

$$\text{minimize} \quad \|\boldsymbol{p} - \boldsymbol{A}\boldsymbol{q}\|_{\mathbf{2}}^{\mathbf{2}} + \|\boldsymbol{q}\|_{\mathbf{1}} \, , \tag{5. 46}$$

The formulation is equivalent to,

$$\text{minimize } \|\boldsymbol{q}\|_1 \quad \text{subject to} \quad \|\boldsymbol{p} - \boldsymbol{A}\boldsymbol{q}\|_2^2 < \delta \, , \tag{5. 47}$$

where δ is parameter chosen to guarantee the accuracy of the solution. To solve the current problem, the residual vector $\boldsymbol{r}$ is defined as

$$r(\boldsymbol{q}) = \boldsymbol{p} - \boldsymbol{A}\boldsymbol{q} \, , \tag{5. 48}$$

where $\boldsymbol{r}(\boldsymbol{q})$, can be written vector in the quadratic form,

$$\boldsymbol{F} = \frac{1}{2}\|r(\boldsymbol{q})\|_{\mathbf{2}} \, . \tag{5. 49}$$

Then, the problem can be solved by iterative steps as follows. Suppose $\boldsymbol{q}_i$ is the solution at the i^{th} step and the next step $\boldsymbol{q}_{i+1}$ is calculated by

$$\boldsymbol{q}_{i+1} = \boldsymbol{q}_i + \alpha\Delta\boldsymbol{q}_i \, , \tag{5. 50}$$

where α is the relaxation factor ranging between 0.5-1 and $\Delta\boldsymbol{q}_i$ is the step length that can be determined by the steepest descend method,

$$\Delta\boldsymbol{q}_i = \frac{\boldsymbol{g}_i^H(\boldsymbol{p} - \boldsymbol{A}\boldsymbol{q}_i)}{\boldsymbol{g}_i^H\boldsymbol{g}_i}\boldsymbol{A}^H(\boldsymbol{p} - \boldsymbol{A}\boldsymbol{q}_i) \, , \tag{5. 51}$$

where $\boldsymbol{g}_i = \boldsymbol{A}\boldsymbol{w}_i$, and $\boldsymbol{w}_i = \boldsymbol{A}^H(\boldsymbol{p} - \boldsymbol{A}\boldsymbol{q}_i)$. To remove the ghost monopole sources, the source strength of the monopole $\boldsymbol{q}_{i+1}(x, y)$ will be set to 0 if it lies below a certain threshold value. The threshold T_i is set as D_i decibels below maximum monopole strength $q_{i+1,max}$, i.e.

$$T_i = 10^{-\frac{D_i}{20}} q_{i+1,max} \,. \tag{5. 52}$$

Therefore, the source strength will be set in the next iteration as,

$$\boldsymbol{q}_{i+1}(x,y) = \begin{cases} \boldsymbol{q}_{i+1}(x,y) & \text{if } \boldsymbol{q}_{i+1}(x,y) > T_i \\ 0 & \text{otherwise} \end{cases} . \tag{5. 53}$$

For each of the step, D_i is updated by including a monotonically increasing dynamic range,

$$D_{i+1} = D_i + \Delta D \,. \tag{5. 54}$$

The iteration process is repeated until a converged result is obtained or the threshold reaches the maximum value,

$$D_i > D_{max} \quad or \quad \|\nabla F_{i+1}\|_2 < \varepsilon \|\nabla F_0\|_2 \,, \tag{5. 55}$$

where D_{max} is the maximum dynamic range value for the iteration process.

The parameters that can be changed in the wideband holography procedures are α, D_i, D_{max}. The parameter α controls the speed of convergence for each step. The parameter D_i controls the number of ghost source eliminated in each step.

5.4.2 Convex Optimization of L1 Norm Penalty Form Minimization

The objective function that balances the sparsity and accuracy in NAH is introduced as an unconstraint convex optimization problem,

$$\text{minimize} \qquad \lambda \|\boldsymbol{p} - \boldsymbol{A}\boldsymbol{q}\|_2 \ + \|\boldsymbol{q}\|_1 \,, \tag{5. 56}$$

where $\boldsymbol{p}$ is the measurement from the microphones, $\boldsymbol{q}$ is the source strength vector, $\boldsymbol{A}$ is the transfer matrix between source and receiver, λ is a parameter that controls the proportion between the solution sparsity and accuracy. The formulation is different from wideband holography but achieves similar goal. The L_1 norm of $\boldsymbol{q}$ can be expressed as,

$$\|\boldsymbol{q}\|_1 = \sum_{m=1}^{M} q_i \,. \tag{5. 57}$$

And the L_2 norm can be expressed as,

$$\|\boldsymbol{q}\|_2 = \sqrt{q_1^2 + q_2^2 + \cdots + q_M^2} \,. \tag{5. 58}$$

The first term represents the relative error between the actual measurement and reconstruction. Minimizing this term reduces the error between the reconstructed sound field and the actual sound field. The second term represents the total source strength in the source plane. By minimizing the

L1 norm of $\boldsymbol{q}$, the source sparsity is guaranteed. Both the L1 norm and L2 norm terms are convex functions. Hence, the formulation represents a convex optimization problem in which this optimization approach can be applied to obtain an estimation of the sound fields generated by the source. In this study, a commercial CVX solver is utilized to solve the convex problem (Boyd, 2004).

To understand the process of applying the L_1 norm minimization for holographic reconstruction process, fundamentals of the convex optimization is briefly introduced in this section. First, define the convex function, a function f is convex if domain f is a convex set and for all $x, y \in domain\ f$, we have,

$$f(\theta x + (1-\theta)y) \leq \theta f(x) + (1-\theta)f(y), \tag{5. 59}$$

where θ is a variable and $0 \leq \theta \leq 1$. This function can be visualized as Figure 5.11.

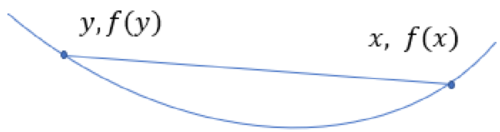

Figure 5.11. Convex function illustration

A convex problem can be formulated as,

$$\begin{gathered} \text{minimize } f_0(x) \\ \text{subject to } f_i(x) \leq 0 \text{ and } g_i(x) = 0, i = 0,1,2 \ldots\ldots \end{gathered} \tag{5. 60}$$

where x is the convex variable, and $f_0(x)$ is the objective function. The relation $f_i(x) \leq 0$ is the inequality constraints and $g_i(x) = 0$ is equality constraints. There are different approaches to solve the convex problem, however, the fundamentals of convex problem solution will not be detailed in this section.

5.4.3 Hybrid Method

Wideband holography is effective at finding the primary source location. However, the solution of the WBH is not compact enough, and it does not work well with low frequency or closely spaced sources. For the wideband holography, the initial guess usually starts with sources of zero strength. However, if the initial input for the wideband holography is close to the actual source distribution, the source reconstruction accuracy will be significantly improved. This can lead to the removal of the frequency restriction for source reconstruction. Shi (2019) proposed that the outcome of L1 norm optimization can be used as an initial value in wideband holography. In L1 norm optimization, λ can be set to a higher value so that the convex optimization reconstruction can include most sources. This initially estimated solution (by L1 norm optimization) can be used in WBH to get rid of the unwanted ghost sources and preserve the accuracy of the actual sources.

5.4.4 Error Quantification of Holography Reconstruction

The holographic reconstruction error needs to be quantified in order to study the performance of the VRA signal based reconstruction. Two parameters are quantified for sound source error analysis, they are source strength error and source localization error. In order to quantify those errors, the reconstructed sources are identified around the true source locations. A rectangular area will be selected near sources, as shown in Figure 5.12. Then, identify the strongest location within the area and select all the hotspots that are within 15 dB difference with the strongest source. After the selection of the source locations, the source strengths is calculated by add the strength of all selected sources coherently.

On the other hand, the source location error is calculated similarly compared to the source strength error. After identifying the location of all reconstructed source locations near one source. The distance between the reconstructed locations and true location for all hotspot are calculated and then averaged.

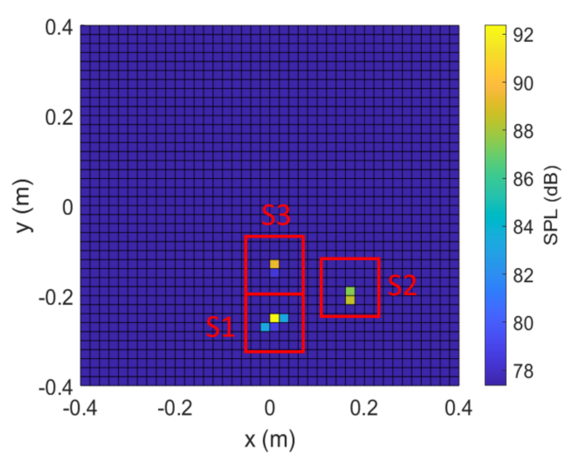

Figure 5.12. Holography Source Error Quantification

6. NUMERICAL VALIDATION OF HOLOGRAPHY DEVELOPMENT

In this chapter, the validation of VRA signal based CESM holography reconstruction will be performed using numerical signals. This first section detailed the approach for simulated rotating source signal generation. The advanced time approach procedures to generate the sound fields of rotating monopoles are introduced. In addition, the simulation setup for the numerical validation is also introduced in this section. The second section performs numerical validation for the time domain virtual rotating array and the holography reconstruction using the VRA signals. The holography reconstructions of both tonal and broadband sources are shown, and source strength reconstruction accuracy is analyzed. The third section validates the frequency domain virtual rotating array based holography with the simulated signal.

6.1 Numerical Signal Generation and Simulation Setup

The sound fields of rotating sources are investigated by many previous studies, as discussed in the literature review in Chapter 2. Among those methods, the numerical approaches are most suitable for the sound field generation to validate VRA methods and CS holography performance. In the holography process for the equivalent source based CS holography, the sources are assumed to be sparse, and equivalent monopole sources are used. Therefore, in the current simulation, monopole sources are used to represent the actual sources. In addition, both tonal signals and broadband signals are generated for those monopole sources. Several numerical methods can be used to generate the sound fields for moving monopole sources. The advanced time approach is selected for its high computational efficiency and accuracy in the current study. According to acoustical reciprocity, the numerically generated signals are validated by reconstructing the source signals reversely using the receiver signals. The simulated signal received by the stationary receiver array will be used as input for the holography reconstruction process in the following sections.

6.1.1 Numerical Signal Generation

6.1.1.1 Advanced Time Approach Introduction

This section describes the sound field signals generation process used in the holography developments numerical validation. The geometry of a general rotating source sound propagation problem is shown in Figure Figure 6.1. The plot for simplicity shows only one source and receiver pair (the n^{th} source and the m^{th} receiver). For a situation involving multiple sources and multiple receivers, the contribution of all sources will be added together for each receiver, and the same process is repeated for all receivers.

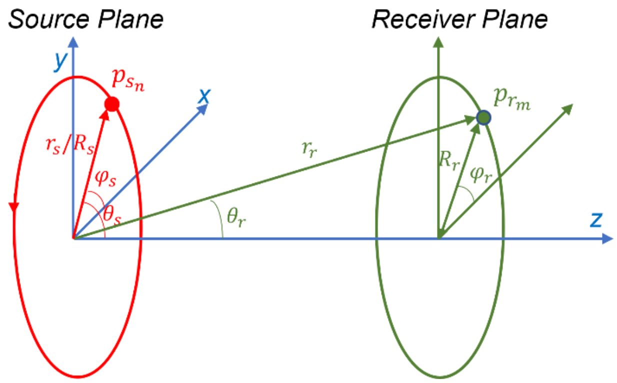

Figure 6.1. The sound transmission illustration

The n^{th} rotating source signal is emitted at time τ_n, and then propagated to and received by m^{th} receiver at $t_{m,n}$ with the following relation between emission time and the corresponding receiving time:

$$t_{m,n} = \tau_n + \Delta t_{m,n} = \tau_n + \frac{R_{n,m}}{c}, \qquad 6.\ 1$$

where

$$R_{n,m} = \sqrt{\left(x_{s_n}(\tau_n) - x_{r_m}\right)^2 + \left(y_{s_n}(\tau_n) - y_{r_m}\right)^2 + \left(z_{s_n}(\tau_n) - z_{r_m}\right)^2}. \qquad 6.\ 2$$

Assume the source strength time history is $p_{s_n}(t_{s_n})$, so that the signal at the receiver $p_{r_{m,n}}\left(t_{r_{m,n}}\right)$ can be expressed as,

$$p_{r_{m,n}}\left(t_{m,n}\right) = \frac{p_{s_n}(\tau_n),}{4\pi R_{n,m}}, \qquad 6.\ 3$$

where $R_{n,m}$ is the distance between n^{th} source and the m^{th} receiver. The received signals from different sources need to be added together to synthesize the total received signals. However, in the signal synthesis process, since the emission time is chosen to be time samples with equal intervals, which results in non-uniform time intervals for corresponding receiver time samples, the calculated sound pressure signals at the irregular sampled receiver time samples need to be resampled onto a time samples with uniform intervals, $\bar{t}_{r_{m,n}}$. The resampling can be performed by linear interpolation. Then, the resampled signals from different sources are added together

$$p_{r_m}(\bar{t}_m) = \sum_{n=1}^{N} p_{r_{m,n}}(\bar{t}_{m,n})\,. \qquad 6.\ 4$$

where p_{r_m} is the total received pressure for receiver m, N is the number of sources.

6.1.1.2 Advanced Time Approach Numerical Validation

To ensure the accuracy of numerically generated rotating sound signals, the signal quality validation needs to be performed first. Validating the signal generation process predicts the source signal reversely using the received signals and compares the reconstructed source signals with the source signals. If the reconstructed sound sources signal matches with the source signal, it can be concluded that the simulated signals are accurate. The relation between the source and receiver time can be found,

$$\Delta t_{n,m} = \frac{R_{n,m}}{c}\,. \qquad 6.\ 5$$

Using the relation in Eq. 6. 5, when the uniform receiver time is given, the source time can be calculated backwards,

$$\tau_n = t_{m,n} - \Delta t_{m,n}\,. \qquad 6.\ 6$$

The calculation can be performed numerically, and the calculated τ_n is not uniformly distributed. An example of $\Delta t_{m,n}$ is shown in the following plot.

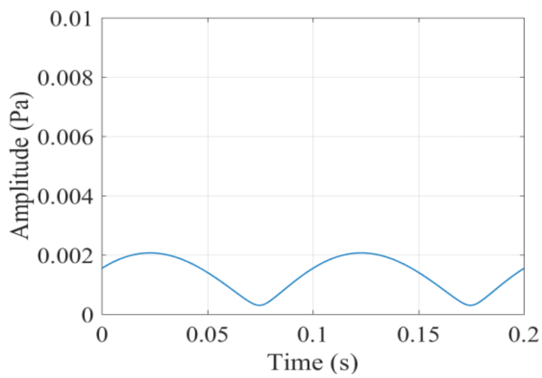

Figure 6.2. The time delay between source and receiver for a rotating source.

One case for the reconstructed source signal and the source signal is shown in Figure 6.3. It can be observed in the plot that the reversely predicted source signal time history using the resampled receiver signals match perfectly with the source signal time history. The results validate that the numerically generated rotating source signal is accurate. Therefore, it can be used in holography reconstruction.

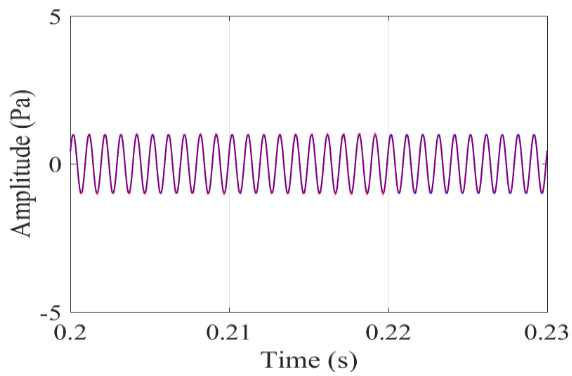

Figure 6.3. Signal Validation using Backward Prediction. Blue line is the emitted signal, red dotted line represents the reconstructed source signal.

6.1.2 Simulation Setup

The geometrical setup for the numerical simulations, which is shown in Figure 6.4, is the same as the benchmark cases detailed in literature (Herold et al., 2018). There are two sources (S_1, S_2) at a radial distance of 0.25m and at the respective azimuthal angles starting at -90° and -50°. The third source (S_3) is located at radial distance of 0.125m and an azimuthal angle starting at -90°. All three sources rotate at a constant speed of 1500rpm counterclockwise. All sources, S_1, S_2, and S_3, are point monopoles and their relative source strengths, Δ_1, Δ_2 and Δ_3 are 0, -3 and -6dB respectively (where $\Delta_1 = S_j - S_1$ for $j = 1{,}2{,}3$).

Regarding to receiver signals, two stationary arrays were used for the VRA interpolation to produce acoustic data on rotating arrays, one circular array (Array-1) and one irregular array (Array-2), as shown in Figure 6.5. The circular array is an array with 64 channels distributed on four rings, with 10, 14, 18, 22 microphones on each ring respectively and microphones on each ring spaced equally. The radii for each ring are: 0.1m, 0.2m, 0.3m, 0.4m, respectively. The randomized array has totally 84 randomly arrange microphones with 1 meter aperture size. Since the number of microphones used for circular array is fewer than the irregular array, the aperture of the circular array is smaller to ensure similar microphone density.

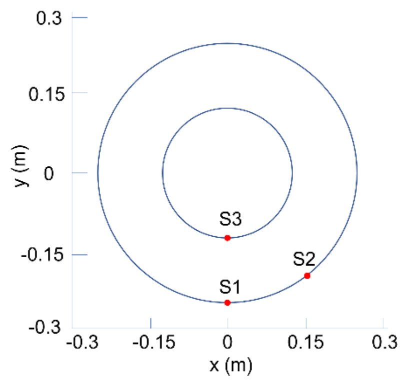

Source Configuration

Number of Sources	3
Rotating Speed	1500rpm
Rotating Radius	0.25m/0.25m/0.125m
Source Starting Azimuth Angle	-90°/-90°/-50°

Figure 6.4. Simulation Geometry of Source Configuration

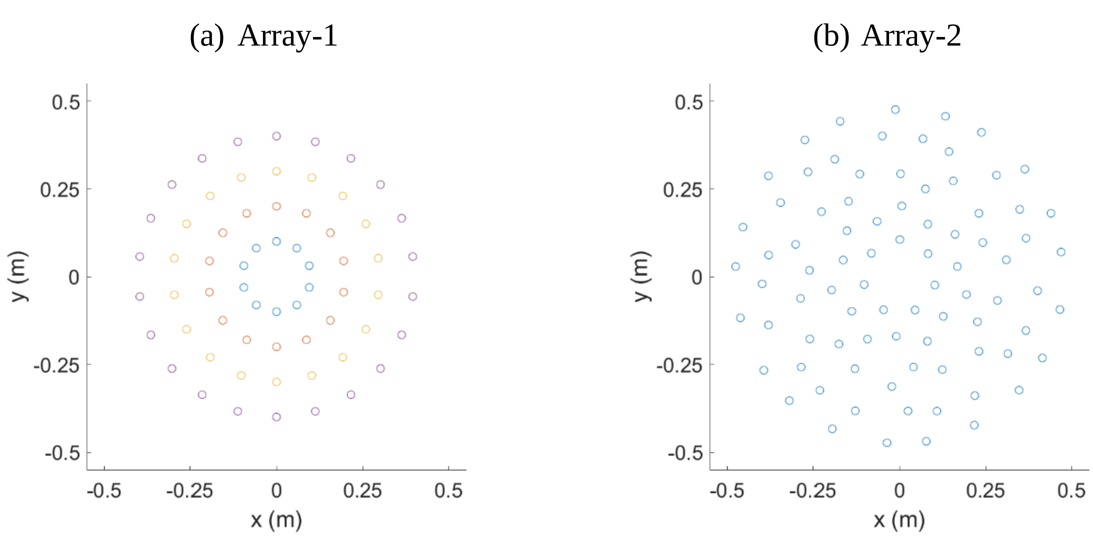

Figure 6.5. Array Geometry for Simulation Validation

6.2 Numerical Experiment for Time Domain Virtual Rotating Array

This section uses four time-domain virtual rotating array approaches to interpolate the numerically generated stationary array signals to generate virtually rotating array signals. As discussed in the last section, the benchmark B11b source configuration is investigated in the current study to validate the effectiveness of the combination between the virtually rotating array signal and the CESM holography algorithm, in particular, CVX holography in this section. Therefore, the first goal of this section is to validate the holographic reconstruction performance of the rotating sources using the VRA signals. The second goal of this section is to compare the performance of the zeroth order interpolation based holography with other time-domain methods.

6.2.1 Data Processing Procedures for Simulation Signals

The numerical simulations are based on three types of source signals (see Table 6.1). Case 1: all sources emit monochromatic signals; and Case 2: all sources emit white noise for frequency ranging from 0.5 to 10kHz.

Table 6.1. Source Signal Parameters, Frequency Domain VRA Processing

	Case 1	Case 3
Source Signals	• S1, S2, S3: 1250Hz/ 1600Hz/ 2000Hz/ 2500Hz/ 3150Hz/ 4000Hz/ 5000Hz	• S1, S2, S3: white noise
Source Strength	• S1:100dB@2500Hz • S2:97dB@2500Hz • S3:94dB@2500Hz	• S1: 99.4dB • S2: 96.4dB • S3: 93.4dB
Time Duration	2s	10s
Sampling Rate	32768Hz	32768Hz

The signal processing parameters for each case are shown in Table 6.2. It can be seen that the data processing procedures are different for tonal cases and broadband cases. For the first step, time-domain VRA interpolation is performed to the time history, and the interpolated VRA signals are generated. Then, the VRA array signals are transformed to the frequency domain using Fast Fourier Transform (FFT) without time averaging for tonal source cases. One second of data is used, which results in a frequency domain resolution of 1 Hz. Finally, the frequency-domain signals are used for holography reconstruction at selected reconstruction frequency. For the broadband case, the VRA data are handled by different procedures. For the broadband signal case, the broadband power spectra of the interpolated data on the virtual rotating array are calculated with a 4096-point Hanning windowed FFT block and a 50% overlap between two adjacent blocks (Proakis et al., 1992). Then, acoustical holography can be performed to the spectrum of the VRA signals at the selected frequency. For the holography reconstruction, the reconstructed source region is a 0.8 m by 0.8 m rectangular plane with 41 by 41 uniformly distributed grids.

Table 6.2. Data Processing Parameters for Simulation

	Case 1	Case 2	Case 3
FFT Block Size	32768	32768	4096
FFT averages	No average	No average	With averages
Segment Overlap	0	0	50% Hanning
Source Plane Grids	41*41	41*41	41*41
Source Plane Grid Size	0.02m*0.02m	0.02m*0.02m	0.02m*0.02m

6.2.2 Receiver Plane Error Analysis

According to common perception, a higher-order interpolation scheme is preferred because it can lead to more accurate numerical results when its performance is compared with a lower-order interpolation scheme. It is therefore of interest to examine the validity of this perception. In order to illustrate the merit of the zeroth-order interpolation scheme, contour plots for different interpolation schemes for the circular array are shown in Figure 6.6. Three tonal sources (S_1, S_2, S_3), which have the same source frequency of 1.25 kHz, are used in the simulations. The locations of these three sources are summarized in Figure 6.4. This figure shows a snapshot of the pressure time signals in these simulated contours for using Array 1. The contour plot with a higher resolution is shown in Figure 6.6 for comparison.

Figure 6.6 (a) shows the contour plot based on the zeroth-order interpolation. A total of 64 polygons (with their centers arranged in 4 rings at different radii) represent the sound fields in the receiver plane where the sound pressure is held constant within each of these polygons. Three higher-order interpolations schemes: the linear interpolation, barycentric, and the radial basis function (referred to as RBF in the contour plots), are shown in Figure 6.6 (b-d), respectively. It is apparent that the zeroth-order interpolation (Figure 6.6 (a)) shows an inferior visual agreement with Figure 6.6 (a) due to the number of polygons (receivers) is not sufficient to afford a better resolution. On the other hand, the contours due to the other three higher-order interpolation schemes have displayed much better agreements at this low source frequency. It is because these three interpolation schemes work pretty well if sufficient high-quality data points are available for approximating the sound fields in the receiver plane.

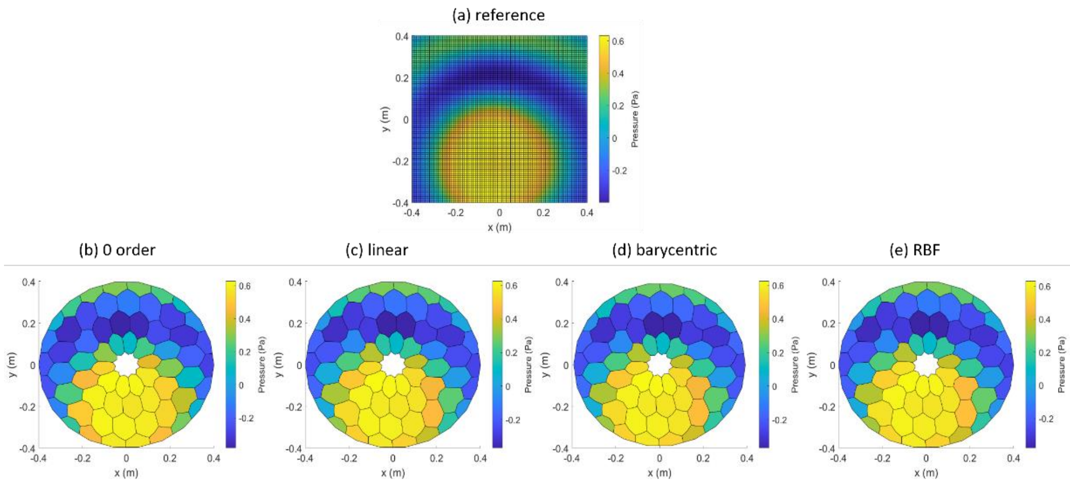

Figure 6.6. Receiver Plane Pressure Mesh, 1250Hz

Next, we display in Figure 6.7 the analogous simulation results where the tonal frequency of has been increased to 5 kHz. The reference contour, Figure 6.7 (b), shows a clear interference pattern in the receiver plane. The contours by the linear interpolation, barycentric, and RBF schemes (Figure 6.7 (c-e)) show poorer visual agreements with the reference result. However, the zeroth-order interpolation scheme has demonstrated a better agreement at this higher frequency, as shown in Figure 6.7 (a) and (b). The sound field can explain this phenomenon in the receiver plane, showing a clear interference pattern from the three spatially-separated sources at 5 kHz. However, a more uniform pattern is observed for the case of 1.25 kHz. Given the limited number of microphones, it is expected that the higher-order interpolation schemes will not resolve the fields correctly, particularly at high frequencies. However, the errors introduced by the zeroth-order interpolation scheme grow more slowly with the increase in the source frequency. Hence, its use is justifiable when a higher interference pattern is observed in the receiver plane. To confirm the above statements, an error analysis will be conducted in the following two sections to quantify the merit of using the zeroth-order interpolation scheme.

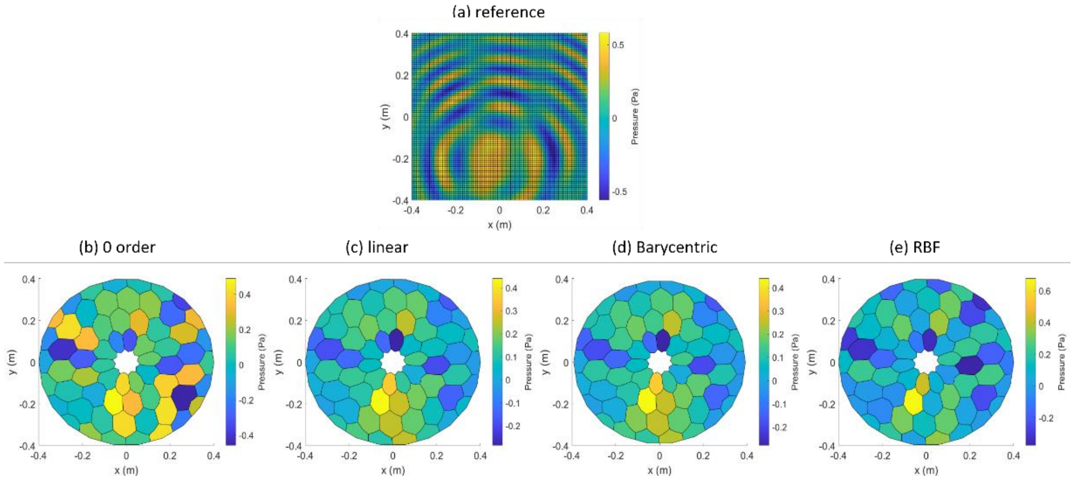

Figure 6.7. Receiver Plane Pressure Mesh, 5000Hz

6.2.3 Holography Results for Tonal Signals

To quantify the errors in the source reconstruction process, it is beneficial to investigate the possible errors in a forward prediction problem as follows. Suppose that the locations of all tonal sources and their strengths are known as *a priori*. The total sound fields can be computed accurately in the receiver plane by reducing the grid size as shown in Figure 6.6 a and Figure 6.7 a. These two plots are prepared by using a nominal receiver plane of size $1\,m \times 1\,m$ with a rectangular grid size of $0.01\ \mathrm{m} \times 0.01\ \mathrm{m}$. The sound fields can be computed at each 'cell' independently at any time t. The computed pressure time signals will be taken as the reference expressed in a form of a column vector of P_{ref} for different cells. The approximate pressure time signals are then computed using different interpolation schemes with *N* sampling points as shown in Figure 6.6 and Figure 6.7 b-e giving a column vector P_n. The error in each cell of the receiver plane is then defined as,

$$E_R = 10log_{10}\frac{P_n^2}{P_{ref}^2}\,. \tag{6. 7}$$

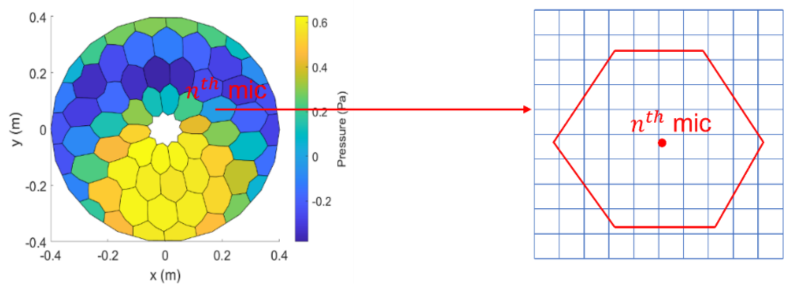

Figure 6.8. Distribution of Rectangle Meshes in Polygon

The mean value of error time history for different interpolation schemes can be calculated at different tonal frequencies. The results for the error spectra are presented in Figure 6.9 for Array 1 (circular array of 64 simulated receivers) and Figure 6.12 for Array 2 (arbitrary array of 84 simulated receivers). The zeroth-order interpolation, linear, barycentric, and RBF schemes are used for comparisons. The details of implementation for other schemes used in the present study were provided in Yang's 2021 paper. The result for a non-moving source is used for reference purposes in the mean error spectra because it usually gives the lowest mean errors in most frequencies. Hence, its use can provide benchmarking results to evaluate the performance of different interpolation schemes.

For Array 1, the mean errors for all interpolation schemes increase with the source frequency, see Figure 6.9 (a). The zeroth-order interpolation scheme has the highest mean errors at low frequencies, but its growth rate with the source frequency is slowest leading to the lowest mean error at 5 kHz. The characteristics for Array 2 are generally comparable with Array 1 except that the mean errors for the barycentric scheme are worse than the zeroth order interpolation at all frequencies. These results have confirmed the validity of using the zeroth-order interpolations for source reconstruction, which provide comparable, if not better, results with higher-order interpolation schemes, especially for high-frequency sources.

To complete the error analysis in this section, the CVX holography will be employed to either Array 1 or Array 2, which have been used for the numerical simulations of data acquisition. Again, the same tonal sources will be used operating at the one-third Octave band center frequencies of 1.25, 2.5, and 5.0 kHz, respectively. Figure 6.10 shows the corresponding reconstruction results. The non-moving source (red line) clearly shows the most accurate and clean reconstruction results according to the visual inspection. However, other reconstruction results do not give conclusive evidence for deciding the best available scheme (either zeroth order, linear interpolation, barycentric, or RBF) used to interpolate pressure time signals in the receiver plane.

A more accurate quantitative analysis is thus provided in Figure 6.11. It can be seen that the reconstruction based on the zeroth-order interpolation scheme shows low localization error between 1.25 and 5 kHz, especially at higher frequencies. In comparison, the linear or barycentric based reconstruction schemes show significantly higher location errors below 2.5 kHz. The four methods have similar errors below 3.15 kHz in terms of the source strength prediction. However, the zeroth-order interpolation scheme shows a lower error in reconstructing the source strength at high frequencies. This finding is in accord with the error analysis results in the receiver plane, see Figure 6.9. The RBF-based reconstruction yields the best strength reconstruction results below 3.15 kHz. Although the zeroth-order interpolation scheme shows more significant errors for the receiver plane analysis at lower frequencies, its use does not show much higher errors in the sound source reconstruction. In addition, the CVX holographic reconstruction confirms that the zeroth-order interpolation scheme gives the slowest growth rate in predicting mean errors when frequency increases. Hence, it has demonstrated its superiority for reconstructing sound sources at 5 kHz when the results are compared with other interpolation schemes.

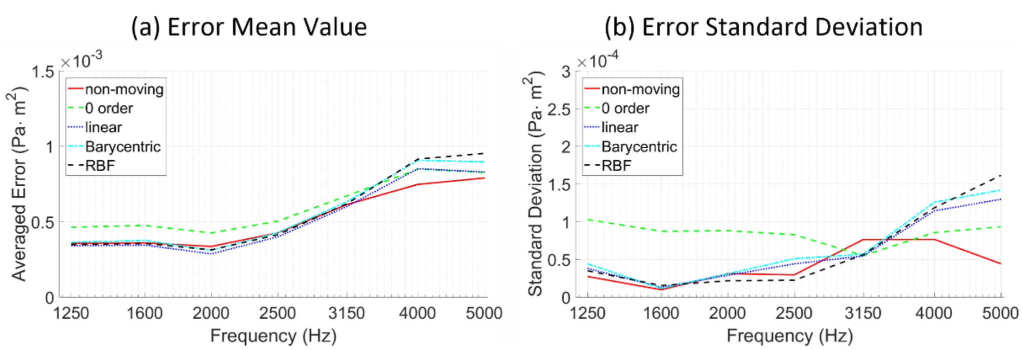

Figure 6.9. Receiver Plane Error, Circular Array

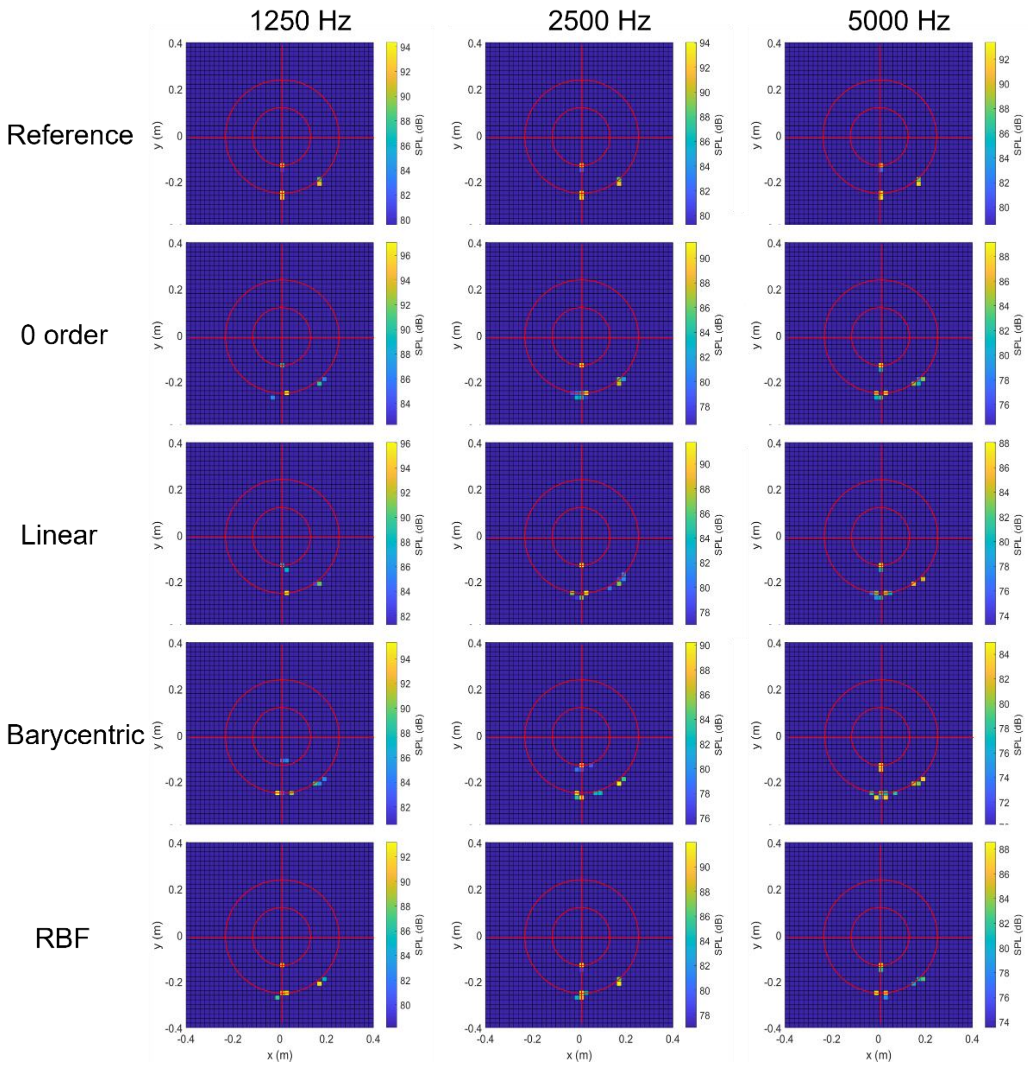

Figure 6.10. CVX Holographic Reconstruction of Source Plane, Circular Array

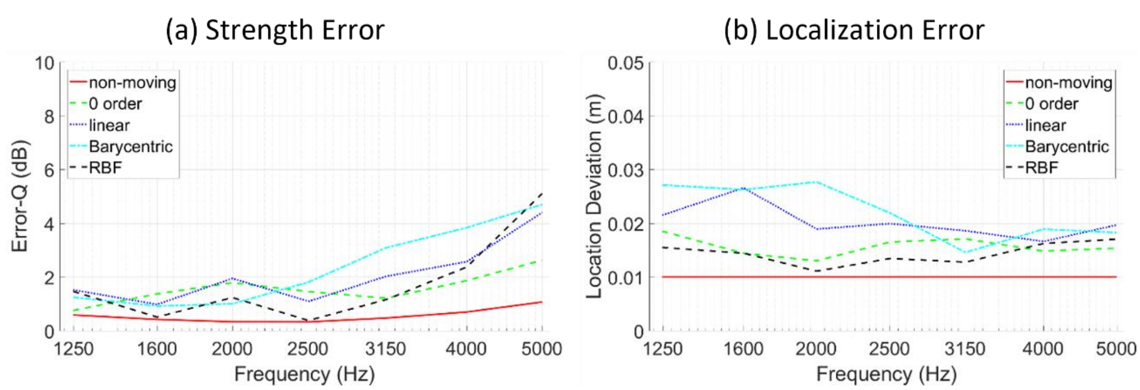

Figure 6.11. CVX Holographic Reconstruction Error, Circular Array

The simulated data for Array 2 is analyzed following the same steps as shown earlier for Array 1. The linear interpolation scheme has not been used for the data analysis because its implementation is rather inconvenient for an arbitrary array. Therefore, only the zeroth order, barycentric, and RBF interpolation schemes are considered. It can be seen that the zeroth interpolation scheme has the slowest growth rate for the mean errors. More detailed analyses show that the three interpolation schemes have comparable mean errors when the source frequency is below 2.5 kHz, while the RBF scheme has shown a much higher growth rate for the mean errors at high frequencies. When comparing the mean errors between the two arrays, it can be observed that Array 2 has a significantly larger error than that of Array 1 if the barycentric or RBF interpolation schemes are performed. On the other hand, the zeroth-order interpolation schemes show comparable results implemented with either array configuration.

Figure 6.13 displays the holographic reconstruction using Array 2. A visual inspection of the results has suggested that the zeroth-order interpolation scheme shows a cleaner source reconstruction with fewer ghost sources. In the reconstruction process, the barycentric interpolation scheme leads to a considerable number of ghost sources at all three frequencies. The results for the source localization show that both zeroth order and RBF reconstruction schemes have lower localization errors than the barycentric scheme. More specifically, the zeroth-order scheme has demonstrated its advantage in the results for source localization at all frequencies. In terms of the source strength predictions, it can be seen that the zeroth-order and barycentric schemes show higher mean errors for the source frequency below 3.15 kHz. The RBF and barycentric schemes show higher mean errors than the zeroth order scheme at a higher frequency. This trend matches quite well with the receiver plane analysis discussed earlier. The reconstruction results also confirm that the zeroth-order scheme shows an enhanced accuracy in mean error when the source frequency goes higher.

From the results obtained from both Array 1 and Array 2, it can be validated that the zeroth-order scheme works well for synthesizing the monochromatic VRA signals. The CESM holography reconstruction using the zeroth-order interpolated data predicts the sources' strengths and locations better. The zeroth-order scheme usually leads to higher mean errors at the receiver plane at lower frequencies. However, the corresponding mean errors in the holography reconstruction are similar to those generated by other interpolation schemes. At a frequency higher than 3.15 kHz, the zeroth-order scheme shows not only a lower interpolation error but a reduced error in the source reconstruction than the other interpolation schemes, especially for the results shown in Array 2.

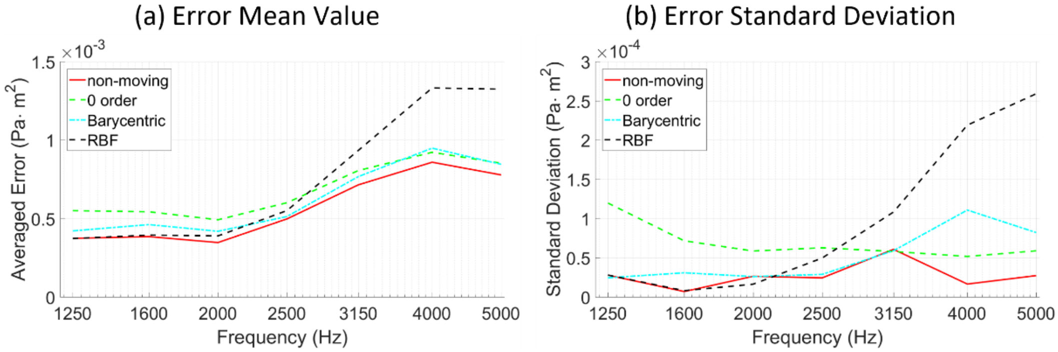

Figure 6.12. Receiver Plane Error

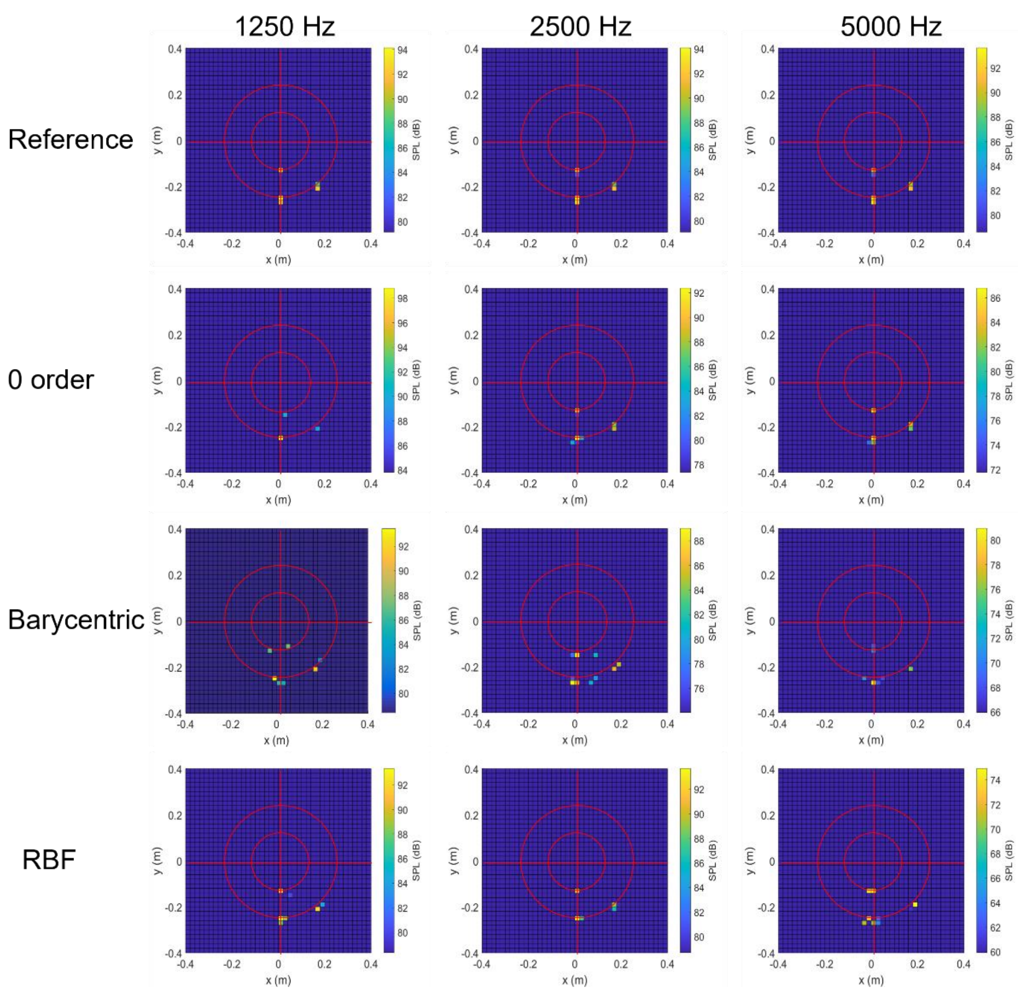

Figure 6.13. CVX Holographic Reconstruction of Source Plane, Irregular Array

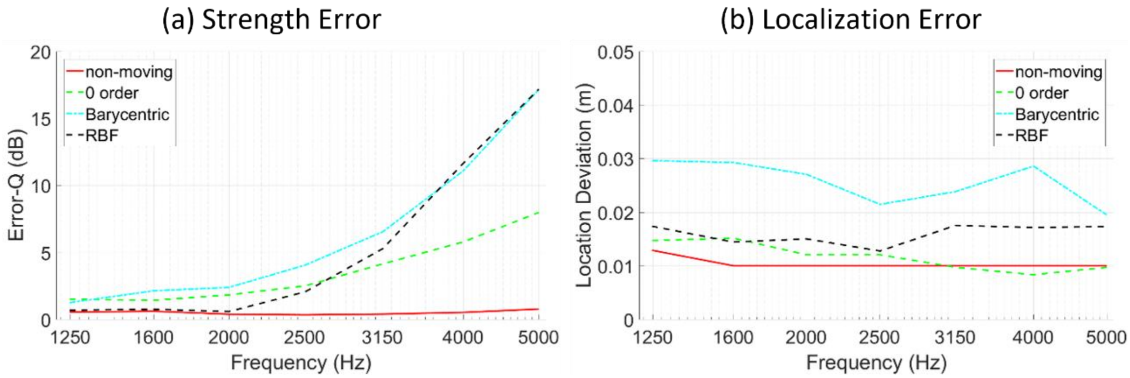

Figure 6.14. CVX Holographic Reconstruction Error, Irregular Array

The comparable simulations have also been conducted for the broadband sources, but their findings are rather similar to the tonal sources. Nevertheless, it is also of our interest to examine the effect of the starting time and the source location in a VRA signal-based source localization scheme. Indeed, the relative locations of the VRA are different if the time domain signals are transformed into frequency domain with different starting times. However, the relative locations between the microphones and the sources within the VRA remain unchanged. In addition, the interpolation error in the VRA is a periodic function in terms of the rotation cycles. It, therefore, follows that the starting location of the reconstruction process does not affect the accuracy of the holography reconstruction. Extensive simulations have been conducted to confirm this observation, and their numerical results are not presented here for succinctness.

6.2.4 Holography Results for Broadband Signals

In this section, the time domain VRA based CESM holography is further validated by broadband signals. The broadband signals are processed with all four interpolation methods. The holographic reconstruction based on VRA signals and reference stationary sources signals are compared with the theoretical source strength for error quantification. The receiver plane errors are not analyzed for the white noise signal because the white noise is not deterministic, and the theoretical virtual rotating array signals cannot be predicted. Therefore, only holographic reconstruction errors are analyzed in this section. As shown in Figure 6.15 and Figure 6.17, three frequencies at the center of 1/3 Octave bands (1250Hz, 2500Hz, 5000Hz) are selected for holographic visualization. In addition to the source visualization results using CSESM holography, the reconstructed source strength and localization error results for all 1/3 Octave bands center frequencies from 1250Hz to 5000Hz are calculated and shown Figure 6.16 and Figure 6.18.

As shown in Figure 6.15, the first row shows the holographic reconstruction results of the non-moving case. The second, third, fourth, and fifth rows show the source plane reconstruction using the signal interpolated by 0 order interpolation, linear interpolation, Barycentric interpolation, and RBF interpolation. It can be visually confirmed that the source location reconstructed by VRA signals distribute close to the theoretical locations. However, the visual inspection of the reconstructed source does not show a clear difference between different VRA methods. Therefore, a more accurate quantitative analysis is shown in Figure 6.16. All four VRA-based reconstructions show close capabilities in terms of source localization. However, 0 order interpolation shows better results than linear and Barycentric interpolation for most frequency ranges. In addition, 0 order interpolation also shows the lowest error among all four interpolation schemes at 5000 Hz. The source strength prediction analysis shows that 0 order, linear, RBF interpolation based reconstructions show close source strength error from low to high frequency, while Barycentric interpolation based reconstruction shows higher source strength prediction error. The results match with tonal signal simulation results and confirm that 0 order interpolation works well for the VRA signal synthesis, especially at higher frequencies.

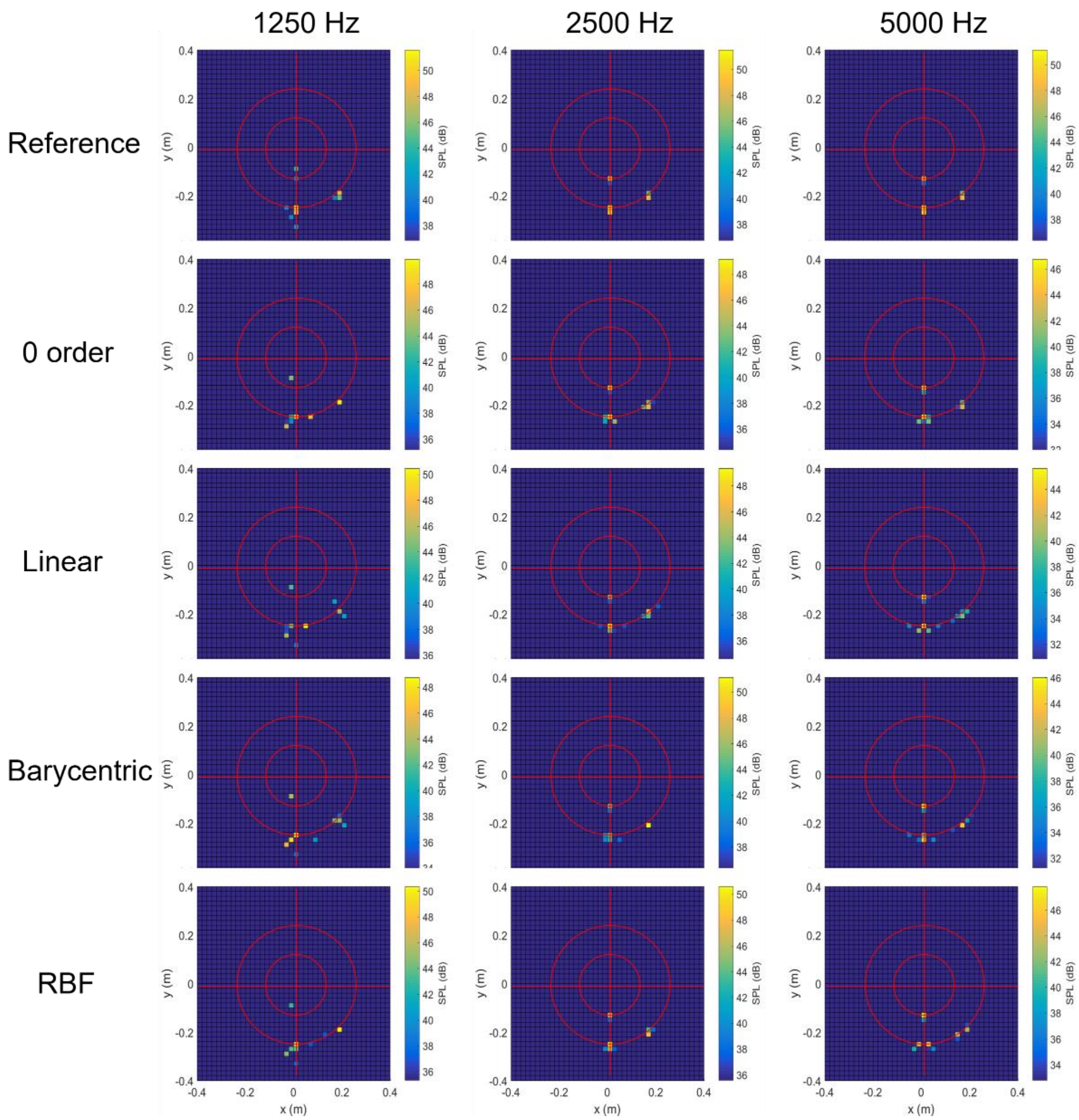

Figure 6.15. CVX Holographic Reconstruction of Source Plane, Circular Array

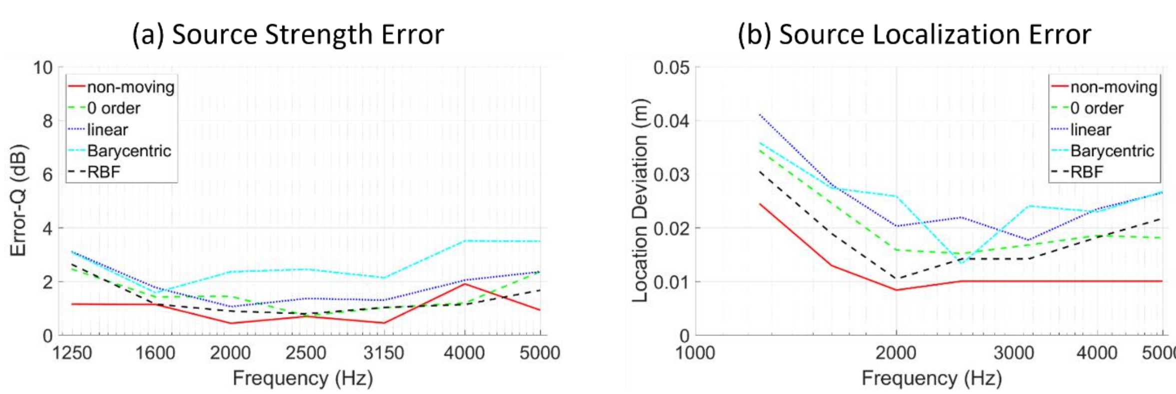

Figure 6.16. CVX Holographic Reconstruction Error, Circular Array

After the analysis with a circular array, the broadband rotating source holography reconstruction results are shown for the irregular array. The performance of the 0 order interpolation, Barycentric interpolation, and RBF interpolation is compared. As shown in Figure 6.16, the first row shows the holographic reconstruction results of the non-moving case. The second row shows the 0 order interpolation results, the third row shows the Barycentric interpolation results, and the fourth row shows the RBF interpolation results. Generally, it can be visually confirmed that the source location reconstructed by all three VRA interpolation and the non-moving case distribute close to the theoretical source location, which is expected. It can be visually observed that 0 order VRA based reconstruction and stationary reference reconstruction has a clean source region at all three frequencies. However, 0 order and Barycentric interpolation based reconstruction show apparent location deviation for S3 prediction at low frequency. The quantitative results also show the same at low frequency, in which 0 order interpolation and Barycentric interpolation based reconstruction show slightly higher localization error. However, with the increase of frequency, 0 order VRA based holography shows lower error while Barycentric based holography shows higher localization error. Regarding the source strength reconstruction, 0 order interpolation and Barycentric interpolation show a higher error below 2500Hz. However, 0 order interpolation based holography shows a significantly lower error growth rate than the other two interpolation schemes as frequency goes up. It can be seen that the broadband signal results of the irregular array also match with tonal signals results well.

Generally, the reconstruction of broadband and tonal signals shows similar source localization and strength reconstruction trends. Similar to the tonal signal results, the irregular array interpolation reconstruction shows higher error than using a circular array for broadband signals, especially at higher frequencies. However, 0 order interpolation shows its advantage, with consistent error regardless of the array configuration. It can be concluded from the simulation signal analysis that zeroth order interpolation based holography prediction has comparable errors as other interpolation scheme based reconstruction at a lower frequency. Furthermore, with the frequency increase, zeroth-order interpolation performs better than other schemes, especially with an irregular array.

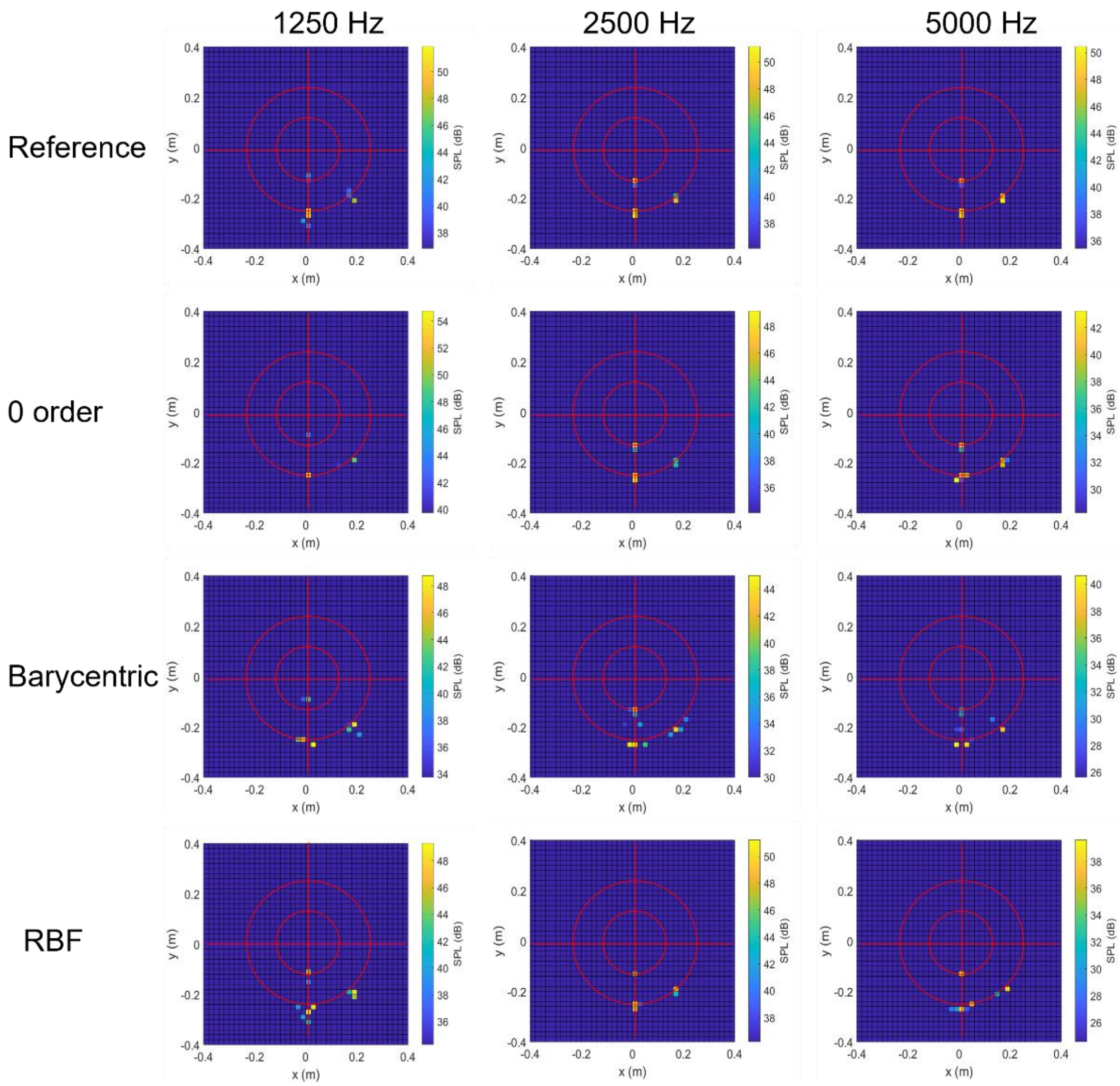

Figure 6.17. CVX Holographic Reconstruction of Source Plane, Irregular Array

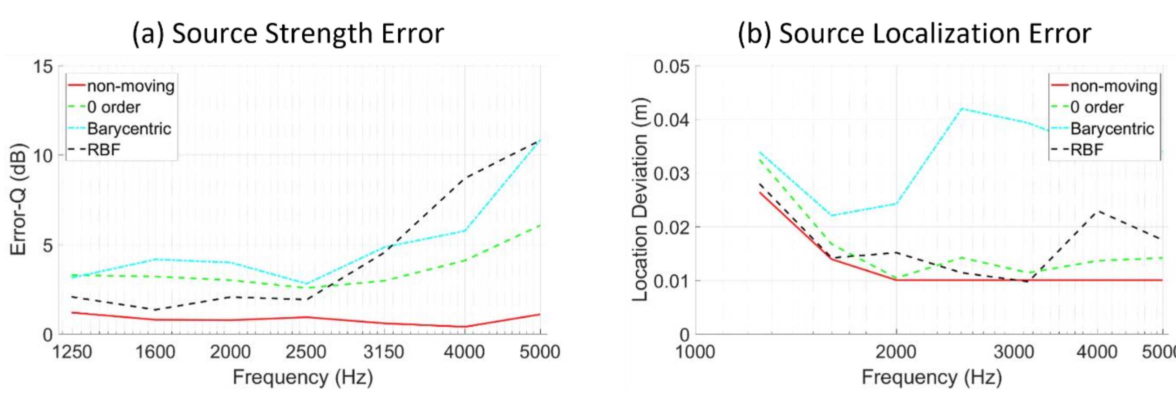

Figure 6.18. CVX Holographic Reconstruction Error, Irregular Array

6.3 Numerical Experiment for Frequency Domain Virtual Rotating Array

In this section, the frequency domain virtual rotating array based source reconstruction is validated against the same cases. The benchmark B11b case is simulated and processed with frequency domain de-Dopplerization. Both tonal and broadband rotating sources are investigated. FS-VRA and Op-VRA-based holography performance are studied by comparing the source localization and source strength prediction accuracy. In addition to the source strength, the relative strengths of sources are also calculated and compared. It should be noted that Array 2 is referred to as optimized array in this section.

6.3.1 Simulation Signals and Processing Procedures

The numerical simulations are based on three types of source signals (see Table 6.3). Case 1: all sources are monochromatic with a single frequency of 2.5kHz; Case 2: three tonal components at 2.475 kHz, 2.5 kHz, 2.525 kHz are emitted by all sources; and Case 3: all sources emit white noise for frequency ranging from 0.5 to 10kHz.

As shown in the last section for time-domain VRA signal processing, the data processing procedures differ between tonal and broadband cases. For the frequency domain VRA process, the signal processing parameters are also different for tonal and broadband sources, shown in Table 6.2. The array signals are transformed to the frequency domain using Fast Fourier Transform (FFT) for tonal source cases without averaging. One second of data is used, which results in a frequency domain resolution of 1 Hz. First, the VRA methods are performed in the frequency domain to the selected frequency (2500Hz for the simulated case). Then, the VRA signal at a particular frequency on the virtual rotating array can be used for holography processing. For the broadband case, the data are handled by different procedures. Firstly, the array data of 10 seconds in time length are transformed into the frequency domain using FFT. Then, the frequency domain VRA procedures are performed to the FFT values. Finally, the newly generated FFT values for VRA are inversely transformed into the time domain. The broadband power spectra of the time history on the virtual rotating array are calculated with a 4096-point Hanning windowed FFT block and a 50% overlap between two adjacent blocks (Proakis et al., 1992). Then, acoustical holography can be performed to the spectrum of the VRA signals at the selected frequency. For the holography reconstruction, the reconstructed source region is a 0.8 m by 0.8 m rectangular plane with 41 by 41 uniformly distributed grids.

Table 6.3. Source Signal Parameters, Frequency Domain VRA Processing

	Case 1	Case 2	Case 3
Source Signals	• S1:2500Hz • S2:2500Hz • S3:2500Hz	• S1:2475Hz/2500Hz/2525Hz • S2:2475Hz/2500Hz/2525Hz • S3:2475Hz/2500Hz/2525Hz	• S1: white noise • S2: white noise • S3: white noise
Source Strength	• S1:100dB@2500Hz • S2:97dB@2500Hz • S3:94dB@2500Hz	• S1:100dB@2500Hz • S2:97dB@2500Hz • S3:94dB@2500Hz	• S1: 99.4dB • S2: 96.4dB • S3: 93.4dB
Time Duration	2s	2s	10s
Sampling Rate	32768Hz	32768Hz	32768Hz

Table 6.4. Data Processing Parameters for Simulation

	Case 1	Case 2	Case 3
FFT Block Size	32768	32768	4096
FFT Block Overlap	0	0	50% Hanning
Source Plane Grids	41*41	41*41	41*41
Source Plane Grid Size	0.02m*0.02m	0.02m*0.02m	0.02m*0.02m

6.3.2 Holography Reconstruction for Tonal Sources

The array signals are processed using the frequency domain Fs-VRA and Op-VRA methods. The reconstruction results due to a stationary source where the same source configuration (see Figure 6.4 for the source locations) is used to benchmark the performance of the holographic results for the rotating sources, S_1, S_2, and S_3. The Op-VRA method is applied in Array 2 (optimized array) and Array 1 (circular arrays) for the holographic reconstruction of sources. This additional set of calculations allows an assessment of the performance of using different arrays of a virtual microphone in the receiver plane.

The sound pressures can be predicted in the source region by employing the WBH on the simulated dataset in the receiver plane. The total source strength is then calculated by integrating the reconstructed sound pressure levels (SPLs) within the source plane. Figure 6.19 displays the SPL contour plots of the WBH reconstruction results of the predicted SPLs. Table 6.5 summarizes the reconstructed source strength according to the two VRA methods using the simulated data in Array 1 and Array 2.

As shown in Figure 6.19, the first column shows the holographic results for Case 1, and the second column shows those results for Case 2. Both VRA methods show holographic reconstruction with high accuracy for the single tonal case (i.e., Case 1). Not only are the sources' locations predicted correctly, but the reconstructed source strengths from different methods are within 1 dB from the input source strength (see Table 6.5). Furthermore, the results from Array 2 using Op-VRA also show a high level of accuracy in source reconstruction, which is also within 1 dB error compared with the input values. The simulation results for reconstructing the tonal source show that the WBH works well with the Fs-VRA method. In addition, the source reconstructed with the Op-VRA method demonstrates that the sideband summation can be used to de-Dopplerize a rotating tonal source with high accuracy. These comparison results validate Eq. 5. 34 for predicting the sound fields without using the Fourier summation method given in Eq. 5. 31.

For the holographic reconstruction of Case 2 at 2.5 kHz (see the right column of Figure 6.19), the locations of three sources can be predicted quite well with both VRA methods for the holographic reconstruction of the source region. More specifically, the source localization results for the Op-VRA method applying on the circular arrays (Array 1) and the optimized array (Array 2) display reasonably good agreements with the input parameters. However, this is not the case for reconstructing the strengths of $S_1,\ S_2$, and S_3. The numerical simulations show that the Fs-VRA method and the reference case have a high level of agreement with the input source strengths, but the Op-VRA method underestimates the source strengths by as large as 4.5 dB in Array 2. A close examination of Eq. 5. 34 suggests that the Op-VRA method coherently sums all modal contributions from all rotating sidebands. This is a possible source of errors for predicting the absolute source strength using the Op-VRA method. There is an encouraging observation, in any case. By considering the simulation results, the relative source strengths $\Delta_1,\ \Delta_2$, and Δ_3. are given by (a) 0 dB, -2.6 dB and -5.6 dB for Array 1, and (b) 0 dB, -3.3 dB and -6.5 dB for Array 2. The predicted relative source strengths are within 0.5 dB from the input parameters. It is noteworthy that the ability to predict the relative source strengths accurately is of practical interest when the Op-VRA method is used to diagnose noise sources.

In summary, Op-VRA has the advantage of reducing the computational time and a reasonably good capability in source localization of tonal sources. Moreover, despite its weakness in reconstructing the magnitudes of the source strengths, the Op-VRA method can still give a good prediction of the relative source strengths among noise sources in the region of interest.

Table 6.5. Wideband Holography Source Strength at 2500Hz

	Case 1			Case 2		
	S1	S2	S3	S1	S2	S3
True Values	100	97.0	94.0	100	97.0	94.0
Reference Array-1	99.7	96.5	93.1	99.7	96.5	93.1
FS-VRA Array-1	99.7	97.1	93.3	99.7	97.1	93.3
Op-VRA Array-1	99.7	97.1	93.4	95.8	93.2	90.2
Op-VRA Array-2	99.4	96.6	93.4	95.5	92.2	89.0

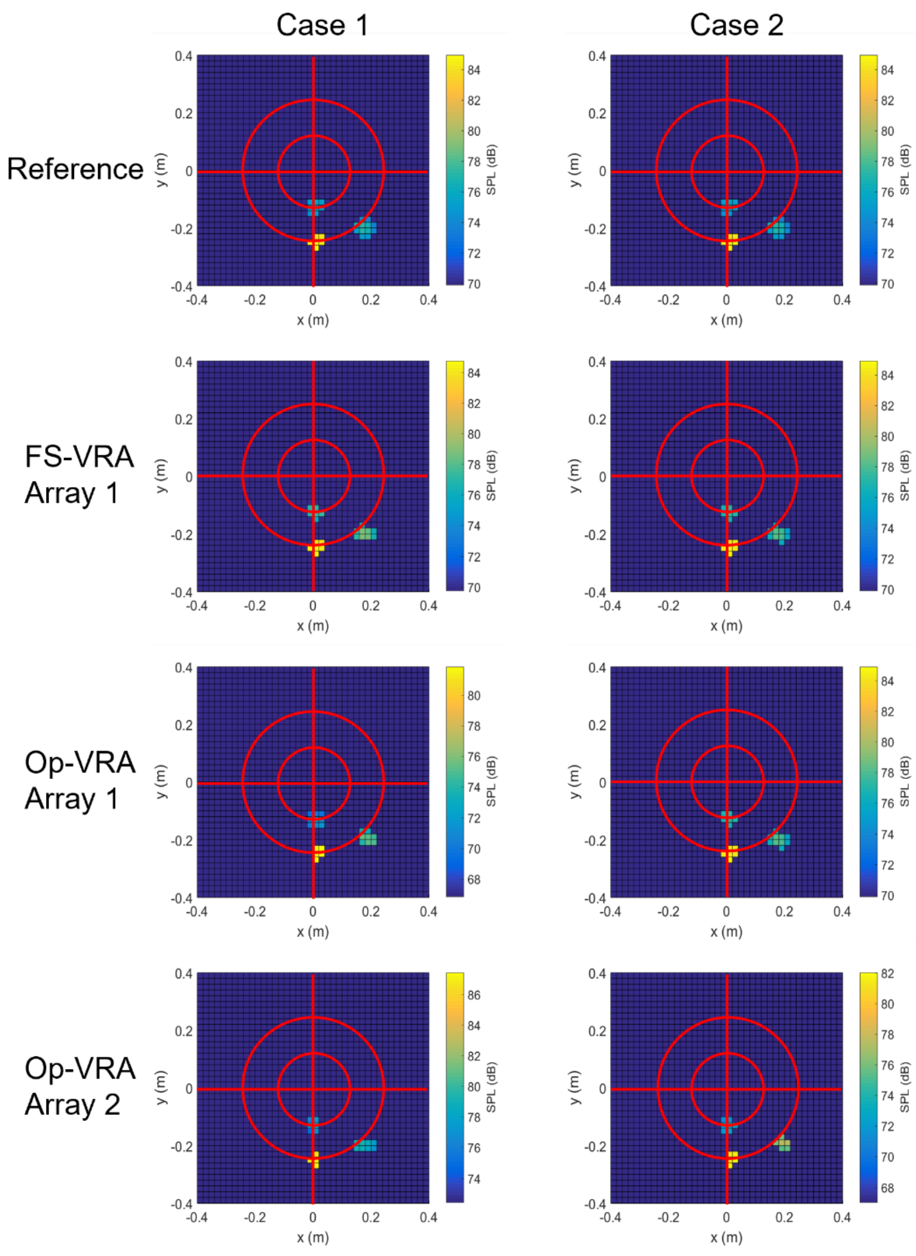

Figure 6.19. Wideband Holography Reconstruction at 2500Hz

6.3.3 Holography Reconstruction for Broadband Sources

In this section, simulated broadband sources are investigated for studying the relative performance of the two VRA methods. The WBH reconstruction results are shown in Figure 6.20. Simulation results at the center frequency of 3 one-third Octave bands (1.25 kHz, 2.5 kHz, 5 Hz) are selected for visualization in the source plane. Again, the Fs-VRA and Op-VRA results are compared to the reference (baseline) case where the holographic reconstruction of the stationary sources and non-moving circular arrays is considered. In addition to the contour plots of the simulated SPLs, the strengths for S_1, S_2, and S_3, are also calculated for the center frequency of all one-third Octave bands between 1.25 and 5 kHz, see Figure 6.22. The dominant source is usually of more interest than other weaker sources for most noise control tasks. Therefore, the relative source strength is also an essential criterion for the diagnostics of noise sources in the region of interest. A comparison of the relative source strength spectra results will be presented.

As shown in Figure 6.20, the first row shows the holographic reconstruction results of the reference case. The second row displays the reconstruction results using the Fs-VRA method. The third and fourth row shows the corresponding simulations where the Op-VRA method has been used with the circular arrays and the optimized array in the receiver plane. It can be visually confirmed from the SPL contour plots that the reconstruction using the two VRA methods match pretty well with the reference case at 1.25 kHz. In addition, the Op-VRA method enables an optimized array to be used, which enhances the accuracy of source localization at the low-frequency regime. However, the WBH reconstruction for all four cases shows large source areas in the contour plots at 1.25 kHz. This leads to a higher level of uncertainty on the specific locations of the noise sources. The two VRA methods using circular arrays produce good source locations predictions at the mid-frequency regime, and Op-VRA uses the optimized random array. Both Fs-VRA and Op-VRA methods give clean and accurate results in the source localization at the high frequency regime. It should be pointed out that the holographic reconstruction using the optimized array shows more ghost sources around the region of interest at high frequency. However, it can still provide a reasonable estimation of the source locations. The source localization using either VRA method generally exhibits good agreements with the baseline reconstruction for a broad range of frequencies. These reconstruction results of broadband sources endorse the effectiveness of the Op-VRA method in reconstructing the locations of rotating sources.

Notably, the WBH for source reconstruction has a notable weakness in resolving low-frequency sources: the source localization is not as accurate for the source with high frequencies. This weakness is confirmed with the results shown in the first column of Figure 6.20, in which the SPL contours for the one-third octave frequency band centering at 1.25 kHz are presented. This reconstruction inaccuracy is a general characteristic highlighted in an earlier study on the WBH method (Hald, 2016). The low-frequency issue is not related to the signal generation process of the two VRA methods. Therefore, it is beneficial to consider an alternative method, i.e., the hybrid method (Shi et al., 2019), to improve the resolution of the source reconstruction process at low frequencies. The hybrid method, which combines convex optimization and the WBH approach, is employed for sound source visualization at low frequencies. The hybrid method can reconstruct sound sources with smaller separation distances than those offered by WBH and other beamforming methods. The results are exhibited in Figure 6.21. The SPL contours confirm that the regions of the reconstructed sound fields are more compact, see Figure 6.20 and Figure 6.21. The simulation for the reference case shows a compact source region with a high reconstruction accuracy. Therefore, the holographic reconstruction based on the Fs-VRA method matches well with the reference case. Suppose circular arrays are used in the receiver plane. In that case, the Op-VRA method has a somewhat lower quality in source localization by comparing the 2^{nd} and 3^{rd} columns of the contour plots in Figure 6.21. Nevertheless, the simulation results improve when the optimized array is used instead of the circular arrays; see the simulated results in the 4^{th} column of Figure 6.21. These comparisons justify using the sideband summation using optimized array (Op-VRA) in favor of the Fourier summation (Fs-VRA) method because of its improved computational speeds and a more convenient arrangement in placing receivers.

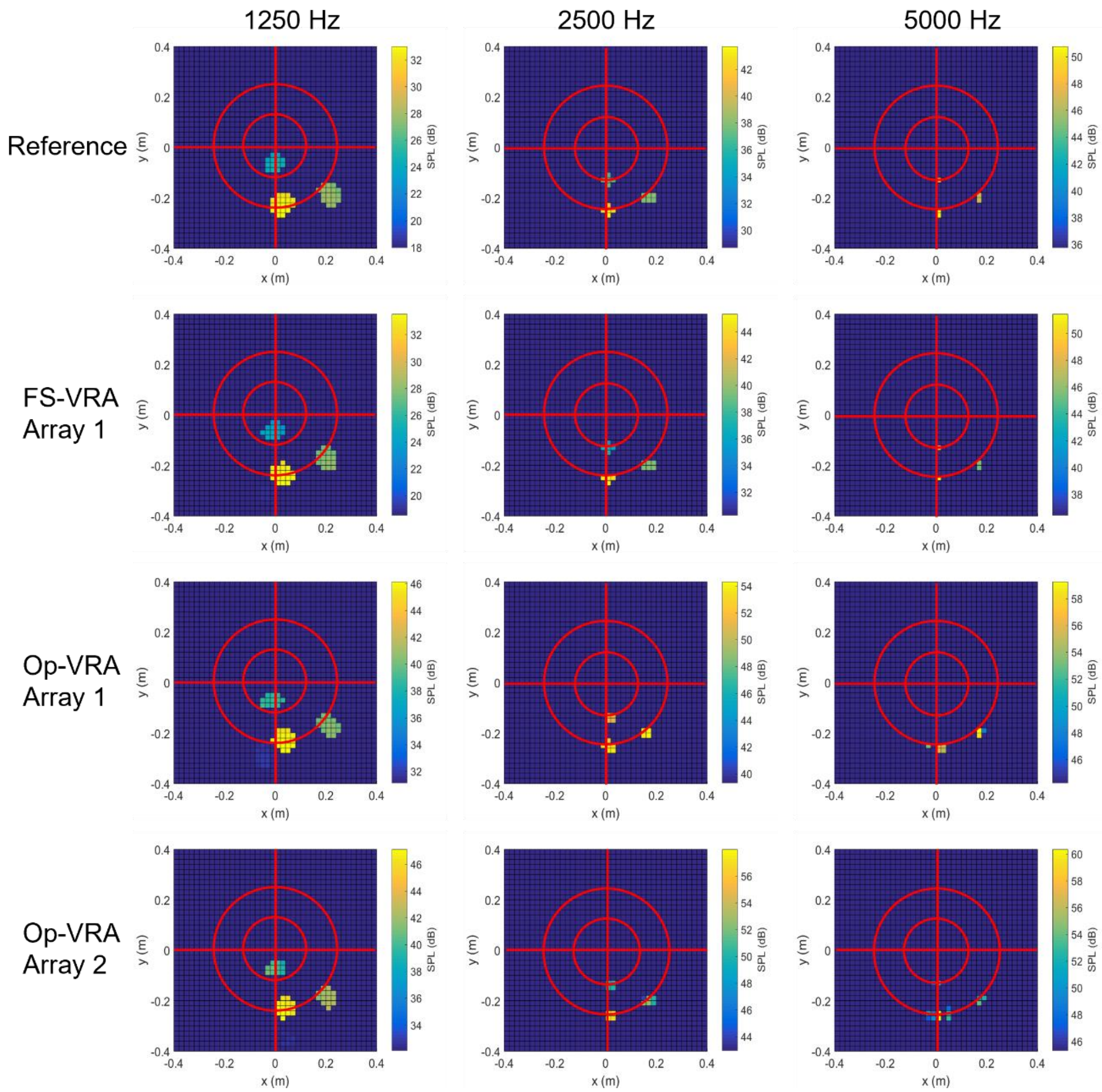

Figure 6.20. Wideband Holography Reconstruction for Broadband Sources

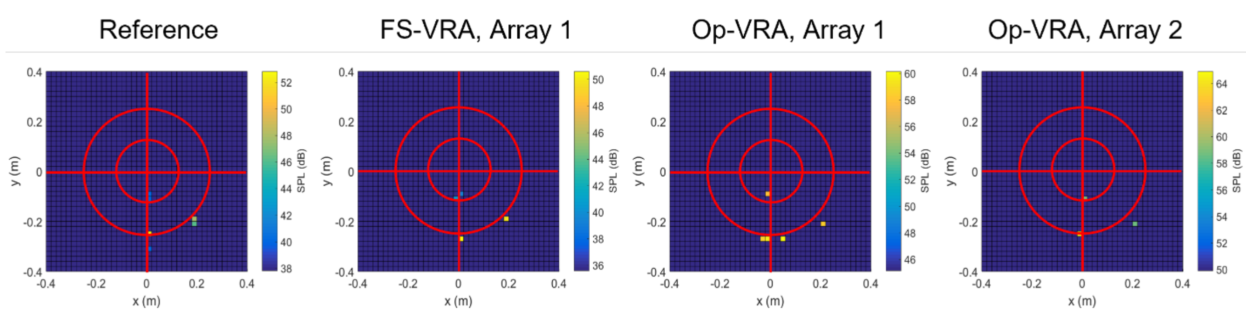

Figure 6.21. Hybrid Holography Source Plane Reconstruction

In the next step, the accuracy in source strength reconstruction is analyzed quantitatively by comparing the predictions for the frequency ranging from 1.25 to 5.0 kHz. It is observed from Figure 6.22 that the use of the Fs-VRA method in conjunction with WBH has led to a smaller error in predicting the source strengths. Typically, the Fs-VRA predictions are within 2 dB from the reference reconstruction case simulations. However, the Op-VRA prediction results do not have this level of accuracy. Comparable simulations at the same frequency range indicate much larger discrepancies (10 - 15 dB) when the results are compared with the reference reconstruction case. This is expected because of the broadband nature of the source: a simple sideband summation, see Eq. 5. 34, does not accurately capture the contributions around the reconstruction frequency of $\omega \pm m\Omega$. These discrepancies in predictions are relatively independent of the receiver array used in the analysis. The respective simulations for Array 1 (circular arrays) and Array 2 (optimized array) have comparable source strengths, which are well within 3 dB of the two VRA methods over the frequency range of interests.

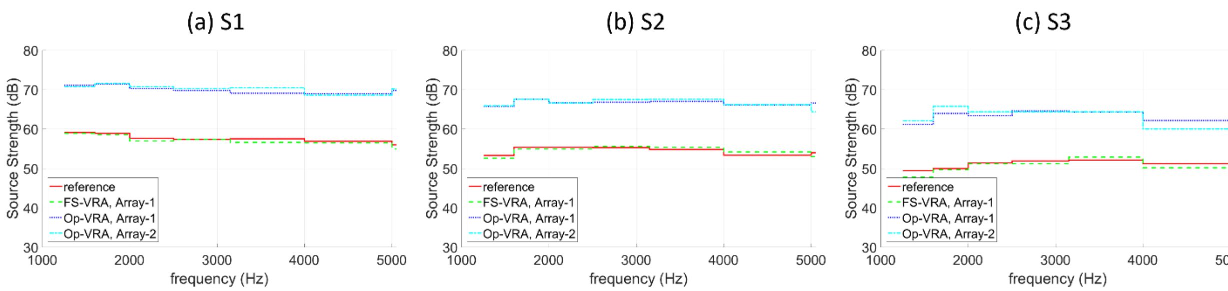

Figure 6.22. Source Strength Prediction by Wideband Holography for Broadband Sources, 1250Hz-5000Hz

The use of the Hybrid method in the source reconstruction does not improve the accuracy in estimating the source strength, see Table 6.6. It is because use of the sideband summation in predicting the rotating sound fields is the main reason for causing these discrepancies. Nonetheless, it can be seen that the Hybrid method can reconstruct source strengths accurately if the Fs-VRA method is used. For the Op-VRA method, the predicted source strengths are significantly higher (between 10 and 13 dB) than the reference cases, but the predicted relative strengths have comparable results. The findings of these simulation results for the hybrid method are in line with the findings of the WBH reconstruction results. Therefore, it further strengthens the case for using the optimized array in the holographic reconstruction of sources if the relative source strength is required.

Table 6.6. Hybrid Holography Source Strength Reconstruction

	S1	S2	S3
Reference Array-1	57.0	50.8	46.2
FS-VRA Array-1	57.0	50.8	45.6
Op-VRA Array-1	68.5	63.5	59.0
Op-VRA Array-2	67.6	63.0	60.2

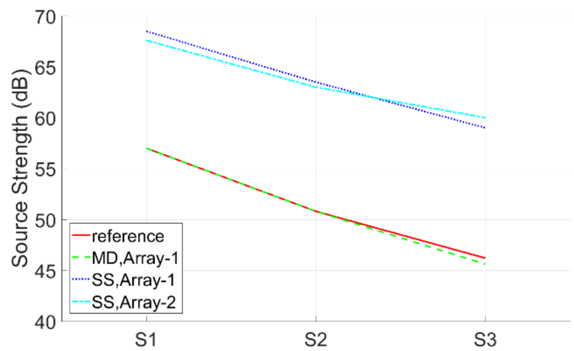

Figure 6.23. Hybrid Holography Source Strength Reconstruction

Generally speaking, the Op-VRA method does not provide accurate source strength reconstruction, see Figure 6.22. Nevertheless, its capability for estimating of the relative source strengths is as good as the Fs-VRA method. This is demonstrated in Figure 6.23 where a plot of the relative source strengths for S_1, S_2, and S_3 are presented for the broadband sources.

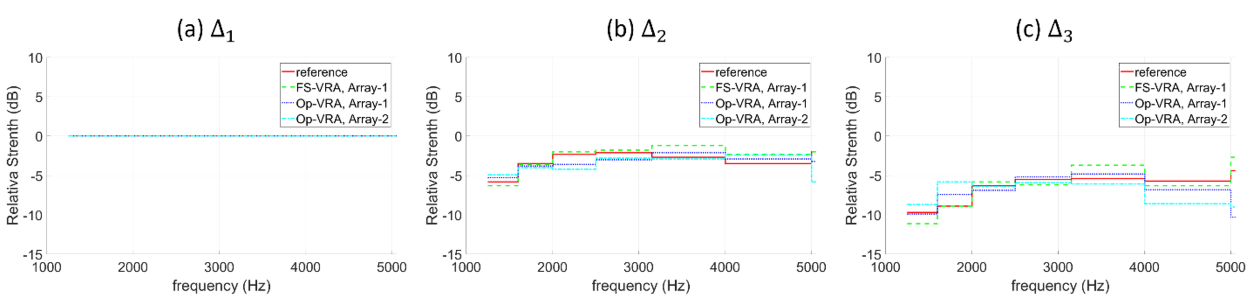

Figure 6.24. Source Strength Difference for Broadband Sources, 1250Hz-5000Hz

From the above simulation results, it has been demonstrated that the frequency-domain VRA signals can be used for localization of the near-field rotating sources. The modal decomposition algorithm uses the VRA to de-Doppler input for the CS-NAH process. The simulation results match well with the reference results in terms of source localization. Furthermore, an efficient sideband summation can also be used to de-Doppler the array signals from rotating sources with high accuracy for monochromatic sources. For broadband sources, the holographic reconstruction using the Op-VRA signals can localize sound sources accurately, but the source strengths' prediction is less satisfactory. However, the relative source strengths between different sources can be estimated with high accuracy using the sideband summation algorithm. Another advantage of using the sideband summation VRA algorithm is its capability of using an optimized array, which improves the source localization performance. The Op-VRA method is also much more efficient in the required computational efforts when its simulations are compared with that of the Fs-VRA method. For example, to perform a typical 64-channel VRA signal synthesis with a time length of 10 seconds on a typical personal computer on the MATLAB platform, the Op-VRA method only requires 4 seconds, while the Fs-VRA method requires 12 seconds. It has also been shown that the source localization accuracy at low frequencies can be improved significantly by using the hybrid in the compressive sensing holography.

6.4 Comparison of Computation Efficiency for VRA Methods

In this section, the computational efficiency for VRA interpolation is compared. MATLAB coding is used for the VRA signal generation. The simulation setup is shown in Table 6.8. A 10-seconds of 64-channel circular array data with 32768 Hz sampling rate are processed with four time-domain and two frequency-domain VRA methods.

The computational time is shown in Table 6.7, and it is evident that time-domain 0 order interpolation has the highest efficiency. Then, the time domain linear interpolation has the second-highest efficiency. The frequency-domain direct sideband summation also has high efficiency. Furthermore, time-domain Barycentric interpolation and frequency modal decomposition have very close computational costs. The least efficient method is RBF interpolation because, for each time step, it involves the information from all microphones on an array.

Table 6.7. Computational Efficiency of Time Domain VRA Methods

	Computational Time (seconds)
Zerorth order interpolation	0.8
Linear interpolation	2.5
Barycentric interpolation	10
RBF interpolation (cubic)	25
FS-VRA	12
Op-VRA	4

Table 6.8. Simulation Setup for VRA Efficiency Comparison

	Computational Time (seconds)
Array	Array-1 (64 channels)
Sampling Rate	32768 Hz
Data Time Length	10 seconds

7. EXPERIMENTAL VALIDATION OF HOLOGRAPHY DEVELOPMENT AND APPLICATION

In this chapter, the validation of holographic reconstruction using the VRA signals will be performed using experimentally measured array signals. In this first section, the experimental setup is shown. In the second section, the experimental array data are processed with time-domain VRA methods, and the holography reconstruction is performed using the VRA signals. The holography reconstructions of both tonal and broadband sources are shown, and source strength reconstruction accuracy is analyzed. In the third section, the frequency domain virtual rotating array based holography is validated with the experimental signal following the same procedures as time-domain VRA validation. In the last section of the chapter, both new developments of time domain and frequency domain VRA utilizing irregular array are applied to the target of the current study, which is the unground pinion localization in the nested planetary gear.

7.1 Experimental Setup

This section introduces the experimental setup for examining the sound fields generated by a pair of rotating loudspeakers (see Figure 7.1), and the resulting signals were measured by a set of stationary microphones arranged either in (a) circular arrays or (b) an optimized array (see Figure 7.2). The indoor experiment was conducted in an anechoic chamber with an approximate size of $3.6\,m \times 3.6\,m \times 3.6\,m$. The distance between source rotating plane and array plane is 0.45m for all experiments.

Two wireless loudspeakers (Bose Soundlink Micro Bluetooth) with a driver size of 0.040 m were used for the sound generation. Each loudspeaker was mounted on a rotating arm at a radial distance of 0.18 m from the center. The two rotating arms, made of wood, were aligned at apart. The arms were driven by a stepper motor (NEMA 34) with a maximum torque capability of 8.5 N-m. Figure 7.1 shows the sound generation system with the pair of loudspeakers labeled as S_1 and S_2 respectively. During the experiments, the stepper motor drove the wooden arms at a rotational speed of 180 rpm (3 Hz) in the counter-clockwise direction. Because of the rotational motion of the source, a sound pressure with the sidebands of $f \pm 3n$ Hz (where n is an integer) centering at the source frequency. A laser Tachometer (B&K Type 2981) was used to monitor the source rotation in real-time. The tachometer signals were fed into a desktop computer. A suite of computer software (B$\&$K Connect V2019.5) was used to record the signals and the acoustic data for subsequent processing. Figure 7.2 shows an array of receivers: (a) a set of 64-channel circular arrays and (b) an 84-channel optimized array. The geometrical configurations of these two receiver arrays are identical to Arrays 1 and 2 described in the preceding section; see Figure 7.3 for comparison. The distance between the source and receiver plane was chosen to be 0.45 m for all experiments presented in this work. One-quarter-inch microphones (B&K type 4958) were used as the receivers in the arrays for all measurements. Calibrations of all microphones in the receiver array were conducted prior to each set of experimental measurements.

The geometrical configurations of the sources and the corresponding parameters used in the experiments are displayed in Table 7.1. In the experiments, three types of acoustic input signals were used for driving the pair of loudspeakers where two tonal cases and one broadband case were considered. They are referred to as Cases A, B, and C, respectively. The choice of noise sources in the experiments was similar to the benchmark cases (Cases 1, 2, and 3, respectively). Therefore, in the last section, these benchmark cases were chosen to verify the CS-NAH schemes developed in Chapter 5.

In each of the 4 cases, the same input signals were fed simultaneously to the loudspeakers. Case A: monochromatic signals of 2 kHz frequency; Case B: 3 separate tones with the respective frequencies of 1.985, 2.0, 2.015 kHz; Case C: 7 separate tones with the respective frequencies of 1.25, 1.6, 2.0, 2.5, 3.15, 4.0, 5.0 kHz; Case D: white noise between 0.5 and 10 kHz. Case A was analogous to Case 1, in which the source's spectral components did not interfere with the rotating sidebands generated by the Doppler effect. However, an excitation frequency of 2 kHz was chosen in this set of experiments which was different from Case 1 in the numerical simulations. Case B was similar to Case 2, in which three tonal sources were used. However, two out of the three excitation frequencies (1.985 and 2.015 kHz) were chosen to interfere with the rotating sidebands. For Case D, uncorrelated white noise (broadband) signals were used as the input signals similar to Case 3 in the numerical simulations. The signal processing parameters for use in the experiments are identical to those used in the numerical experiments.

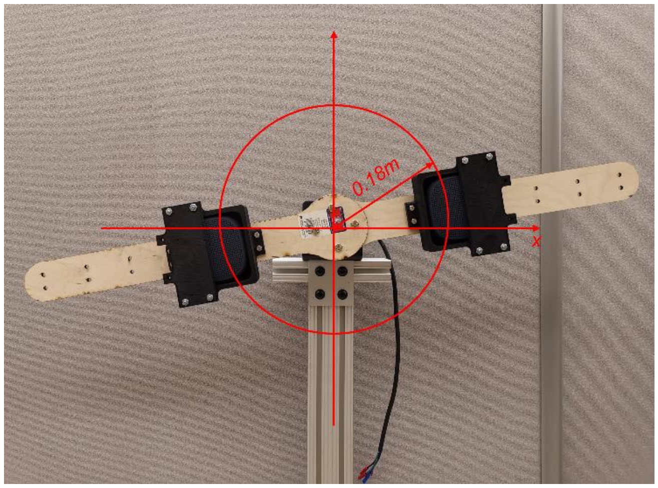

Figure 7.1. Experimental Setup, Source Plane Configuration

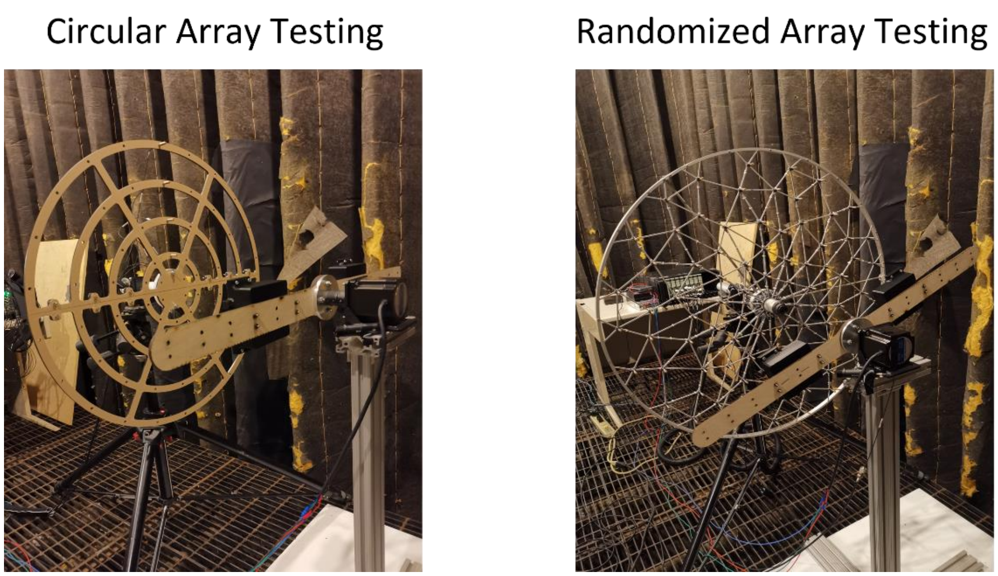

Figure 7.2. Experimental Setup, Measurement Configuration

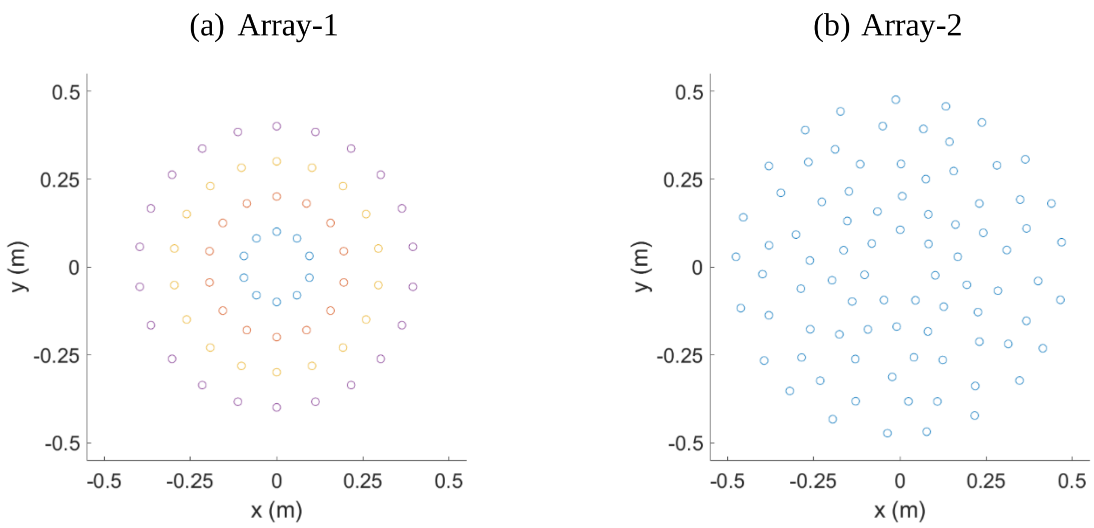

Figure 7.3. Array Geometry

Table 7.1. Source Configuration for Experiment

	Case 1	Case 2	Case 3	Case 4
Source Signals	• S1, S2: 2000Hz	• S1, S2: 1985Hz/2000Hz/ 2015Hz	• S1, S2: 1250Hz/1600Hz/2000Hz/2500Hz/ 3150Hz/4000Hz/5000Hz	• S1, S2: white noise
Rotational Speed	180 rpm	180 rpm	180rpm	180 rpm
Source Azimuth Angle	• S1: 0° • S2: 180°	• S1: 0° • S2: 180°	• S1: 0° • S2: 180°	• S1: 0° • S2: 180°

7.2 Experimental Validation of Time Domain VRA

7.2.1 Data Processing Procedures

The signal processing parameters for each case are shown in Table 7.2. The processing of the experimental data is the same as processing simulation data; however, the processing procedures are explained here again to make the document easier to understand. Firstly, time-domain VRA interpolation is performed to the measured array time history. Then, the array signals are transformed to the frequency domain using Fast Fourier Transform (FFT) for tonal source cases without time averaging. One second of data is used, which results in a frequency domain resolution of 1 Hz. Next, the frequency-domain signals are used for holography reconstruction at selected reconstruction frequency. The data are handled by different procedures than tonal signals for the broadband case. Instead of calculating FFT without averaging, the broadband power spectra of the interpolated data on the virtual rotating array are calculated with a 4096-point Hanning windowed FFT block and a 50% overlap between two adjacent blocks (Proakis et al., 1992). Then, acoustical holography can be performed to the spectrum of the VRA signals at the selected frequency. For the holography reconstruction, the reconstructed source region is a 0.8 m by 0.8 m rectangular plane with 41 by 41 uniformly distributed grids.

Table 7.2. Data Processing Parameters for Simulation

	Case 1	Case 2	Case 3
FFT Block Size	32768	32768	4096
FFT Averages	No Average	No Average	With Average
Segment Overlap	0	0	50% Hanning
Source Plane Grids	41*41	41*41	41*41
Source Plane Grid Size	0.02m*0.02m	0.02m*0.02m	0.02m*0.02m

7.2.2 Holography Reconstruction for Tonal Signals

In this subsection, the source distribution on a plane rotating together with the loudspeakers is visualized using the convex optimization holography for Case C, which are shown in Figure 7.4 and Figure 7.6. The first column shows the results for 1250Hz, the second column shows the results for 2500Hz, and the third column shows the results for 5000Hz. In addition to source visualization, the source strength at 1/3 Octave bands center frequencies between 1250Hz to 5000Hz are also calculated for all the cases, see Figure 7.5 and Figure 7.7. The non-moving sources reconstructed by CESM holography are used for the source strength error quantification.

In Figure 7.4, it can be visually observed that, for circular array reconstruction, there are significant ghost sources at low frequency (1250Hz) for VRA signal based reconstruction. At 2500 Hz, the reconstructed sources are more compact than 1250 Hz. In addition, the performance for all four VRA methods is comparable at 2500Hz. The source reconstructed by Barycentric interpolated signals at high frequency shows more ghost sources than the other three VRA methods. The experimental results confirm the effectiveness of the VRA methods in processing the experimentally measured tonal rotating source signals. Furthermore, it can be seen from the source localization results that zeroth order interpolation shows comparable results as other interpolation schemes.

Besides source locations, the source strength estimation accuracy at all 1/3 Octave band center frequencies between 1250Hz to 5000Hz is also analyzed for circular array results, shown in Figure 7.5. As mentioned in Chapter 5, the source strength is calculated by integrating the reconstructed source pressure of the source region on the holography plane. For the reconstruction of the tonal sources, it can be seen that the source estimation accuracy is very close for all four interpolation schemes below 2500Hz. Barycentric interpolation based reconstruction shows higher source strength estimation accuracy between 2000-4000 Hz. However, 0 order interpolation and RBF interpolation at high frequency shows the lowest strength error. Generally, the source strength prediction using a circular array with different interpolation schemes shows comparable accuracy across a wide range of frequencies. In particular, 0 order interpolation shows consistent results between 1250Hz to 5000Hz. The experimental results match with simulation results well for the tonal signals.

In addition to circular array results, irregular array results are also analyzed in this section, as shown in Figure 7.6. In addition, the source strengths at multiple 1/3 Octave band center frequencies are also calculated for all the cases (see Figure 7.7) to compare the VRA methods performance quantitatively.

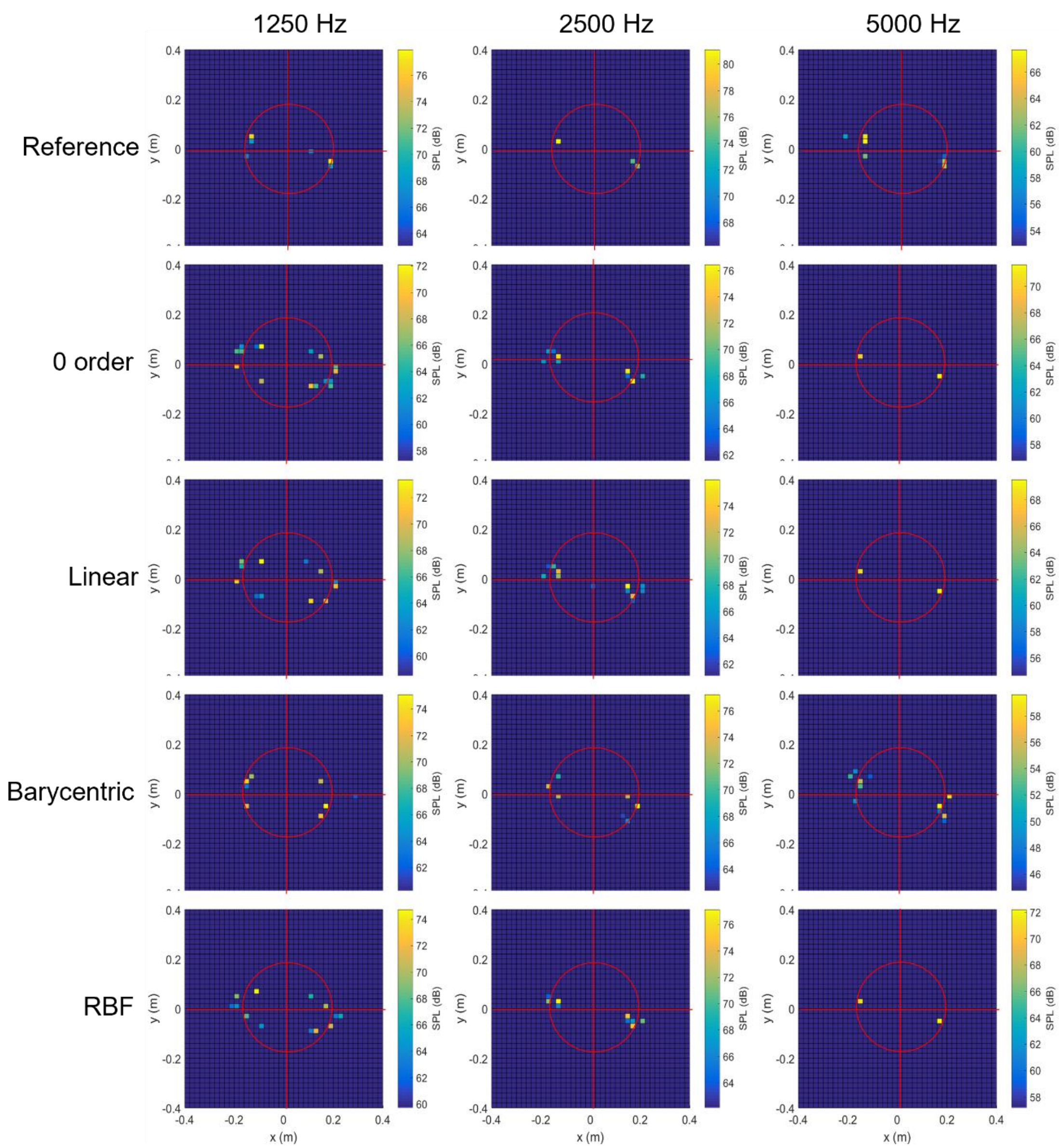

Figure 7.4. CVX Holography Reconstruction, Circular Array

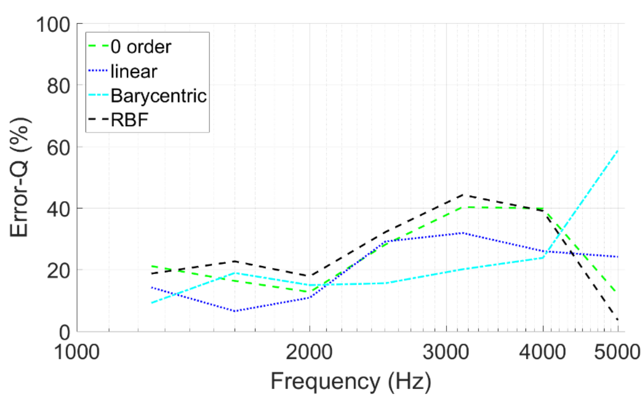

Figure 7.5. CVX Holography Reconstruction Source Strength Error, Circular Array

As shown in Figure 7.6, for rotating speakers emitting tonal noises, the source locations can be identified with high accuracy using the de-Dopplerized signals obtained by irregular array de-Dopperized by all three VRA methods. The experimental results confirm that the zeroth order interpolation works well with both irregular array signals and circular array signals. Besides source locations, the source strength estimation accuracy is also analyzed, shown in Figure 7.7. Barycentric interpolation shows the highest error for all reconstructed frequencies. At the same time, 0 order interpolation based holography shows very close accuracy compared to RBF based reconstruction. In general, all three interpolation methods can de-Dopplerized the measured signal well, and the interpolated signal can be used for high-accuracy localization of rotating source. However, 0 order interpolation and RBF interpolation show better performance in the source strength estimation. In the next section, the performance of the time domain VRA methods in processing broadband rotating source signals will be analyzed.

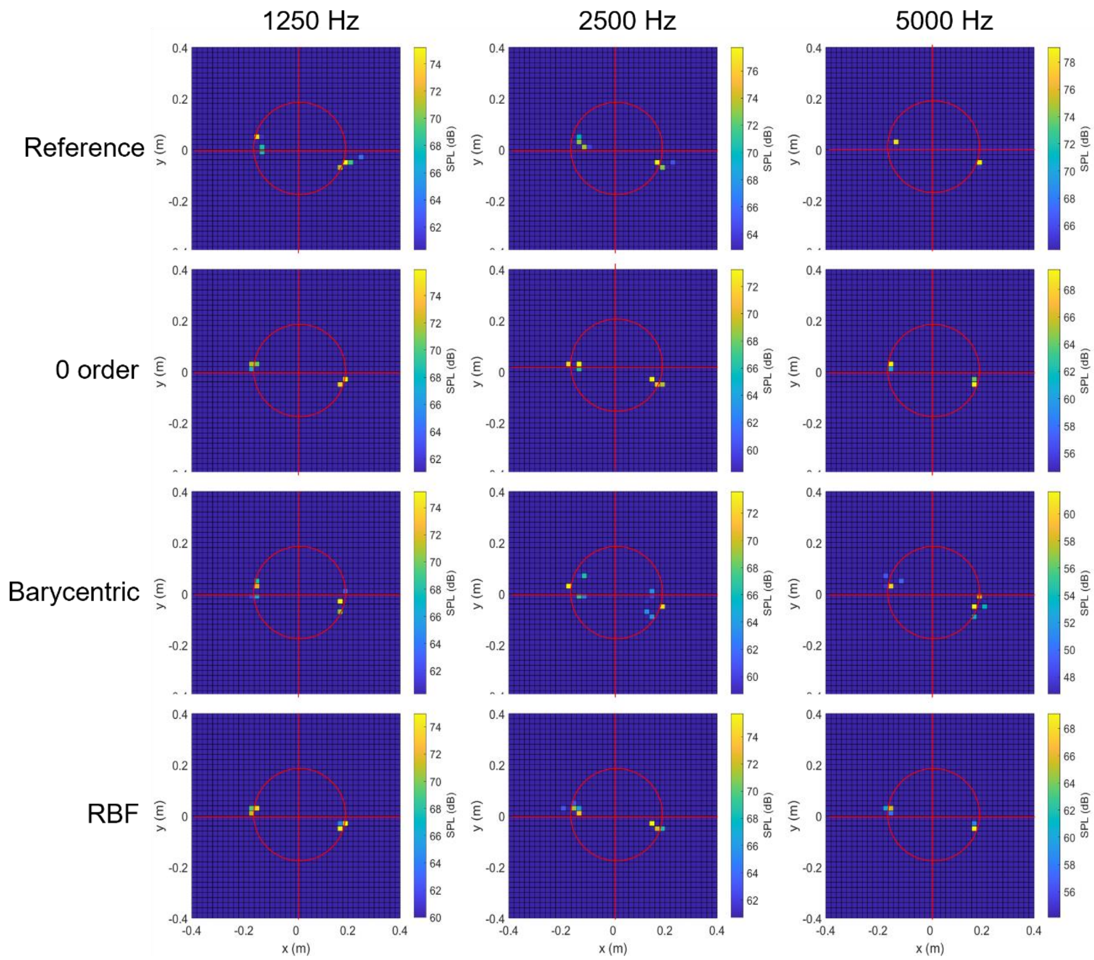

Figure 7.6. CVX Holography Reconstruction, Irregular Array

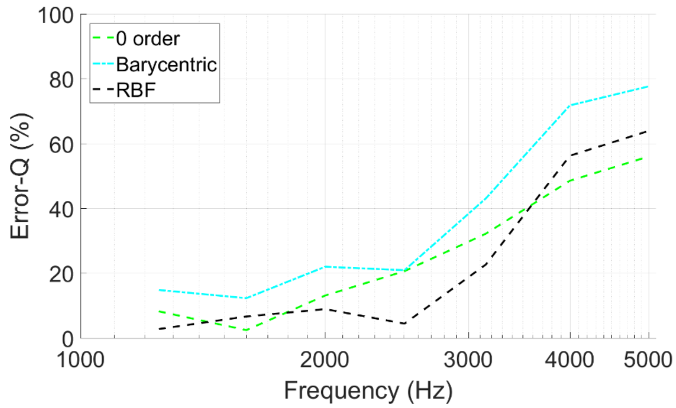

Figure 7.7. CVX Holography Reconstruction Source Strength Error, Irregular Array

7.2.3 Holography Reconstruction for Broadband Signals

The holographic reconstructions of rotating broadband sources are the main focus of this section. Again, Array 1 (circular arrays with 64 microphones) and Array 2 (an arbitrary array with 84 microphones) are used for data acquisitions. For the results of the broadband signals, the sound fields at the source plane will be visualized at three one-third center band frequencies: 1.25, 2.5, and 5 kHz, respectively, as shown in Figure 7.9 and Figure 7.11. In those source plane plots, the dynamic range of the sound pressure level (SPL) for display was 15dB. Measurements of the stationary sources were used as the reference case for benchmarking the strengths and locations of sources.

As illustrated in Sec. 6.2, the CESM holography shows high accuracy in reconstructing the sparsely distributed sources. However, there are inherent limitations on the experimental data, e.g., the recordings of the pressure time signal the determination of the precise locations of the source and receiver, which are unavoidably subjected to measurement errors. The possible error in the source reconstruction will be estimated by comparing it with the reference benchmark results.

A typical snapshot of the sound pressure contours in the receiver plane is shown in Figure 7.8. Results for Array 1 are displayed where the interpolated pressures are used in all contour plots shown in the illustrations. For these contours, two monopole sources emitting broadband signals were used, and the snapshot was taken when the two sources were located at their starting points, see Table 7.2. In the plots, (a) the zeroth order, (b) linear interpolation, (c) barycentric, and (d) RBF schemes are used for the interpolations of sound fields in the receiver plane. Unlike the sound fields due to tonal components (see Figure 6.6 and Figure 6.7), no clear patterns are observable in Figure 7.8 for the broadband signals.

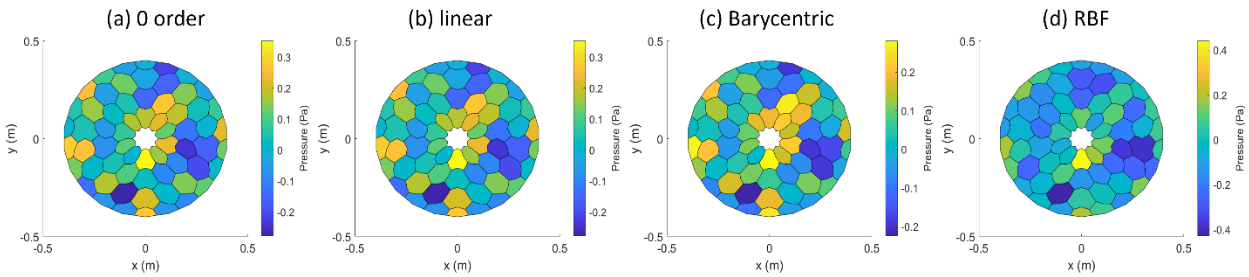

Figure 7.8. Receiver Plane Pressure Distribution Spatshot

The CESM holographic scheme was now applied to the pressure time signals at the receiver plane for the reconstruction of sound fields at the source plane. Figure 7.9 shows the source construction results according to the different interpolation schemes where Array 1 was used for data acquisition. Three frequencies, 1.25, 2.5, and 5 kHz, are selected to present the experimental results. As shown in Figure 7.9, it can be seen that the two monopole sources can be accurately localized at 1.25 kHz without any apparent ghost sources for the reference case (non-moving source) and various interpolation schemes for CESM holographic reconstructions. At 2.5 kHz, all results show ghost sources in the sound source reconstruction using different interpolation schemes. According to the measured results, the locations of the primary sources can still be identified in any case. However, at 5 kHz, the reconstructed sources are more scattered around the speaker locations. According to the zeroth-order and linear interpolation schemes, the holographic indicates more ghost sources, but the source distribution is more concentrated at the actual source locations. In addition, the holographic results according to the linear interpolation scheme show more ghost sources near the source location, especially for the source located at the left side of the source region.

It can be concluded that the source reconstruction using different interpolation schemes had demonstrated comparable capability when Array 1 was used. To determine the source strength, the error spectra between the one-third octave band frequencies of 1250Hz and 5000Hz are shown in Figure 7.10 for Array 1 using different interpolation schemes. A close examination suggests that the source strength reconstructed using the zeroth-order, linear interpolation, and RBF schemes match well. The mean error is less than 1.5 dB for all one-third octave band center frequencies from 1.25 to 4 kHz. However, the barycentric scheme shows noticeably higher errors than all other interpolation schemes at most frequencies.

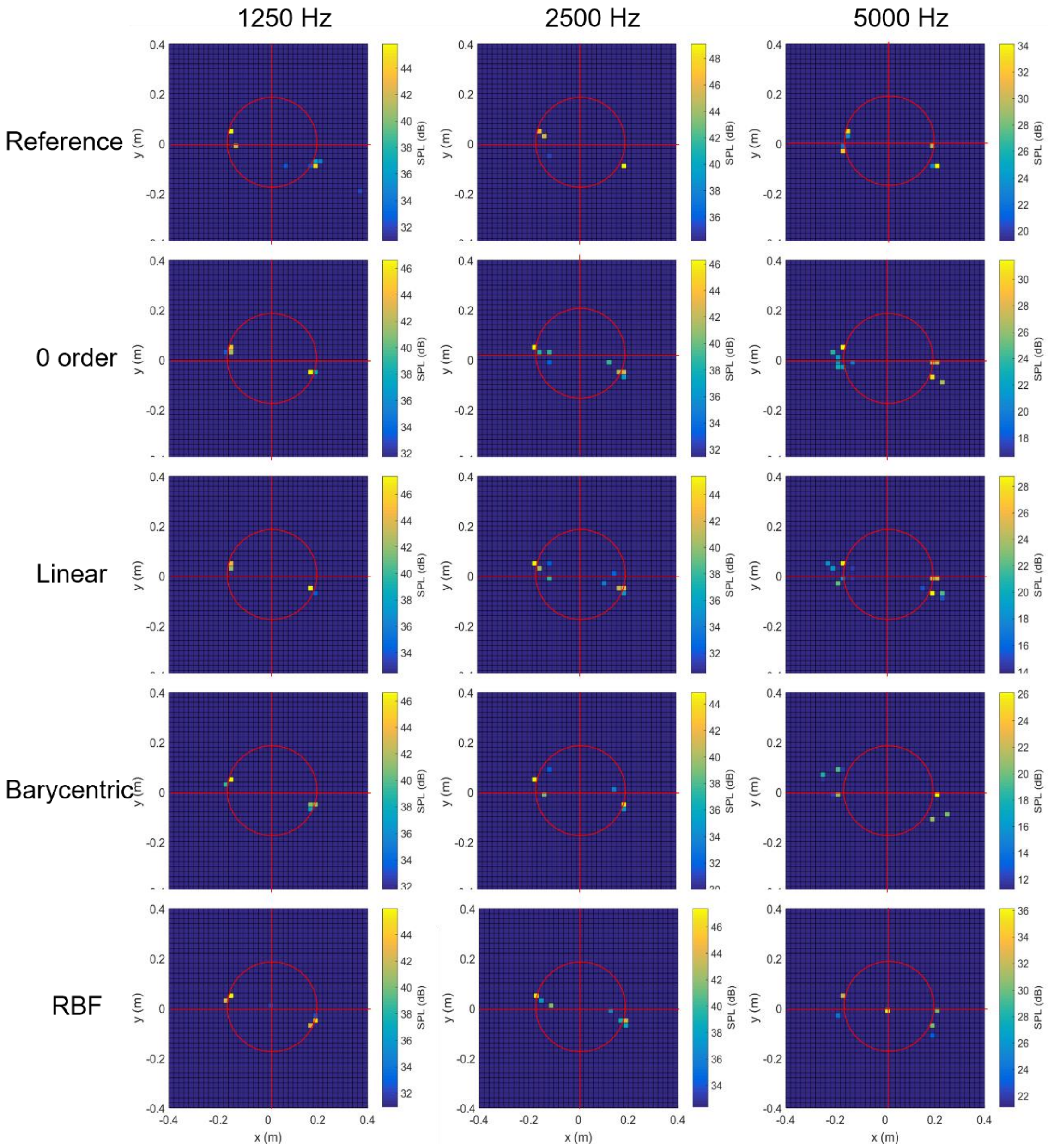

Figure 7.9. Holographic Reconstruction of Source Plane, Circular Array

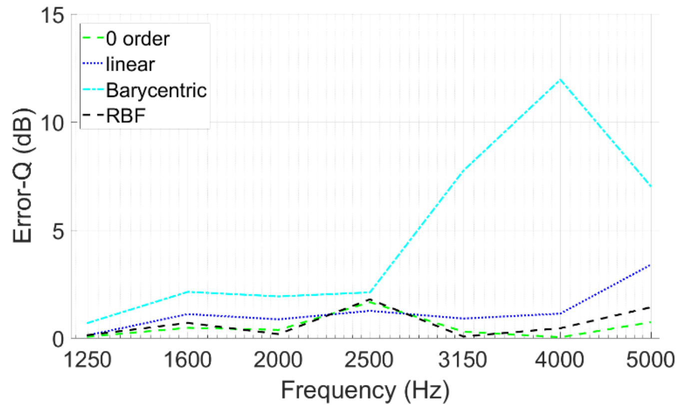

Figure 7.10. Holographic Reconstruction Error, Circular Array

Figure 7.11 shows the holographic reconstruction of rotating broadband sources with the data acquired by Array 2. In this case, the holographic reconstruction results are compared according to the zeroth-order, barycentric, and RBF schemes. At 1.25 kHz, it can be visually confirmed that sound source reconstruction using Array 2 dataset has indicated better agreements than those using Array 1 dataset. Furthermore, column 1 of Figure 7.9 and Figure 7.11 has demonstrated that the reconstructed source region is more compact in Array 2 than in Array 1. Furthermore, all holography results in accurate locations of two sources.

At a mid-frequency (2.5 kHz), the zeroth-order and RBF schemes continue to display more accurate predictions of the source region. On the other hand, the barycentric scheme has shown a significant number of ghost sources around the source locations. The reference reconstruction still shows clean source reconstruction at a high frequency (5 kHz). However, all interpolation schemes have led to a number of ghost sources in the source plane. Comparing the three interpolation schemes, the zero-order and RBF scheme shows fewer ghost sources than the barycentric schemes. However, it is remarkable that the RBF scheme has led to predicting some ghost sources distributed far away from the actual source locations.

The quantitative comparison between the source strength is shown in Figure 7.12. It can be seen that RBF interpolation based reconstruction shows the lowest error below 2.5 kHz, while the zeroth-order scheme shows its merit at higher frequencies. This trend matches well with the simulation results. On the other hand, the barycentric scheme shows significantly higher errors at high frequencies.

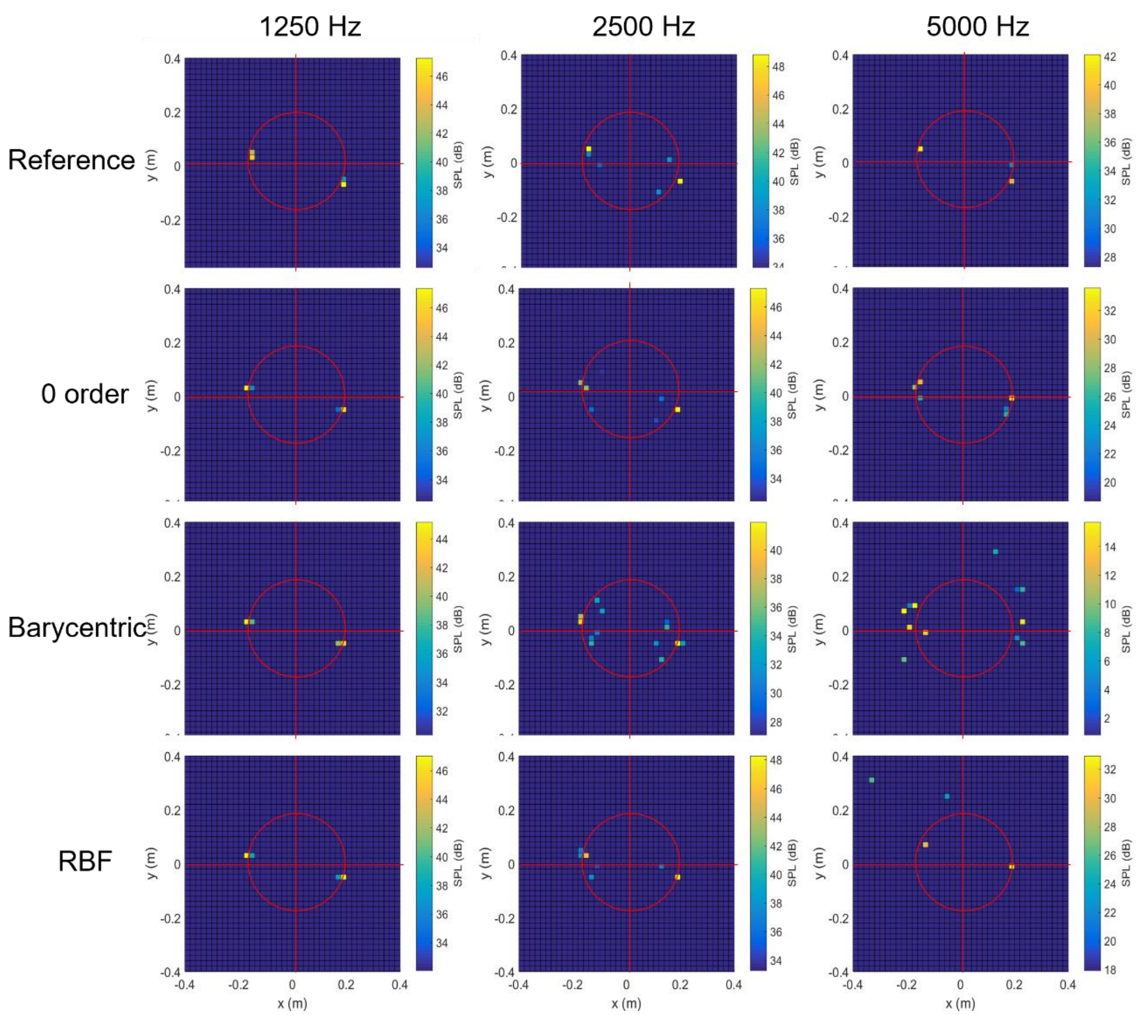

Figure 7.11. Holographic Reconstruction of Source Plane, Irregular Array

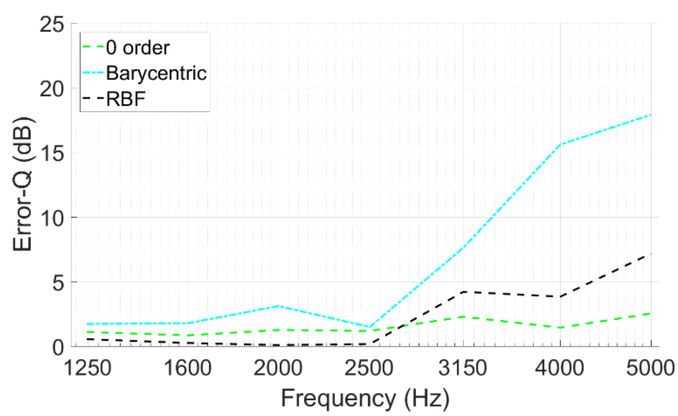

Figure 7.12. Holographic Reconstruction Error, Irregular Array

The reconstruction of experimentally measured sparse sources further confirms that the zeroth-order interpolation scheme works well with compressive sensing holography for rotating source localization and strength prediction. Furthermore, the circular array (Array 1) reconstruction shows lower errors than the arbitrary array (Array 2) for the VRA-based reconstruction using the barycentric and RBF interpolation schemes. However, the zeroth-order interpolation scheme works well with both arrays and does not have significant error growth with an increase of source frequency.

7.3 Experimental Validation of Frequency Domain VRA

7.3.1 Data Processing Procedures

As shown in the last section for time-domain VRA signal processing, the data processing procedures differ between tonal and broadband cases. The signal processing parameters for each case are shown in Table 7.3. The array signals are transformed to the frequency domain using Fast Fourier Transform (FFT) for tonal source cases without time averaging. One second of data is used, which results in a frequency domain resolution of 1 Hz. The VRA methods are performed in the frequency domain to the selected frequency (2500Hz for the simulated case). Then, the reconstructed signals at a particular frequency on the virtual rotating array can be used for holography processing. For the broadband case, the data are handled by different procedures. Firstly, the array data of 10 seconds in time length are transformed into the frequency domain using FFT. Then, the frequency domain VRA procedures are performed to the FFT values. The newly generated FFT values for VRA are inversely transformed into the time domain. The broadband power spectra of the interpolated data on the virtual rotating array are calculated with a 4096-point Hanning windowed FFT block and a 50% overlap between two adjacent blocks (Proakis et al., 1992). Then, acoustical holography can be performed to the spectrum of the VRA signals at the selected frequency. For the holography reconstruction, the reconstructed source region is a 0.8 m by 0.8 m rectangular plane with 41 by 41 uniformly distributed grids.

Table 7.3. Data Processing Parameters for Simulation

	Case 1	Case 2	Case 3
FFT Block Size	32768	32768	4096
FFT Block Overlap	0	0	50% Hanning
Source Plane Grids	41*41	41*41	41*41
Source Plane Grid Size	0.02m*0.02m	0.02m*0.02m	0.02m*0.02m

7.3.2 Holography Reconstruction for Tonal Sources

The WBH is applied to the VRA dataset for source visualization in the source plane at 2 kHz for Cases A and B. Results for source reconstruction are shown in Figure 7.13, where Array 1 (circular arrays) and Array 2 (optimized array) were used. The 1^{st} and 2^{nd} columns show the results for Cases A and C, respectively. In these SPL contour plots, each of the four rows represents (1) the reference case reconstruction with Array 1, (2) the Fs-VRA reconstruction using Array 1, (3), and (4) Op-VRA using Arrays 1 and 2, respectively. In addition, the source strength is calculated for Cases A and B, where the source frequency is centered at 2 kHz (see Table 7.4) to compare the performances of the two VRA methods quantitatively.

It can be observed from Figure 7.13 that the locations of tonal sources can be reconstructed with high precision by using the de-Dopplerized signals. In addition to the excitation frequency, those of the other two sources (at 1.985 and 2.015 kHz, respectively) were deliberately added to induce a possible interference with the modal sidebands for Case B. According to the experimental results, the source localization process has proved to be insensitive to this interference effect, see the 2^{nd} column of Figure 7.13. The experimental results for Cases A and B also confirm the effectiveness of the Op-VRA and Fs-VRA in determining the source locations because their results are in an excellent accord with the results of the reference case obtained for the stationary sources measured with Array 1 at rest.

Besides the source localization, the accuracy in estimating source strengths is also examined. Table 7.4 summarizes the reconstruction results for S_1's and S_2's source strengths. The Fs-VRA reconstruction results show excellent agreements with the reference cases for the reconstruction of the tonal sources. The errors of the reconstructed source strengths are well within 1 dB difference with the reference levels for S_1 and S_2 in both cases. Using the Op-VRA method on Array 1, the estimated source strength shows an excellent agreement with the reference case, but the agreements deteriorate (to within 1.6 dB) if Array 2 is used for Case B, where there are three tonal components in the source. Simple use of sideband summations becomes increasingly inadequate in predicting the rotating sound fields for the situation with multiple tonal sources. Nevertheless, the difference is within 2.5 dB between predictions using Arrays 1 and 2.

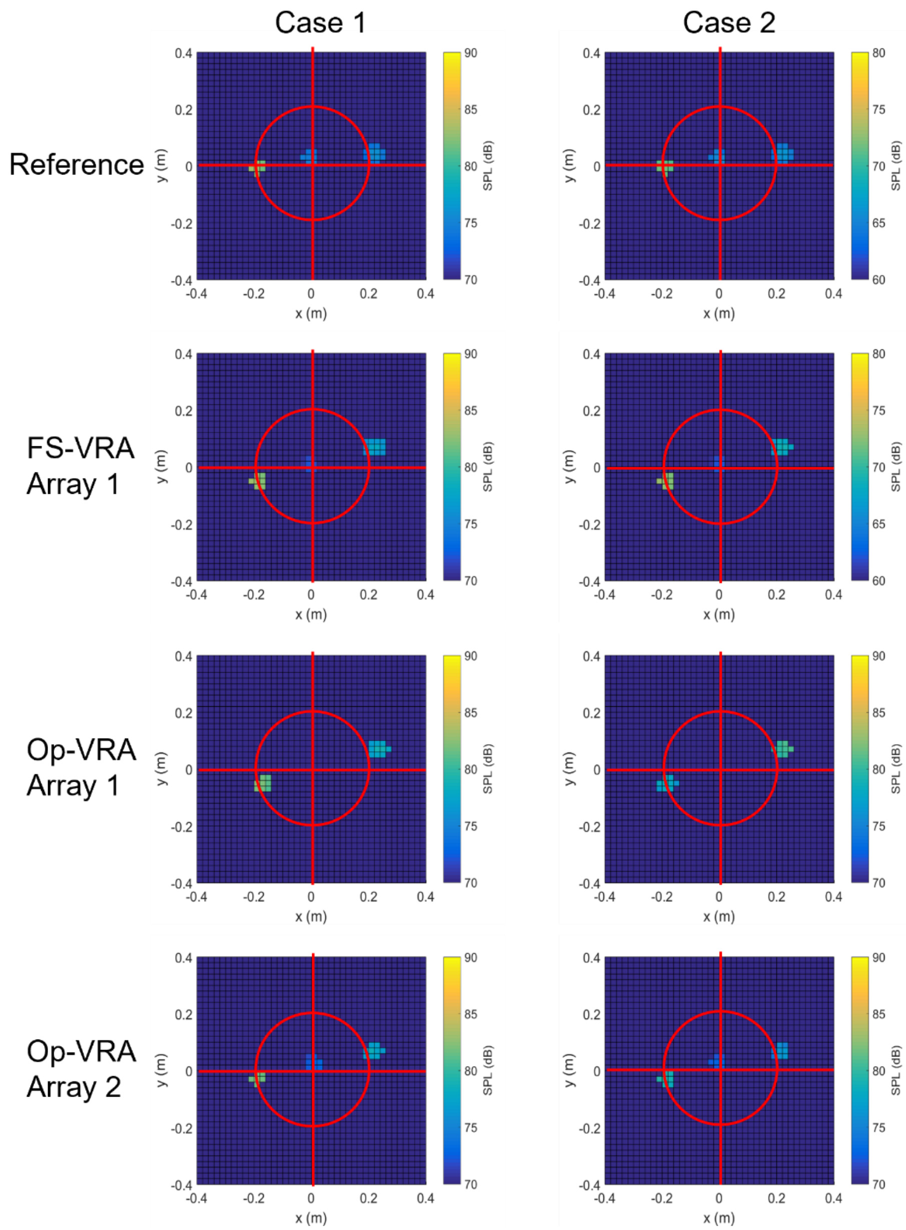

Figure 7.13. Wideband Holography Reconstruction, Tonal Signals

Although the use of the sideband summation method for estimating the source strength is not as accurate as of the Fourier summation method, its use in predicting relative source strength is in good accord with the reference results. This conclusion is similar to the earlier results presented in Sec. 6.3 for the numerical validations of VRA based CESM schemes.

Table 7.4. Wideband Holography Source Strength at 2000Hz

	Case 1		Case 2	
	S1	S2	S1	S2
Reference, Array-1	99.6	98.2	89.8	88.6
FS-VRA, Array-1	99.4	97.8	89.4	88.0
Op-VRA, Array-1	99.6	97.7	98.0	96.5
Op-VRA, Array-2	97.7	96.7	95.9	94.2

7.3.3 Holography Reconstruction for Broadband Sources

A broadband sound source was used in the experiments to verify the CS-NAH scheme used for source localization. The reconstructed sound fields in SPL contour plots for visualization at the respective frequencies of 1.25, 2.5, and 5 kHz are shown in Figure 7.15. In the reference case, experimental results are processed by WBH, where the measured data was obtained from a stationary circular array due to two stationary sources. The total source strengths of these two sources at the center frequencies of the one-third bands between 1.25 kHz and 5 kHz are shown in Figure 7.15. In addition, the relative source strength (Δ_j = S_j - S_1) between the two sources is also calculated, see Figure 7.16.

The source localization is pretty successful for the one-third octave bands centering at 1.25 kHz and 2.5 kHz; see the 1^{st} and 2^{nd} columns of Figure 7.15. Regardless of the choice of the VRA methods and the array configurations, the WBH results agree well with the reference case shown in the 1^{st} row. At 5 kHz, ghost sources can be found in reconstruction results around the actual source locations when Array 1 is used for the Fs-VRA and Op-VRA methods. These ghost sources are present even in the reference case where the sources and receivers are stationary. The issue with the ghost sources is less prominent if Array 2 is used in reconstruction instead. Overall, the experimental results confirm that the use of WBH in the Fs-VRA and Op-VRA methods can localize the broadband rotating sources with reasonable accuracy.

In terms of the source strength prediction (see Figure 7.15), it can be seen that the reconstruction results from the Fs-VRA method generally agree reasonably well with those results shown in the reference case. The sideband summation method gives an overestimation of the source strength. However, the predictions of the relative source strengths generally show good agreement with the reference case for either the Fs-VRA or Op-VRA (less than 3 dB for all selected frequencies). The predicted relative source strengths are shown in Figure 7.16 for information. These two findings are consistent with the simulated results of the source reconstruction presented in Sec 3.3. The holographic results of the experimental broadband data further substantiate using the sideband summation method on an optimized array, which is also referred to as the Op-VRA method.

The Op-VRA method has demonstrated its capability to de-Dopplerize the rotating sound signals and generate a VRA dataset for subsequent processing in a CS holographic method instead of the traditional beamforming approach. Although the Op-VRA overestimates the source strength, the relative strength can be reconstructed with reasonable accuracy. In addition, the processing speed of the Op-VRA is much faster than that of the Fourier summation method. In summary, the combination of the Op-VRA method with CS-NAH has the potential to become a helpful tool for source localization with high accuracy and low computational costs in addition to a broad range of source frequencies.

As shown in the WBH results, the reconstruction of low-frequency sound still shows a large source area which yields a higher level of uncertainty in the source locations. Therefore, the hybrid CS holography is also applied here to represent the source locations at low frequencies better. It can be seen from Figure 7.17 that the source region reconstructed by the hybrid method is reduced significantly. The reconstruction based on both the VRA signals shows good agreement with the reference case. In addition, the source strength is also estimated for this reconstruction, which can be found in Table 7.5. As shown in the table, the source strength predicted by the Fs-VRA method is in good agreement with the baseline case. The typical error is below 1 dB for S_1 and S_2. In addition, the Op-VRA still shows a significant overestimation of the source strengths. For the relative strength between the two sources, the reference case has a 1.1 dB difference. The reconstruction based on Fs-VRA has a larger deviation between two sources than the reference case (2.2 dB). The Op-VRA reconstruction shows a marginally better performance in estimating the relative source strength under 2 dB for both circular and non-circular arrays.

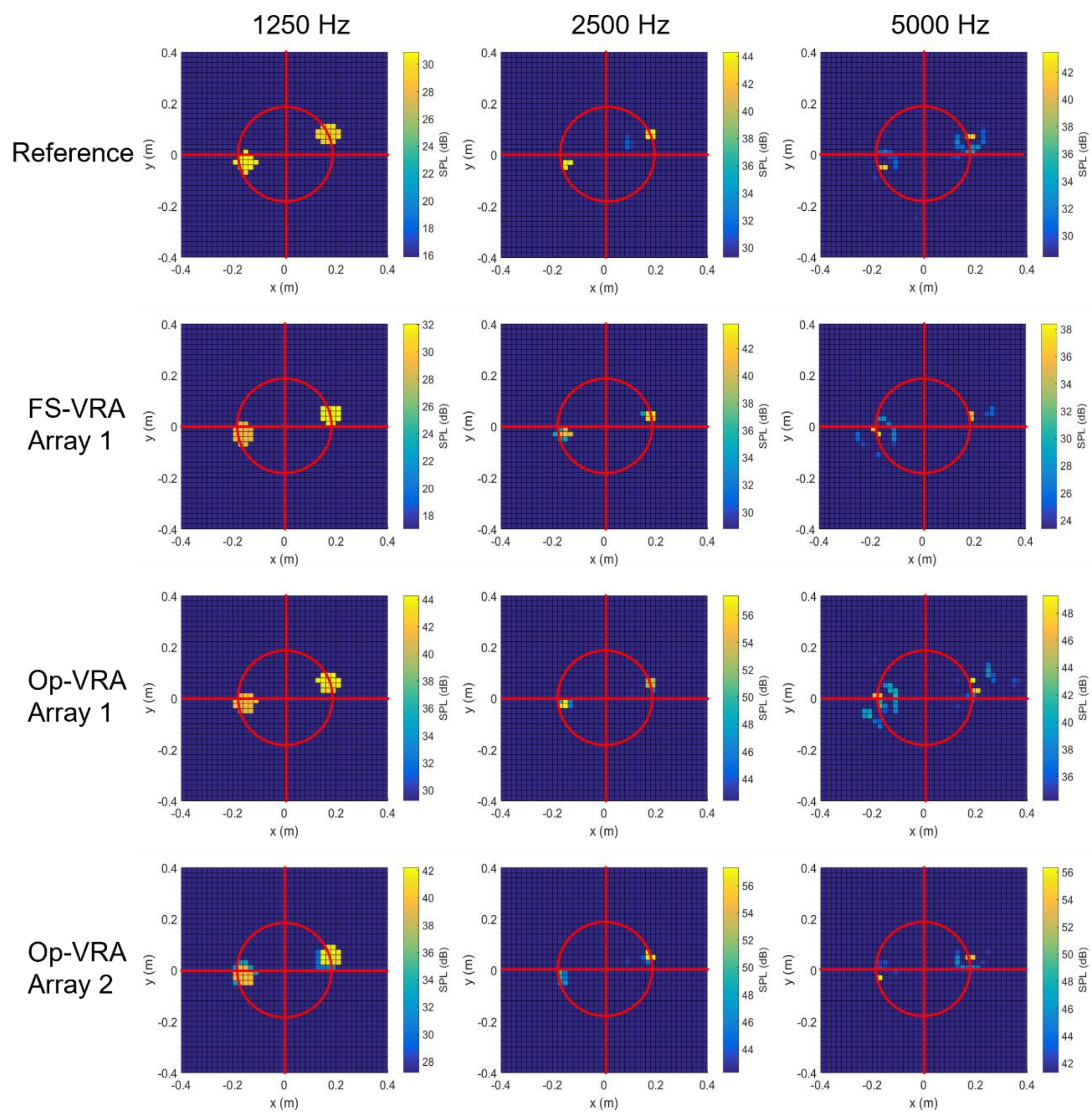

Figure 7.14. Wideband Holography Reconstruction, Broadband Signals

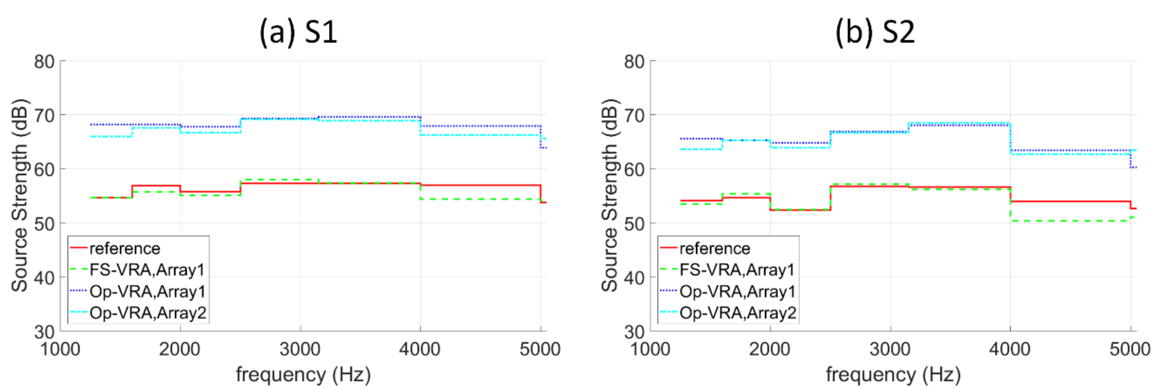

Figure 7.15. Wideband Holography Source Strength Reconstruction, Broadband Signals

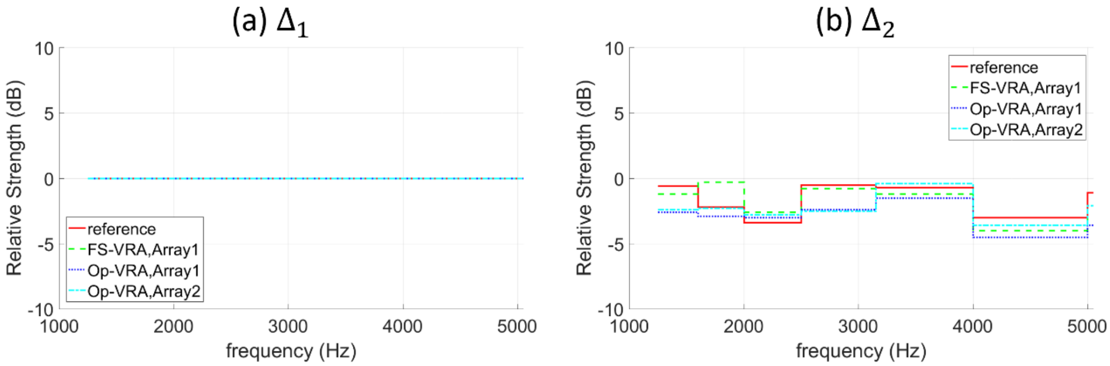

Figure 7.16. Wideband Holography Source Strength Difference, Broadband Signals

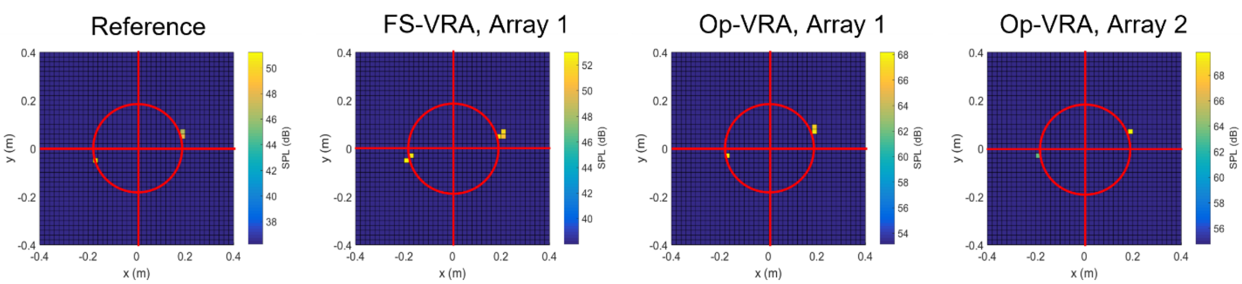

Figure 7.17. Hybrid Holography Source Reconstruction at 1250Hz

Table 7.5. Hybrid Holography Source Strength at 1250Hz

	S1	S1
Reference, Array-1	53.2	52.1
FS-VRA, Array-1	53.9	51.8
Op-VRA, Array-1	72.5	71.1
Op-VRA, Array-2	71.1	68.2

7.4 Application of Holography Development to Gear Experimental Data

An experiment has been performed to monitor nested planetary gear, and acoustical array data were measured by a 64-channel array parallel to the gear rotation plane. The details of the experimental setup can be found in Chapter 3. In this section, the first subsection shows the details of the data processing procedures to process the measured gear data. Carrier-2 is exposed to the air for the nested planetary gear, so the gear meshing signals of the outer gearset can be measured with microphones. The second section applies the time domain 0 order VRA and frequency domain VRA to the measured array signals. Finally, the VRA signals are used for the holographic reconstruction of the source plane.

7.4.1 Data Processing Procedures

Four planet gears rotate concentrically at the same speed. The contact region between the planet gear and the annulus gear is compact so that the sound source can be regarded as sparsely distributed sources. The experiment is conducted at 1000rpm input shaft speed with errors within 0.5%, which means the rotating speed of the carrier is about 6.75r/s, and the fundamental contacting frequency is 932 ∓ 5 Hz. The rotating radius for gear is approximately 10cm, which leads to the distance between the adjacent planetary gears at about 7.1 cm. The distance is smaller than the wavelength of the sound wave at the meshing frequency of 932 Hz. In addition, the wideband holography reconstruction resolution is limited by source signal frequency, and the distance between the sources has to be larger than a wavelength. According to the above discussion, wideband holography is not suitable for application in gear rotation tracking. Due to the close spacing between sources and frequency limit, the L_1 norm penalty minimization is chosen for utilization for the current case. The approach, which utilizes the convex optimization solver, can resolve the sources placed closer than a wavelength. In summary, in the current experimental study, it is proposed that the virtual rotating array approach works with the L_1 norm minimization to visualize the rotating gear sound sources.

The geometry of the measurement array is shown in Figure 7.18. The plate has a total of 84 holes for array mounting; 64 holes are selected for measurement due to the limitation of the number of channels for the data acquisition system (see Figure 7.18 (b)). The microphones of the array are randomly located, and the aperture of the array is about 0.5m. Furthermore, the array is placed at 0.3-0.35 m above the gear rotating plane.

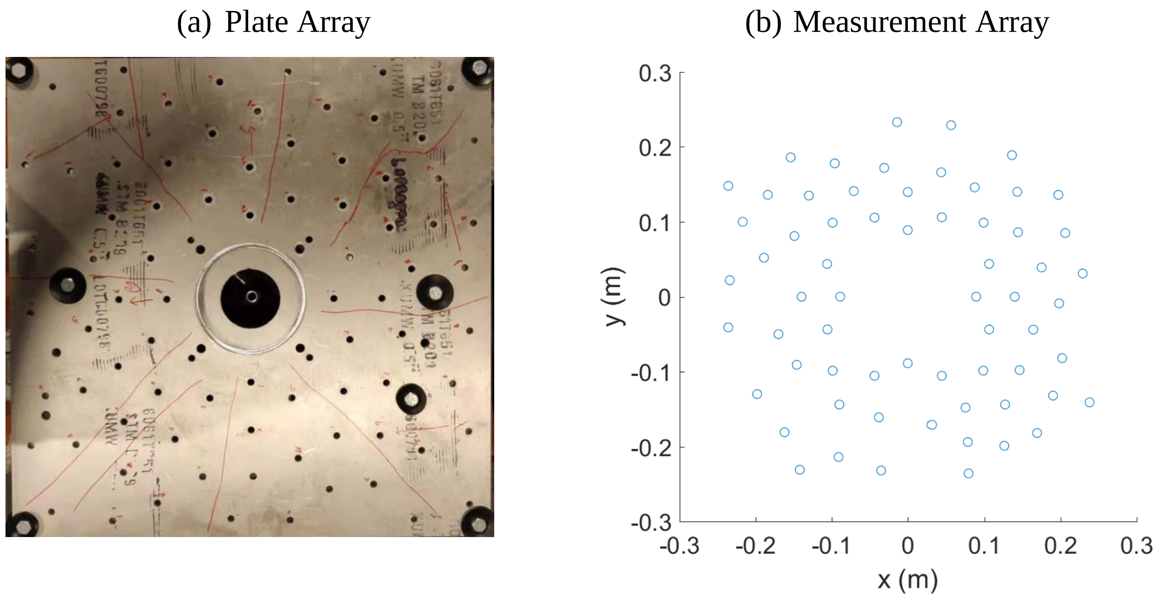

Figure 7.18. Array Geometry for Gear Noise Measurement

The experimental data processing procedures are given in Figure 7.19. The measured microphone array data are processed with time synchronous averaging to eliminate the signals unrelated to the gear rotation. The averaged array signals are then interpolated with a virtual rotating array. The virtual rotating array signals are used as input for near-field holography reconstruction. BoB and WoW-1 data are processed and analyzed for the current experimental results analysis. The data are both tested at around 1000rpm input shaft speed. The meshing frequency for BoB is 930Hz, while the meshing frequency for WoW-1 is 935Hz due to the slight input speed variation.

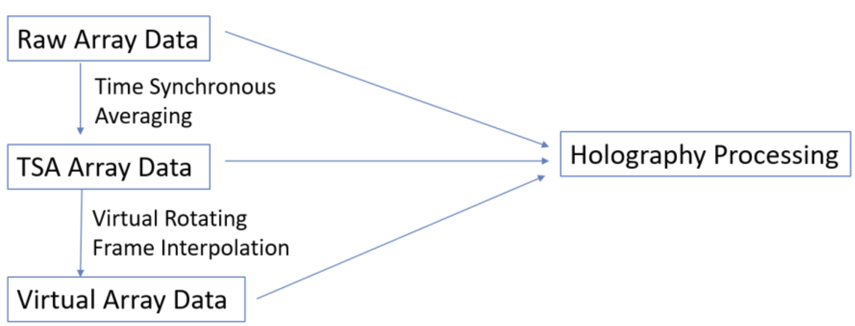

Figure 7.19. Holography Processing Procedures for Gear Experimental Data

7.4.2 Gear Rotating Plane Sound Field Reconstruction

This section shows the results for the sound field visualization of the rotating gears. The L1 norm holography reconstructions at the meshing frequency are shown in Figure 7.20 and Figure 7.21. Figure 7.20 (a) and Figure 7.21 (a) show the holography reconstruction using unprocessed array data for BoB1 and WoW1, respectively. It is evident that no sound source is showing at the orbit of pinion rotation. Figure 7.20 (b) and Figure 7.21 (b) show holography reconstruction using time-domain 0 order virtual rotating array. However, there is still no obvious source appearing at the pinion rotational path. In addition, the frequency domain VRA based holography reconstruction shows similar results, see Figure 7.20 (c) and Figure 7.21 (c). The results show that the sources along the rotating path are not reconstructed successfully at meshing frequency. As discussed in the last section, the wavelength at the meshing frequency is much larger than the distance between the pinions, leading to significant errors in holography reconstruction. Therefore, a higher frequency needs to be chosen for the holography reconstruction.

(a) Measured Array Data (b) Time Domain VRA (c) Frequency Domain VRA

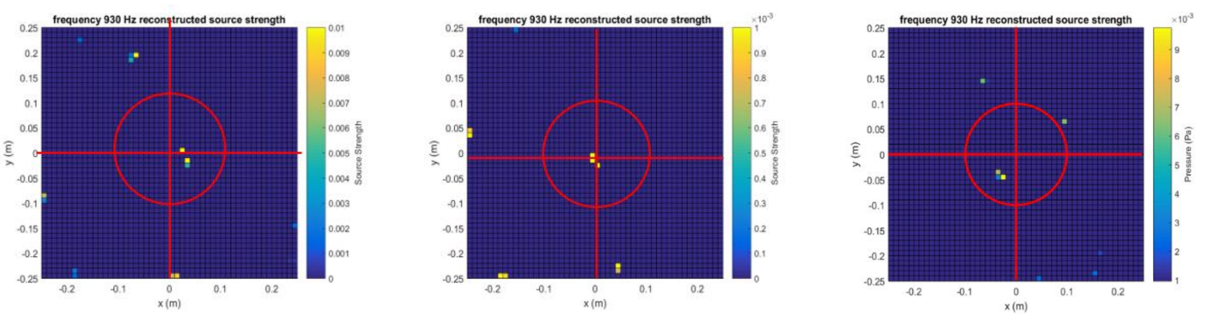

Figure 7.20. L_1 norm holography, BOB-1, 930Hz

(a) Measured Array Data (b) Time Domain (c) Frequency Domain VRA

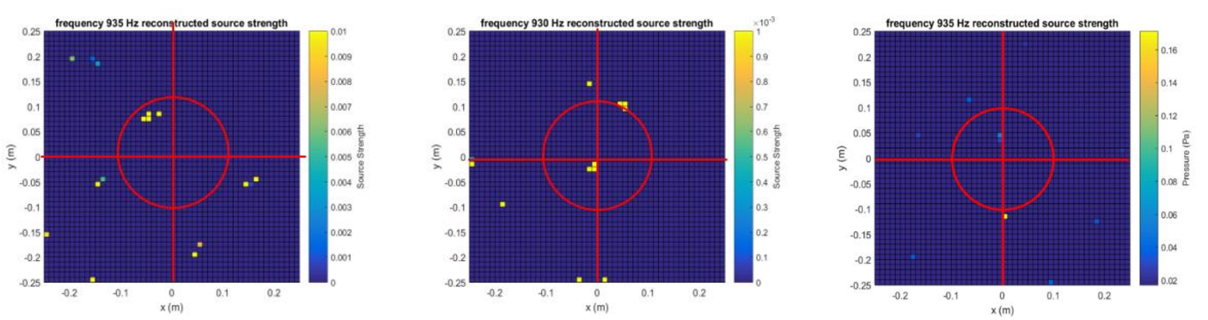

Figure 7.21. L_1 norm holography, WOW-1, 935Hz

For further analysis of pinion localization, the fourth harmonics of the meshing frequency, which is $4 \times 932Hz$, is chosen for holography process. The holography results are presented in Figure 7.23 and Figure 7.25. To further validate the performance of holography reconstruction based on VRA signals, the vibrational time history is shown in Figure 7.22 and Figure 7.24 for BoB and WoW1, respectively.

The holography reconstruction using the stationary array signals does not show helpful information for pinion localization; see Figure 7.23 (a). Figure 7.23 (b) shows that for the time domain VRA-based reconstruction, three major sources out of four can be identified by time-domain VRA-based holography, while S2 is missing in the source plane map. The frequency-domain VRA based holography can also identify three sources, while S1 is missing on the map. In terms of the source strength reconstruction, the three sources identified by time-domain VRA based holography have similar values, which match the results of vibrational data, see Table 7.6. However, the source strength reconstructed by frequency VRA has larger values than time-domain VRA based holography reconstruction, which is discussed in previous chapters and is characteristic of the Op-VRA method. In addition, the frequency domain sideband summation based holography reconstruction shows a more significant deviation for the strength of different sources.

Table 7.6. Source Strength, BoB 1

Source Location	Source Strength		
	Vibration (m/s^2)	Time VRA (Pa)	Frequency VRA (Pa)
S1	2.51	0.0015	N/A
S2	1.92	N/A	0.03
S3	2.16	0.0011	0.04
S4	2.18	0.0015	0.05

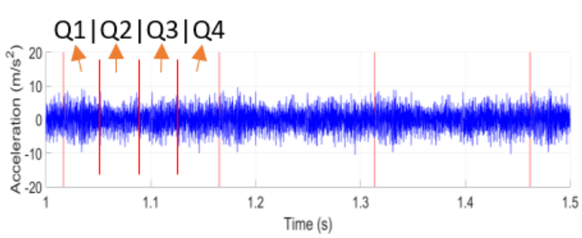

Figure 7.22. L_1 norm holography, BOB-1, 3720Hz

(a) Measured Array Data (b) Time Domain VRA (c) Frequency Domain VRA

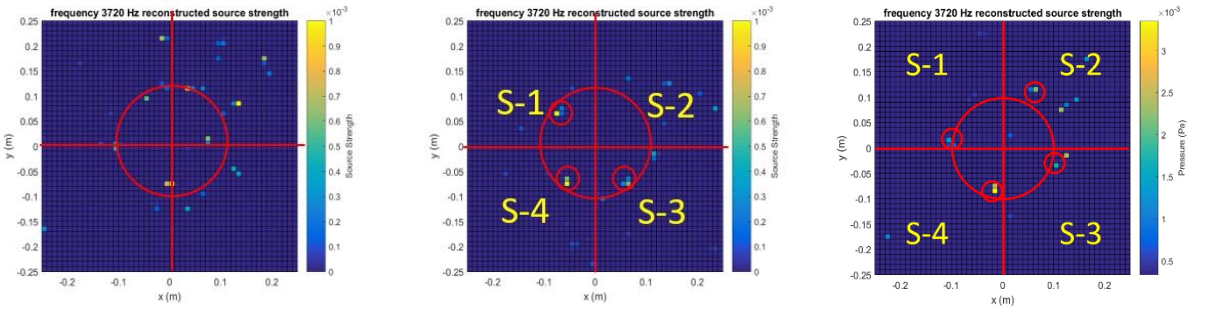

Figure 7.23. L_1 norm holography, BOB-1, 3720Hz

For WOW-1, the holography reconstruction using direct measurement data from an array does not show useful information for source localization, which is expected due to the doppler's effect and the sound signal corruption by structural vibrational noise (see Figure 7.25 (a)). On the other hand, all four sources can be visualized using the time domain VRA signals in the L1 norm holography reconstruction. One of the four sources has significantly higher strength than the other three. In addition, the source location in the hologram matches the unground pinion location in the carrier, which was investigated in Chapter 4. Therefore, strong sources along the pinion rotation orbit can be observed for the sideband summation VRA-based holography reconstruction. However, only two sources can be identified. Furthermore, the reconstruction also confirms that the strongest source shows in the fourth quarter of the quadrant.

Table 7.7. Source Strength, WoW 1

Source Location	Source Strength		
	Vibration (m/s^2)	Time VRA (Pa)	Frequency VRA (Pa)
S1	18.28	0.0093	N/A
S2	12.95	0.0065	0.122
S3	11.94	0.0063	N/A
S4	28.42	0.0159	0.216

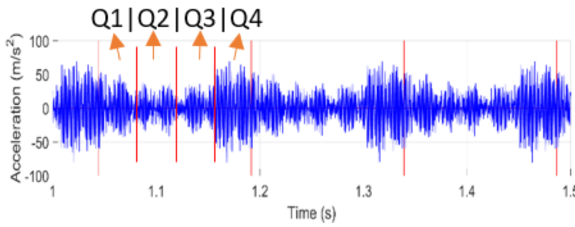

Figure 7.24. L_1 norm holography, BOB-1, 3720Hz

(a) Measured Array Data

(b) Time Domain VRA

(c) Frequency Domain VRA

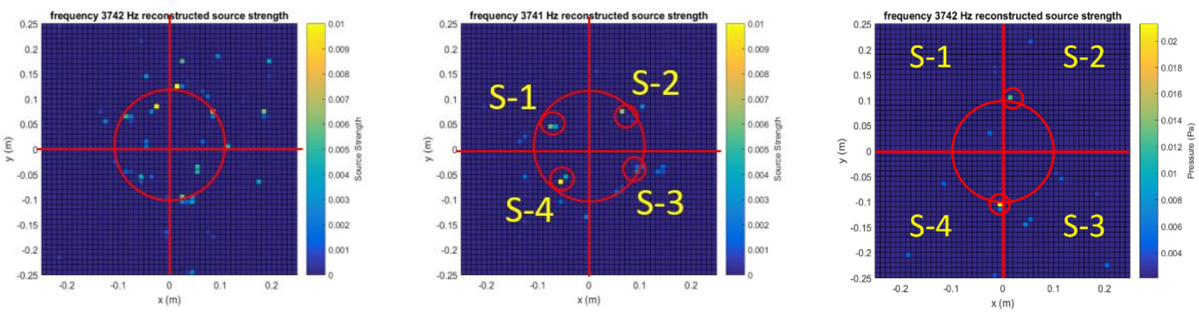

Figure 7.25. L_1 norm holography, WOW-1, 3741Hz

In summary, both time-domain VRA using 0 order interpolation and frequency domain VRA using sideband summation shows the potential to be applied in the sound source tracking of the rotating component of complex rotating machinery. At the same time, the time-domain VRA shows higher accuracy for the sound source localization and strength reconstruction in the current study.

8. SUMMARY AND FUTURE WORK

8.1 Background

With the advancement of engine technology and aerodynamics, there are also increasing needs for quieter and higher-performance transmission. As the key components of most of the transmission, higher requirements are put on the accuracy of the gear manufacturing. Implementing a high-performance monitoring system can improve gear manufacturing accuracy to defect the manufacturing error in the product line. There are various technologies developed for manufacturing quality monitoring: noise emission and vibration signal monitoring. The NVH monitoring has the advantage of being non-destructive and detecting the gear error without taking apart the assembly. In the current study, a vibroacoustic testing fixture and a testing prototype are developed for the gear train sub-assembly monitoring, particularly for the nested planetary gear train.

For the gear transmission chain, the total transmission can be decomposed into different parts, consisting of the combination of planetary gear sets. Furthermore, compound planetary gear trains are designed and applied in the transmission to enhance the transmission's compactness further. Among those compound gear trains, the nested planetary gear set has been widely applied since its invention due to its high robustness and compactness. However, due to its unique integrated structure, the transmission errors of the nested planetary gears are more complicated than the normal planetary gearset, so the monitoring of the nested planetary gear requires the combination of various techniques and procedures.

In the current study, the current vibroacoustic monitoring protocol development for the nested planetary gear monitoring is two-fold: (1) the vibrational signal analysis; (2) acoustical array signal analysis. In order to collect the data from both vibrational sensor and acoustical array, the current testing fixture design utilized a vertical and open setup. The gears are exposed to the air rather than tested in a gearbox or transmission case. The vibrational sensors (accelerometers) were mounted directly to the different gear clutches to monitor the inner planetary gearset and outer planetary gearset separately. The acoustical array is mounted on the top fixture plates for the sound source localization of the rotating pinions. In addition, the revolution data enables several rotating machinery signal processing techniques to be applied to the nested gears. Therefore, the laser tachometer is added to the monitoring system to record the carrier revolution. Only the pinion gears on the carriers are analyzed for the current monitoring work. The sun gear and annulus gear quality monitoring are not within the scope of the current study. Furthermore, three types of carriers are used for analysis:

1. Carriers with high manufacturing accuracy (referred to as BoB).
2. Carrier with ungrounded gears (referred to as WoW).
3. Carriers with gears that have partially damaged teeth (referred as D).

8.2 Vibrational Signal based Monitoring

Several signal processing techniques are applied to the vibrational signals: (1) time synchronous processing; (2) frequency spectra analysis and modulation sideband analysis; (3) narrowband demodulation. Since the nested planetary gears have two integrated planetary systems, the data measured from the outer gearset and inner gearset are analyzed. Three gear monitoring prototypes are established for the diagnostics of different faults:

1. Single unground pinion in either outer or inner carrier
2. One or two unground pinions on the outer carrier
3. Pinion tooth crack

The first gear vibrational monitoring prototype monitors the outer carrier pinion. Furthermore, signal processing techniques applied in this section is the narrowband demodulation techniques. For the first step, the peaks in the frequency spectrum are identified automatically; then, the signals are demodulated around the meshing frequency and the harmonic frequency. Finally, the frequency spectra of the demodulated signals are calculated because time-domain data are corrupted by structural noise. And the demodulated signals show the frequency components at the carrier rotating frequency, which verifies that the carrier rotation modulates the signal. Furthermore, the unground pinions in the carrier can change the modulation behavior, which will be shown in the frequency plot of demodulated signals. However, repeated experiments show that the modulation behavior is consistent regardless of the assembly condition and operation speed. Hence, an indicator can be established to monitor the unground pinions using the demodulated signals.

In the second system, the pinion gear defects located at outer or inner carriers are studied. The time synchronous averaging is applied to both well-manufactured carriers and carriers with unground pinions. The signals are averaged across multiple carrier revolutions, recorded by laser tachometer sensor. The averaged signals show higher amplitude when the unground gear passes by, which can be used as the criteria for unground gear localization. In addition to enhancing the time history quality, the frequency spectra analysis was conducted for the experimental data to obtain more information from the collected data. It shows that the peaks in the spectrum are distributed around meshing frequency and harmonics regardless of the input speed. Except for the frequency spectrum analysis over broadband, the analysis can also be conducted by zooming in around the meshing frequencies. Around the meshing frequencies, the peaks are called modulation sidebands because the rotational modulation usually generates those sidebands. The time synchronous averaging can reduce the sidebands unrelated to the rotational modulation, thus improving the modulation sideband analysis accuracy. It is shown that the modulation sideband behaviors are different for different carriers with different types of faults. A physical signal model is proposed to explain the modulation sidebands behaviors. The model was developed for explaining the sideband asymmetry for planetary gear with multiple planet gears. In the current study, the model is modified in terms of the amplitude and phase to explain the effects of the ungrounded gear on the carrier location error, thus changing the frequency spectrum distribution.

The third system deals with the local pinion faults, such as gear crack or dent. The pinion cracking or denting is different from pinion grinding defects because they are repeated several times during each revolution of pinions. Therefore, more advanced time synchronous averaging can be applied for the carriers with partial tooth damaged pinions. The signals can be windowed only for single planet gear passing by, and the signals are averaged across multiple windows. The averaged signals show time history with less noise that indicates the existence of the damaged teeth.

8.3 Acoustical Imaging System Development for High Resolution Rotating Source Localization

Except for the vibrational signal monitoring of the system, the acoustical array is also applied to unground gear monitoring. Although vibrational monitoring can fulfill the task of unground pinion monitoring with high precision, acoustic emission monitoring might be required for contactless measurement. For the current type of noise mapping, the equivalent source based compressive sensing is one of the best options because the gear structure is compact, and the noise sources are sparse. However, the author cannot refer to current work regarding the sound source localization of rotating sources using acoustical holography. Due to the abovementioned reasons, the near-field holography methods for rotating source localization are developed in the current study.

It can be found in the previous literature that the localization of the rotating source using the beamforming method has been well-developed. Furthermore, there have been methods developed to de-doppler the array signal, called virtual rotating array methods. The virtual rotating array methods generate the array's signals that rotate at the same speed as the source. Then, the virtual rotating array signals can be used for acoustical imaging, such as beamforming. In the current study, the virtual rotating array signals are proposed to be used as the input for acoustical holography reconstruction, which can further improve the resolution of the rotating source imaging compared to beamforming. Three equivalent source based near-field holography methods are used in this study, which is: (1) wideband holography; (2)L1 norm penalty optimization; (3) the hybrid approach.

Except for modifying the holography reconstructing process, the virtual rotating array methods have also been further developed for improved efficiency. There are two types of virtual rotating array signal generation algorithms: (1) time-domain interpolation; (2) frequency domain modal synthesis. For the time domain VRA interpolation, the virtual rotating array microphone locations are calculated at each time step. Spatial interpolation generates the VRA signals based on the stationary array measurement. Three interpolation methods have been published in previous literature: (1) linear interpolation; (2) Barycentric interpolation; (3) radial basis function interpolation. Linear interpolation can only be performed to the array with ring-shaped configuration and interpolated using two adjacent microphones along the same ring. Barycentric and radial basis function interpolation can be performed to the signals measured by randomized array configuration. However, the computational cost is significantly increased compared to linear interpolation. Therefore, a more efficient interpolation method, which is referred to as 0 order interpolation, is developed in this study. The 0 order interpolation utilized the closest microphone for signal interpolation at each time step. It can be applied to the randomized array measurement and has improved efficiency compared to the other time-domain interpolation methods.

In addition to the time domain interpolation, frequency domain interpolation is also studied. Compared to the time domain interpolation, it has enhanced VRA signal synthesis performance at higher frequencies. However, the well-known modal decomposition algorithm has a higher computational cost than the time domain interpolation methods. In addition, the modal decomposition method is restricted to be applied to the measurement performed by a circular array with equally spaced microphones. Therefore, to overcome these disadvantages, a more efficient sideband summation is proposed for the sound field de-dopplerization in the frequency domain. The sideband summation works well for the monochromatic source. However, for the source with the broadband spectrum, the application of the methods is limited to the following cases: (1) low-speed rotation; (2) the spectrum is symmetric around particular frequencies. In addition, the holographic reconstruction using sideband summation can predict the source location accurately with strength prediction errors. However, the strength difference between different sources can be predicted accurately in most conditions.

For the virtual rotating array method validation, both simulation signals and experimental measurement are sued. The widely applied benchmark B11b case is used for simulation validation (Herold et al., 2018). For this case, three closely placed sources rotate at 1500rpm, and tonal signals and broadband white noise signals are generated and processed by VRA methods. All four time-domain VRA methods and two frequency domain VRA methods performed well in de-dopplerizing the array measurement. Furthermore, it was shown that the correct source locations could be reconstructed using the VRA signals. The source strength reconstruction is also compared. It was shown that the proposed 0 order interpolation has the best performance among all four time-domain methods. For the frequency domain VRA methods, sideband summation based holography shows the capability of reconstruction both the source location and the relative source strength. In contrast, the source strength evaluation shows significant error. However, the efficiency of sideband summation is significantly higher than the modal decomposition method. The experimental validation is performed using two rotating speakers rotating at 180 rpm. The signal types are the same as simulation validation. In general, the validation using the rotating speaker signal leads to the same conclusion as the simulation validation.

After the current holographic and VRA development has been validated by simulation and simple experimental sources, the virtual rotating array method is also applied to the gear operation monitoring. Two new VRA developments in this study, the 0 order time-domain method, and the sideband summation frequency-domain method, are applied to de-dedopplerized the rotating gear sound fields. In addition, the VRA signals are used for the holographic mapping of source plane sound fields. The L1 norm optimization based CVX method is used for the holographic reconstruction due to its high spatial resolution. The reconstruction frequency for the experimental data is chosen to be meshing frequency and the fourth harmonics. It was shown that the reconstruction at meshing frequency does not contains much information of source location because the reconstruction frequency is lower than the spatial sampling requirement of CVX holography. On the other hand, the reconstruction results at the fourth harmonics of meshing frequency show that time-domain interpolation works well to de-dopplerze the measured data. The holographic reconstruction can capture the main features of the rotating pinion sound field, and the localization results are compared well with the vibrational data. The VRA's sideband summation can also capture the stronger sources while the weaker ones are not reconstructed.

In summary, the current works combine the application and extension of traditional signal monitoring techniques and new development of the array signal processing tools to achieve the function of monitoring a nested gear structure that has not been systematically studied before. The application and extension of several classical vibrational signal processing techniques can detect the gear faults. In addition, two new development of the near-field holography techniques is achieved for near-field rotating source localization. The application of holography development to gear monitoring shows excellent potential for using an acoustical imaging system to monitor compact rotating structures.

8.4 Future Work

For the current experiment of nested planetary gear NVH data collection, one of the issues that have not been solved perfectly is the slight misalignment of the input shaft and gear train caused by the coupling. In addition, the connection between the motor coupling and the input shaft caused the shaft tilting because the diameter of the coupling hole is larger than the input shaft dimension. Hence, a different type of coupling with better tightening mechanisms can be purchased and applied to the current fixture design to improve the test's consistency further.

In terms of vibrational signal analysis, more techniques, such as kurtosis analysis and order tracking analysis, can be applied except for the current signal processing techniques. Furthermore, except for the application of other signal processing techniques, the current sideband models will be further improved to explain the sideband high order sideband behavior for WoW1 monitoring. In addition to the vibrational data measuring and signal analysis, the dynamics of the nested planetary gears can also be investigated using a lumped-parameter or finite-element model. By modeling the gear dynamics theoretically and numerically, a better understanding of the signals can be achieved.

The holographic methods for compact rotating sources have been well-developed in this study. However, the application of the current methods to real engineering cases is limited in the current study due to the restriction of time. In a later study, more data from planetary gear rotation can be measured and processed by the VRA methods based on holography. In addition to the gear monitoring, other types of the engineering problems, such as axial fan, turbo engine, bearing monitoring, can also be investigated with the methods developed in the current study.

REFERENCES

1. V.K. Ambarisha, R. G. Parker. Nonlinear dynamics of planetary gears using analytical and finite element models. *Journal of sound and vibration* 302, no. 3: 577-595, 2007.
2. A. Al-Shyyab, A. Kahraman. A non-linear dynamic model for planetary gear sets. *Proceedings of the Institution of Mechanical Engineers, Part K: Journal of Multi-body Dynamics* 221, no. 4: 567-576, 2007.
3. A. Al-Shyyab, K. Alwidyan, A. Jawarneh, H. Tlilan. Non-linear dynamic behaviour of compound planetary gear trains: model formulation and semi-analytical solution. *Proceedings of the Institution of Mechanical Engineers, Part K: Journal of Multi-body Dynamics* 223, no. 3: 199-210, 2009.
4. R. August, R. Kasuba. Torsional Vibrations and Dynamic Loads in a Basic Planetary Gear System. ASME. *J. Vib., Acoust., Stress, and Reliab*., 108(3): 348–353, 1986.
5. M. R. Bai, C. Chen. Application of convex optimization to acoustical array signal processing. *Journal of Sound and Vibration*, 332 (25): 6596-6616, 2013.
6. A. Bodas, A. Kahraman. Influence on Carrier and Gear Manufacturing Errors on the Static Load Sharing Behavior of Planetary Gear Set. *JSME International Journal*, 47 (3), 908-915, 2004.
7. F. Bonnardot, M. El Badaoui, R.B. Randall, J. Danie` re, F. Guillet, Use of the Acceleration Signal of a Gearbox in order to Perform Angular Resampling (with limited speed fluctuation). *Mechanical Systems and Signal Processing*, 19: 766–785, 2005.
8. M. Botman. Epicyclic Gear Vibrations. *J. Eng. Ind.*, 98(3): 811–815, 1976.
9. K. S. Brentner. Prediction of Helicopter Discrete Frequency Rotor Noise-A Computer Program Incorporating Realistic Blade Motions and Advanced Formulation, October 1986, NASA TM 87721.
10. L. C. Caldas, P. C. Greco, C. C. Pagani, L. A. Baccalá. Acoustic Imaging of In-Duct Aeroengine Noise Sources Using Rotating Beamforming and Phased Arrays. *IEEE Transactions on Computational Imaging*, 3 (3): 485-492, 2017.
11. M. Carley. Propeller noise fields. *Journal of Sound and Vibration*, 233 (2): 255-277, 2000.
12. M. Carley. Series Expansion for the Sound Field of Rotating Sources. *J. Acoust. Soc. Am.*, 120 (3): 1252-1256, 2006.

13. M. Carley. Series Expansion for the Sound Field of a Ring Source. *J. Acoust. Soc. Am.*, 128 (6): 3375-3380, 2010.

14. D. Casalino. An advanced time approach for acoustic analogy predictions. *Journal of Sound and Vibration*, 261 (4): 583-612, 2003.

15. G. Chardon, L. Daudet, A. Peillot, F. Ollivier, N. Bertin, R. Gribonval. Near-field acoustic holography using sparse regularization and compressive sampling principles. *The Journal of the Acoustical Society of America*, 132 (3): 1521-1534, 2012.

16. G. Cheon, R. G. Parker. Influence of manufacturing errors on the dynamic characteristics of planetary gear systems. *KSME international journal* 18 (4): 606-621, 2004.

17. C. J. Chapman. The Structure of Rotating Sound Fields. *Proc. R. Soc. Lond.* A, 440: 257-271, 1993.

18. F. Cunliffe, J. D. Smith, D. B. Welbourn. "Dynamic Tooth Loads in Epicyclic Gears*," J. Eng. Ind.*, 96(2): 578–584, 1974.

19. F. Combet, L. Gelman. An Automated Methodology for Performing Time Synchronous Averaging of a Gearbox Signal without Speed Sensor. *Mechanical Systems and Signal Processing*, 21: 2590-2606, 2007.

20. B. Delaunay. Sur la sphère vide. Cl. Des Sci. Math. 1934, 6, 793–800.

21. H. Doepfert, A. Bucher, P. Ziemer, U. Hankte. Planetary Gearbox having Nested Planetary Gear Stages. *US Patent 8613687B2*.

22. R. Dougherty, B. Walker. "Virtual rotating microphone imaging of broadband fan noise." In *15th AIAA/CEAS Aeroacoustics Conference (30th AIAA Aeroacoustics Conference)*, 3121. 2009.

23. F. Farassat. Theory of Noise Generation From Moving Bodies With an Application to Helicopter Rotors, NASA Technical Report R-451, 1975

24. F. Farassat, G. P. Succi. A review of propeller discrete frequency noise prediction technology with emphasis on two current methods for time domain calculations, *Journal of Sound and Vibration*, 71(3): 399-419, 1980.

25. F. Farassat. Linear acoustic formulas for calculation of rotating blade noise, *AIAA Journal*, 19(9): 1122-1130, 1981.

26. F. Farassat. Derivation of Formulations 1 and 1A of Farassat. *NASA TM-2007-214853*, 2007.

27. J. E. Ffowcs, D. L. Hawkings. Sound Generation by Turbulence and Surfaces in Arbitrary Motion. *Philosophical Transactions of the Royal Society of London. Series A, Mathematical and Physical Sciences*, 264 (1151): 321-342, 1969.
28. Y. Guo, and R. G. Parker. Purely Rotational Model and Vibration Modes of Compound Planetary Gears. *Mech. Mach. Theory*, 45(3): 365–377, 2010.
29. Y. Guo, Q. Liu, X. Wu, J. Na. Gear Fault Diagnosis Based on Narrowband Demodulation with Frequency Shift and Spectrum Edit. *International Journal of Engineering and Technology Innovation*, 6 (4): 243-254, 2016.
30. J. Hald, Wideband Acoustical Holography, *Proc. INTER-NOISE 2014*.
31. J. Hald, Fast Wideband Acoustical Holography, *Journal of Acoustical Society of America*, 139 (4), 1058-1517, 2016.
32. G. Herold, E. Sarradj. Microphone array method for the characterization of rotating sound sources in axial fans. *Noise Control Engineering Journal*,63 (6): 546-551, 2015.
33. G. Herold, C. Ocker, E. Sarradj, and W. Pannert. "A comparison of microphone array methods for the characterization of rotating sound sources." In *Proceedings of the 7th Berlin Beamforming Conference*, pp. 1-12. 2018.
34. Y. Hu, D. Talbot, A. Karahman. A Load Distribution Model for Planetary Gear Sets. Journal of Mechanical Design. *Journal of Mechanical Design*, 140: 1-14, 2018.
35. M. Inalpolat, A. Kahraman. A Theoretical and Experimental Investigation of Modulation Sidebands of Planetary Gear Sets. *Journal of Sound and Vibration*, 323: 677-696, 2009.
36. M. Inalpolat, A. Kahraman. "A dynamic model to predict modulation sidebands of a planetary gear set having manufacturing errors." *Journal of Sound and Vibration* 329 (4): 371-393, 2010.
37. A. Inalpolat, A. Kahraman, "Dynamic Modelling of Planetary Gears of Automatic Transmissions," *Proc. Inst. Mech. Eng.*, Part K, 222(3): 229–242, 2008.
38. S. Jekosch, E. Sarradj. "An Extension of the Virtual Rotating Array Method Using Arbitrary Microphone Configurations for the Localization of Rotating Sound Sources." In *Acoustics*, 2 (2): 330-342, 2020.
39. A. Kahraman, "Free Torsional Vibration Characteristics of Compound Planetary Gear Sets," *Mech. Mach. Theory*, 36(8), pp. 953–971, 2001.
40. A. Kahraman. "Free torsional vibration characteristics of compound planetary gear sets." *Mechanism and machine theory*, 36 (8): 953-971, 2001.

41. A. Kahraman, “Natural Modes of Planetary Gear Trains,” *J. Sound Vibration*, 173(1): 125–130, 1994.

42. A. Kahraman, “Planetary Gear Train Dynamics,” *ASME J. Mech. Des.*, 116 (3): 713–720, 1994.

43. A. Kahrahman. Load Sharing Characteristics of a Planetary Transmission. *Mechanism and Machine Theory,* 29 (8): 1151-1165, 1994.

44. A. Kahraman. Static Load Sharing Characteristics of Transmission Planetary Gear Sets: Model and Experiment. *SAE Transactions-JOURNAL OF PASSENGER CARS*, PART 2, 108 (6) 1954-1963, 1999.

45. A. Kahraman, S. Vijayakar. "Effect of internal gear flexibility on the quasi-static behavior of a planetary gear set." *J. Mech. Des.,* 123 (3): 408-415, 2001.

46. A. Kahraman, A. A. Kharazi, M. Umrani. "A deformable body dynamic analysis of planetary gears with thin rims." *Journal of sound and vibration,* 262(3): 752-768, 2003.

47. D. R. Kiracofe, R. G. Parker, “Structured Vibration Modes of General Compound Planetary Gear Systems,” *ASME J. Vib. Acoust.*, 129(1): 1–16, 2007.

48. G. Krishnappa. Gear Faults Detection Parameter Development Based on Modulation Techniques. *Proceedings of the Fifth International Congress on Sound and* V*ibration,* vol. II, *Adelaide, Australia,* December 1997.

49. G. Kotán, T. Bence, V. János. "Comparison of the rotating source identifier and the virtual rotating array method." *Periodica Polytechnica-Mechanical Engineering,* 62 (4): 261-268, 2018.

50. W. Lepak, W. Sung, T. Shi, Y. Liu, W. Thor. Localization of Noise Sources in an Outdoor HVAC Unit by using the Arbitrary Source Location Method in Combination with Wideband Acoustical Holography. *Proc. INTER-NOISE 2019*.

51. C. Liao. Nested Planetary Geartrain Design for Vibration Reduction Using Augmented Direct Gear Design Methodology, Purdue University, 2018.

52. H. Ligata., A. Kahraman, A. Singh. A Closed-Form Planet Load Sharing Formulation for Planetary Gear Sets Using a Translational Analogy. ASME J. Mech. Des., 131(2): 021007, 2009.

53. L. Lin, R. G. Parker, Analytical Characterization of the Unique Properties of Planetary Gear Free Vibration, *ASME J. Vib. Acoust.,* 121(3): 316–321, 1999.

54. J. Lin, R. G. Parker. Sensitivity of planetary gear natural frequencies and vibration modes to model parameters. *Journal of sound and vibration*, 228 (1): 109-128, 1999.

55. J. Lin, R. G. Parker. Planetary gear parametric instability caused by mesh stiffness variation. *Journal of Sound and vibration*, 249 (1): 129-145, 2002.

56. J. Lin, R. G. Parker. Mesh stiffness variation instabilities in two-stage gear systems. *J. Vib. Acoust.* 124 (1): 68-76, 2002.

57. Lowis, C. R., and P. F. Joseph. Determining the strength of rotating broadband sources in ducts by inverse methods. *Journal of Sound and Vibration*, 295 (3-5) : 614-632, 2006.

58. J. Ma, C. J. Li. Gear Defect Detection through Model-based Wideband Demodulation of Vibrations. *Mechanical Systems and Signal Processing*, 10 (5): 653-665, 1996.

59. Y. Mao, Y. Gu, D. Qi, and H. Tang. "An exact frequency-domain solution of the sound radiated from the rotating dipole point source." *The Journal of the Acoustical Society of America* 132, no. 3 (2012): 1294-1302.

60. W. Ma, B. Huan, C. Zhang, and X. Liu. "Beamforming of phased microphone array for rotating sound source localization." *Journal of Sound and Vibration* 467 (2020): 115064.

61. J. D. Maynard, E. G. Williams, Y. Lee. Near Field Acoustical Holography: I. Theory of Generalized Holography and the Development of NAH. *The Journal of the Acoustical Society of America*, **78**, 1395-1413, 1985.

62. Y. Mao, Y. Gu, D. Qi, H. Tang. An Exact Frequency-domain Solution of the Sound Radiated from the Rotating Dipole Point Source. *J. Acoust. Soc. Am.*, 132 (3), 1294-1302, 2012.

63. Y. Mao, C. Xu, D. Qi, H. Tang. Series Expansion Solution for Sound Radiation from Rotating Quadrupole Point Source. *AIAA JOURNAL*, 52 (5): 1086-1095, 2014.

64. T. Mast, F. Yu. Simplified Expansions for Radiation from a Baffled Circular Piston. *J. Acoust. Soc. Am.*, 118 (6): 3457-3464, 2005.

65. P. D. McFadden, J. D. Smith. A Signal Processing Technique for Detecting Local Defects in a Gear from the Signal Average of the Vibration. *Proc. Instn. Mech. Engrs*, 199 (4): 287-292, 1985.

66. P. D. McFadden. A Revised Model for the Extraction of Periodic Waveforms by Time Domain Averaging. *Mechanical Systems and Signal Processing*, 1 (1): 83-95, 1987.

67. P. D. McFadden. Examination of a Technique for the Early Detection of Failure in Gears by Signal Processing of the Time Domain Average of the Meshing Vibration. *Mechanical Systems and Signal Processing*, 1 (2): 173-183, 1987.

68. P. D. McFadden. Interpolation Techniques for Time Domain Averaging of Gear Vibration. *Mechanical Systems and Signal Processing*, 3 (1): 87-97, 1989.

69. P. D. McFadden. Detection of Gear Faults by Decomposition of Matched Differences of Vibration Signals. *Mechanical Systems and Signal Processing*, 14 (5): 805-817, 2000.

70. P. D. McFadden. A Technique for Calculating the Time Domain Averages of the Vibration of the Individual Planet Gears and the Sun Gear in an Epicyclic Gearbox. *Journal of Sound and Vibration*, 144 (1): 163-172, 1991.

71. P. D. McFadden. Window Functions for Calculation of the Time Domain Averages of the Vibration of the Individual Planet Gears and Sun Gear in an Epicyclic Gearbox. *Journal of Vibration and Acoustics*, 116: 179-187, 1994.

72. P. D. McFadden. Low Frequency Vibration Generated by Tooth Impact. *NDT International,* 18 (5): 279-282, 1985.

73. P. D. McFadden, J. D. Smith. An Explanation for the Asymmetry of the Modulation Sidebands about the Tooth Meshing Frequency in Epicyclic Gear Vibration. *Proc. Instn. Mech. Engrs,* 199 (1): 65-70, 1985.

74. P. D. McFadden. Detecting Fatigue Cracks in Gears by Amplitude and Phase Demodulation of the Meshing Vibration. *Journal of Vibration, Acoustics, Stress, and Reliability in Design*, 108: 165-170, 1986.

75. P. D. McFadden. Determining the Location of a Fatigue Crack in a Gear from the Phase of the Change in the Meshing Vibration. *Mechanical Systems and Signal Processing*, 2 (4): 403-409, 1988.

76. J. McNames. Fourier Series Analysis of Epicyclic Gearbox. *Journal of Vibration and Acoustics*, 124: 150-152, 2002.

77. O. Minck, N. Binder, O. Cherrier, L. Lamotte, V. Budinger. Fan noise analysis using a microphone array. *International Conference on Fan Noise, Technology, and Numerical Methods*, Senlis, France, 2012.

78. M. Mosher. Understanding the Vibration Spectra of Planetary Gear Systems for Fault Detection. *Proceedings of ASME Design Engineering Technical Conferences*, Paper No.PTG-48082, IL, USA, September 2003.
79. Motion control clip, https://www.motioncontroltips.com/helical-gears-what-are-they-and-where-are-they-used/.
80. W. Pannert, C. Maier. "Rotating beamforming–motion-compensation in the frequency domain and application of high-resolution beamforming algorithms." *Journal of Sound and Vibration*, 333 (7): 1899-1912, 2014.
81. R. G. Parker, V. Agashe, S. M. Vijayakar. "Dynamic response of a planetary gear system using a finite element/contact mechanics model." *J. Mech. Des.*, 122 (3): 304-310, 2000.
82. M. A. Poletti. Series Expansions of Rotating two and three Dimensional Sound Fields. *J. Acoust. Soc. Am.*, 128 (6): 3363-3374, 2010.
83. M. A. Poletti, P. D. Teal. Comparison of Methods for Calculating the Sound Field due to a Rotating Monopole. *J. Acoust. Soc. Am.*, 129 (6): 3515-3520, 2011.
84. J. G. Proakis, D. G. Manolakis. "Digital signal processing." *MPC, New York* (1992).
85. R. B. Randall. A New Method of Gear Modelling. Journal of Mechanical Design, 104: 259-267, 1982.
86. P. D. Samuel, D. J. Pines. Vibration separation methodology for planetary gear health monitoring. *Proc. SPIE 3985, Smart Structures and Materials 2000: Smart Structures and Integrated Systems*, 2000.
87. P. Sijtsma, O. Stefan, H. Hermann. "Location of rotating sources by phased array measurements." In *7th AIAA/CEAS Aeroacoustics Conference and Exhibit*, p. 2167. 2001
88. A. Singh. Application of a system level model to study the planetary load sharing behavior. Journal of Mechanical Design, 127: 469-476, 2005.
89. A. Singh. Influence of planetary needle bearings on the performance of single and double pinion planetary systems. In *International Design Engineering Technical Conferences and Computers and Information in Engineering Conference*, 4742: 853-862. 2005.
90. T. Shi, Y. Liu, J. S. Bolton. The use of Wideband Acoustical Holography for Noise Source Visualization. INTER-NOISE and NOISE-CON Congress and Conference Proceedings, 252 (2), 479-490.

91. T. Shi, Y. Liu, J. S. Bolton. Diesel Engine Noise Source Visualization with Wideband Acoustical Holography, *SAE Technical Paper*, 2017-01-1874, 2017.

92. T. Shi, J. S. Bolton. Separation of closely-spaced acoustics sources in an under-determined system with convex optimization. INTER-NOISE and NOISE-CON Congress and Conference Proceedings, 2018.

93. T. Shi, Y. Liu, J. S. Bolton. "Spatially sparse sound source localization in an under-determined system by using a hybrid compressive sensing method." *The Journal of the Acoustical Society of America* 146, no. 2 (2019): 1219-1229.

94. P. Sondkar, A. Kahraman, A Dynamic Model of a Double- Helical Planetary Gear Set, *Mech. Mach. Theory*, 70:157–174, 2013.

95. T. Sun, H. Hu. Nonlinear dynamics of a planetary gear system with multiple clearances. *Mechanism and Machine Theory*, 38 (12): 1371-1390, 2003.

96. T. Suzuki. L1 generalized inverse beam-forming algorithm resolving coherent/incoherent, distributed and multipole sources. *Journal of Sound and Vibration,* 330 (24): 5835-5851, 2011.

97. R. M. Stewart. Some Useful Data Analysis Techniques for Gearbox Diagnostics. *Report MHM/R/10/77*, 1977, Machinery Health Monitoring Group, Institute of Sound and Vibration Research, University of Southampton.

98. C. R. Trimble. *What is signal averaging?* Hewlett-Puck& Journal, 19(8): 2-7, 1968.

99. W. A. Veronesi, J. D. Maynard. Nearfield acoustic holography (NAH) II. Holographic reconstruction algorithms and computer implementation. *The Journal of the Acoustical Society of America*, **81**, 1987, 1307-1322.

100. C. M. Vicuna. Theoretical Frequency Analysis of Vibrations from Planetary Gearboxes. *Forsch Ingenieurwes*, 76: 15-31, 2012.

101. S. M. Vijayakar, 2005, "Calyx User's Manual," http://ansol.us.

102. S. Wang, C. Meesap. Investigation on Mesh and Sideband Vibrations of Helical Planetary Ring Gear Using Structure, Excitation and Deformation Symmetries. *Chin. J. Mech. Eng.*, 31:104, 2018.

103. W. Wang. Early Detection of Gear Tooth Cracking using the Resonance Demodulation Technique. *Mechanical Systems and Signal Processing*, 15 (5): 887-903, 2001.

104. L. Xiang, N. Gao, A. Hu. Dynamic analysis of a planetary gear system with multiple nonlinear parameters. *Journal of Computational and Applied mathematics,* 327: 325-340, 2018.

105. Wikipedia, https://en.wikipedia.org/wiki/Spur_gear.

106. J. Yang, C. Zhang, W. Ma. "Spatial interpolation methods for virtual rotating array beamforming with arbitrary microphone configurations." *Aerospace Systems* (2021): 1-10.

107. C. Yuksel, A. Kahraman. Dynamic tooth loads of planetary gear sets having tooth profile wear. *Mechanism and Machine Theory* 39 (7): 695-715, 2004

108. X. Zhang, C. Bi, Y. Zhang, L. Xu. A time-domain inverse technique for the localization and quantification of rotating sound sources. *Mechanical Systems and Signal Processing*, 90: 15-29, 2017

APPENDIX

1. Appendix-1, calculation of gear meshing frequencies

The first torque transmission path to be considered is the condition fixing S1. For the carrier-1 gearset, if the input shaft speed is 1000rpm, which means that A1's rotational speed is $f_{A1} = 16.667\, r/s$. Because S1 is engaged, the rotational speed of the gear is $f_{S1} = 0\, r/s$. The carrier speed can be calculated as,

$$f_C = \frac{N_A}{N_A + N_S} f_{A1} = \frac{86}{86+42} 16.667\, r/s = 11.198\, r/s\,. \qquad \text{A.1. 1}$$

With the knowledge of the input shaft speed, it is easy to calculate that the time to complete one revolution for input shaft is $\frac{1}{16.667}$ s. In this time duration, the carrier moves $\frac{11.198}{16.667}$ revolution. So that the relative rotation between annulus gear and carrier is $(1 - \frac{11.198}{16.667})/\text{rev}$. So the number of the teeth contact per revolution between S1/P1 and P1/A1 is,

$$O_{c1} = \frac{f_C}{f_{A1}} N_S = (1 - \frac{f_C}{f_{A1}}) N_A = 28.22 \qquad \text{A.1. 2}$$

For 1000 rpm input shaft speed, the meshing frequency is,

$$F_{c1} = O_{c1} * f_{A1} = 28.22 * 16.6667 \ = \ 470.34 Hz \qquad \text{A.1. 3}$$

For the meshing frequency of carrier-2, the same procedures can be followed as carrier-1 calculation. However, in this case, the speed for S2 is $f_{S2} = 16.667 r/s$ and the speed for annulus gear A2 is $f_{A2} = 0$. The carrier rotating speed is the same as carrier-1, which is $f_C = 11.98\text{r/s}$. The time to complete one revolution for S2 is $\frac{1}{16.667}$ s. In the meanwhile, the carrier moves $\frac{11.198}{16.667}$ revolution. Therefore, the relative rotation between annulus gear A2 and carrier is $(1 - \frac{11.198}{16.667})$. So the number of the contact per revolution between S2/P2 and P2/A2 is:

$$O_{\text{c2}} = \left(1 - \frac{11.198}{16.667}\right) \times 94 = \left(\frac{11.198}{16.67} - \frac{7.473}{16.67}\right) \times 138 = 30.84\,. \qquad \text{A.1. 4}$$

For 1000 rpm input shaft speed, the meshing frequency of the inner circle is,

$$F_{\text{c2}} == O_{c2} * f_{S2} = 30.84 * 16.6667 \ = \ 514.05 \text{ Hz}\,. \qquad \text{A.1. 5}$$

For the second transmission path when A2 is engaged, the calculation needs to start with the outer carrier. Assume that the input shaft speed is 1000rpm which is equivalent to $f_{S2} =$

$16.667\ r/s$. In addition, annulus gear A2 is engaged, so that $f_{A2} = 0\ r/s$. Using the above information, the carrier frequency can be calculated as,

$$f_{C2} = \frac{N_A}{N_A + N_S} f_{A1} = \frac{94}{94 + 138} 16.667\ r/s = 6.753 r/s\,. \qquad \text{A.1. 6}$$

The meshing order can be calculated using the carrier rotating frequency and gear teeth number,

$$O_{C2} = \frac{6.753}{16.67} \times 138 = \left(1 - \frac{6.753}{16.67}\right) \times 94 = 55.91\,. \qquad \text{A.1. 7}$$

Using the meshing order, meshing frequency can be subsequently derived,

$$F_{C2} = 55.91 * 16.6667 \ = \ 931.9Hz\,. \qquad \text{A.1. 8}$$

For the inner carrier the known parameters are $f_{C1} = f_{C2} = 6.753 r/s$, and the A1 speed is $f_{A1} = 16.667 r/s$. So the S1 speed can be calculated using 0,

$$f_{S1} = -\frac{86}{42}(16.667 - 6.753) + 6.753 \ = \ -13.55 r/s\,. \qquad \text{A.1. 9}$$

In addition, the carrier-1 meshing order can be calculated,

$$O_{C2} = \ \left|\left(1 - \frac{6.753}{16.667}\right) * 86\right| = \ 51.155\,. \qquad \text{A.1. 10}$$

Using the meshing order information, it is straightforward that meshing frequency for 1000rpm input shaft speed is,

$$F_{C2} = \ 51.155 * \frac{16.667 r}{s} = 852.6Hz\,. \qquad \text{A.1. 11}$$

2. Appendix-2, sound field of stationary receiver due to a moving source

The frequency domain sound pressure can be calculated by applying Fourier transform to Eq. 5. 4,

$$\hat{p}(\vec{x},\omega) = \int_{-\infty}^{\infty}\int_{-\infty}^{\infty} \frac{Q(\tau)}{4\pi R(\tau)} \delta(t - \tau - \frac{R(\tau)}{c}) d\tau e^{-i\omega t} dt\,, \qquad \text{A.2. 1}$$

Therefore, switch the order of integration, we can obtain,

$$\hat{p}(\vec{x},\omega) = \int_{-\infty}^{\infty}\int_{-\infty}^{\infty} \delta(t - \tau - \frac{R(\tau)}{c}) e^{-i\omega(t-\tau)} dt \frac{Q(\tau)}{4\pi R(\tau)} e^{-i\omega\tau} d\tau\,. \qquad \text{A.2. 2}$$

It was noted that the Green's function has the following property,

$$\frac{e^{ikR(\tau)}}{4\pi R(\tau)} = \int_{-\infty}^{\infty} \delta(t - \tau - \frac{R(\tau)}{c}) e^{-i\omega(t-\tau)} dt\,, \qquad \text{A.2. 3}$$

In addition, the exponential function $\frac{e^{iR(\tau)}}{4\pi R(\tau)}$ in this equation can be expressed using spherical harmonic expansion form,

$$\frac{e^{ikR(\tau)}}{4\pi R(\tau)} = -ik \sum_{m=-\infty}^{m=\infty} e^{im(\varphi-\varphi_s(\tau))}$$
$$\sum_{n=|m|}^{\infty} N^2(n,m) j_n(kr_<)\, h_n^2(kr_>) P_m^n(cos\theta) P_m^n(cos\theta_s) \,, \quad \text{A.2. 4}$$

where the normalization factor $N(n,m) = \sqrt{\frac{(2n-1)(n-m)!}{4\pi(n+m)!}}$, j_n is the spherical Bessel function of first kind, h_n is spherical Hankel function, P_m^n is the associated Legendre function of n^{th} order and m^{th} degree, $r_<$ is the smaller value of r_s and r, $r_<$ is the larger value of r_s and r, and k is wave number. Assuming the sound source is composed of infinite number of tonal components,

$$Q(\tau) = \sum_{\alpha=-\infty}^{\infty} Q_\alpha e^{i\omega_\alpha \tau} \,, \quad \text{A.2. 5}$$

Substitute Eq. A.2. 3, Eq. A.2. 4 and Eq. A.2. 5 into Eq. A.2. 2, the frequency domain sound field expression of the rotating source at a stationary receiving location is,

$$\hat{p}(\vec{x},\omega) = \sum_{\alpha=1}^{\infty} Q_\alpha \int_{-\infty}^{\infty} -ik \sum_{m=-\infty}^{m=\infty} e^{im(\varphi-\varphi_{s_0})}\, e^{-i(\omega-\omega_\alpha+m\Omega_s)\tau}$$
$$\sum_{n=|m|}^{\infty} N^2(n,m) j_n(kr_<)\, h_n^2(kr_>) P_m^n(cos\theta) P_m^n(cos\theta_s) d\tau \,. \quad \text{A.2. 6}$$

Calculate the integration, we can obtain,

$$\hat{p}(\vec{x},\omega) = \sum_{\alpha=1}^{\infty} -iQ_\alpha k j_n(kr_<) h_n^2(kr_>) \sum_{m=-\infty}^{m=\infty} e^{im(\varphi-\varphi_{s_0})}$$
$$\delta(\omega-\omega_\alpha+m\Omega_s) \sum_{n=|m|}^{\infty} N^2(n,m)\, P_m^n(cos\theta) P_m^n(cos\theta_s) \quad \text{A.2.7}$$

Assuming interval between discrete frequency $\Delta\omega = \omega_{\alpha+1} - \omega_\alpha$ is infinitely small, the summation can be expressed as integral form,

$$\hat{p}(\vec{x},\omega) = \int_{-\infty}^{\infty} -iQ(\omega) \sum_{m=-\infty}^{m=\infty} e^{im(\varphi-\varphi_{s_0})} k j_n(kr_>) h_n^2(kr_>)$$
$$\delta(\omega-\omega_\alpha+m\Omega_s) \sum_{n=|m|}^{\infty} N^2(n,m) P_m^n(cos\theta) P_m^n(cos\theta_s)\, d\omega \,. \quad \text{A.2. 8}$$

After this integral is evaluated, the final expression for the series expression representation of frequency domain pressure field due to a rotating source is,

$$\hat{p}(\vec{x},\omega) = \sum_{m=-\infty}^{m=\infty} g_m(\omega)\, e^{im(\varphi_0-\varphi_{s_0})} Q(\omega+m\Omega_s) \,. \quad \text{A.2. 9}$$

where $g_m(\omega)$ can be expressed as

$$g_m(\omega) = -ikj_n(kr_<) h_n^2(kr_>) \sum_{n=|m|}^{\infty} N^2(n,m) P_m^n(cos\theta) P_m^n(cos\theta_s) \,. \quad \text{A.2.10}$$

In the last section, spherical harmonic expansion expression of the sound field at stationary receiver due to rotating sources is calculated, and it was shown that,

$$\frac{e^{ikr(\tau)}}{4\pi r(\tau)} = \int_{-\infty}^{\infty} \delta(t-\tau-\frac{r(\tau)}{c}) e^{-i\omega(t-\tau)} dt \,, \quad \text{A.2. 11}$$

With this transformation, it can be

$$G(t;\tau) = \delta(t - \tau - \frac{r(\tau)}{c}) = \int_{-\infty}^{\infty} \frac{e^{ikr(\tau)}}{4\pi r(\tau)} e^{i\omega(t-\tau)} d\omega \ , \qquad \text{A.2. 12}$$

Expand the exponential function with spherical harmonics terms, it can be expressed as,

$$G(t;\tau) = \delta\left(t - \tau - \frac{r(\tau)}{c}\right) =$$

$$\int_{-\infty}^{\infty} e^{i\omega(t-\tau)} d\omega - ik \sum_{m=-\infty}^{m=\infty} e^{im(\varphi_r - \varphi_s(\tau))} \qquad \text{A.2. 13}$$

$$\sum_{n=|m|}^{\infty} N^2(n,m) j_n(kr_<)\, h_n^2(kr_>) P_m^n(cos\theta_r) P_m^n(cos\theta_s) \ \ ,$$

If the receiver is also rotating at speed Ω_r, so the azimuth angle of the receiver can be expressed has $\varphi_r(t) = \varphi_{r_0} + \Omega_r t$.

$$G_\Omega(t;\tau) = \delta\left(t - \tau - \frac{r(t,\tau)}{c}\right) =$$

$$\int_{-\infty}^{\infty} e^{i\omega(t-\tau)} d\omega - ik \sum_{m=-\infty}^{m=\infty} e^{im(\varphi_r(t) - \varphi_s(\tau))} \qquad \text{A.2. 14}$$

$$\sum_{n=|m|}^{\infty} N^2(n,m) j_n(kr_<)\, h_n^2(kr_>) P_m^n(cos\theta_r) P_m^n(cos\theta_s) \ ,$$

This derivation also starts from the time domain expression of rotating source sound fields,

$$\hat{p}(\vec{x}_r, \omega) = \int_{-\infty}^{\infty} \int_{-\infty}^{\infty} G(t;\tau) Q(\tau) d\tau \, e^{-i\omega t} dt \ . \qquad \text{A.2. 15}$$

The source term still follows Eq.A.2. 5. Substitute Eq.A.2. 5 and Eq. A.2. 14 into Eq. Eq. A.2. 15, the generalized spherical harmonic expression of the sound field at the receiver with arbitrary rotating speed can be obtained,

$$\hat{p}(x, \omega) = \sum_{m=-\infty}^{m=\infty} g_m(\omega - m\Omega_r)\, e^{im(\varphi_{r_0} - \varphi_{s_0})} Q(\omega + m(\Omega_s - \Omega_r)) \ . \qquad \text{A.2. 16}$$

If the receiver is stationary, so that $\Omega_r = 0$, the expression can be reduced to the same form as Eq.A.2. 9. If source and receiver are rotating at the same speed, i.e. $\Omega_s = \Omega_r$, the receiver sound pressure at frequency ω is,

$$\hat{p}(x, \omega) = \sum_{m=-\infty}^{m=\infty} g_m(\omega - m\Omega_r)\, e^{im(\varphi_{r_0} - \varphi_{s_0})} Q(\omega) = G_{\Omega_1}(\omega) Q(\omega) \ , \qquad \text{A.2. 17}$$

where $G_{\Omega_1}(\omega)$ is Green's function for rotating receiver and source, which is different from the stationary Green's function.

3. Appendix-3, zeroth order interpolation error analysis example

The error analysis explains why zero-order interpolation algorithm works for the signal spatial interpolation. Therefore, the virtual array interpolating error will be analyzed in this section using a simulation case. It will be shown that the interpolating error is significantly smaller than the signal amplitude if the microphone array is dense enough. The source is a 2000Hz monochromatic rotating monopole, which has the period of $T = 5 \times 10^{-4} s$. To achieve the interpolation of high accuracy, the sound travelling time difference between virtual rotating microphone and stationary microphone has to be much smaller than the period of source signals, as shown in Figure A 1. The schematic illustration of the source and receiver is shown in Figure A 1, where the red dot on the receiver plane represents the virtual rotating receiver. The travelling distance from source to two receivers are calculated as,

$$r_{s,r}(t) = \sqrt{(x_s - x_r)^2 + (y_s - y_r)^2 + (z_s - z_r)^2}\ , \qquad \text{A.3. 1}$$

where $r_{s,r}(t)$ is the distance between the source and receiver. The parameters for the simulated case are shown in **Error! Reference source not found.**. Assuming the receiver array is arranged in a ring shape with 0.3m radius and 16 microphones. The virtual rotating microphone is rotating on the circle of microphones, and the largest distance between the virtually rotating microphone and the receiver is reached when the virtually rotating microphone is at the middle of two stationary microphone, which is shown in Figure A 2. In this situation, the coordinates of the stationary receiver is $\left(x_{r_1}, y_{r_1}, z_{r_1}\right) = (-0.3\ m, 0, 0.5\ m)$, and the coordinates of the VRA receiver is $\left(x_{r_2}, y_{r_2}, z_{r_2}\right) = (-0.3\cos(\frac{\pi}{32})\ m, 0.3\sin(\frac{\pi}{32})\ m, 0.5\ m)$. The source rotating radius is 0.25m, so the source coordinates can be expressed as $(x_s, y_s, z_s) = (0.25\cos(\varphi_s)\ m, 0.25\sin(\varphi_s)\ m, 0)$. So that the travelling distance difference between source to r_1 and r_2 can be calculated as,

$$\Delta r_{s,r}(t) = \left| r_{s,r1}(t) - r_{s,r2}(t) \right|\ , \qquad \text{A.3. 2}$$

Therefore, the travelling time difference is calculated by $\Delta t_{s,r}(t) = \Delta r_{s,r}(t)/c$. The travelling time difference and the source signals period ratio is calculated for sources azimuth location φ_s from 0 to 2π,

$$D_{s,r}(t) = \frac{\Delta t_{s,r}(t)}{T}\ . \qquad \text{A.3. 3}$$

As shown in Figure A 3, the ratio between the time travelling difference and the signal period is within 25% for the current case. The error analysis shows that the signals on two adjacent microphones are close to each other, which explains why 0 order interpolation works for VRA signal generation.

Table A 1. Error Analysis Example

Source parameter	• Frequency: 2000Hz • Rotating radius: 0.25m
Array parameter	• Radius: 0.3m • Number of mics: 16
Source to receiver distance	• 0.5m

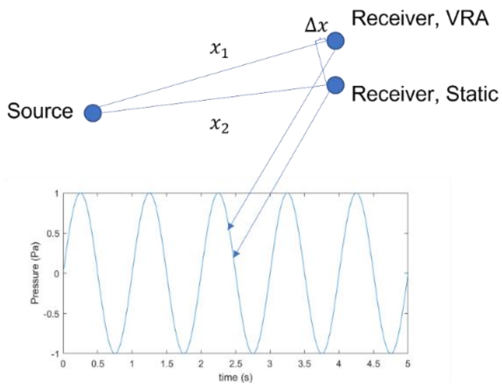

Figure A 1. Error Analysis of 0 order Interpolation using Monochromatic Signal

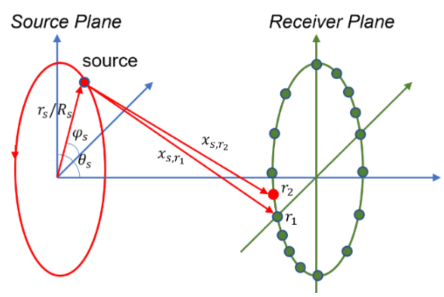

Figure A 2. Schematic Illustration of Source and Receiver

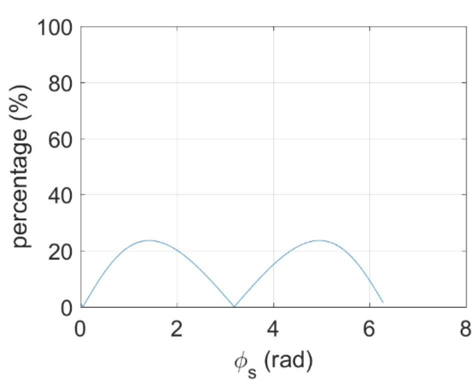

Figure A 3. The percentage of time travelling difference over signal period T